CNWRA 95-012

AN EXPERIMENTAL SCALE-MODEL STUDY OF SEISMIC RESPONSE OF AN UNDERGROUND OPENING IN JOINTED ROCK MASS

Prepared for

Nuclear Regulatory Commission
Contract NRC-02-93-005

Prepared by

Center for Nuclear Waste Regulatory Analyses
San Antonio, Texas

June 1995

CNWRA 95-012

AN EXPERIMENTAL SCALE-MODEL STUDY OF SEISMIC RESPONSE OF AN UNDERGROUND OPENING IN JOINTED ROCK MASS

Prepared for

Nuclear Regulatory Commission
Contract NRC-02-93-005

Prepared by

Daniel D. Kana
Douglas J. Fox
Sui-Min (Simon) Hsiung
Asadul H. Chowdhury

Center for Nuclear Waste Regulatory Analyses
San Antonio, Texas

June 1995

PREVIOUS REPORTS IN SERIES

Number	Name	Date Issued
CNWRA 90-004	Qualification Studies on the Distinct Element Code UDEC Against Some Benchmark Analytical Problems	January 1990
CNWRA 90-005	Development of a Rock Joint Dynamic Shear Test Apparatus	January 1990
CNWRA 90-006	Qualification Studies on the Finite Element Code HONDO II Against Some Benchmark Analytical Problems	February 1990
NUREG/CR-5440	Critical Assessment of Seismic and Geomechanics Literature Related to a High-Level Nuclear Waste Underground Repository	June 1991
CNWRA 92-005	Thermo-Hydro-Mechanical Coupled Modeling: Multiple Fracture Model, BMT2 Coupled Stress — Flow Model, TC1 DECOVALEX — PHASE I	April 1992
CNWRA 92-012	Field Site Investigation: Effect of Mine Seismicity on a Jointed Rock Mass	December 1992
CNWRA 93-002	Thermo-Hydro-Mechanical Coupled Modeling: Near Field Repository Model, BMT3 DECOVALEX — PHASE II	August 1993
NUREG/CR-6178	Laboratory Characterization of Rock Joints	May 1994
NUREG/CR-6216	Evaluation of Rock Joint Models and Computer Code UDEC Against Experimental Results	November 1994
CNWRA 94-021	Thermo-Hydro-Mechanical Coupled Modeling: Big Ben Experiment, TC3 DECOVALEX—Phase III	September 1994
NUREG/CR-6283	Field Site Investigation: Effect of Mine Seismicity on Groundwater Hydrology	April 1995

ABSTRACT

This report describes an experimental investigation conducted by the Center for Nuclear Waste Regulatory Analyses (CNWRA) to (i) obtain a better understanding the seismic response of an underground opening in a highly-fractured and jointed rock mass and (ii) generate a data set that can be used to evaluate the capabilities (analytical methods) to calculate such response. This report describes the design and implementation of simulated seismic experiments and results for a 1/15 scale model of a jointed rock mass with a circular tunnel in the middle. The discussion on the design of the scale model includes a description of the associated similitude theory, physical design rational, model material development, preliminary analytical evaluation, instrumentation design and calibration, and model assembly and pretest procedures. The thrust of this discussion is intended to provide the information necessary to understand the experimental setup and to provide the background necessary to understand the experimental results. The discussion on the experimental procedures and results includes the seismic input test procedures, test runs, and measured excitation and response time histories. The closure of the tunnel due to various levels of seismic activity is presented. A threshold level of seismic input amplitude was required before significant rock mass motion occurred. The experiment, though designed as a two-dimensional representation of a rock mass, behaved in a somewhat three-dimensional manner, which will have an effect on subsequent analytical model comparison.

CONTENTS

CONTENTS

FIGURES

FIGURES

FIGURES

FIGURES

FIGURES

TABLES

ACKNOWLEDGMENTS

The authors wish to express their sincere appreciation to several colleagues who provided special assistance during the conduct of this work. A.M. Pickens contributed his talents throughout the project and provided the primary technical efforts for conduct of the experiments. J.K. Dean aided with design and fabrication, while D.E. Massey, G.L. Escobedo, and D.C. Scheidt aided with design, assembly, calibration, and checkout of the apparatus. J.F. Unruh and T.A. Grimley provided hardware and software assistance, while J.F. Unruh and M.P. Ahola performed preliminary analytical calculations, which aided the preparation of the experimental details.

This report was prepared to document work performed by the Center for Nuclear Waste Regulatory Analyses (CNWRA) for the Nuclear Regulatory Commission (NRC) under Contract No. NRC-02-93-005. The activities reported here were performed on behalf of the NRC Office of Nuclear Regulatory Research, Division of Regulatory Applications. This report is an independent product of the CNWRA and does not necessarily reflect the views or regulatory position of the NRC.

The authors would like to thank D.J. Pomerening for the technical review and W.C. Patrick for the programmatic review of the report. The authors are thankful to E. Cantu, C. Garcia, Y. Lozano, and R. Sanchez for skillful typing of the report and to J.W. Pryor, who provided a full range of expert editorial services to the preparation of the final document.

QUALITY OF DATA

DATA: CNWRA-generated original data contained in this report meets quality assurance requirements described in the CNWRA Quality Assurance Manual.

ANALYSES AND CODES: UDEC computer code was used for the preliminary analysis contained in this report. This computer code is controlled under the CNWRA's Development and Control of Scientific and Engineering Software procedure.

EXECUTIVE SUMMARY

A state-of-the-art literature review conducted by the Center for Nuclear Waste Regulatory Analyses (CNWRA) revealed that repetitive ground motions due to seismic activities may impact both the short- and long-term performance of a repository. The fundamental failure mechanism for an excavation subjected to repetitive seismic loading is through accumulation of shear displacements along joints. Specific seismic implications to repository design and performance may include cumulative effects of repetitive seismic loads on (i) underground opening stability and (ii) creation of preferential water pathways to connect the emplacement area with perched water zones, neighboring steep hydraulic gradient zones, or the moisture condensation zone above the emplacement area. These cumulative effects cannot be analyzed by extrapolation of response data from a single earthquake or nuclear test. New techniques need to be established for simulation of a rock mass subjected to repetitive episodes of seismic events. The Seismic Rock Mechanics research project conducted studies of repository response due to repetitive dynamic loadings. As part of this research project, an experimental scale-model study on the seismic response of a jointed rock mass has been undertaken at the CNWRA. The goal of the program is to investigate the potential effects of repetitive seismic events on a jointed rock mass near an underground opening.

Major activities performed for this study included developing simulant material, making rock simulant ingots, fabricating and assembling the components to construct the experimental setup, developing testing procedures, and performing dynamic experiments on a small-scale model of a jointed rock mass using a Southwest Research Institute shaking table. This scale model consisted of approximately 670 cast simulated-rock ingots aligned within a testing frame oriented at 45° to the horizontal. The ingredients of the rock-simulant material are Type I Portland cement, barite, water, bentonite, DARACEM-100 (plasticizer), vinsol resin (air entrainment), and Ivory liquid soap. In the center of the simulated rock mass was a 15.2-cm diameter circular tunnel. The simulated-rock ingots were fabricated with appropriate physical and surface (interface) roughness properties to simulate those of naturally jointed Apache Leap welded tuff with a scale of 1/15. However, the density of the simulant material did not strictly follow the similitude requirements due to the need for this material to remain brittle and exhibit surface wear properties approximately similar to those of the prototype material. This physical distortion is judged not to have significant effect on the validity of the experimental results for use in verification of computer codes in predicting rock-mass responses to repetitive dynamic loads and in obtaining a better understanding of rock mass dynamic behavior around underground openings.

Test procedures were based on what can be called an "incremental fragility level" philosophy. Test runs were started at a very low peak excitation displacement level, and this amplitude was incrementally increased as the runs progressed. The input excitation was displacement controlled, that is, in the form of displacement time history and, at each excitation level, four test runs were made. A total of 21 test runs were conducted. The excitation displacement input signal was derived from an accelerogram measured at the Guerrero array for the September 1985 Mexico City earthquake using a 1/15-scale.

The data acquisition system was based on a 486 (66 MHz) personal computer and consisted of 50 data channels. The sampling rate for each channel was 2,800 data points/s for a duration of 10 s for each run. The measurements for the dynamic scale-model experiments included ingot deformation (strain), accelerations, interface (joint) normal and shear displacements, variations of cable loads that provided the initial stress boundary condition for the scale model, and opening convergences.

The dynamic response is found to occur throughout the seismic event, while permanent offsets (dislocation or displacement) occur only at specific times during event. These permanent dislocations generally occur at local amplitude extremes of displacement and not at acceleration peaks. Dislocations do not necessarily occur at the overall peak displacements. Acceleration measurements near the tunnel wall on both sides of the rock mass model show apparent differences, an indication that the rock mass was responding in a three-dimensional manner.

The results of this experimental investigation show that a threshold level of seismic input amplitude is required before any significant amount of permanent rock mass deformation will occur and begin to accumulate. Thus, lower amplitude seismic events may not have much effect on underground opening stability. Multiple seismic events at higher amplitudes, on the other hand, are likely to have an impact through cumulative effect of permanent deformations around underground tunnels or openings. Thus, once the threshold seismic amplitude can be determined, this level can be used as a limiting value for seismic design of underground facilities. This investigation confirmed the CNWRA field study result at the Lucky Friday Mine which shows that rock mass deformation around an excavation as a result of repetitive episodes of seismic events is in the form of accumulation of joint shear displacement, which gradually weakens the rock mass.

1 INTRODUCTION

1.1 BACKGROUND

In 1987, the United States Congress designated Yucca Mountain (YM), located approximately 160 km northwest of Las Vegas, Nevada, as the only site to be characterized to determine its suitability for building a repository for high-level nuclear waste (HLW). The proposed waste emplacement horizon is about 300 m beneath YM, in a densely welded prominently vertically and subvertically jointed tuff. The unit was chosen as the proposed repository horizon because of its thickness, lateral continuity, dense welding, and its location in the unsaturated zone about 200 to 400 m above the water table.

An important phenomenon that could affect the short- and long-term performance of a repository is repeated ground motion due to seismic activities (Kana et al., 1991; Nuclear Waste Technical Review Board, 1992). The fundamental failure mechanism for an excavation in a jointed rock mass subjected to repetitive episodes of seismic events is the accumulation of shear displacements at joints. Specific seismic implications for repository design and performance may include cumulative effects of repetitive seismic loads on (i) underground opening stability and (ii) creation of preferential water pathways to connect the emplacement area with perched water zones, neighboring steep hydraulic gradient zones, or the moisture condensation zone above the emplacement area.

The cumulative effects of these repetitive seismic loadings cannot be analyzed by extrapolation of response data from a single earthquake or nuclear test. New techniques need to be established to simulate rock mass that has been subjected to repetitive episodes of seismic events. To develop an appropriate technique, it is necessary to (i) determine the significance of the geomechanical responses due to repetitive seismic events, (ii) establish reliable data sets that permit a better understanding of important parameters controlling the joint behavior and that reflect the relation between geomechanical responses and repetitive seismic events in a properly characterized rock mass, and (iii) determine if currently available rock joint models and the associated computer codes adequately describe the behavior of rock joints.

The Seismic Rock Mechanics (SRM) research project, conducted by the Center for Nuclear Waste Regulatory Analyses (CNWRA), investigated repository response due to repetitive seismic loadings. This research project has the dual focus of (i) understanding the key parameters affecting repository performance under repeated seismic loadings, and (ii) evaluating current capabilities for calculating such effects. A primary goal of this research project is to evaluate, validate, and reduce uncertainties in the prediction models. These models eventually will be used to assess the effects of possible earthquakes as well as ground shock events on the short- and long-term performances of a proposed underground repository at YM. The Nuclear Regulatory Commission (NRC) staff and its contractors anticipate using the results of this study during the process of License Application (LA) review to determine the adequacy of the U.S. Department of Energy (DOE) repository design relevant to seismic activities.

As part of this research project, CNWRA has undertaken an experimental scale-model study of seismic response of an underground opening in a jointed rock mass. Its aim is to generate a reliable data set, with special emphasis on effects of repetitive seismic loads, for the dynamic response of the rock mass surrounding underground openings for understanding the key seismic parameters that will affect repository design and performance. This experimental model study is an extension of the CNWRA study on "Laboratory Characterization of Rock Joints" (Hsiung et al., 1993). This study also complements the

field study "Field Site Investigation: Effect of Mine Seismicity on a Jointed Rock Mass" (Hsiung et al., 1992) that has been conducted by the CNWRA at Lucky Friday Mine, Idaho.

1.2 PURPOSE AND SCOPE

The purpose of the experimental model study is to investigate jointed rock mass behavior surrounding underground openings subjected to repetitive seismic loads and to develop experimental data on the behavior of a rock mass under controlled conditions. These data can then be used for validation of models and verification of associated computer codes for dynamic analysis of rock masses.

The activities associated with this laboratory experimental model study included: (i) physical model design; (ii) model material development; (iii) preliminary analytical evaluations to assist the preparation of the experimental details; (iv) instrumentation design, construction, and calibration; (v) model assembly and experimental procedures development; (vi) dynamic experiments of the physical model using a shaking table; and (vii) result analysis and evaluation.

2 DESIGN OF ROCK MASS MODEL

2.1 THEORY OF PHYSICAL MODEL

A conceptual diagram of a two-dimensional (2D) representation of an underground rock mass with a central opening is shown in Figure 2-1. It is assumed that the rock mass may be conceptualized as an aggregate of welded-tuff blocks, stacked one on the other so that multiple layers result. Some physical parameters and dimensions pertinent to this system subjected to seismic excitation are also identified thereon. The square cross section rock mass is assumed to be influenced by the overburden mass M_0 and lateral boundary masses M_1. The value of M_0 will be determined by an assumed overburden height of 42.4 m (140 ft), while the value of M_1 will be determined by an assumption that M_1 also consists of a square cross section. The assumed overburden height will produce approximately 1 MPa overburden pressure at the location of the opening. This overburden pressure was selected arbitrarily.

The seismic excitation is assumed to be purely horizontal and to have a wavelength much greater than the affected rock mass segment. Under these conditions, the excitation can be represented by spatially uniform displacement motion.

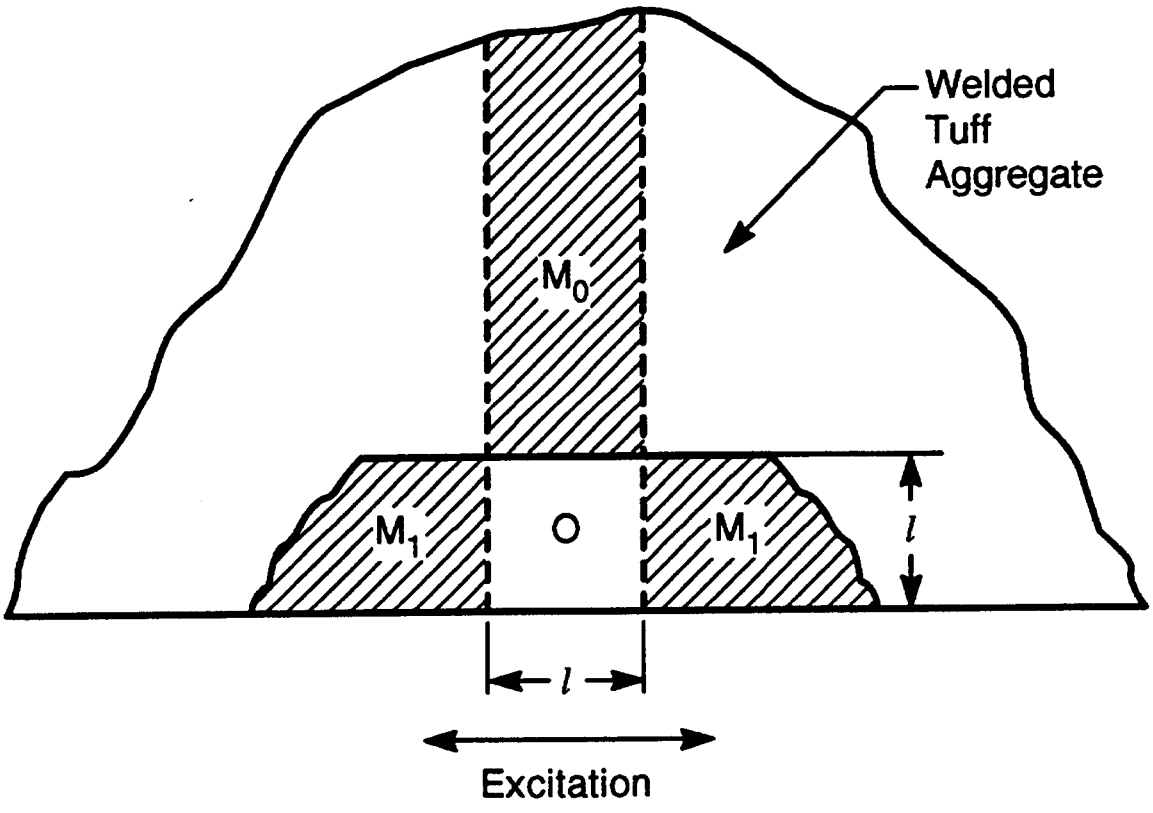

Figure 2-1. Conceptual model of underground rock mass with opening

Selected values for some dimensions were judged to be a reasonable representation of a practical physical problem, and, at the same time, were appropriate for a 1/15-scale model system. Both geometric dimensions and weight capacity of the seismic simulator had to be considered.

A similitude analysis of the model in Figure 2-1 results in the following nondimensional equation for shear and relative displacement response:

$$\left(\frac{\sigma}{\rho l}, \frac{u}{l}\right) = \Im\left(\frac{E}{\rho l}, \phi, \nu, \frac{\sigma_N \phi}{\rho l}, \frac{M_0 g}{\rho l^3}, \frac{M_1 g}{\rho l^3}, \frac{a}{l}, \frac{X_0}{l}, \frac{\omega^2 l}{g}, \omega t\right) \qquad (2\text{-}1)$$

where

a	—	width of segment into paper, 9.14 m (30 ft)
M_0	—	effective overburden mass, 1.72×10^7 kg (3.78×10^7 lb)
l	—	opening dimension, 18.3 m (60 ft)
E	—	material Young's modulus, 4×10^4 MPa (5.8×10^6 lb/in^2)
ν	—	material Poisson ratio
ρ	—	material density, 2403 kg/m^3 (150 lb/ft^3)
M_1	—	effective boundary mass, 7.36×10^6 kg (1.62×10^7 lb)
σ_N	—	normal stress on rock mass, 1.0 MPa (145 lb/in^2)
σ	—	shear stress, MPa
u	—	shear relative displacement, m
ϕ	—	friction factor, 0.5
g	—	gravity, 9.86 m/s^2
x_0	—	excitation displacement, m
ω	—	excitation frequency, rad/s
t	—	time duration, s

Note that by employing physical intuition, it is possible to make the nondimensional numbers more meaningful. That is, the following similitude numbers are ratios of:

$$\left(\frac{\sigma_N \phi}{\rho l} \frac{la}{la}\right) = \frac{\text{Overburden Shear Force}}{\text{Segment Inertia Force}} \qquad (2\text{-}2a)$$

$$\left(\frac{M_0 g}{\rho l^3} \frac{lg}{ag}\right) = \frac{\text{Overburden Inertia Force}}{\text{Segment Inertia Force}} \qquad (2\text{-}2b)$$

$$\left(\frac{M_1 g}{\rho l^3} \frac{lg}{ag}\right) = \frac{\text{Lateral Boundary Interia Force}}{\text{Segment Inertia Force}} \qquad (2\text{-}2c)$$

Thus, system boundaries can be replaced with normal and lateral pressures and masses, and σ_N is the effective overburden pressure. This is the concept on which the scale model design is based.

2.2 PHYSICAL DESIGN

It was desirable to design the scale model with as little distortion of similitude as possible, consistent with dimensions and force capacity of the available seismic simulator. As in any scale model design, several independent variables could be chosen, and others then were determined by satisfying similarity requirements. It was decided that a 1/15-geometric scale would be feasible. Therefore, if

$$\frac{l_m}{l_p} = \frac{1}{s}, \text{ then } s = 15 \tag{2-3}$$

Furthermore, we let

$$\frac{\phi_m}{\phi_p} = \frac{1}{k}, \text{ with } k = 2.0 \tag{2-4}$$

This number is justified later by shear tests results on jointed rock simulant samples discussed in Section 3. Finally, we let

$$\frac{\rho_m}{\rho_p} = \frac{1}{q}, \text{ with } q = 6.67 \tag{2-5}$$

This value was based on preliminary estimates of total model weight compared to the maximum capacity of the seismic simulator. Note that the subscript m indicates that the associated parameter is in the model scale while the parameters with a subscript p denotes that they are in the full or prototype scale.

With these independent parameters, the following similarity requirements resulted:

$$\sigma_{Nm} = \frac{k}{qs}\,\sigma_{Np} = 0.02 \text{ MPa } (2.9 \text{ lb/in.}^2) \tag{2-6a}$$

$$M_{0m} = \frac{1}{qs^3}\,M_{0p} = 762\text{kg } (1{,}680 \text{ lb}) \tag{2-6b}$$

$$M_{1m} = \frac{1}{qs^3}\,M_{1p} = 327 \text{ kg } (720 \text{ lb}) \tag{2-6c}$$

$$E_m = \frac{1}{qs}\,E_p = 400 \text{ MPa } (57{,}971 \text{ lb/in.}^2) \tag{2-6d}$$

$$\rho_m = \frac{1}{q}\,\rho_p = 360 \text{ kg/}m^3 \text{ } (22.5 \text{ lb/ft}^3) \tag{2-6e}$$

The above modeling requires that the rock simulant effective density be significantly reduced over that for the prototype tuff material. This requirement would be very useful for controlling overall model weight. However, such an approach generally requires a change of rock simulant material, or a hollowing out of simulated rock ingot centers. In any case, it was felt that the simulant material needed to remain brittle and exhibit surface wear properties approximating those of the prototype material. Therefore, as a practical compromise, it was decided to use simulated rock of solid material and a density ratio of

$$q = 1.43 \tag{2-7}$$

which would be applied for the rock simulant within the rock mass segment only. The original value of

$$q = 6.67 \tag{2-8}$$

would be applied to the material outside the segment. This value effectively produces a model whose exterior masses are more manageable in terms of seismic simulator capacity, but at the same time makes the interior rock mass 4.67 times too large. Furthermore, it was not possible to develop a material with the Young's modulus given by Eq. (2-6c). Therefore, the corresponding value was allowed to be a factor of 34.1 low. Although this physical distortion is obvious, it was felt that the result was still within useful practical ranges for validation of the analytical model. Furthermore, since the greatest shear load on the interior segment was anticipated to result from the overburden mass lateral moment, it was felt that the effects of mass exaggeration within the segment would be less pronounced on the dynamic response. Therefore, the overburden mass M_0 was maintained approximately as required, but the boundary masses were reduced in order to maintain total model mass within the shaker table capacity, and in some measure to counteract the effects of exaggerated segment mass. It was hoped that material elastic properties would become secondary to effective joint stiffness properties so that the Young's modulus distortion would be of less importance. Confirmation of these assertions was established by the use of a preliminary discrete element analytical model of the system. More information on this evaluation is presented in Section 4.0.

The final physical design and associated dimensions are given in Figure 2-2 and Table 2-1. The model is comprised of an aggregate of many stacked rock simulant ingots, each 61 cm long. The ingot cross sections vary from 5×5 cm square (2×2 in.) for basic ingots, to half-section ingots at the boundaries, to curved-section ingots around the center circular opening. This opening is 15.2 cm (6 in.) in diameter. The four boundaries of the stack are interfaced with a 6.4-mm (0.25-in.) thickness of rubber, which is bonded to the rock on the inside and lubricated with silicone at the interface with the confining box boundaries. These boundaries are very stiff construction of welded aluminum plates and 10.2-cm (4-in.) I-beam frames. The proper pressure σ_N is maintained on the system by eight vertical cables and eight horizontal cables. The two end structures are hinged to the bottom support structure at the bottom (Figure 2-3), and are held against rollers at each upper corner (Figure 2-4). Therefore, the end structures can pivot laterally, while the top structure can pivot and float up and down as necessary to follow the confined rock motion.

An overall view of the model mounted on the seismic simulator is shown in Figure 2-5. Here the complete top mass, including additional inertia weights, is installed by bolting four heavy steel plates to the top structure. Furthermore, in this view it can be seen that the orientation of the ingot layers is at 45°

Table 2-1. Model construction details

Bottom support structure weight	142 kg (312 lb)
End structure/mass weight	75 kg (165 lb)
Top structure weight	95 kg (210 lb)
Additional top weight	567 kg (1,250 lb)
Single normal ingot weight	2.6 kg (5.8 lb)
Ingot surface friction factor	0.5
Ingot density	1,682 kg/m^3 (105 lb/ft ^{3})
Total ingot load weight	1,508 kg (3,326 lb)
Tunnel cable diameter	15.2 cm (6 in.)
Tension cable diameter	0.32 cm (1/8 in.)
Total model weight	2,504 kg (5,520 lb)

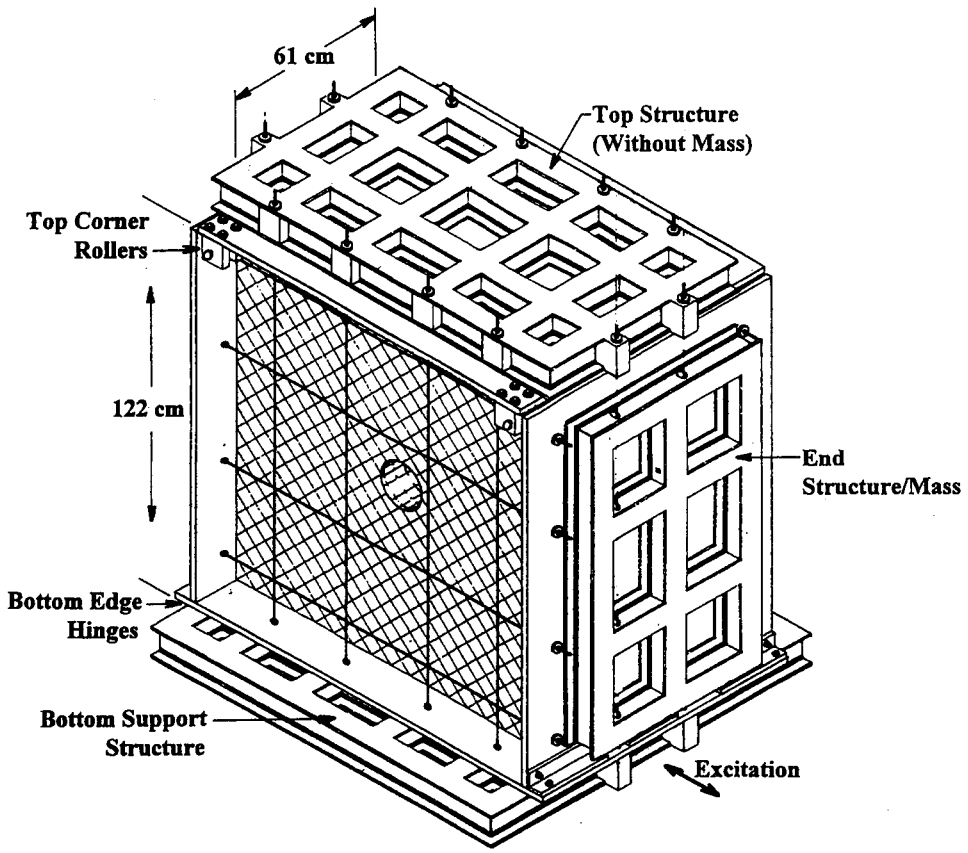

Figure 2-2. Physical design of scale model rock mass with opening

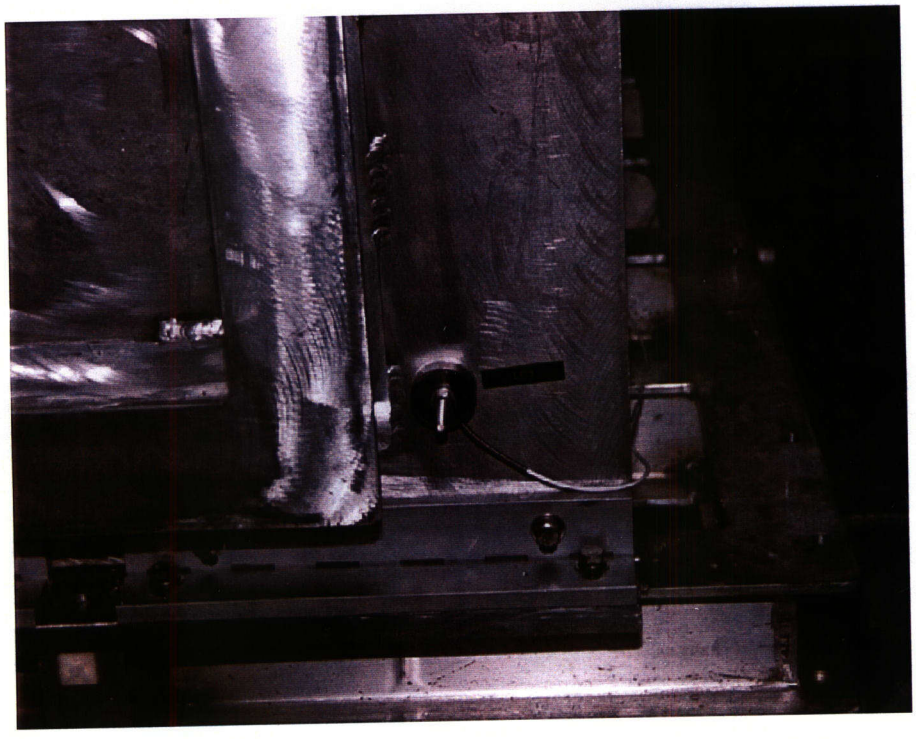

Figure 2-3. Detail of bottom edge hinge

Figure 2-4. Detail of top corner roller

to the horizontal. This configuration was chosen as useful for experimental purposes. Likewise, the basic ingot cross sections were chosen to be as uniform as possible before dynamic excitation was applied. Further details of construction are be given in Section 7.

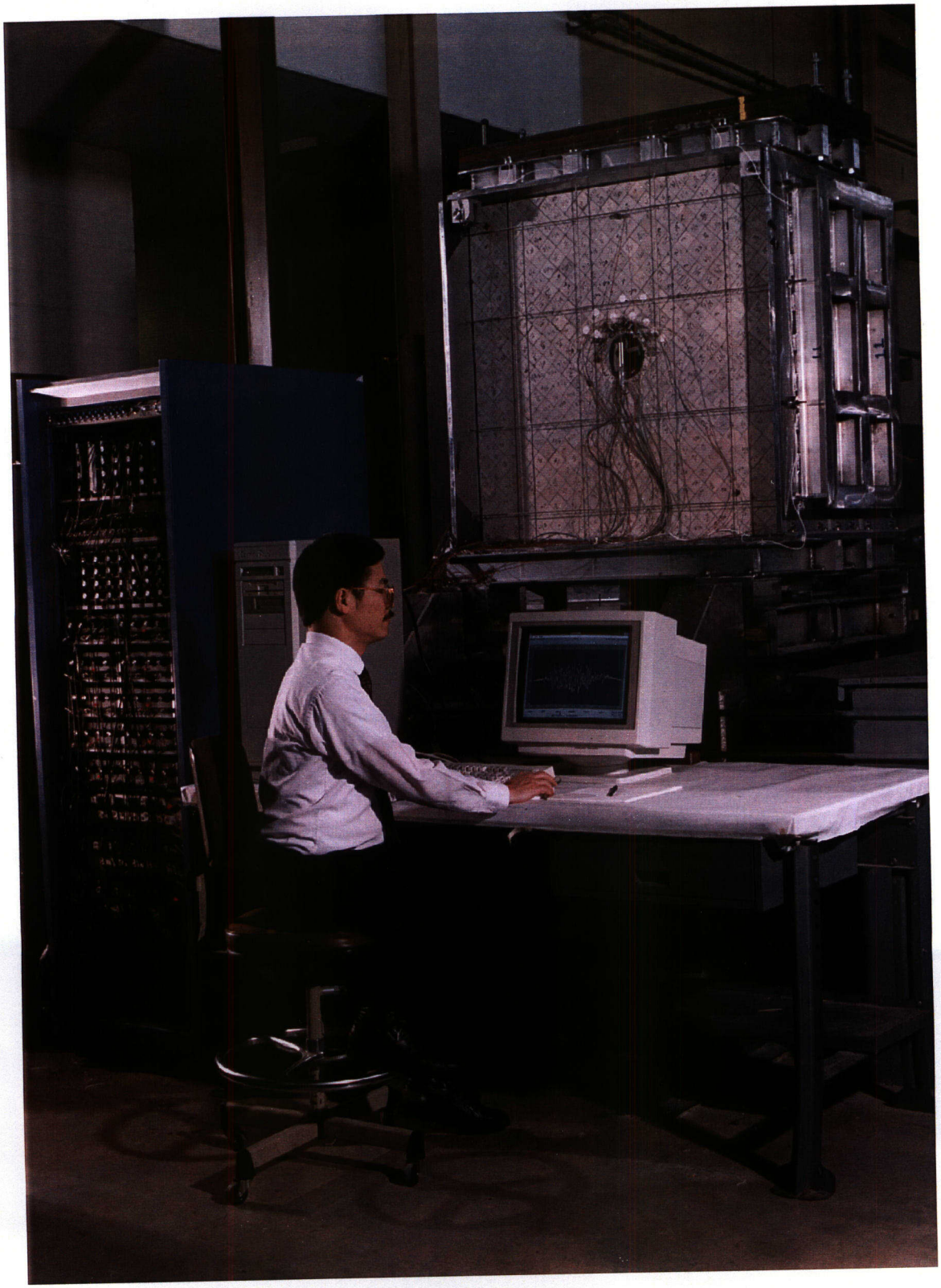

Figure 2-5. Overall view of experimental apparatus

3 DEVELOPMENT OF ROCK SIMULANT

3.1 MATERIAL COMPOSITION AND CASTING

As noted previously, several rock properties were identified as important for modeling purposes. However, it was felt that the brittle nature and associated wear properties of the interface were the most important for model characterization. Furthermore, it was recognized that an exact modeling of welded tuff behavior was probably not possible, nor actually necessary for a successful verification of numerical computer codes. Therefore, the philosophy adopted for development of a suitable rock simulant consisted of following the previously presented similitude guidelines as much as practical, but allowing distortions as long as they could be quantified by associated tests. Thus, the essential behavior of welded tuff, which was sought to be similarly established for the rock simulant, is illustrated in Figures 3-1 and 3-2. More details of results for various tests on welded tuff can be obtained from Hsiung, et al. (1993).

3.2 MATERIAL PROPERTIES TESTS

Initial development of the rock simulant was based on repeated trials of various constituent mixtures and testing of material properties of cylindrical specimens cast from these mixtures. The specimens were cast as 5.0-cm (2-in.) diameter by 10.0-cm (4-in.) long specimens that were instrumented with strain gages and tested in uniaxial compression test machines. Table 3-1 lists the ingredients that were ultimately selected for rock simulant development. Sixty-six cylindrical specimens cast from the mixtures as indicated in Table 3-1 were tested under compression. The average uniaxial compressive strength is 16.3 MPa (2,364 1b/in.^{2}) with a standard deviation with 1.39 MPa (200 lb/in.^{2}).

After developing the above described material, it was necessary to develop a scale model rough surface. No matter how a surface roughness was to be developed, the intent was to cast specimens of the same size as were originally used for the welded tuff and to perform combined normal and shear tests in the same apparatus in order to obtain data analogous to Figures 3-1 and 3-2. However, it was recognized that scale-model conditions also must be considered for these tests. Rock simulant specimens were cast in wooden molds with a special material used as mold liner that formed the interfacing surfaces. This liner was made of acrylonitrile butadiene styrene (ABS) plastic sheet, which had a "Lavant" roughness pattern. It was found that this material produced a random roughness with the properties identified in Table 3-1. It was noted that the average asperity peaks produced were approximately 1/15 geometric scale to those observed for typical welded tuff specimens. It was recognized that with each of the two surfaces being independently random, no significant interlocking of surfaces would occur, as is typical for welded tuff. However, the effects of these differences would be quantified by shear tests.

3.3 JOINT INTERFACE PROPERTIES TESTS

A series of rock simulant specimens was subjected to both pseudostatic and dynamic shear tests. For these tests, normal stress was determined by Eq. (2-6a). That, is for the previously established model values

$$(1 \text{ MPa})_m = (0.02 \text{ MPa})_p \tag{3-1}$$

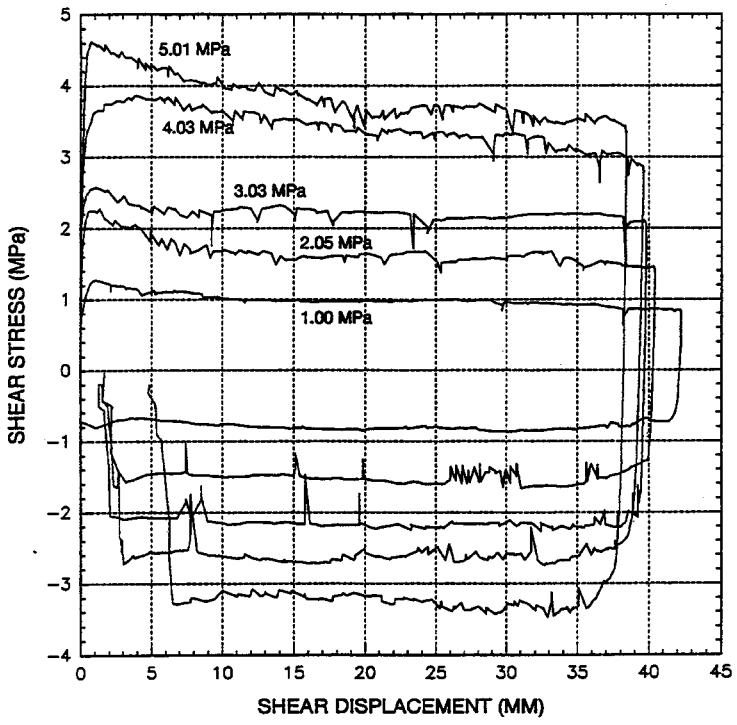

Figure 3-1. Shear test results for tuff specimen under various normal loads and pseudostatic shear

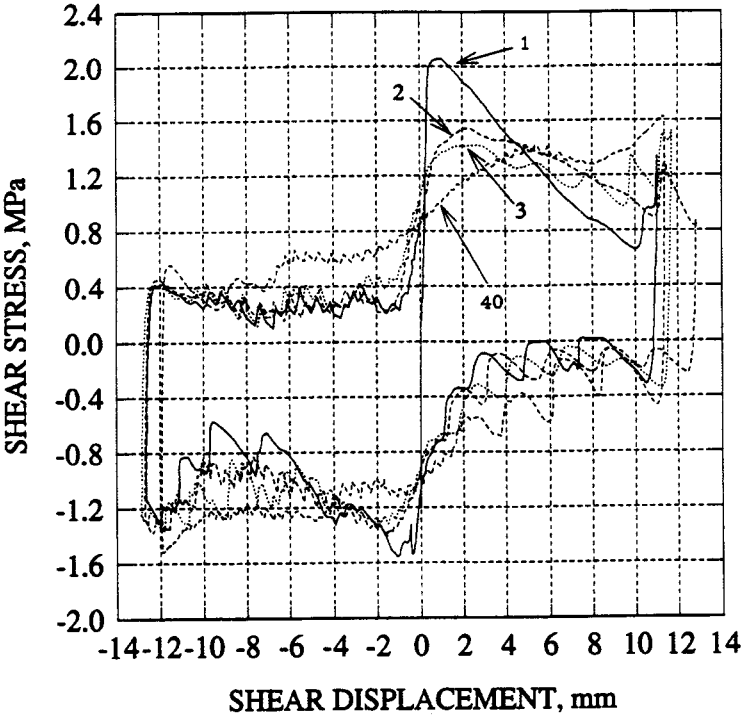

Figure 3-2. Hysteresis for tuff specimen under 1 MPa normal stress and 1.4 Hz harmonic shear

Table 3-1. Properties of rock simulant specimen

Material Constituents, wt %	
25.11	Type I Portland Cement
45.74	Barite
25.41	Water
3.39	Bentonite
0.3	DARACEM-100 (Plasticizer)
8.57×10^{-3}	Vinsol Resin (Air Entrainment)
4.58×10^{-2}	Ivory Liquid Soap
Uniaxial Compressive Strength	
16.3 MPa (2,364 lb/in.^{2})	
Material Density	
1,682 kg/m^3 (105 lb/ft^3)	
Roughness Data	
Average Peak	±0.2 mm (0.008 in.)
Average Wave Length	6.4 mm (0.25 in.)

However, with the existing apparatus, it was not possible to obtain this low value. Therefore, all tests were carried out at 0.065 MPa normal stress, which resulted from just the vertical dead weight of the normal loading frame. Furthermore, cyclic amplitudes and frequencies were scaled to correspond to 1/15-scale for those used for the welded tuff specimens.

Figures 3-3 to 3-5 show results for scaled harmonic tests. By comparing Figure 3-3 with Figure 3-2, it is obvious that, indeed, no offset in hysteresis occurs for the rock simulant. By comparing the friction factor ϕ for the hystereis shown in Figure 3-3 (scaled harmonic test) to that shown in Figure 3-2 (harmonic test on tuff specimen), it can be concluded that

$$\frac{\phi_m}{\phi_p} = \frac{1}{k} = \frac{1}{2} \tag{3-2}$$

is a reasonable estimate for the results. Thus, this value was considered appropriate for the model process. Furthermore, the stated material density provides

$$\frac{\rho_m}{\rho_p} = \frac{1}{q} = \frac{1}{1.43} \tag{3-3}$$

as was previously noted Eq. (2-7). In general, the mixture listed in Table 3-1 produces rock simulants that are considered acceptable for this study since the primary objectives of this study are to (i) understand rock mass response subjected to repetitive episodes of seismic loads and (ii) generate a data for verification of analytical methods.

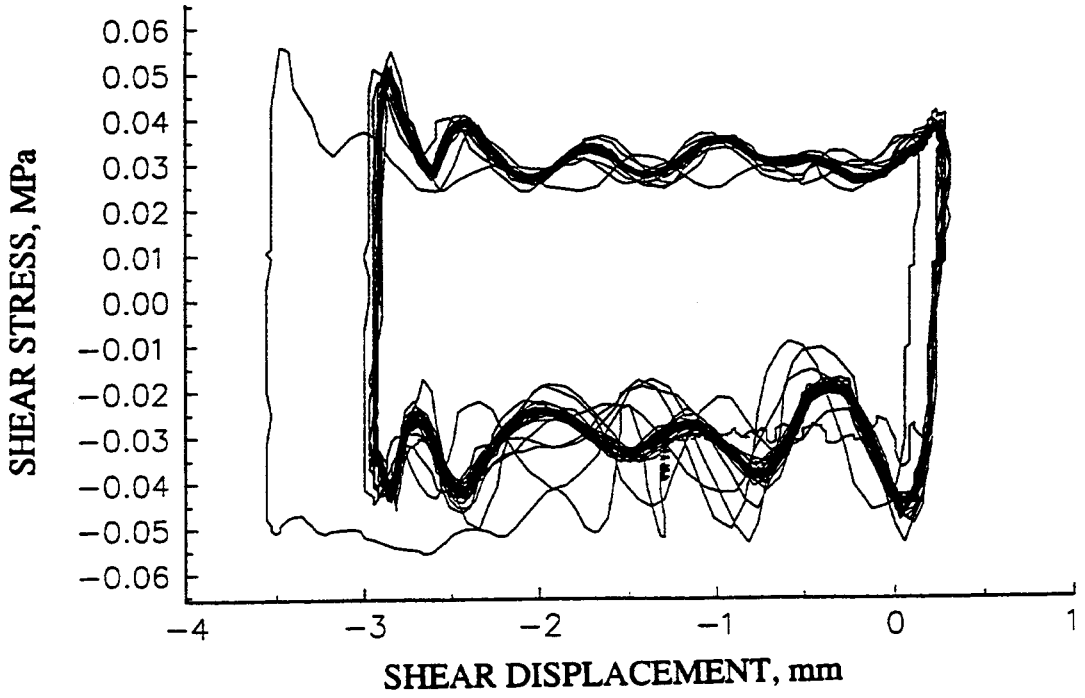

Figure 3-3. Hysteresis for rock simulant under 0.065 MPa normal stress and 5.4 Hz harmonic shear

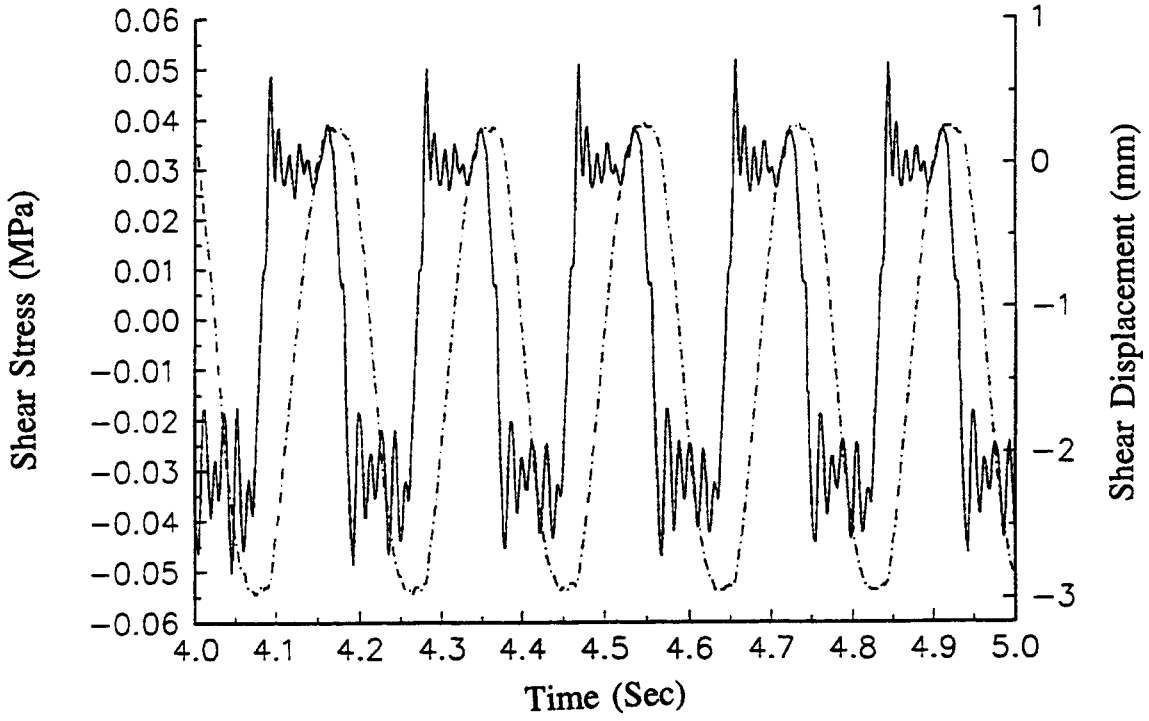

Figure 3-4. Shear stress for rock simulant under 0.065 MPa normal stress and 5.4 Hz harmonic shear

4 PRELIMINARY ANALYTICAL EVALUATION

In order to estimate the validity of the various assumptions used in the design of the scale model, a preliminary numerical simulation of the scale model was performed using the UDEC computer code (ITASCA Consulting Group, Inc., 1992) under various types of excitation. A diagram of this model and associated responses for one set of input conditions are shown in Figure 4-1. The ingot interface simulated in the analysis was assumed to have a Mohr-Coulomb friction behavior. The potential uses of several different types of boundary conditions were studied with this model. Other parameters identified in Table 2-1 were employed. For each case a procedure was first evaluated for the pseudostatic application of inertial compression sequentially in the vertical and horizontal cables. The intent was to determine to what degree the central opening might close in the process. Then, various levels of harmonic base excitation were applied, and the responses were determined. From this preliminary study, it was estimated that fully measurable tunnel displacements should occur for excitations at levels that were within the capability of the seismic simulator system. Furthermore, a better selection of the types and locations of response transducers was possible from this information.

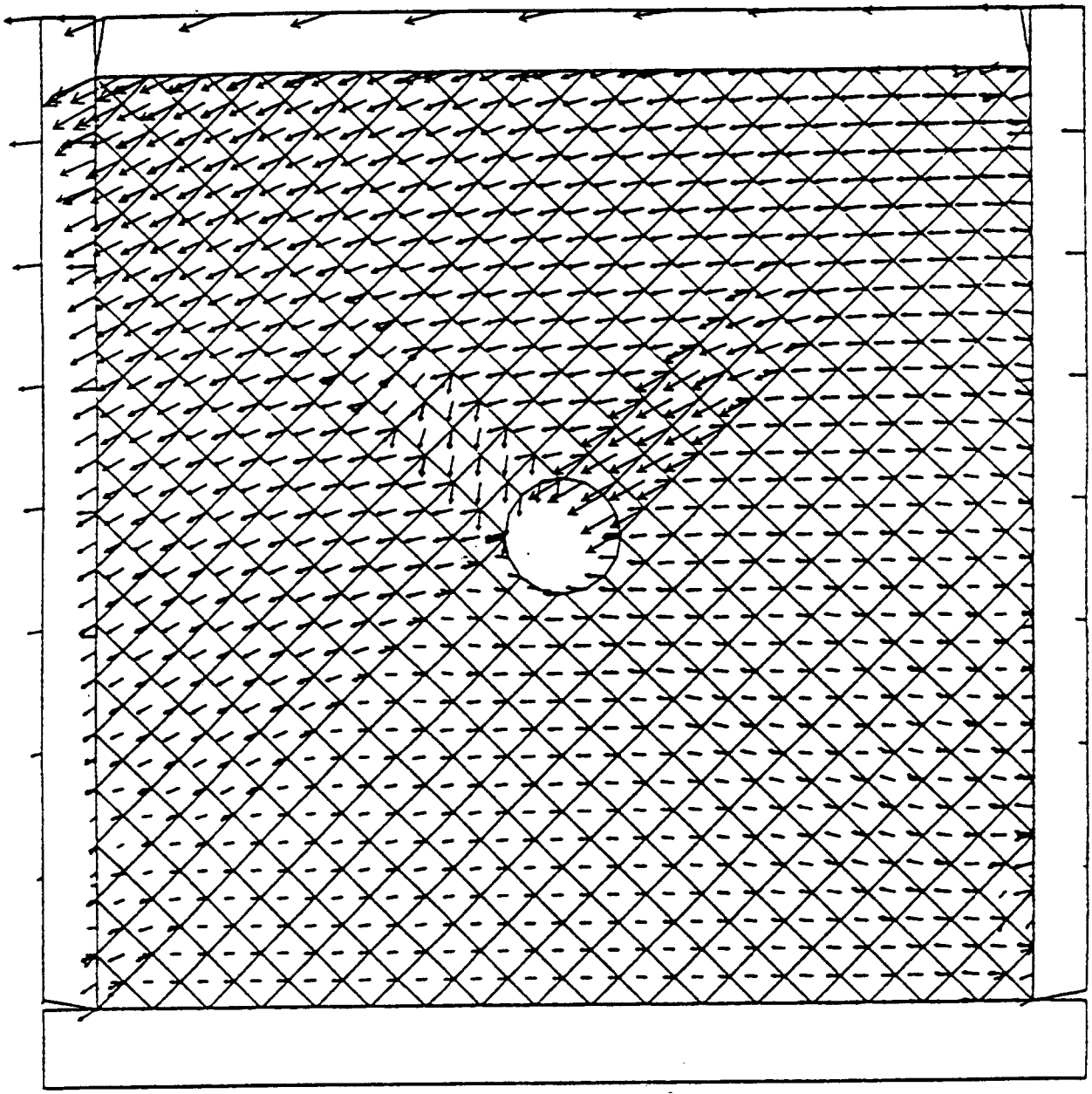

Figure 4-1. UDEC model displacement pattern for 3.8-mm peak earthquake excitation

5 INSTRUMENTATION PLAN

5.1 TRANSDUCER TYPES AND LOCATION

The scale-model response to seismic excitation was estimated, and this information was used to develop a corresponding instrumentation design. Generally, it was recognized that rock interface relative normal and shear, and overall structure motions were of interest, and the transducers should offer negligible resistance to rock interface movement. Therefore, several types of transducers were selected to measure these responses. It was decided that up to 50 channels of data measurement would be employed. Identification and location for the various transducers are given in Figures 5-1 and 5-2, and in Table 5-1, along with citations of subsequent figures that provide more description. In addition, photographs of the instrumentation on and near the two opening ends are shown in Figures 5-3 and 5-4. In the description to follow, the opening near side is understood to be that shown in Figures 2-5 and 5-1, with the far side being the opposite face.

Response accelerometers AC1–AC5 were located at various positions 2.5 cm (1 in.) in from the ends of the central opening. These devices were intended to measure higher frequency responses near the opening. Accelerometers AC6–AC11 were located to measure various vertical and horizontal higher frequency responses on the confining structure. By comparing these responses with the table input, the dynamic distortion of the rock mass boundaries could be determined. All accelerometers were mounted with 5-min epoxy bond.

Strain gages SG1–SG10 were mounted at various near side locations at the center of full cross section ingots. The intent was to use these gages to determine the extent that elastic deformation of the rock occurred.

Cantilever beam displacement transducers were specifically designed to measure relative shear displacements at the interface of two adjacent ingots. Essentially, the thin steel cantilever beams included uniaxial strain gages bonded on each side at the beam root. The gages had the ability to measure relative shear displacements up to 3.0 mm (1/8 in.). They were located to measure relative shear in the near vicinity of the openings. The positions of CB1–CB8 are indicated in the figures. In each case, the cantilever root is anchored into the face of one ingot, and its tip contact is anchored into the face of the adjacent ingot.

Bentley proximeter transducers BP1–BP8 were used to measure relative normal displacements between adjacent ingots. These 6.3-mm (1/4-in.) threaded devices are noncontacting eddy-current transducers. As such, their base was anchored in holes drilled into the face of one ingot, while their steel target plates were mounted onto a cantilever into the adjacent ingot face. These transducers also could measure normal displacements of up to 3.0 mm (1/8 in.). Their output was not affected by shear displacements within their intended range.

Linear variable differential transformers (LVDT) LV1–LV6 were designed to measure relative peak displacements up to 1.3 cm (0.5 in.). From Figure 5-4, it can be seen that the LVDT barrel was mounted in a plastic tube that was anchored in holes drilled in one ingot, while the core was attached to a pin that was anchored in a hole drilled in an opposite ingot. LV1 was oriented vertically (Figure 5-5), LV6 was oriented horizontally (Figure 5-6), while LV2–LV5 were mounted within the interior at various angles, shown in Figure 5-5. The latter four LVDTs were located on equal-distant centers over a 15.2-cm (6-in.) space near the opening interior center, as shown in Figure 5-2.

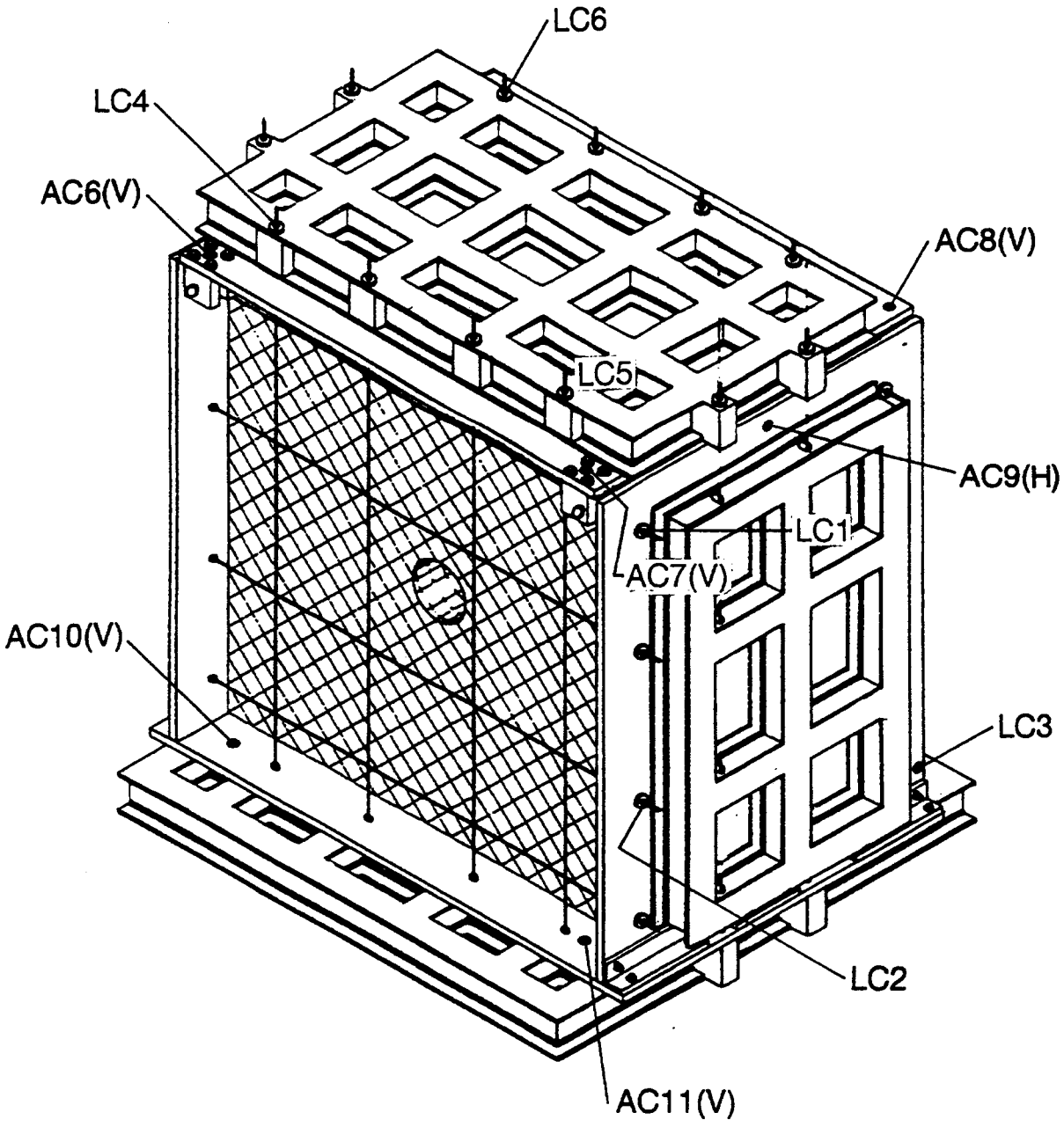

Figure 5-1. Overall instrumentation identification

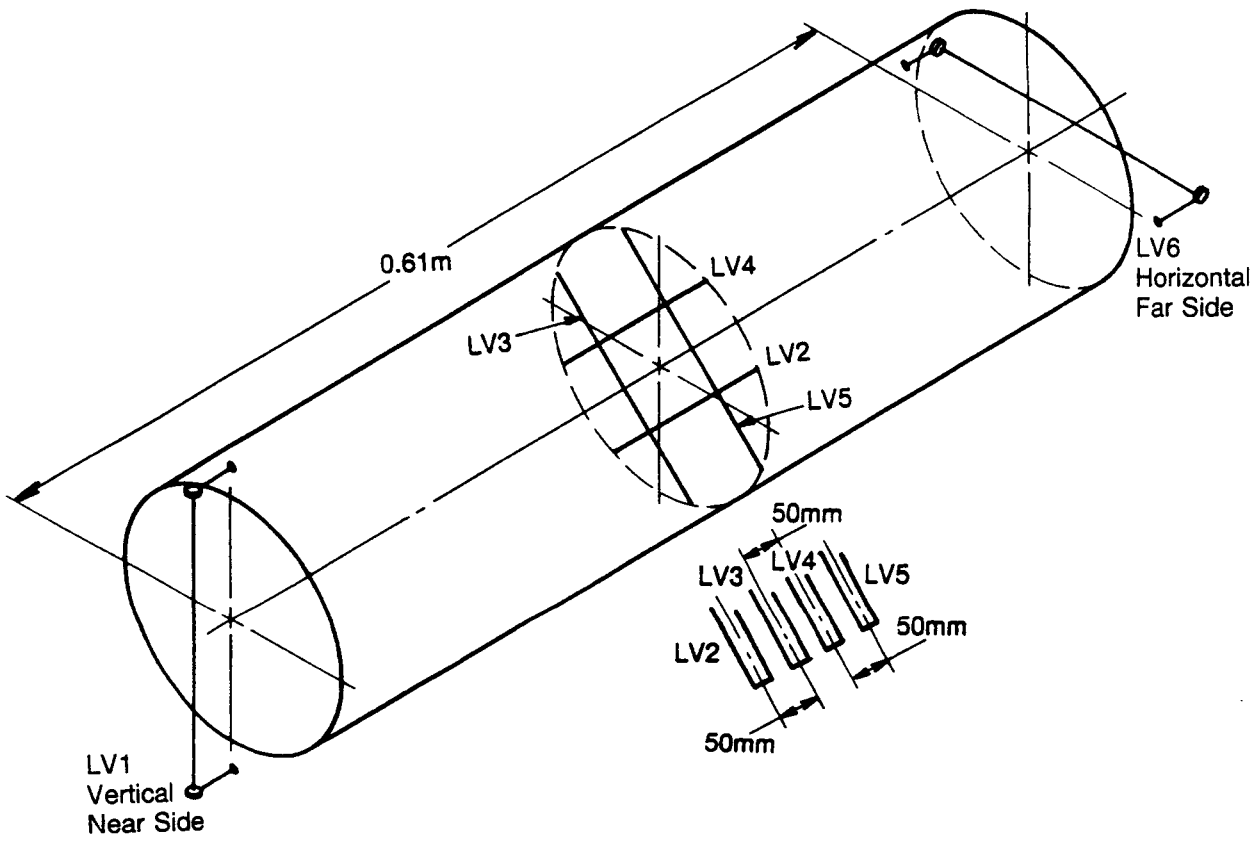

Figure 5-2. Opening interior instrumentation identification

Table 5-1. Transducer identification and locations

Response Accelerometers	
AC1–AC5	Opening interior, 2.54 cm from ends (Figure 5-5)
AC6–AC11	Exterior structure (Figure 5-1)
Strain Gages	
SG1, SG2	Tangential, radial upper left corner (Figure 2-4)
SG3, SG4	Radial, tangential upper right (similar)
SG5–SG10	Opening near side (Figure 5-5)
Cantilever Beam Displacements	
CB1–CB6	Opening near side (Figure 5-5)
CB7, CB8	Opening far side (Figure 5-6)
Bentley Proximeter Displacements	
BP1–BP6	Opening near side (Figure 5-5)
BP7, BP8	Opening far side (Figure 5-6)
Linear Variable Differential Transformers (LVDT)	
LV1	Opening near side (Figure 5-2, 5-5)
LV2–LV5	Opening interior (Figure 5-2)
LV6	Opening far side (Figure 5-2, 5-6)
Load Cells	
LC1–LC6	Various tension cables (Figure 5-1)
Excitation	
AT1	Seismic table acceleration
DT1	Seismic table displacement
CD1	Seismic table drive signal

Load cells LC1–LC6 were used to measure the tension cable initial static load, plus the superposed dynamic load that occurred during seismic testing. These transducers were compression devices mounted in line at the cable base, as shown in Figures 2-3 and 5-7. Various cables were selected for data sampling, as identified in Figure 5-1.

One accelerometer and one displacement transducer were mounted on the Seismic Table to measure the horizontal base excitation. They were identified as AT1 and DT1, respectively.

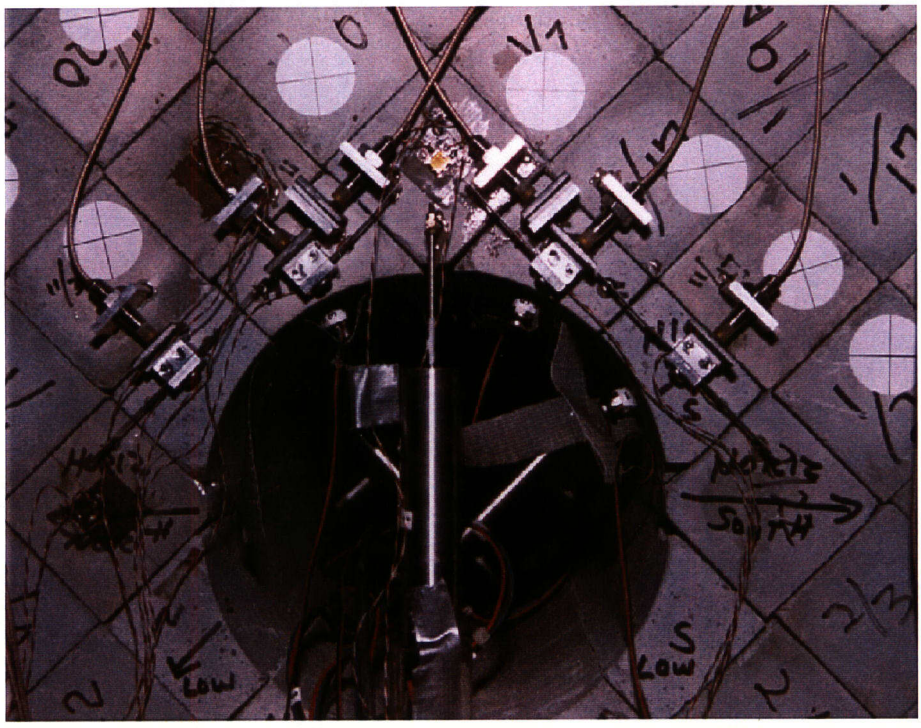

Figure 5-3. Opening near side instrumentation

Figure 5-4. Opening far side instrumentation

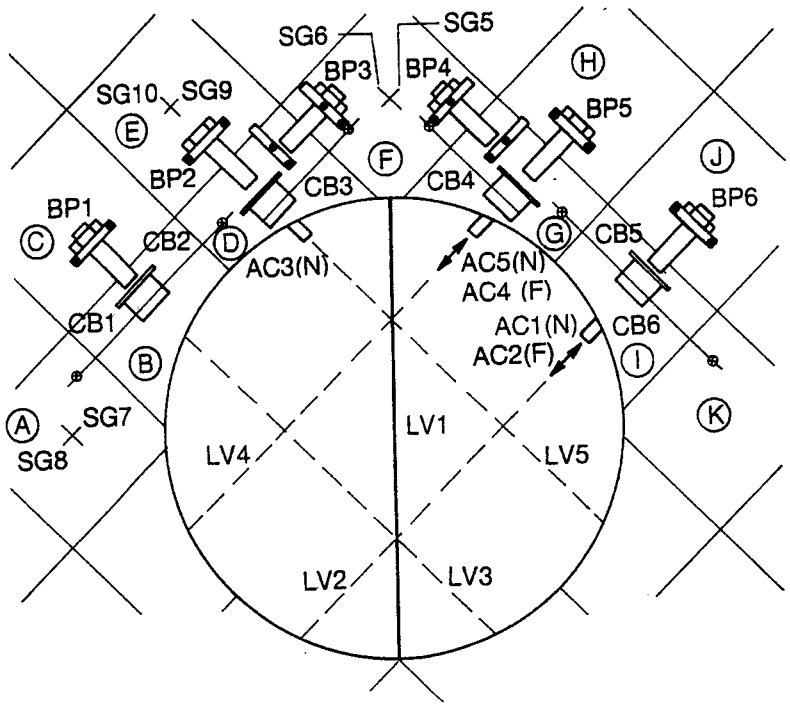

Figure 5-5. Opening near side instrumentation and rock ingot identification

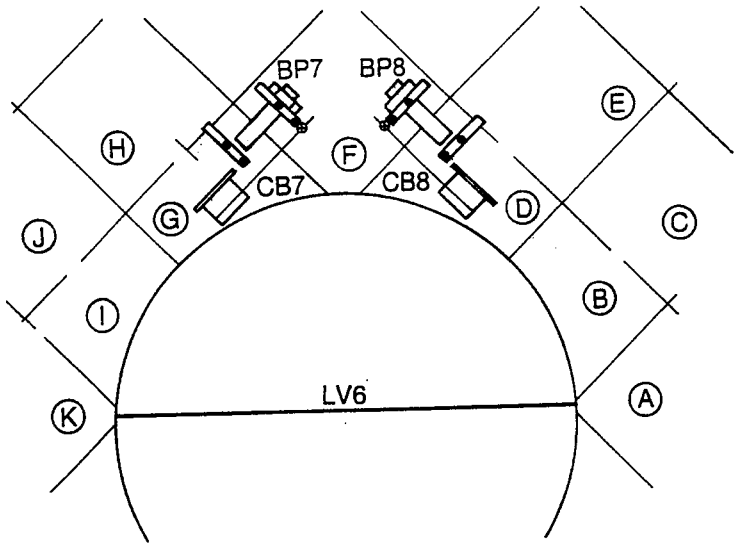

Figure 5-6. Opening far side instrumentation and rock ingot identification

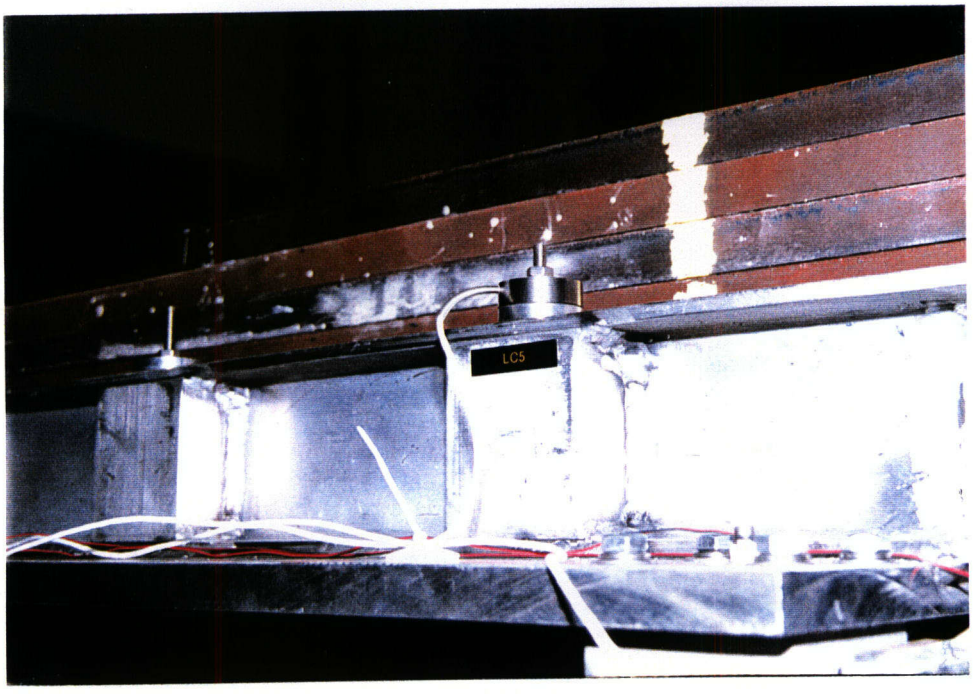

Figure 5-7. Installation for load cell LC5 and accelerometer AC7

In addition to the above identified transducers, larger motions were measured by a video camera mounted axially with the near-side opening. (This camera is not shown in Figure 2-5.) Furthermore, a second video camera was used to monitor overall motions on the far side of the opening as well.

5.2 TRANSDUCER DESIGN

All transducers identified in the previous section were commercially available devices except for the cantilever beams. Therefore, only details of these devices will be presented herein, while identification of the commercial items is given in Appendix A.

Figure 5-8 shows a close-up of a cantilever beam design. The base is made of a split aluminum block (12.7×12.7×12.7 mm) (0.5-in. square), which is held together by a central screw. The 0.76-mm-(0.03-in.) thick cantilever beam root is compressed between the split halves of the block. This block is also drilled with two holes that hold dowel pins that are ultimately cemented into holes drilled in an ingot face. The 1.27×3.8-cm (0.5×1.5-in.) cantilever forms the active part of the transducer. The cantilever tip is mounted into a slip pin that also is cemented into an adjacent ingot drilled hole. (The slip pin is not shown in Figure 5-8.) The cantilever slip pin consisted of a 3.2-mm (1/8-in.) thin-wall tube, with thin dowel pins inserted and protruding above the tip of the tube. The dowel pins were spaced so that they just allowed the thin cantilever to slide freely along its length, but maintained contact for displacements normal to the beam. Thus, only relative shear displacements were measured, and no resistance was offered to relative normal motions of adjacent ingots. Finally, it may be noted that the device shown in Figure 5-8 shows a single-version cantilever beam. A double-version was also employed, as can be seen from Figures 5-3 and 5-8.

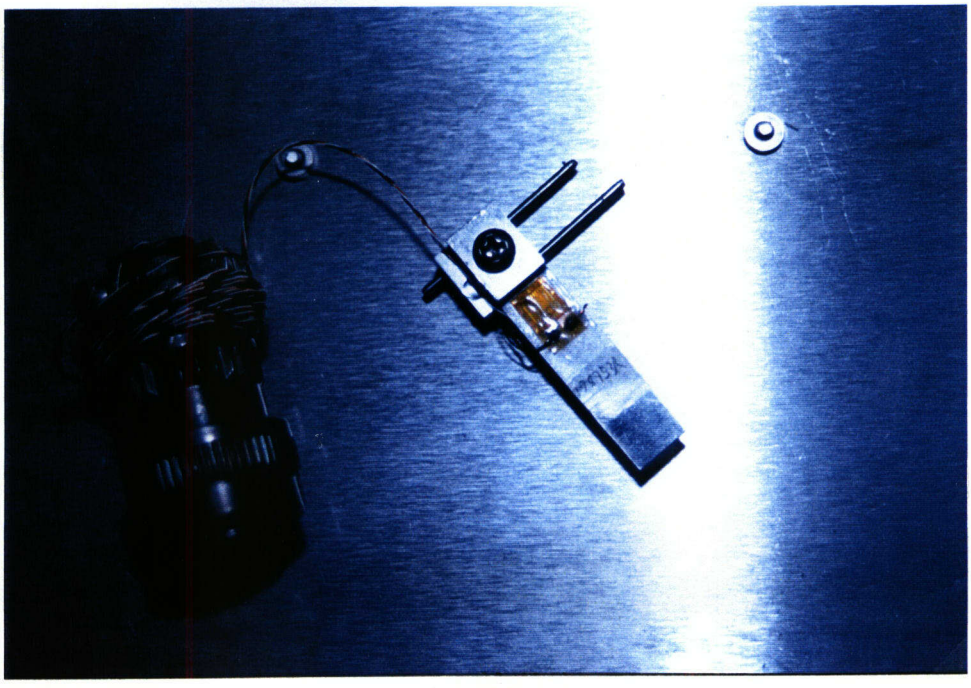

Figure 5-8. Detail of a single cantilever beam design

6 DATA ACQUISITION SYSTEM

6.1 INSTRUMENTATION DIAGRAM

A block diagram of the 50-channel instrumentation system is shown in Figure 6-1, while a photograph of this apparatus is shown in Figure 6-2. More information on individual data channels is given in Appendix B. Only 34 filter channels were available, so they were assigned to those channels that were anticipated to have highest frequency content.

Data rates were dictated by the capacity of the 486 (66 MHz) digital computer with a 1-gigabyte hard drive and its associated data acquisition cards. As shown later, total run time duration was 10 s. It was determined that a rate of 2,800 samples/sec was the fastest data rate feasible for each of 50 data channels sampled sequentially. Hence, for each run, a total of 1.4 million samples of data were acquired. For 2,800 samples/s for each channel, the Nyquist frequency is 1,400 Hz. Therefore, to avoid aliasing of data, the low-pass filters were set with a 1,600 Hz cutoff. Thus, for full-scale data, this rate corresponded to $1/\sqrt{15}$ times this, or 433 Hz. Data acquisition was initiated manually for each data run by responding to a mark on the drive signal tape. This mark was observed visually on an oscilloscope.

6.2 CALIBRATION PROCEDURES

Calibration procedures for some transducers were quite standard, while others were not. Accelerometers were calibrated by mounting them on an electrodynamic shaker along with a calibration standard accelerometer and comparing outputs with a digital voltmeter. Strain gages were calibrated by shunting a standard resistor across an arm of the amplifier bridge and reading the output on a digital voltmeter. Other transducers required somewhat different procedures. Accuracy was about 0.01 g and 10 μ-strain, respectively.

Cantilever beams were calibrated by means of the apparatus shown in Figure 6-3. The base of the cantilever beam was mounted into two holes drilled into the left aluminum block which was fixed to the table. The beam tip pin was mounted into a hole drilled into a contacting companion aluminum block so that the beam length corresponds to that drilled for the holes on the faces of adjacent ingots. The companion block was moved along the contact face, which simulated a relative shear displacement that was read visually on a calibrated dial gage. Output of the amplifier was read on a digital voltmeter to an accuracy of about 0.013 mm (0.0005 in.).

A setup similar to that described for cantilever beams was also used for calibrating Bentley proximeters and LVDTs. In each case the base was fixed to the table, and the core or target plate was moved a calibrated distance, while the output was read on a digital voltmeter.

Load cells were calibrated by means of the simple apparatus shown in Figure 6-4. The load cell was placed on a hard steel plate while connected to its readout amplifier. Increments of steel block weights were sequentially added up to about 142 kg (310 lb). Accuracy was to about 4.45×10^{-3} dynes (1.0 lb).

A totally nonstandard method was used for calibrating the tension cables for proper loads. The apparatus shown in Figure 6-5 was used to measure the natural frequency of each cable to a high degree of accuracy. Initially an accelerometer was clipped to a cable that was fitted with a load cell at its mounting. The load cell output was compared with the natural frequency where the cable was hand-

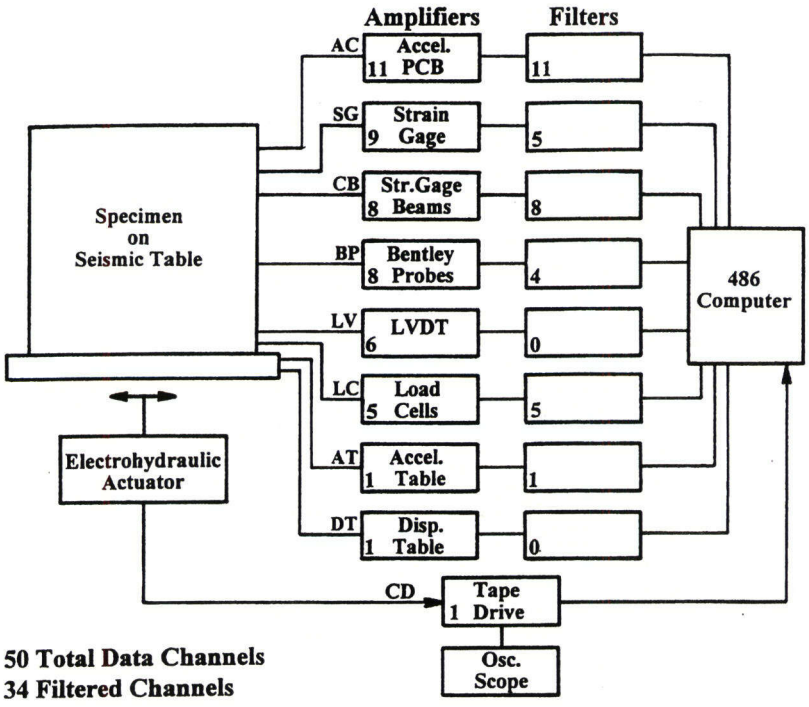

Figure 6-1. Block diagram of data acquisition system

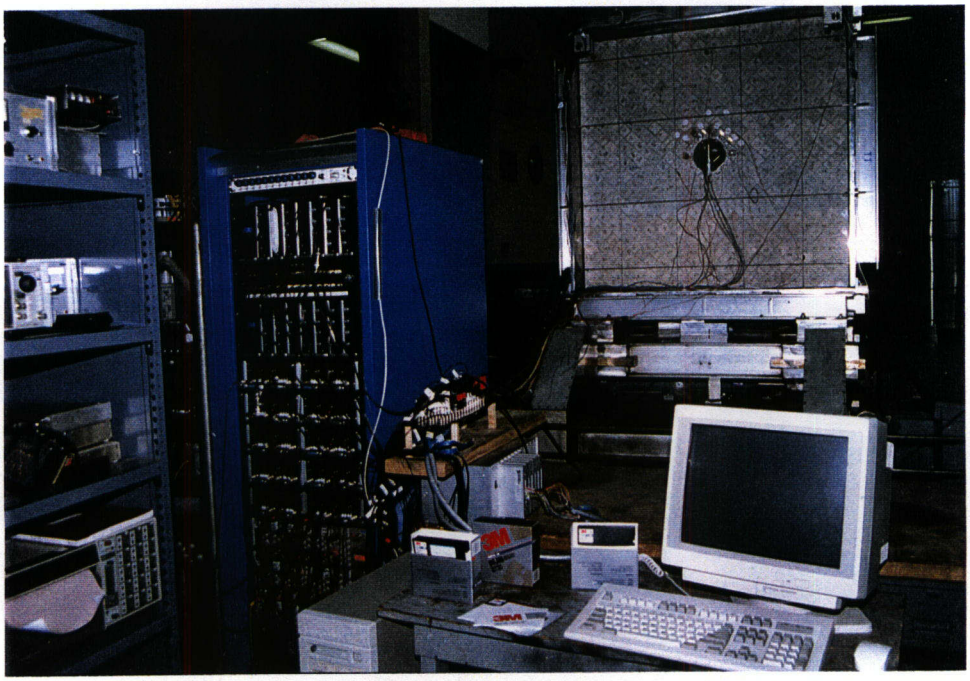

Figure 6-2. Overall view of data acquisition system

Figure 6-3. Calibration apparatus for cantilever beams

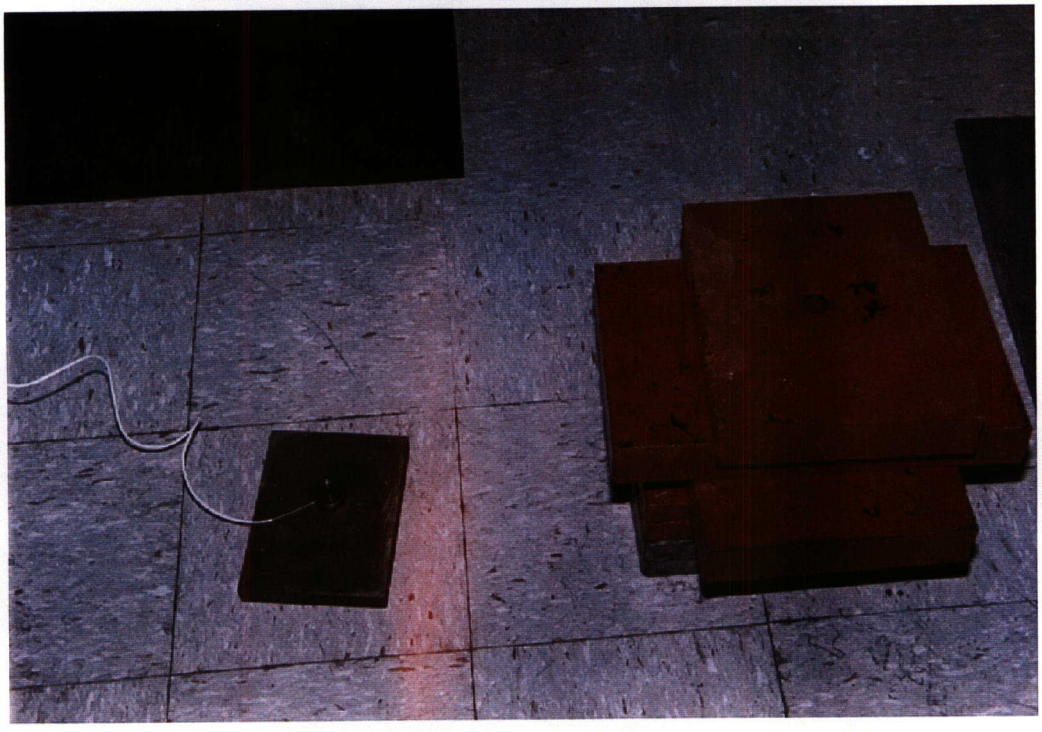

Figure 6-4. Calibration apparatus for load cells

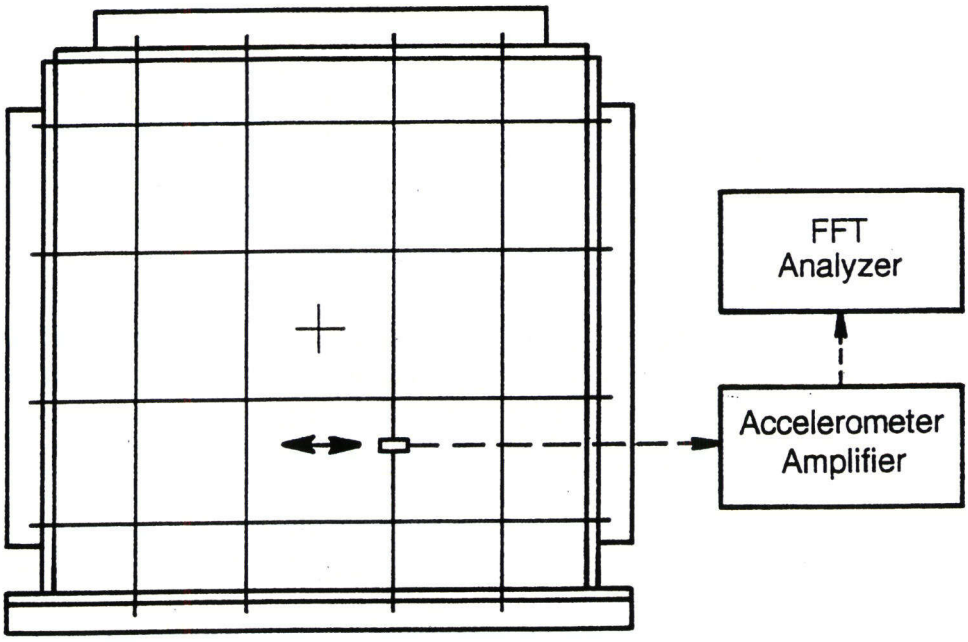

Figure 6-5. Calibration apparatus for tension cables

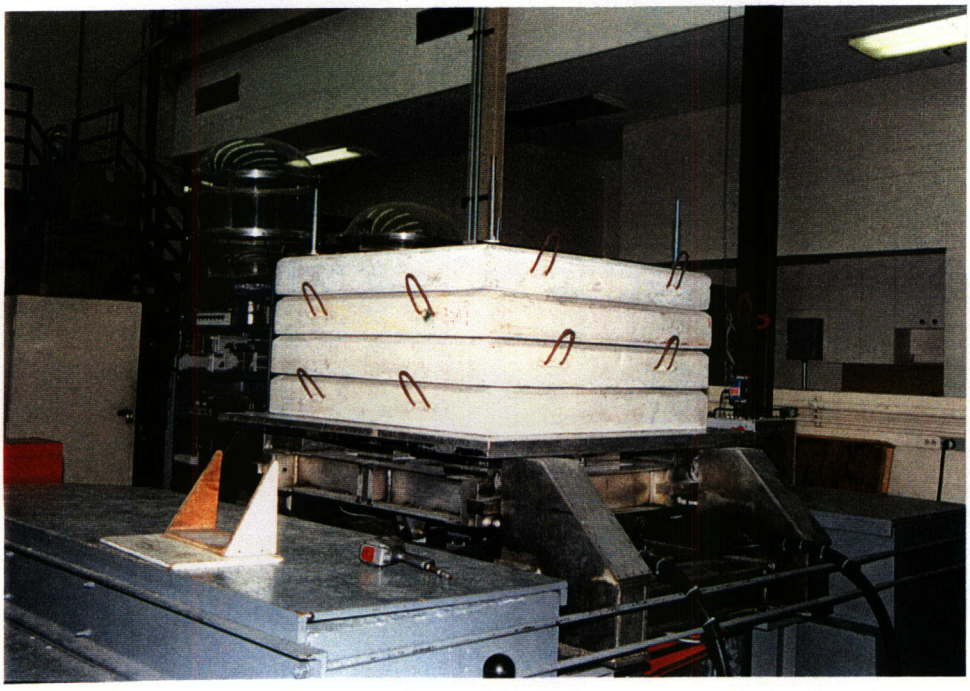

Figure 6-6. Calibration of seismic table

plucked laterally. When the desired tensions were measured by load cell, the other similar cables were tightened until they displayed the same natural frequency.

The table motion accelerometer and displacement transducer were calibrated similarly to the corresponding procedures described above. However, it was also necessary to calibrate the table voltage drive signal so that the desired displacement motion would occur for a given actuator gain setting. This calibration was done with the apparatus shown in Figure 6-6. Four concrete blocks of mass similar to that of the complete model were bolted to the seismic table. The anticipated seismic drive signal was input to the table, and the peak table displacement and associated time history were recorded for each noted actuator gain setting. Thus, an input/output transfer function was developed up to a maximum peak displacement of about 2.0 cm (0.8 in.).

Finally, an initial calibration on the data acquisition computer was performed by inputting a given sine wave of measured amplitude into each of 50 channels at the interconnection panel and feeding each output to designated channels of the 486 computer. The signal was digitized and read out with the software to be used for the tests. This procedure was performed at five different frequencies up to 200 Hz. The outputs were all checked against the independently measured input. Data rates and run duration times were set equal to those to be used for the actual seismic tests.

6.3 SOFTWARE PROGRAMS

The data acquisition computer was programmed with a National Instruments, LABVIEW 2.5.2 data acquisition package. As mentioned previously, a data file of each test run included 1.4-million data points acquired in 10 s. Subsequently, the data time histories were converted to engineering units. This conversion took approximately 3 minutes. Thereafter, one could view all 50 time histories (or any lesser number of data channels) on the computer monitor for preliminary evaluation. This review was completed after each test run to assure that all data channels were working properly before going to a subsequent higher excitation level. Furthermore, a preliminary assessment of the model behavior could be made from this evaluation.

7 MODEL ASSEMBLY AND PRETEST

7.1 ASSEMBLY AND COMPRESSION PROCEDURE

A step-by-step procedure for assembly of the model is given in Appendix C. A brief summary of this procedure is given is this section. The sequence of the procedure was important in order to control the static preload condition of the system, prior to the application of dynamic test runs.

An initial stage of the model assembly is shown in Figure 7-1. The procedure was started by assembling only the bottom structure and two end structures. These units were squared and held together by four 19-cm (0.75-in.) bars and the bottom edge hinges as shown. The inside width was set at 1.23 m (48.5 in.) to allow for the nominal rock mass width, plus 6.4-mm (0.25-in.) rubber pad thickness on each side. All three sides were greased with a silicone compound to produce a slick surface, and the ingot laying process was started from bottom to top. Each ingot was hand placed in order to keep the layers as straight as possible. It may be noted from the figures that some slight interferences at edges eventually built up, as variations in ingot thickness and slight curvatures were inevitably present. As may be noted from the photographs, each ingot was marked with a date of casting on its near side face.

As the ingot laying process approached the center opening, four split ring opening supports were laid in place, as shown in Figure 7-2. At this point also, one end of the opening interior LVDTs was cemented into holes in the appropriate ingots. Thereafter, the ingot laying continued, with the other end of the LVDTs correspondingly being cemented into place. Eventually, the ingot-laying process was completed, as shown in Figure 7-3. The actual number of ingot layers counted vertically turned out to be 16 ½ compared to 17, as was originally intended. This discrepancy resulted from accumulated growth of the stack due to slight oversize of each ingot and its corresponding roughness interfaces. However, this slight difference was considered negligible.

At this stage of the assembly, horizontal cables were installed to an initial tension and the four bars were also loosened. The center opening support rings were also removed. Thereafter the top support structure was installed along with all vertical cables at an initial tension, as shown in Figure 7-4. At this point, the model static compression sequence was started. For this sequence, bottom edge hinges and upper corner rollers were loose, so that they offered no resistance to the contraction of the four boundaries. The detailed load sequence for developing the final compression is given in Appendix C. The final values and associated total pressures that resulted from cable tension plus top mass are given in Table 7-1. When this condition was achieved, the hinges and rollers were tightened in place.

7.2 INSTRUMENTATION INSTALLATION AND CHECKOUT

With the model assembly in full static compression, all remaining instrumentation was installed in positions described in Section 5.1. All amplifiers, filters, and interconnecting cables were installed for an initial checkout. Readout at this point was checked with a digital voltmeter.

7.3 INSTALLATION ON SEISMIC SIMULATOR

A heavy steel frame was designed for attachment to the model and lifting it onto the seismic shaker table. This frame was fabricated of heavy steel channel welded together, and designed for lifting by overhead crane. A proof test of this frame is shown in Figure 7-5, where four concrete blocks plus four

Figure 7-1. Initial stage of rock mass assembly

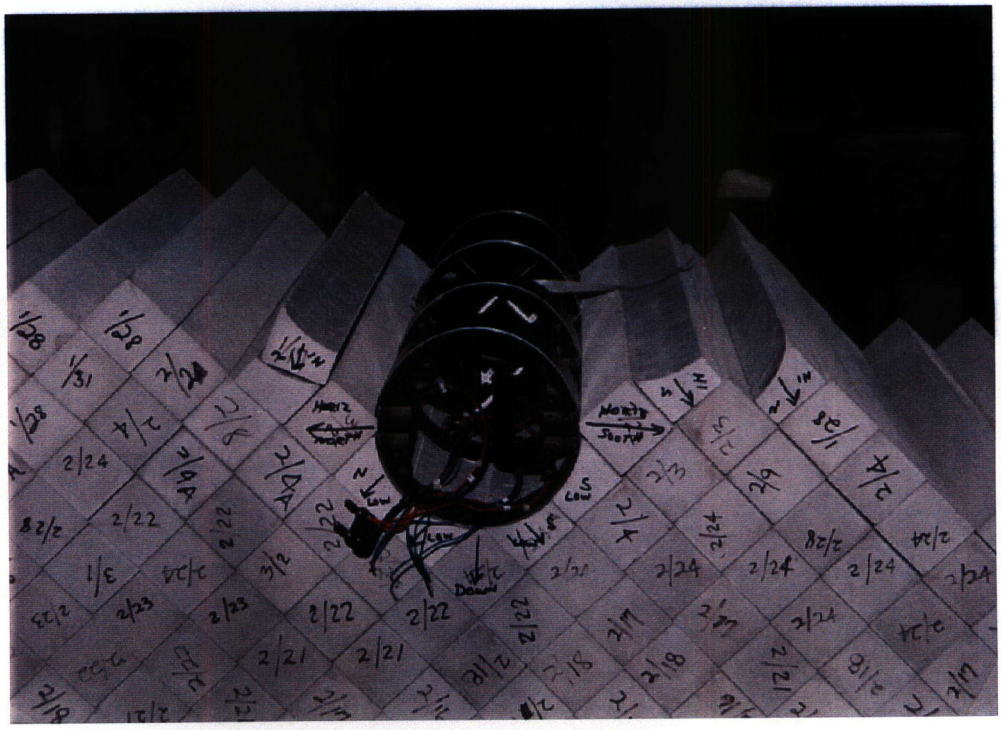

Figure 7-2. Assembly ring support for center opening

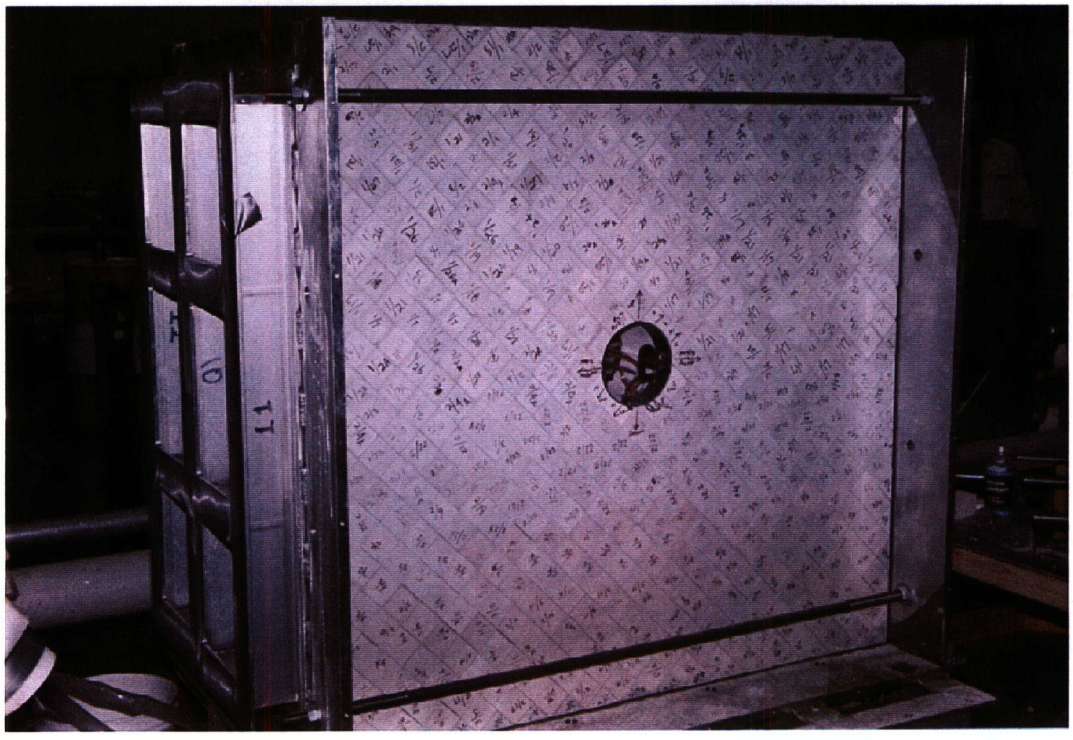

Figure 7-3. Later stage of rock mass assembly

Figure 7-4. Configuration for initial compression

Table 7-1. Model static compression parameters

Cable Tensions:	
Vertical All:	1,050 N (236 lbf)
Horizontal Top:	800 N (180 lbf)
Horizontal Midhigh:	1,040 N (234 lbf)
Horizontal Midlow:	1,223 N (275 lbf)
Horizontal Bottom:	1,303 N (293 lbf)
Total Top Mass:	662 kg (1,460 lb)
Total Normal (Vertical Pressure):	0.02 MPa (2.9 psi)

steel plates were lifted with the model top frame structure as the base. Thereafter, the lifting frame was attached to the model with the same six lifting rods, as shown in Figure 7-6. Here also, 6.4-mm (1/4-in.) aluminum side shear plates were bolted to both sides of the model. These shear plates were used to ensure that lifting and moving transients would cause no undue dynamic excitations of the model.

The model was then lifted onto the seismic simulator as shown in Figure 7-7. The side shear plates were removed, and all instrumentation and data acquisition equipment was connected. However, the model was not yet bolted to the seismic table.

7.4 BUMP TESTS

With the overhead crane still attached to the lifting apparatus and the model, a series of transient "bump tests" was performed to check out all channels of instrumentation through the data acquisition system. For each test, the 10-s data sequence was started, and a vertical transient was imposed by suddenly lifting the apparatus momentarily for about 6.35 cm (0.25 in.) from the simulator and then setting it back down onto the seismic table. By recording all channels of data in the intended acquisition mode, and then subsequently converting all data to engineering units, the time histories of each channel could be evaluated. Any inadvertent channel malfunction or misconnection was repaired. Thereafter, the hoisting apparatus was removed, and the model was bolted to the seismic table. The model was then ready for testing as shown in Figure 7-8.

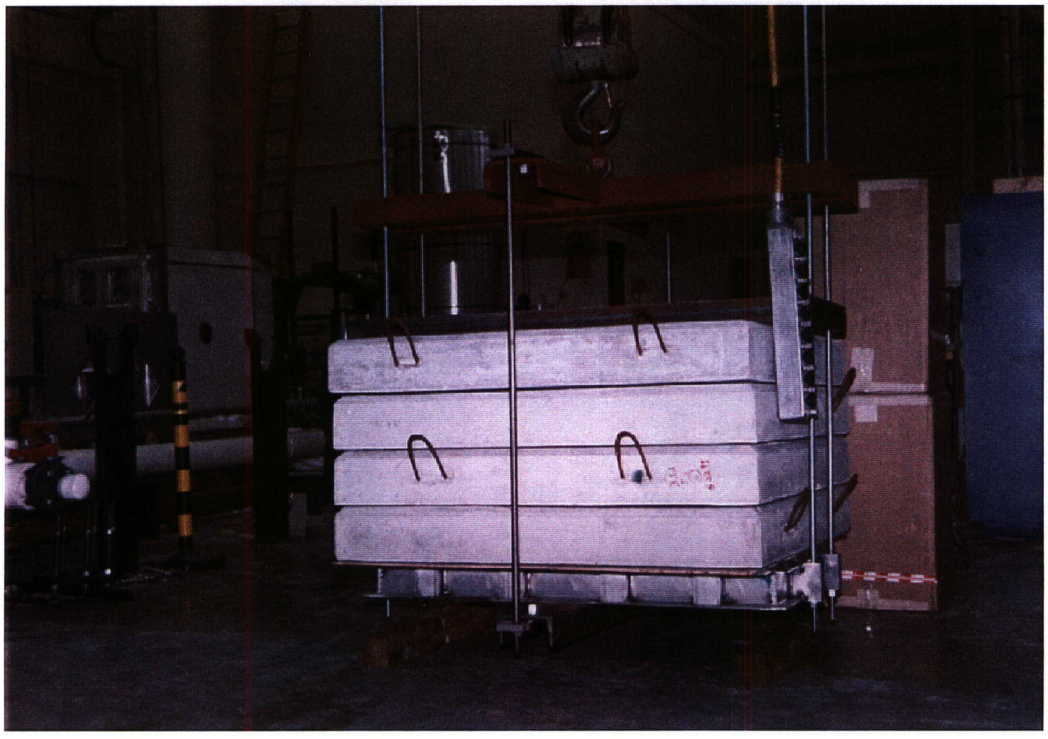

Figure 7-5. Proof test of lifting frame

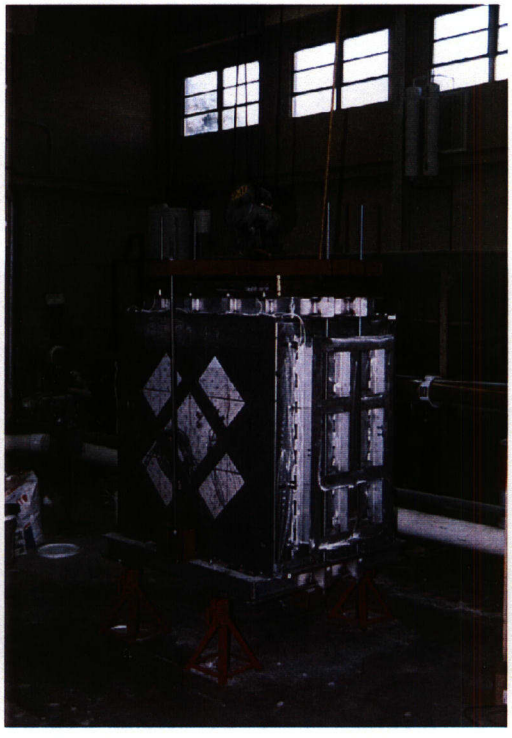

Figure 7-6. Lifting configuration for rock mass model

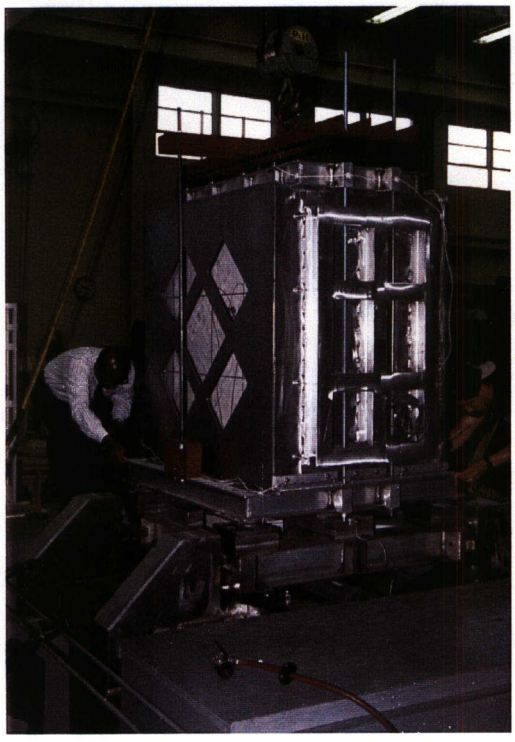

Figure 7-7. Mounting scale model on seismic table

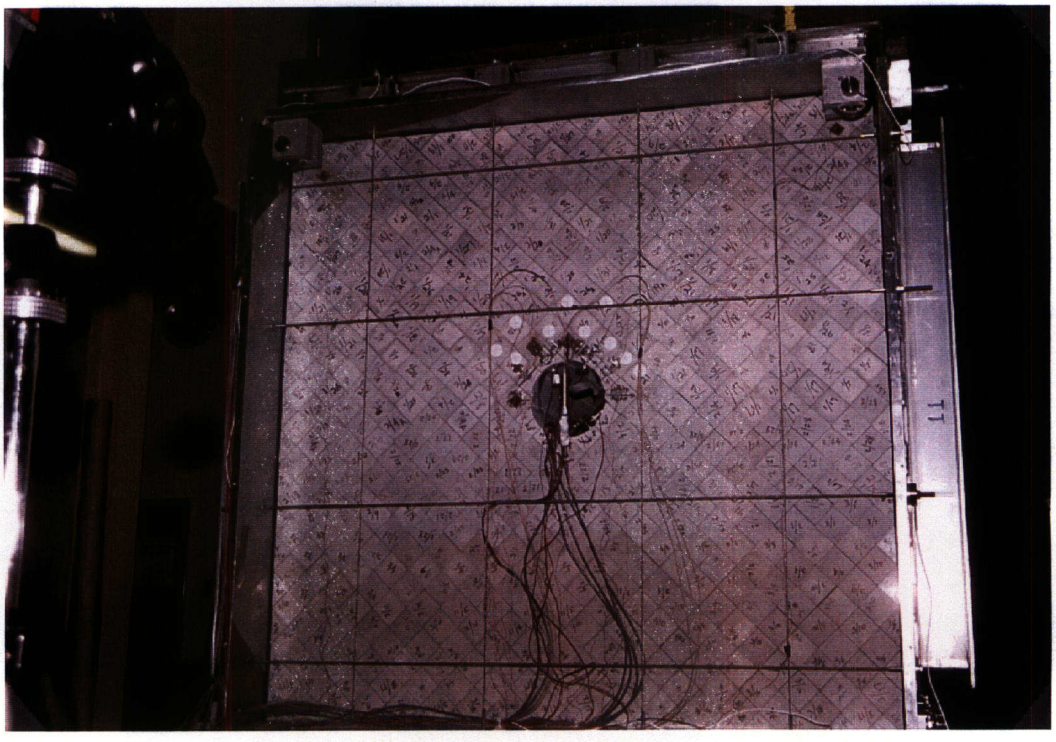

Figure 7-8. Final instrumentation and calibration

8 SEISMIC SIMULATOR SYSTEM

8.1 DRIVE SIGNAL DEVELOPMENT

The drive signal used for the scale model seismic experiments was based on an accelerogram measured at the Guerrero array for the September 19, 1985, Mexico City earthquake. This well-characterized seismic event is the same source that was used for the experiments conducted earlier to determine properties of welded tuff (see Hsiung et al., 1993). The full-scale acceleration time history for the south component of this earthquake is shown in Figure 8-1. A displacement history generated by computer from this acceleration is shown in Figure 8-2, while a displacement spectrum of this signal is shown in Figure 8-3. It may be noted that the displacement signal is somewhat shorter in duration than the original acceleration. This change was made in order to reduce the total time required for data acquisition, but yet remain within accepted test guidelines for earthquake simulations. Thus, the displacement of Figure 8-2 may be considered a "representative" earthquake waveform.

In order to use the displacement waveform as a 1/15-scale drive signal, further operations were performed. As noted from the similarity numbers given in Eq. (2-1), the signal duration had to be time compressed by a factor of the square root of 15; and in doing so, the frequencies had to be extended by the same factor. Thus, the acceleration of Figure 8-4 and the displacement of Figure 8-5 resulted. This latter waveform was used for the direct drive signal for the seismic simulator. The amplitude of the resulting motion was controlled by the gain setting on the seismic table controller.

8.2 ELECTROMECHANICAL SEISMIC SIMULATOR

An electrohydraulic shaker table was used for simulations of seismic events. Some specifications for this facility are given in Appendix D. The system is typically driven by an analog signal input that can be originated by analog tape recorder or by a digital computer via a digital-to-analog conversion. Often the process is based on synthesis of a signal that matches a specified earthquake response spectrum. Details of this process can be obtained from Unruh (1982). However, for the present experiments, the displacement time history of Figure 8-5 was duplicated on an analog tape recorder for use as the drive source. Furthermore, although this table is capable of producing simultaneous independent earthquake motions along both the horizontal and vertical axes, only the horizontal was used for this experiment to simplify the analysis process. Therefore, the vertical drive was bolted down to the table base in order to maximize the table resistance to any rocking excitation. That is, a purely horizontal motion simulation was desired. Finally, although the indicated drive signal was utilized, the actual table motion was anticipated to vary slightly from it because of the transfer function for the electrohydraulic system. However, these differences will be shown to be quite negligible for the present experiments.

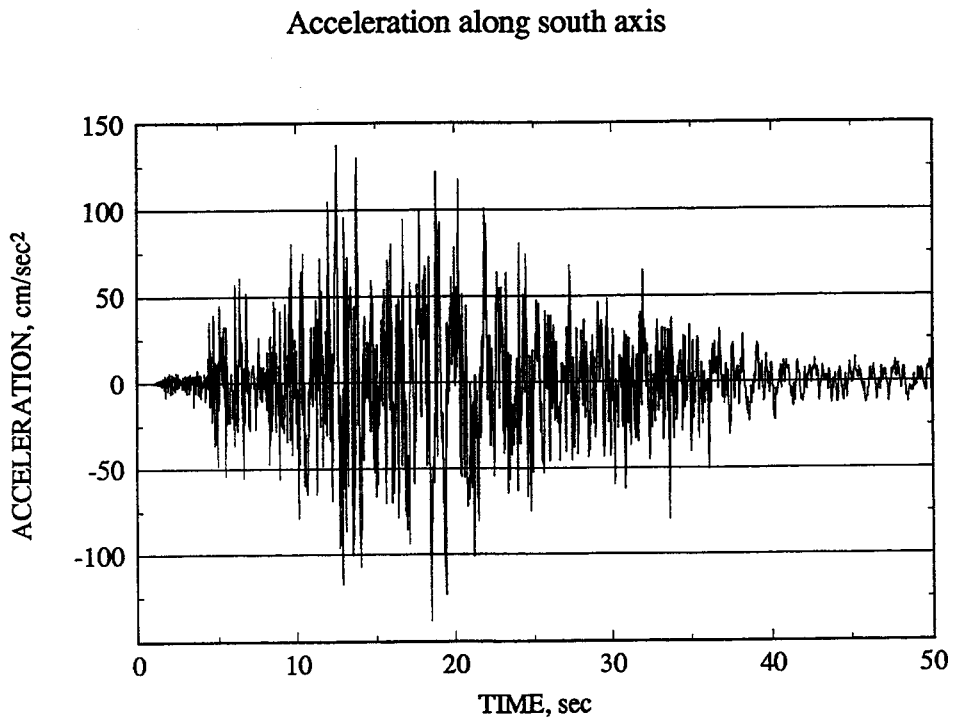

Figure 8-1. South component of acceleration for September 19, 1985, Mexico City earthquake

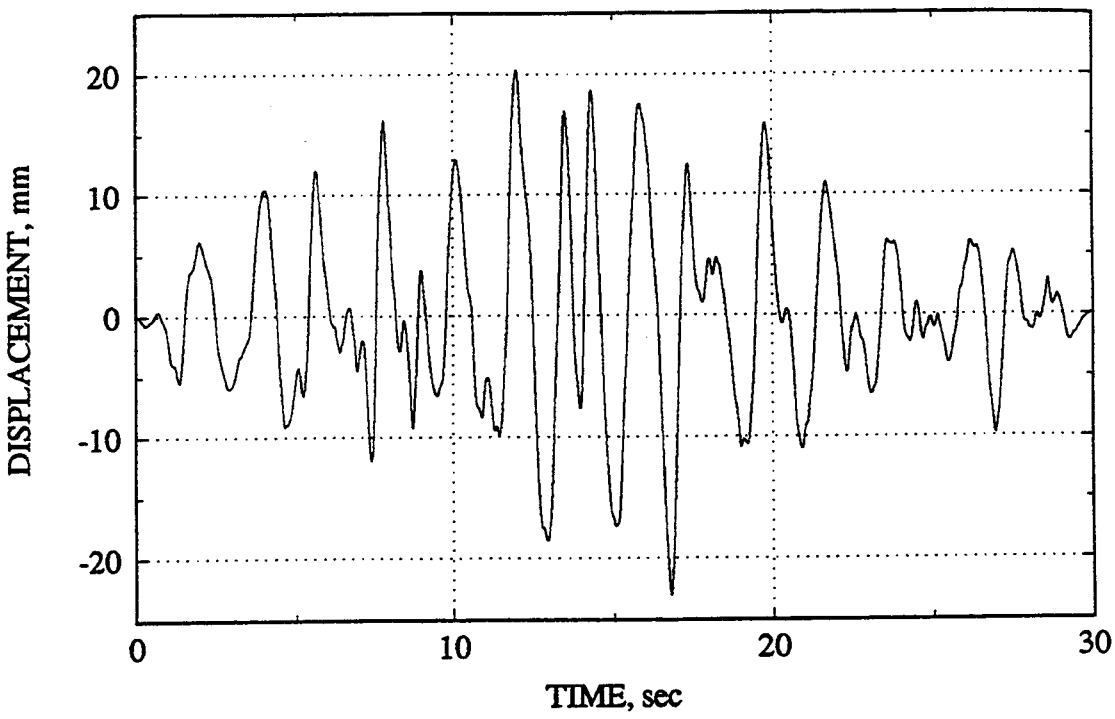

Figure 8-2. Displacement history generated from acceleration history in Figure 8-1

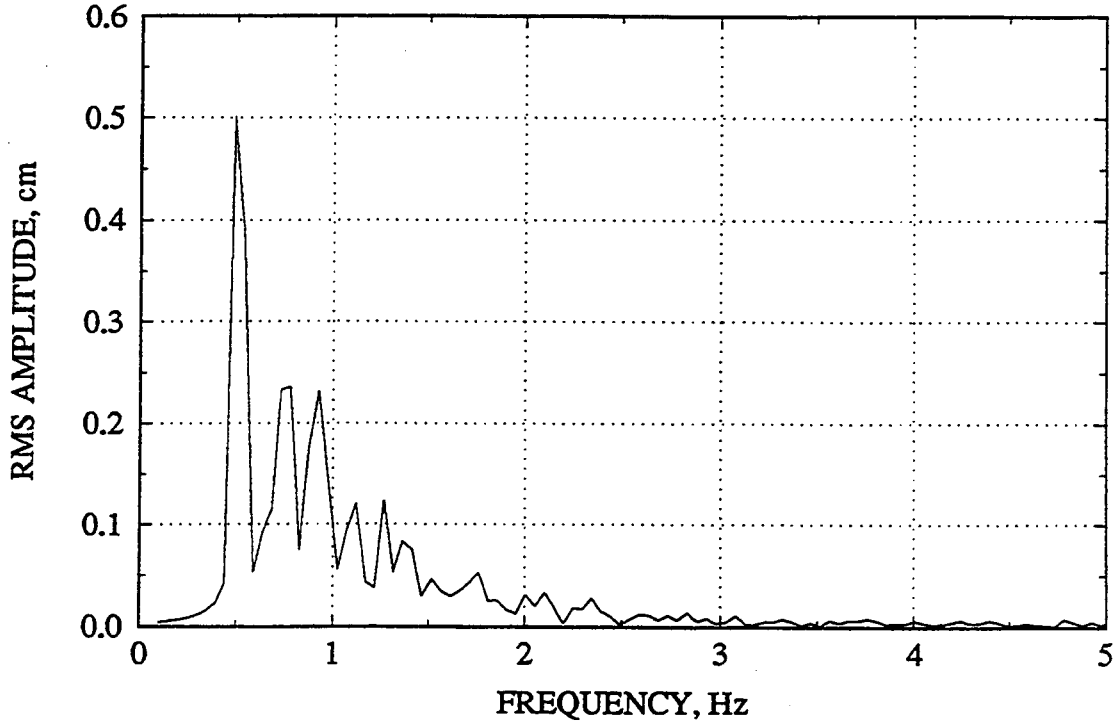

Figure 8-3. Displacement spectrum of the generated displacement history in Figure 8-2

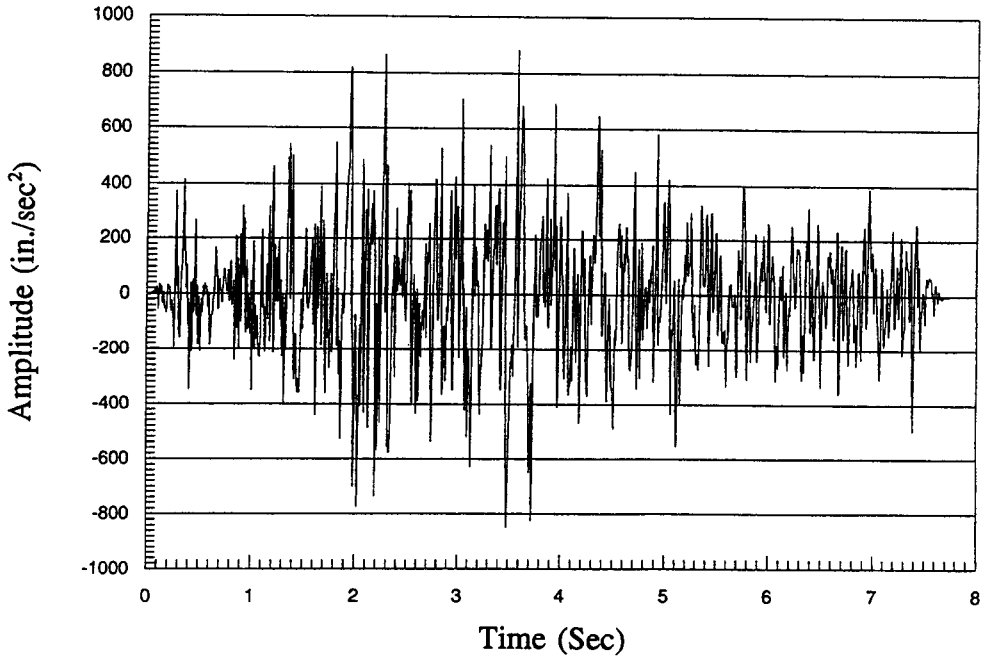

Figure 8-4. Scale model earthquake acceleration history

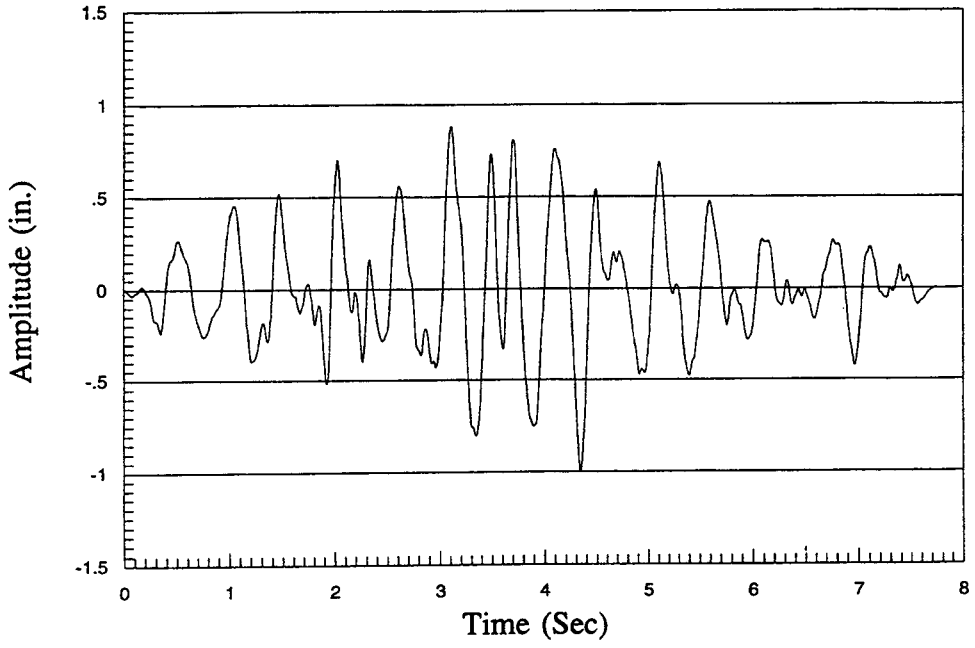

Figure 8-5. Scale model earthquake displacement history

9 SEISMIC TEST PROCEDURES

Test procedures were based on what can be called an "incremental fragility level" philosophy. Test runs were started at a very low peak excitation displacement level, and this amplitude was incrementally increased as the runs progressed. Both videotape and digital data were acquired for each run. At the end of each run, all 50 channels were converted to engineering units, and a preliminary review of the data was performed visually on the 486 computer monitor. In some infrequent cases, transducer or other component malfunction occurred, and adjustments were performed prior to the next run. Furthermore, some shifting of filter channels or transducer locations was performed as response information was acquired. In all cases, the approach was to ensure the fidelity of the data acquired.

Table 9-1 gives a matrix of all tests performed. Included are zero runs performed periodically throughout the testing program. Zero runs consisted of operating the data acquisition with no input to the seismic table. These runs assisted in filling in data gaps that occurred during data taken. The excitation level was incrementally increased until it approached the maximum capacity of the seismic table. Significant permanent shifting of the upper ingots of the central opening occurred toward the end of the test series. Further information on this shifting is provided in the next section. Some loosening of the tension cables also occurred during test runs as would be expected as the ingot mass settled and permanent displacement of rock ingots occurred. Therefore, tension cables were retightened to their initial tensions after several test runs. Furthermore, a series of still photographs was taken for each side of the model in order to help document the initial and final positions of ingots for several runs.

Table 9-1. Matrix for seismic test series

Data Set	Data Run	Peak Excitation	Test Notes
DATA 8	ZERO 8	Zero	
DATA 9	RUN 1	3.8 mm (0.15 in.)	No Data for first 5 s
DATA 10	RUN 2	3.8 mm (0.15 in.)	
DATA 11	RUN 3	3.8 mm (0.15 in.)	
DATA 12	RUN 4	3.8 mm (0.15 in.)	Retuned Cables & Photo Series Following
DATA 13	ZERO 13	Zero	
DATA 14	RUN 5	7.6 mm (0.30 in.)	Retuned Cables Following
DATA 15	RUN 6	7.6 mm (0.30 in.)	Retuned Cables & Photo Series Following
DATA 16	RUN 7	7.6 mm (0.30 in.)	Retuned Cables & Photo Series Following
DATA 17	RUN 8	7.6 mm (0.30 in.)	Retuned Cables Following
DATA 18	ZERO 18	Zero	
DATA 19	RUN 9	11.7 mm (0.46 in.)	Retuned Cables Following
DATA 20	ZERO 20	Zero	
DATA 21	RUN 10	11.7 mm (0.46 in.)	Retuned Cables Following
DATA 22	RUN 11	11.7 mm (0.46 in.)	Retuned Cables Following
DATA 23	RUN 12	11.7 mm (0.46 in.)	Photo Series Following
DATA 24	ZERO 24	Zero	
DATA 25	RUN 13	15.5 mm (0.61 in.)	Checked Cables & Photo Series Following
DATA 26	ZERO 26	Zero	
DATA 27	RUN 14	15.5 mm (0.61 in.)	Checked Cables & Photo Series Following
DATA 28	RUN 15	15.5 mm (0.61 in.)	Checked Cabled & Photo Series Following
DATA 29	ZERO 29	Zero	
DATA 30	RUN 16	15.5 mm (0.61 in.)	Photo Series Following
DATA 31	ZERO 31	Zero	All Cables "As Is"
DATA 32	ZERO 32	Zero	Vertical Cables Tightened to 667 N (150 lb)
DATA 33	RUN 17	15.5 mm (0.61 in.)	Photo Series Following
DATA 34	RUN 18	15.5 mm (0.61 in.)	No Data for last 8 s
DATA 35	ZERO 35	Zero	Photo Series Following
DATA 36	ZERO 36	Zero	
DATA 37	RUN 19	15.5 mm (0.61 in.)	No Data for last 8 s Checked Cables Following
DATA 38	ZERO 38	Zero	Photo Series Following
DATA 39	ZERO 39	Zero	
DATA 40	RUN 20	12.2 mm (0.48 in.)	Checked Cables & Photo Series Following
DATA 41	ZERO 41	Zero	
DATA 42	RUN 21	17.3 mm (0.68 in.)	Photo Series Following

10 SAMPLE RESULTS

To facilitate discussion of the rock mass experiment, a set of sample results from one data run is presented in this section. These sample results will indicate the type of data available to assist in understanding the response of the experimental rock mass apparatus. Since the motion of the ingots near the tunnel was most important, there is a concentration of transducers near the tunnel opening as described in Section 5.1. The sample results presented herein are from Test Run 5 (see Table 9-1). Test Run 5 was the first run at a 7.6-mm (0.30-in.) peak excitation amplitude. From Table 9-1, it can be seen that this value represents an intermediate excitation level.

The response from the seismic table input displacement transducer is shown in Figure 10-1. The corresponding seismic table input acceleration is shown in Figure 10-2. It can be seen that the actual table displacement differs little from the scale model earthquake displacement history shown in Figure 8-5, except for a 180° phase shift. This phase shift is arbitrary since the model is symmetric in the direction of the input axis. More differences are noted in the accelerations (Figures 10-2 and 8-4). This difference is to be expected, as table control feedback circuit rolls off as frequency increases. However, the table input acceleration (Figure 10-2), the scale-model earthquake acceleration history (Figure 8-4), and the Mexico City Earthquake acceleration (Figure 8-1) all contain strong acceleration peaks that occur approximately one-third of the way into the earthquake motion and again approximately one-half of the way into the earthquake.

The response of the overall rock mass model was monitored using accelerometer and load cell measurements as shown in Figure 5-1. Figures 10-3 to 10-8 show the acceleration responses for accelerometers AC6 to AC11. Accelerometers AC6 to AC9 (Figures 10-3 to 10-6) had fairly similar responses with strong accelerations where similar strong amplitudes are present in the input acceleration (Figure 10-2). In addition, a lower frequency response at approximately 7 Hz is present in each of these signals. Accelerometers AC10 and AC11 (Figures 10-7 and 10-8) were mounted on the base of the rock mass and responded almost exclusively with the higher frequency acceleration spikes present in the input acceleration. AC10, in fact, had little low-frequency response at all.

Responses for load cells LC2 to LC6 are shown in Figures 10-9 to 10-13. Load cell LC1 was not monitored during this run. All these load cells show some type of dynamic response in addition to some permanent increase or decrease in load. These figures indicate that the dynamic responses occur throughout the seismic event while permanent offsets occur only at distinct points in the event. Thus the permanent load changes do not occur as a continuous function during the seismic event but in discrete steps.

Rock motion with respect to a single rock ingot was measured using rock surface-mounted strain gages and accelerometers. Figures 10-14 to 10-22 show the strain gages responses for transducers SG1 to SG9. In most cases, only amplitude digitization noise is apparent in the signals. There is negligible strain response present in any of the strain gage data.

Tunnel wall-mounted accelerometer data are shown for accelerometers AC1 to AC5 (Figures 10-23 to 10-27). As with the rock mass accelerometers, high-amplitude acceleration peaks and a lower frequency resonant response are present in these data. However, readily apparent differences are present between each of these tunnel wall accelerometers. These accelerometers were located on rock ingots comprising the tunnel wall and, in some cases, on opposite sides of the same rock ingot, indicating that the tunnel wall response was not uniform. Relative rock motion between rock ingots was monitored using Bentley

proximeter probes, cantilever beams, and LVDTs. The Bentley probes measured normal rock motion between two adjacent ingots, the cantilever beams measured shear motion between adjacent ingots, and the LVDTs measured motion of the top tunnel ingots with respect to the bottom tunnel ingots. The responses of Bentley probes BP1 to BP8 are shown in Figures 10-28 to 10-35. Cantilever beam responses for CB1 to CB8 are shown in Figures 10-36 to 10-43. The responses for LVDT transducers LV1 to LV6 are shown in Figures 10-44 to 10-49. These transducer signals show a general pattern of continuous dynamic response coupled with discrete permanent shifts associated with rock ingot dislocation.

In order to interpret the data properly, the direction of the motion must be determined. The Bentley probes are biased so that an increase in amplitude is associated with an increase in the normal gap between two adjacent rocks. The cantilever beams are biased so that an increase in amplitude indicates that the blocked (or root) portion of the beam has moved into the tunnel with respect to the pinned side. The LVDTs show an increase in amplitude as the LVDT is expanded and a decrease in amplitude as the LVDT is contracted.

The relative rock motion data can be examined with respect to locations of the transducers and ingot identification as indicated in Figures 5-5 and 5-6. Note that each rock ingot has the same identification number whether being looked at from the near side or the far side. For this particular data run, BP2 (Figure 10-29) indicates that ingots D and E moved away from each other as ingot D settled into the tunnel. On the far side, CB7 indicates that ingot G migrated towards the tunnel opening. On the near side, both CB4 and CB5 indicate a similar motion of ingot G towards the tunnel opening. Note that the positive dislocation response of CB4 and the negative dislocation response of CB5 indicate the same direction of motion for ingot G due to the location of the root and pinned ends of the respective cantilevers. Negative permanent offsets were indicated by all the LVDTs except for LV6, which indicated a positive dislocation. This dislocation clearly indicates that the tunnel was closing vertically while expanding horizontally. This process would be expected as the rock settled towards the tunnel opening under the influence of gravity during horizontal shaking.

Thus, a complete set of data for one run has been presented. More detailed discussions concerning the results from single runs and comparisons between multiple runs are contained in the following sections. However, the presentation of this complete set of transducer data gives an indication of the type of signal available from which to analyze the response of the rock mass model. Videotapes of the seismic runs and still photographs taken as indicated in Table 9-1 were also available to aid in data interpretation.

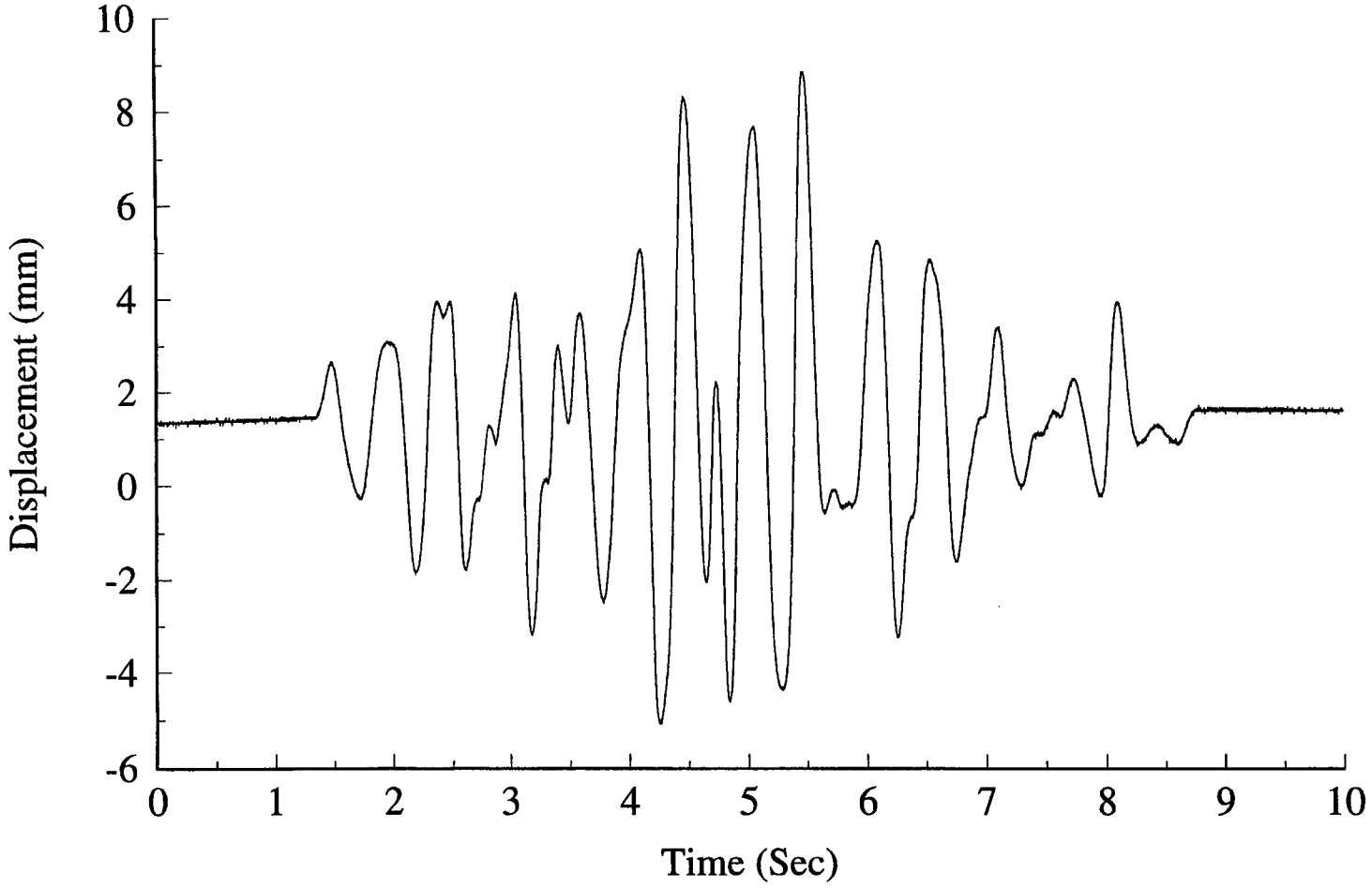

Figure 10-1. Run 5, 7.6 mm peak input: table displacement

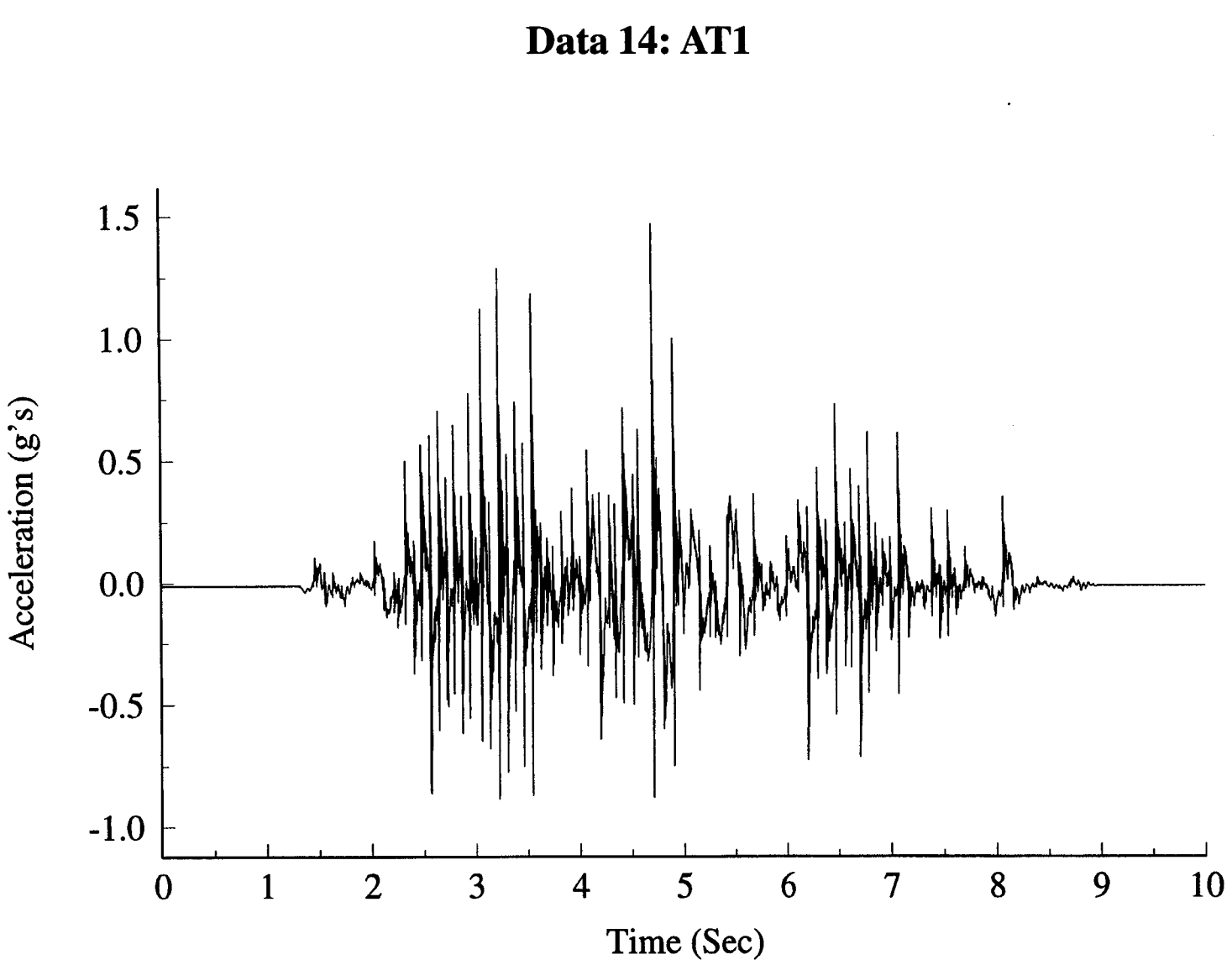

Figure 10-2. Run 5, 7.6 mm peak input: table acceleration

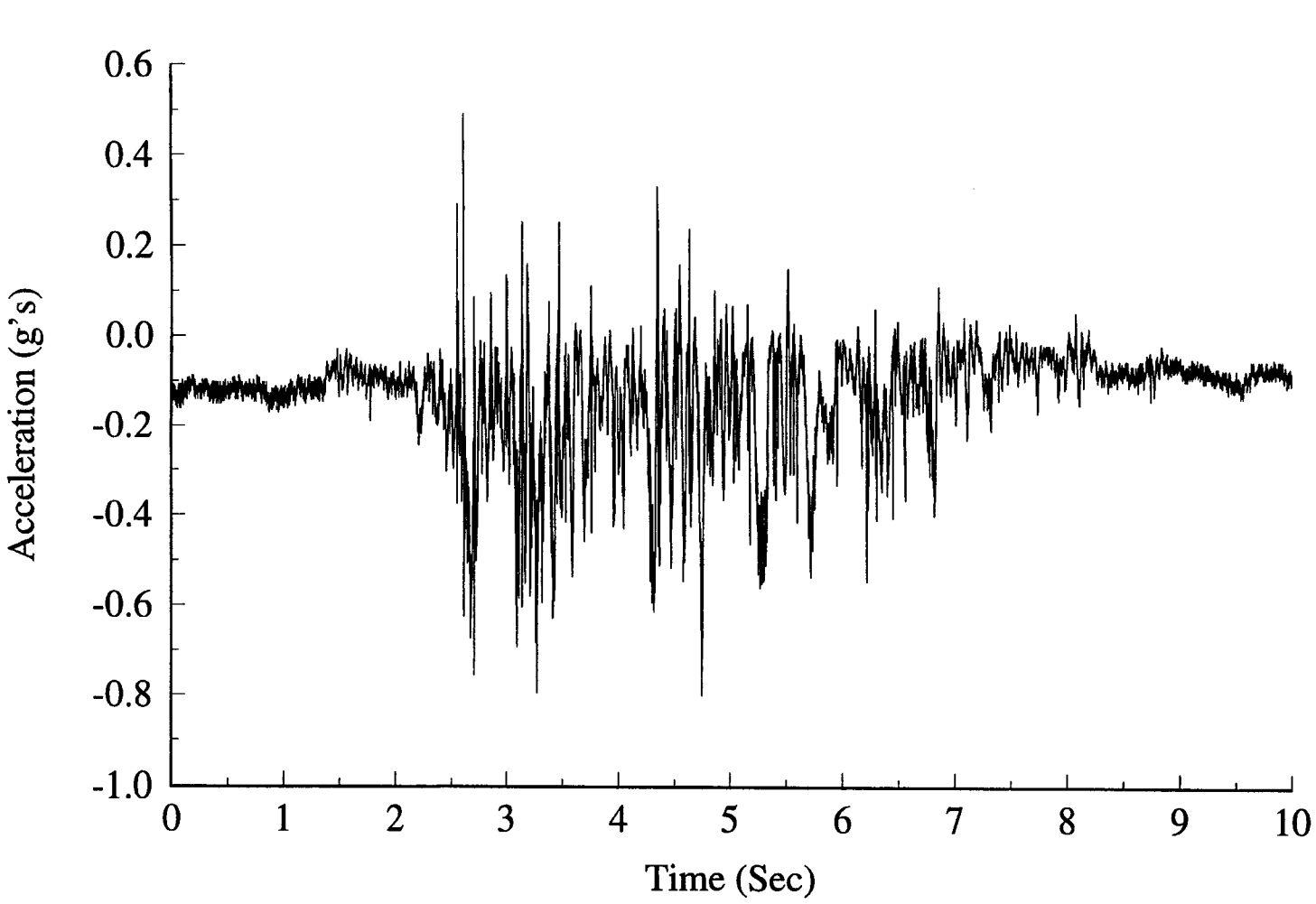

Figure 10-3. Run 5, 7.6 mm peak input: accelerometer AC6

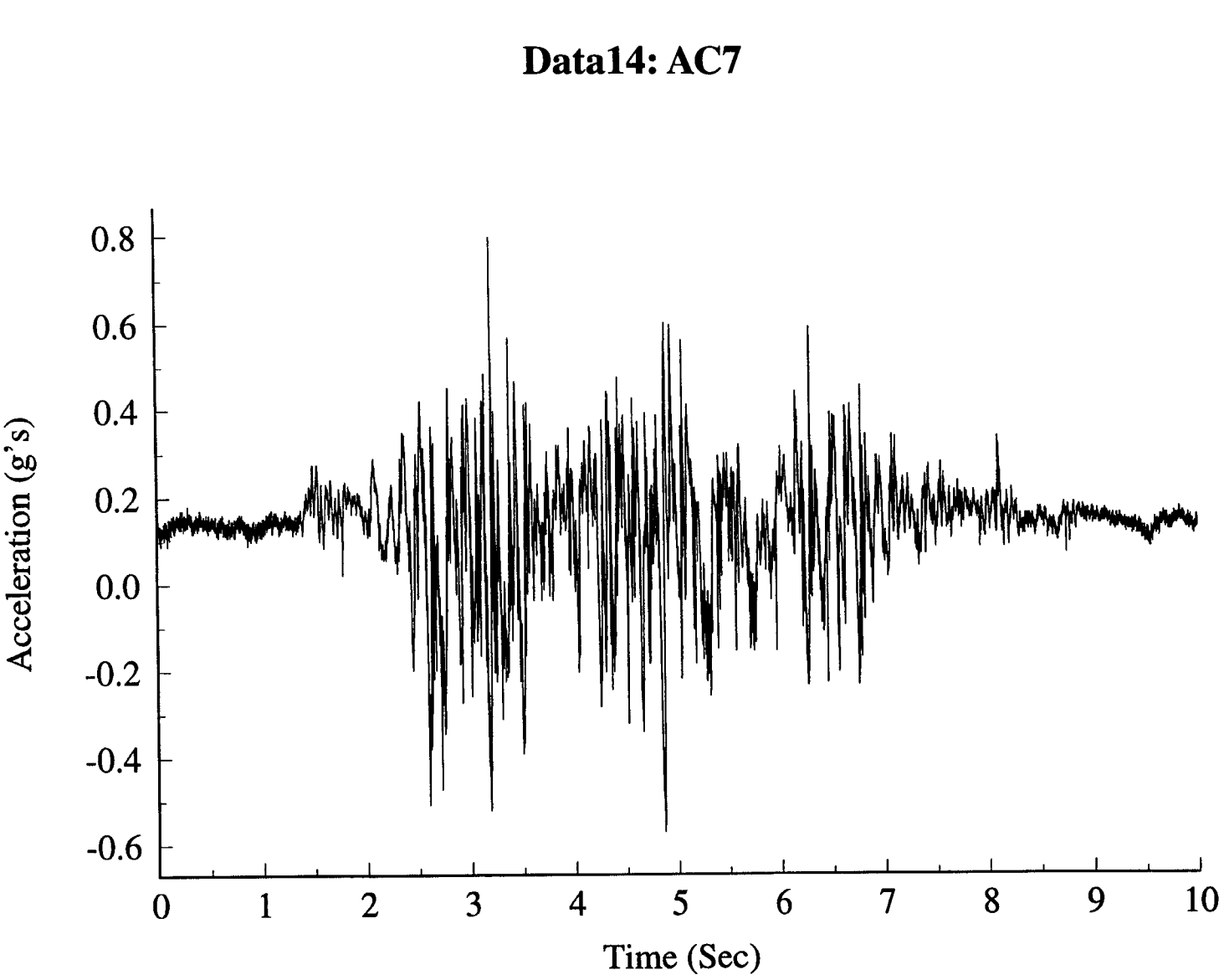

Figure 10-4. Run 5, 7.6 mm peak input: accelerometer AC7

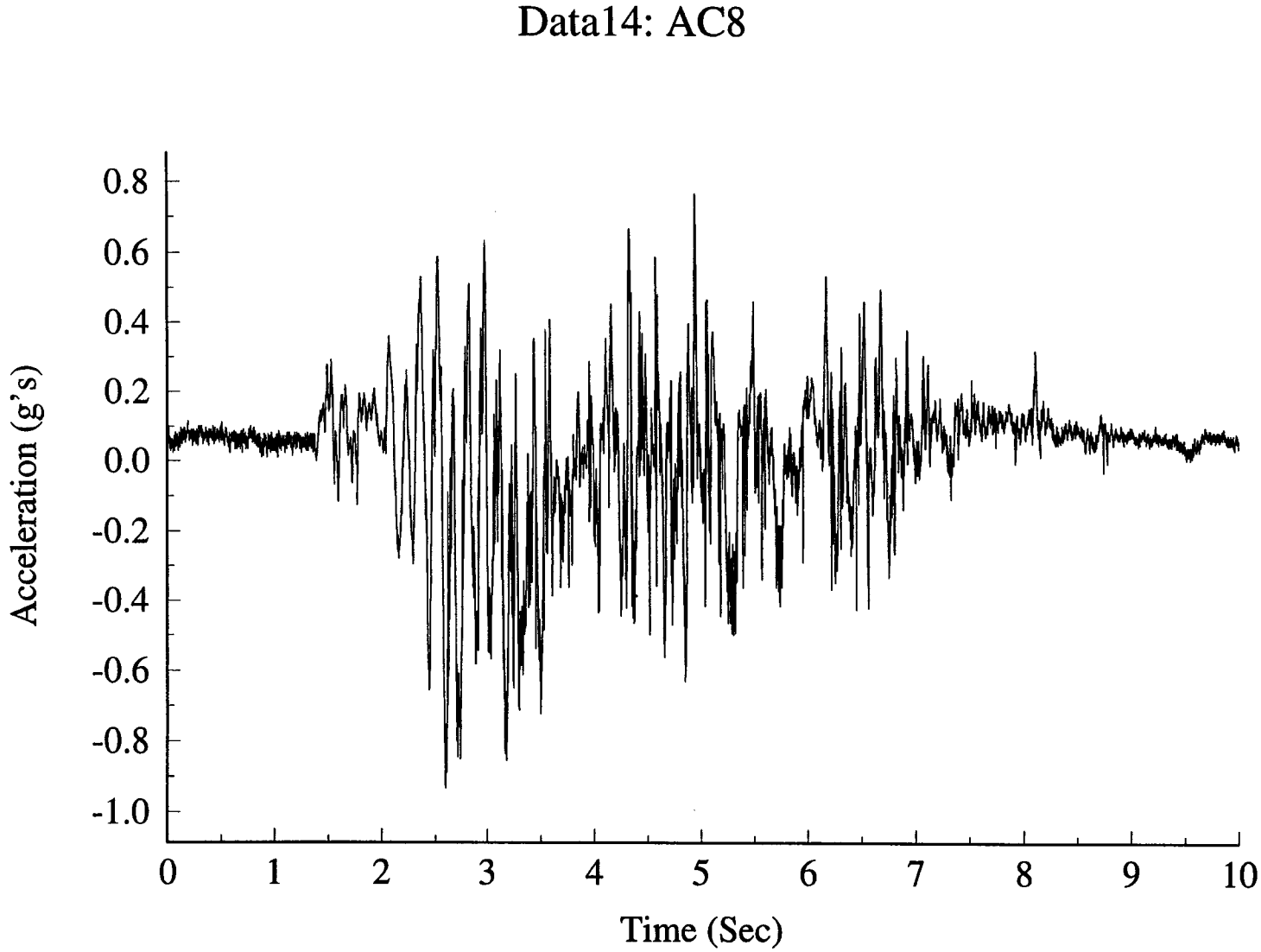

Figure 10-5. Run 5, 7.6 mm peak input: accelerometer AC8

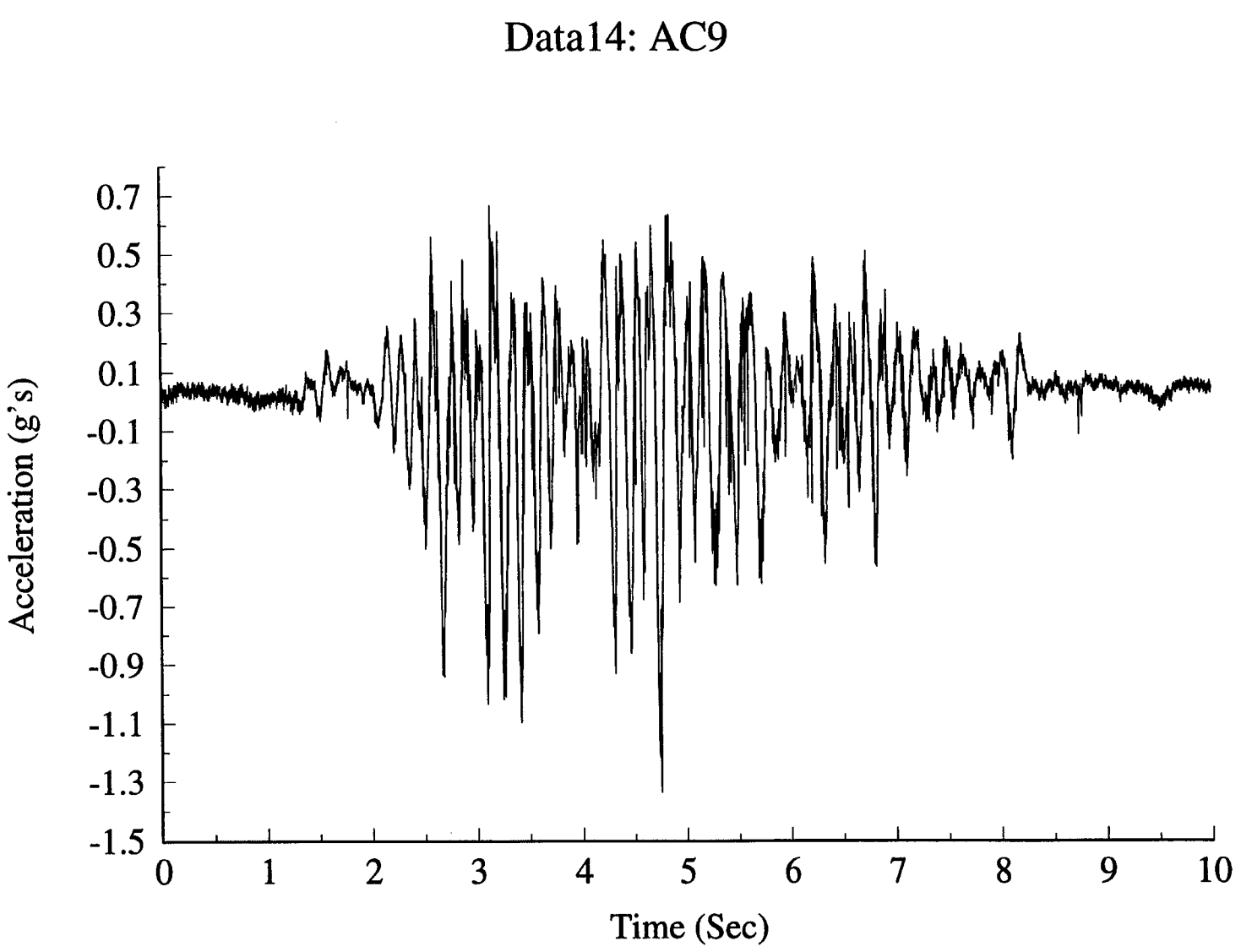

Figure 10-6. Run 5, 7.6 mm peak input: accelerometer AC9

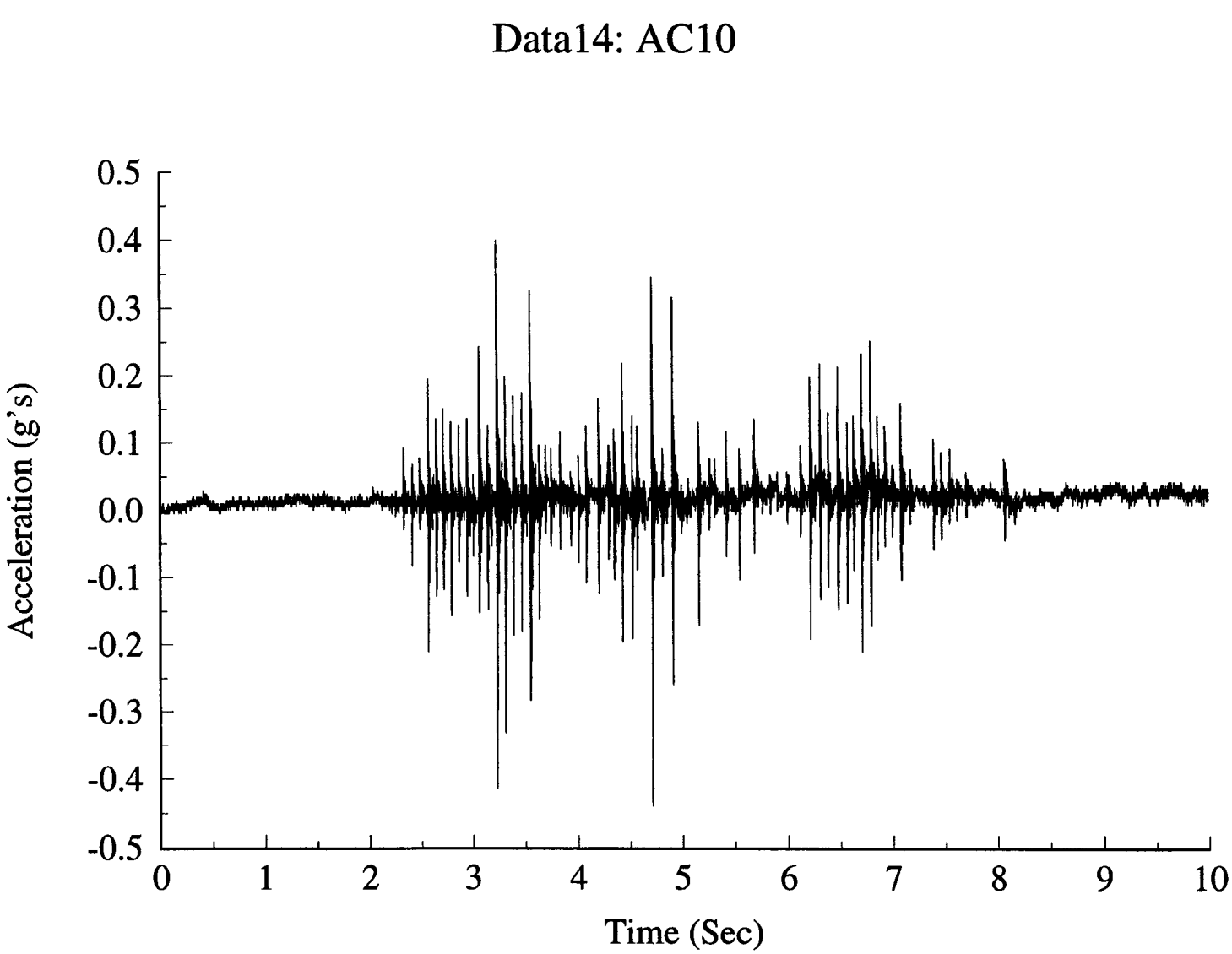

Figure 10-7. Run 5, 7.6 mm peak input: accelerometer AC10

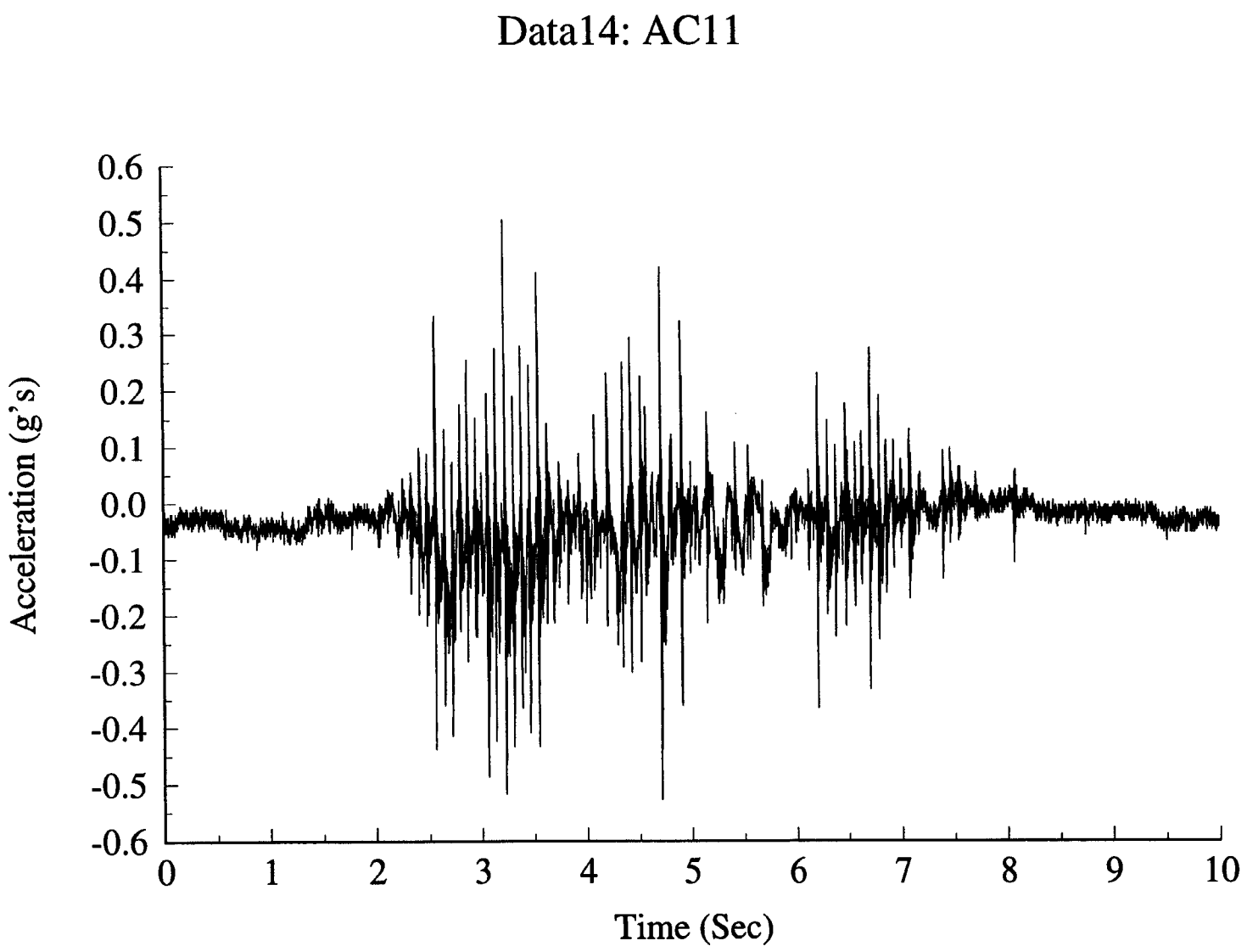

Figure 10-8. Run 5, 7.6 mm peak input: accelerometer AC11

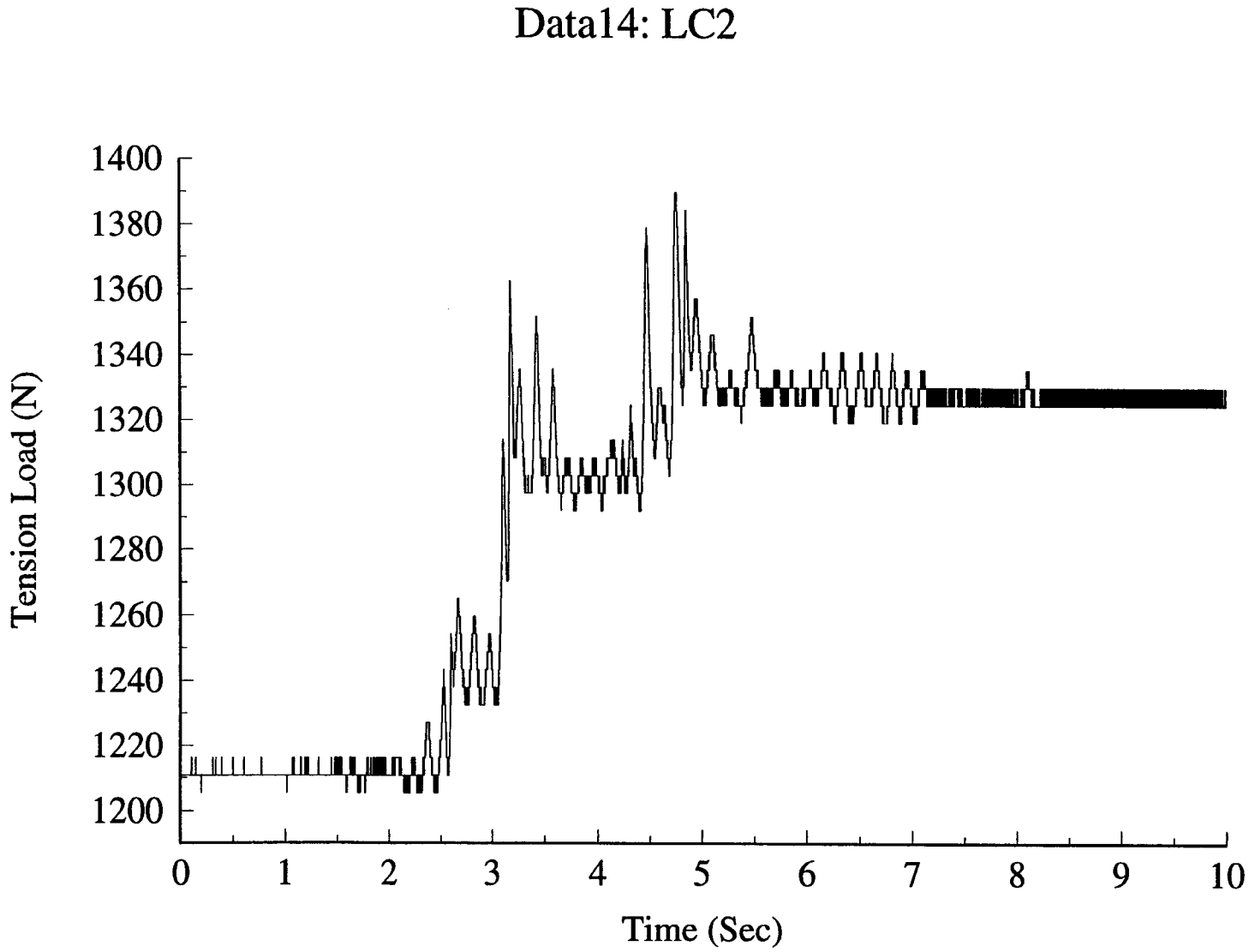

Figure 10-9. Run 5, 7.6 mm peak input: cable tension load cell LC2

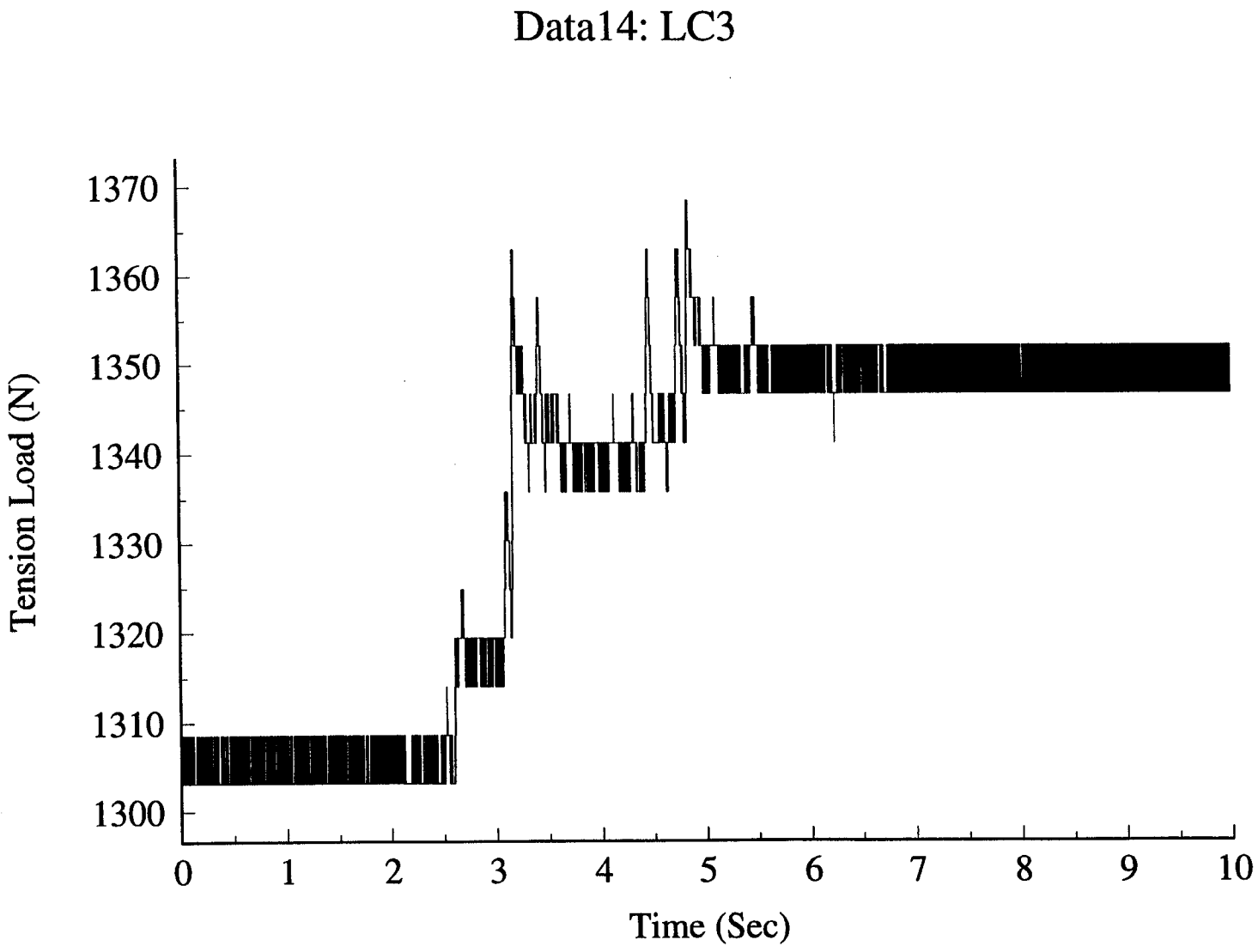

Figure 10-10. Run 5, 7.6 mm peak input: cable tension load cell LC3

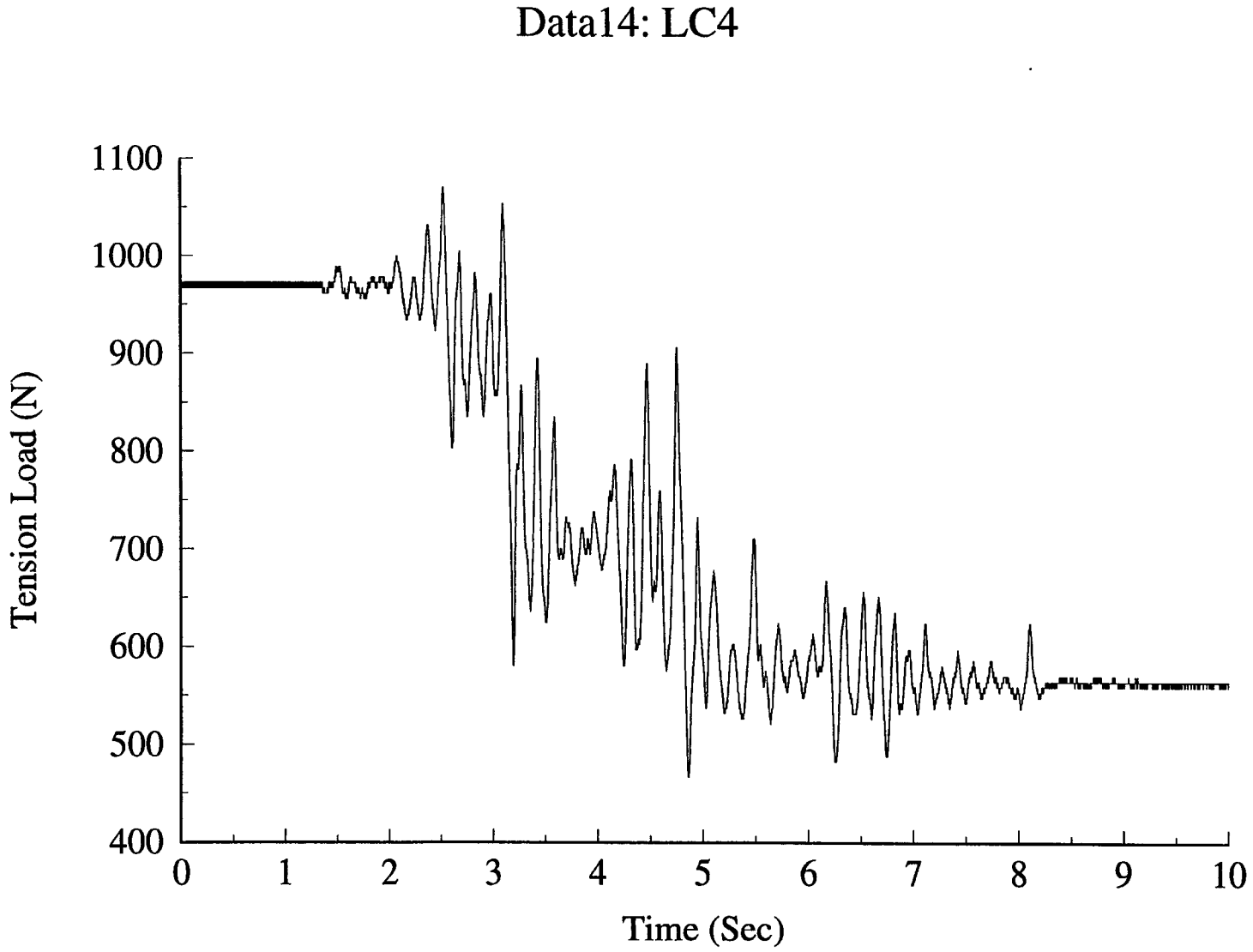

Figure 10-11. Run 5, 7.6 mm peak input: cable tension load cell LC4

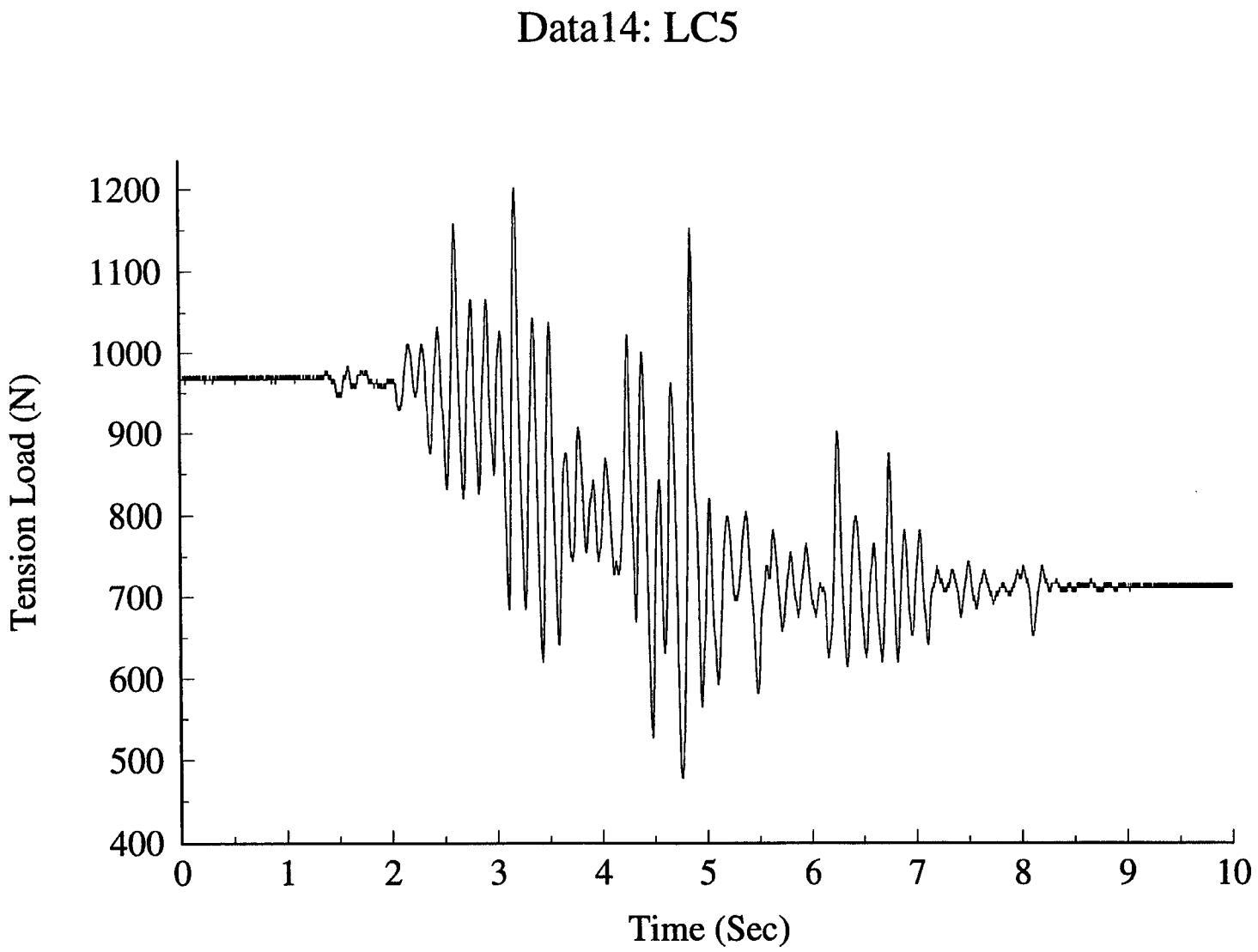

Figure 10-12. Run 5, 7.6 mm peak input: cable tension load cell LC5

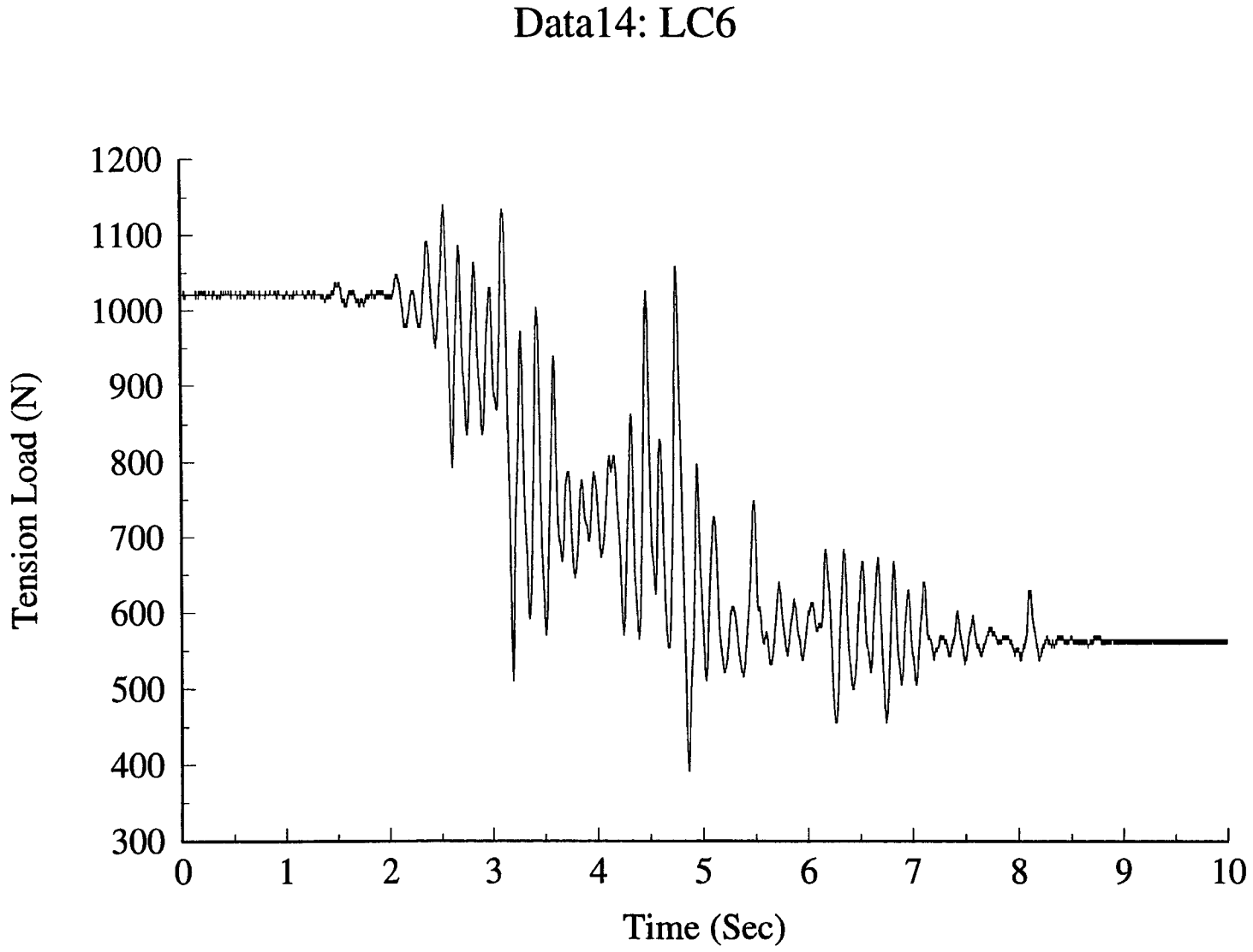

Figure 10-13. Run 5, 7.6 mm peak input: cable tension load cell LC6

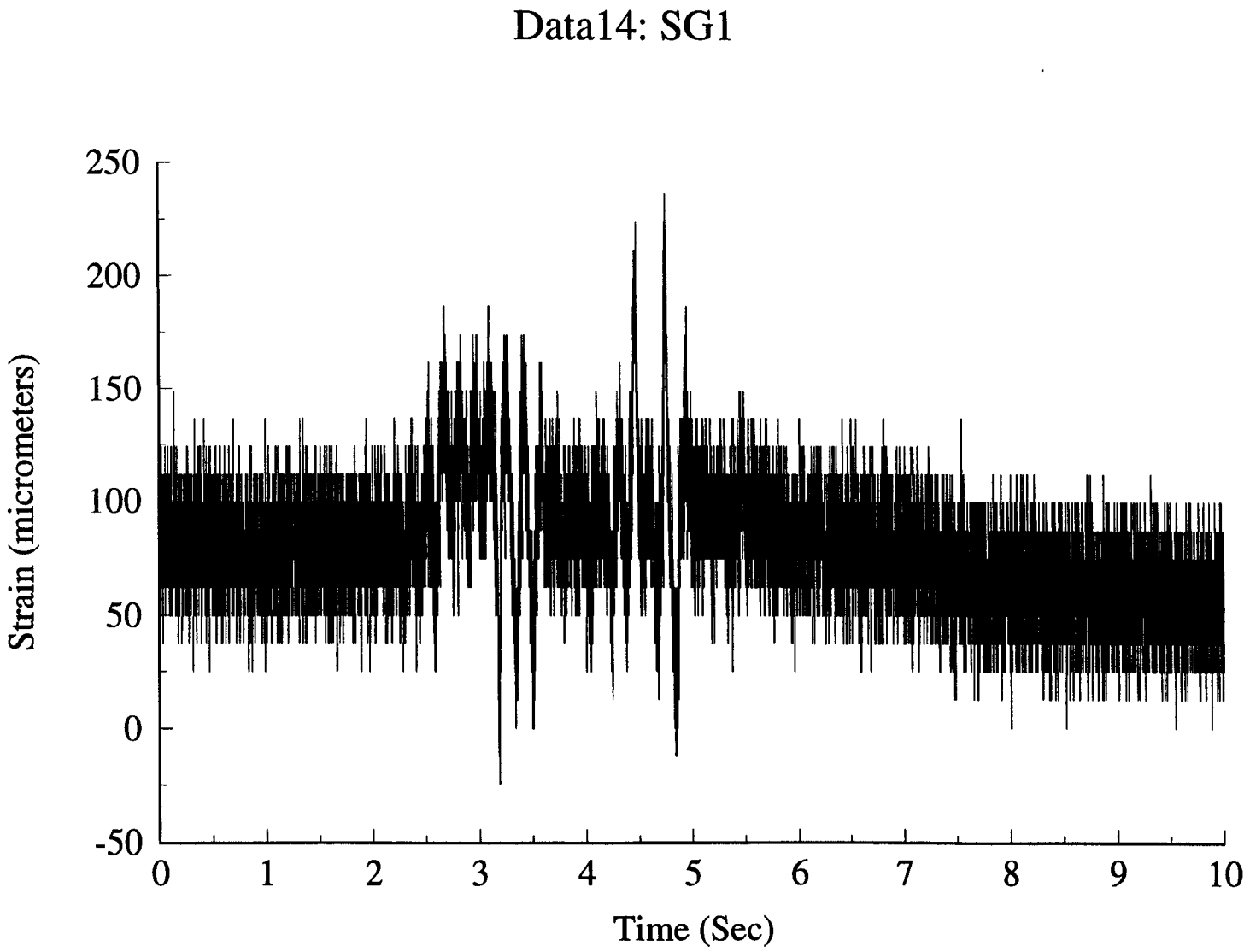

Figure 10-14. Run 5, 7.6 mm peak input: strain gage SG1

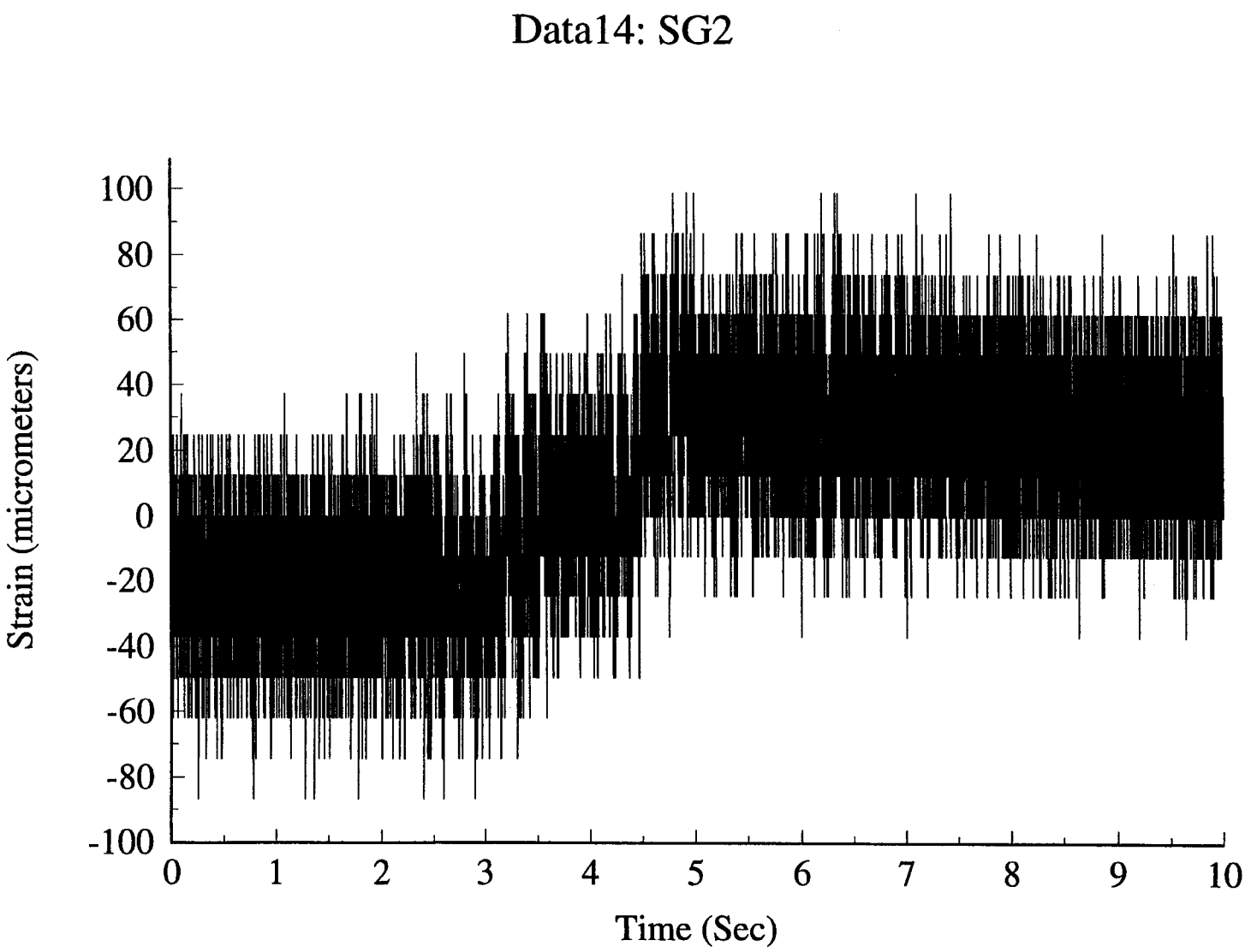

Figure 10-15. Run 5, 7.6 mm peak input: strain gage SG2

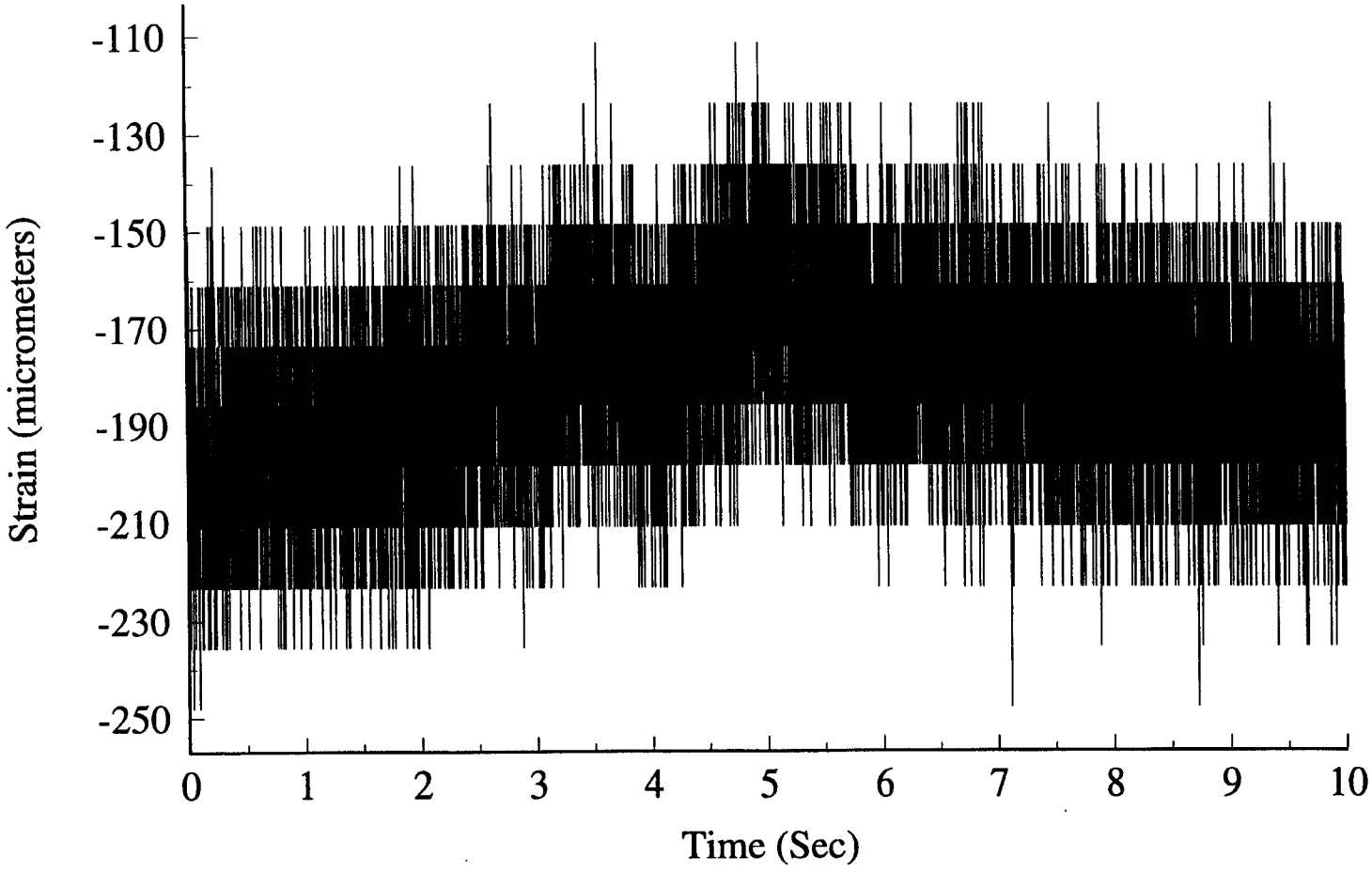

Figure 10-16. Run 5, 7.6 mm peak input: strain gage SG3

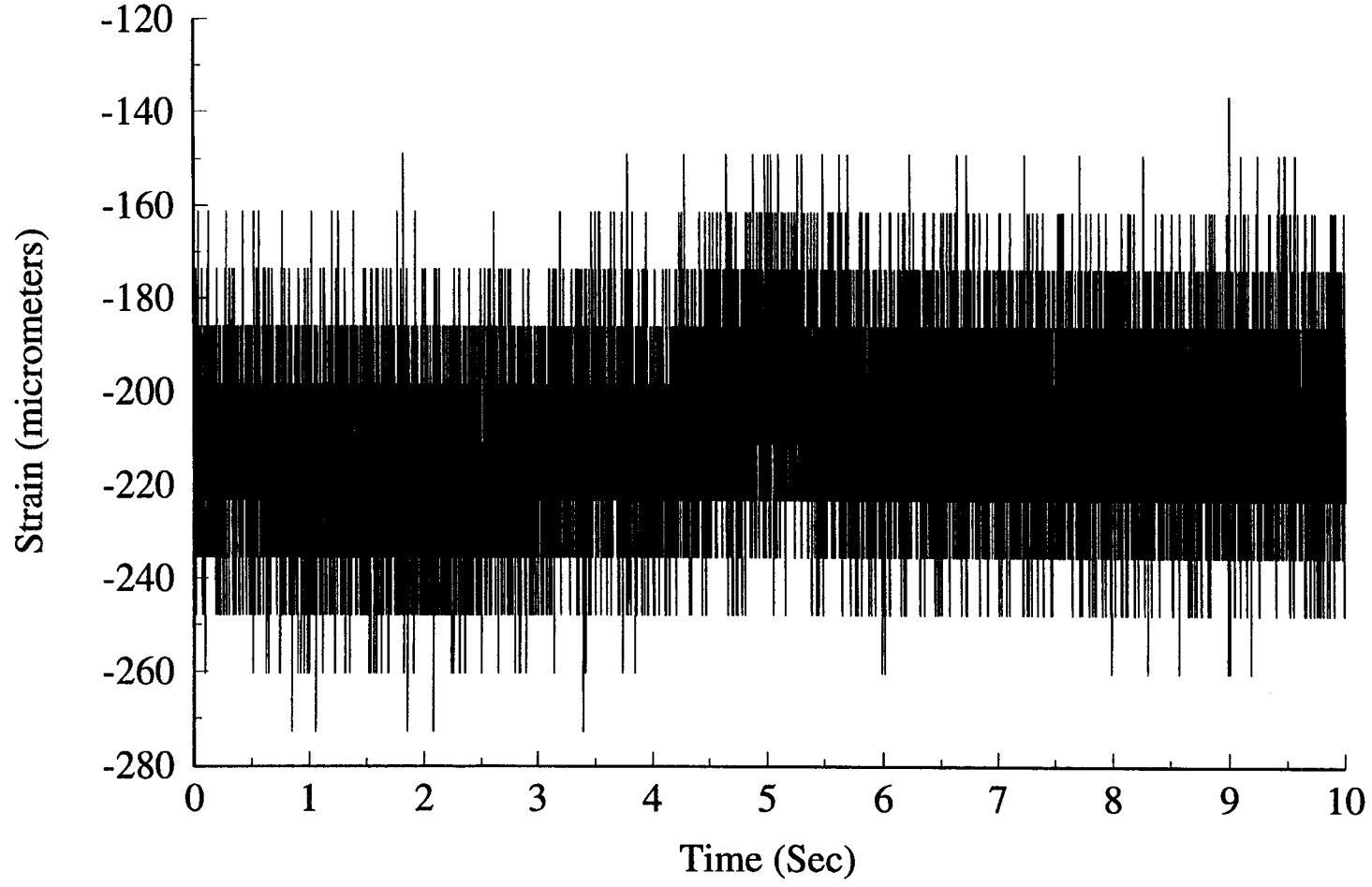

Figure 10-17. Run 5, 7.6 mm peak input: strain gage SG4

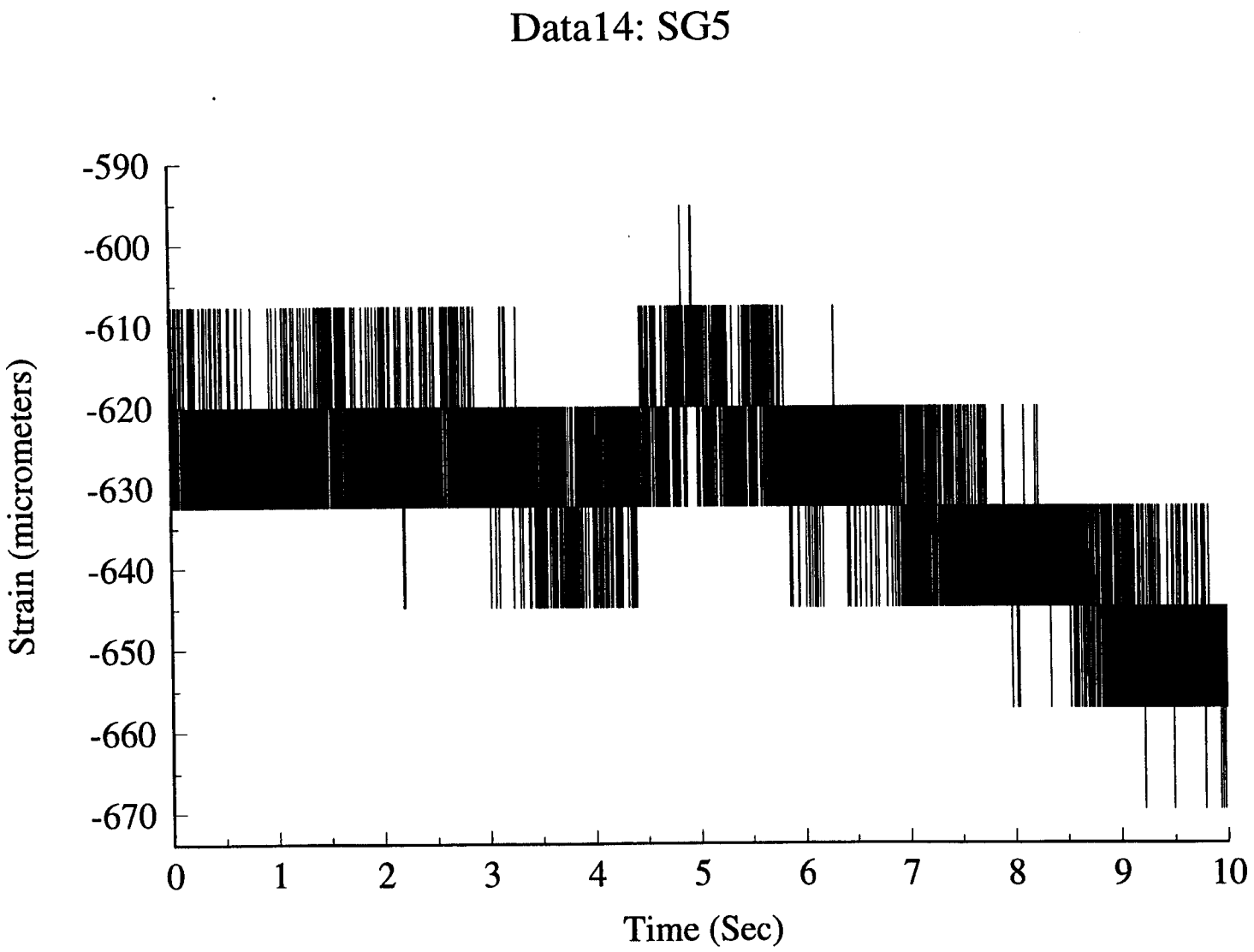

Figure 10-18. Run 5, 7.6 mm peak input: strain gage SG5

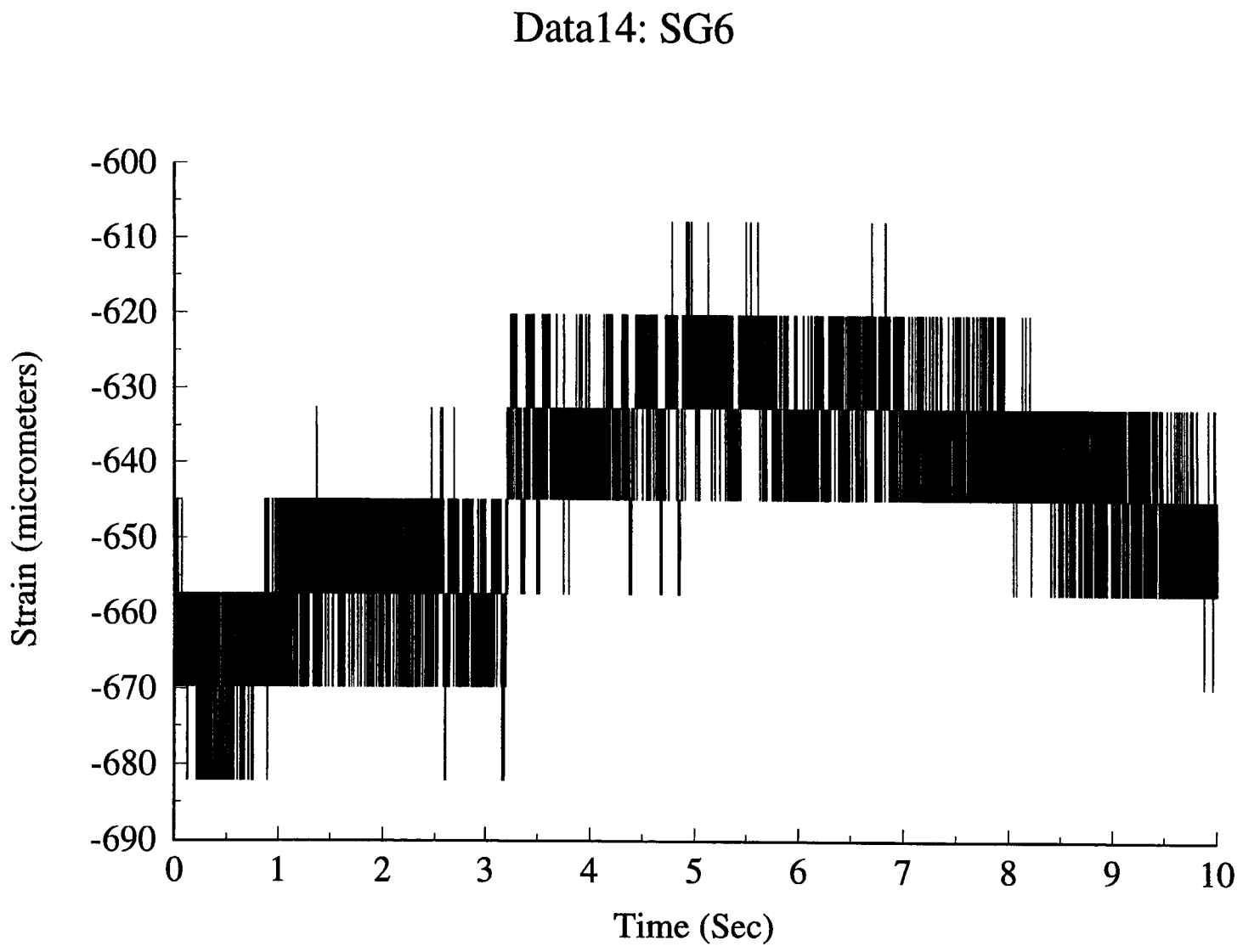

Figure 10-19. Run 5, 7.6 mm peak input: strain gage SG6

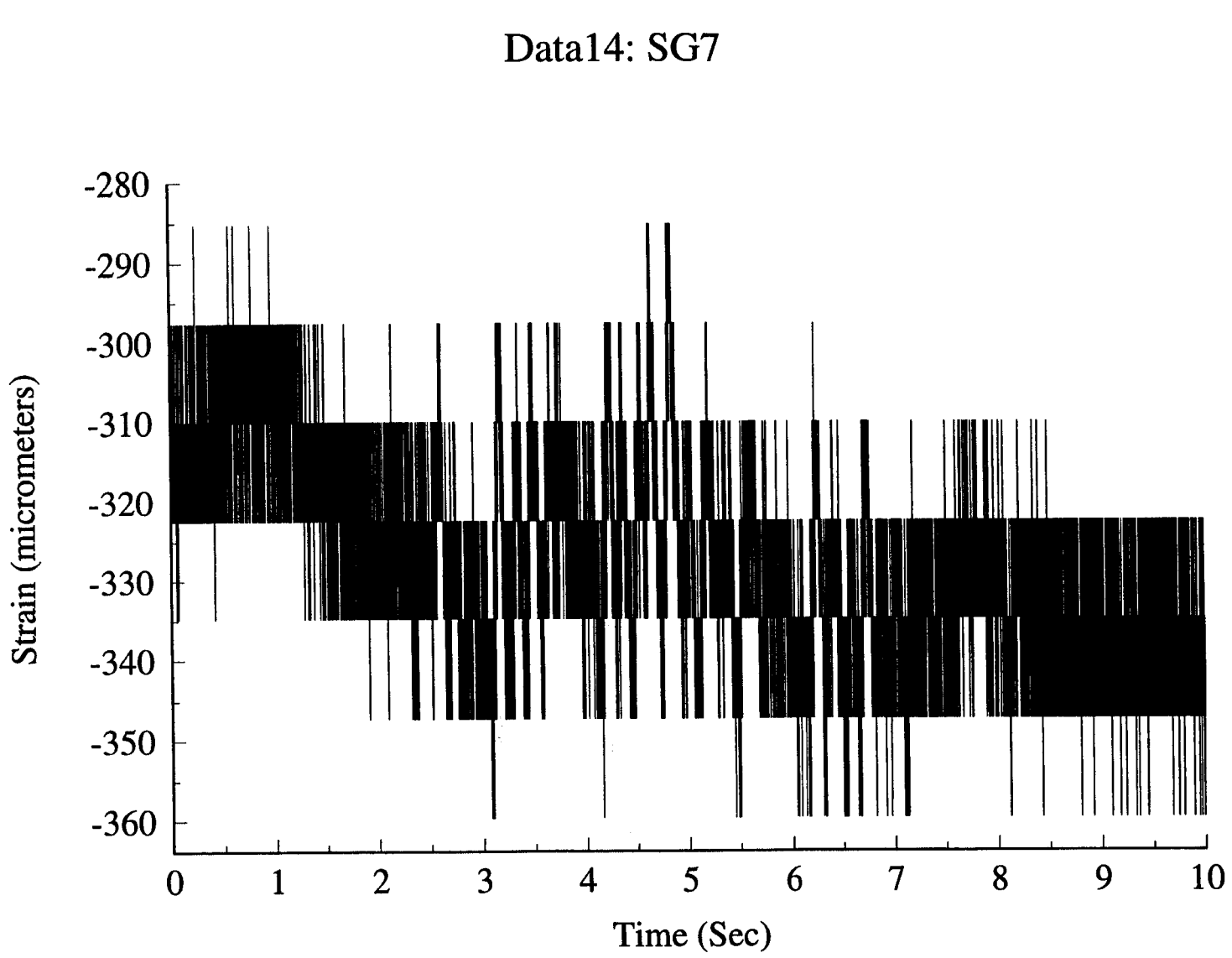

Figure 10-20. Run 5, 7.6 mm peak input: strain gage SG7

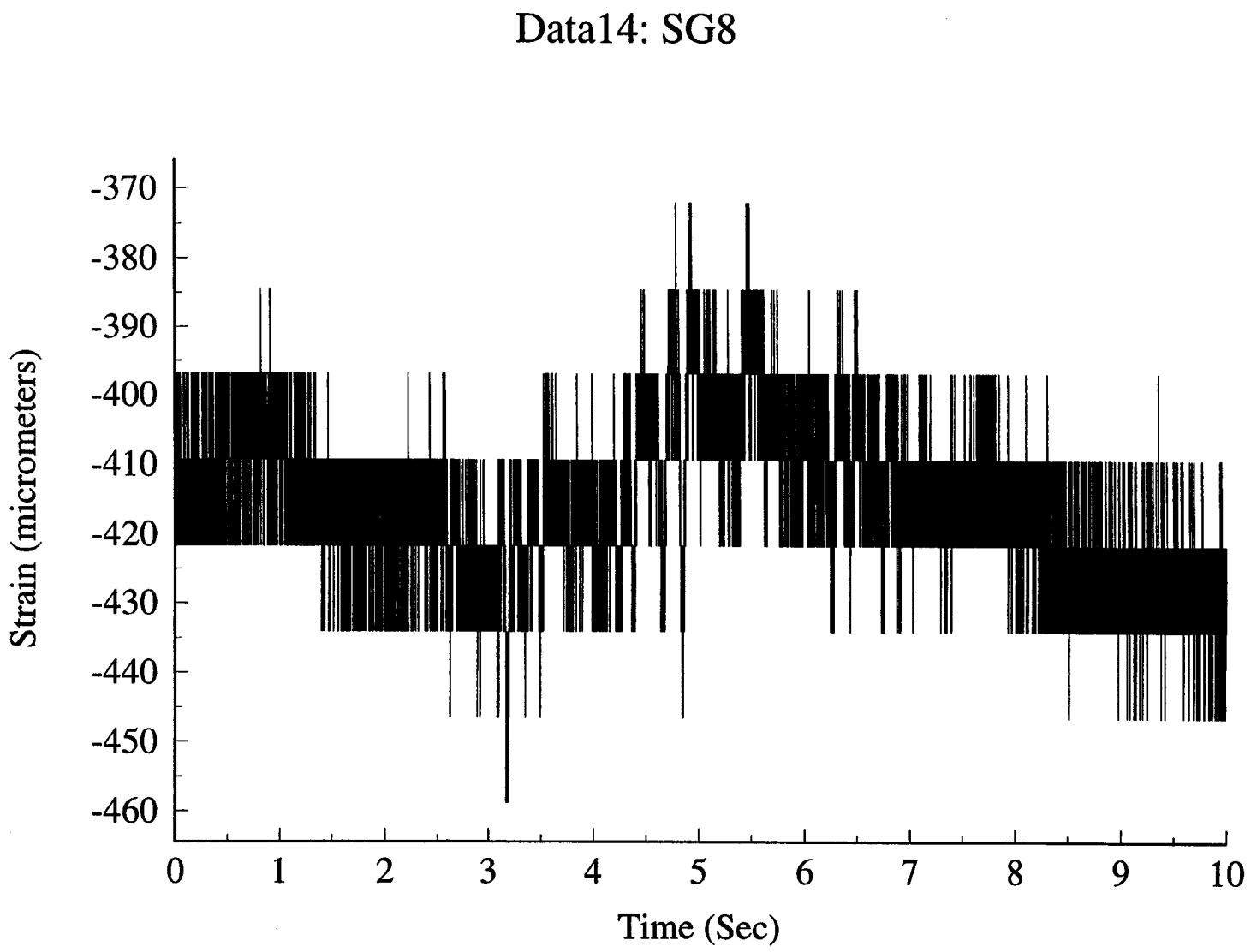

Figure 10-21. Run 5, 7.6 mm peak input: sprain gage SG8

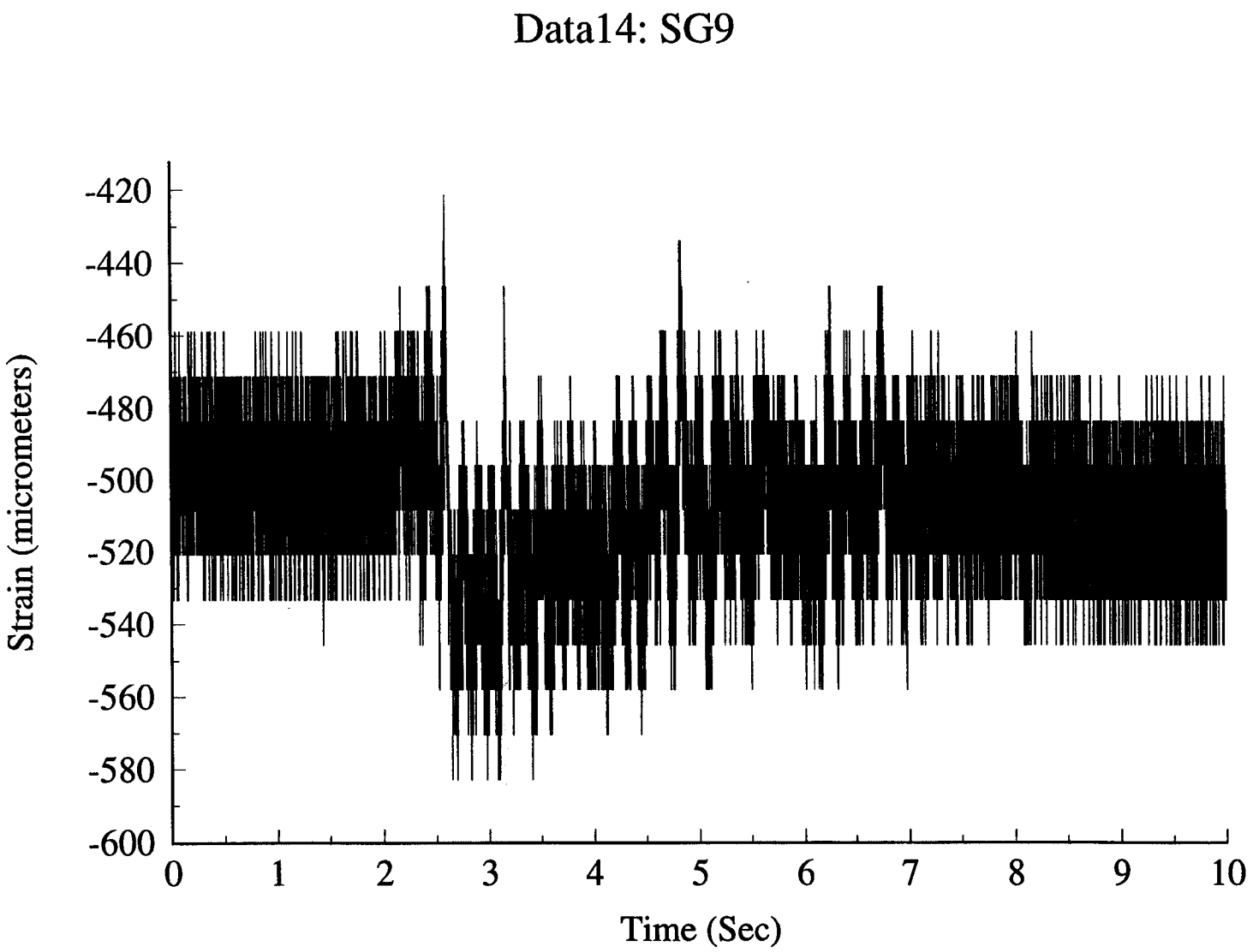

Figure 10-22. Run 5, 7.6 mm peak input: strain gage SG9

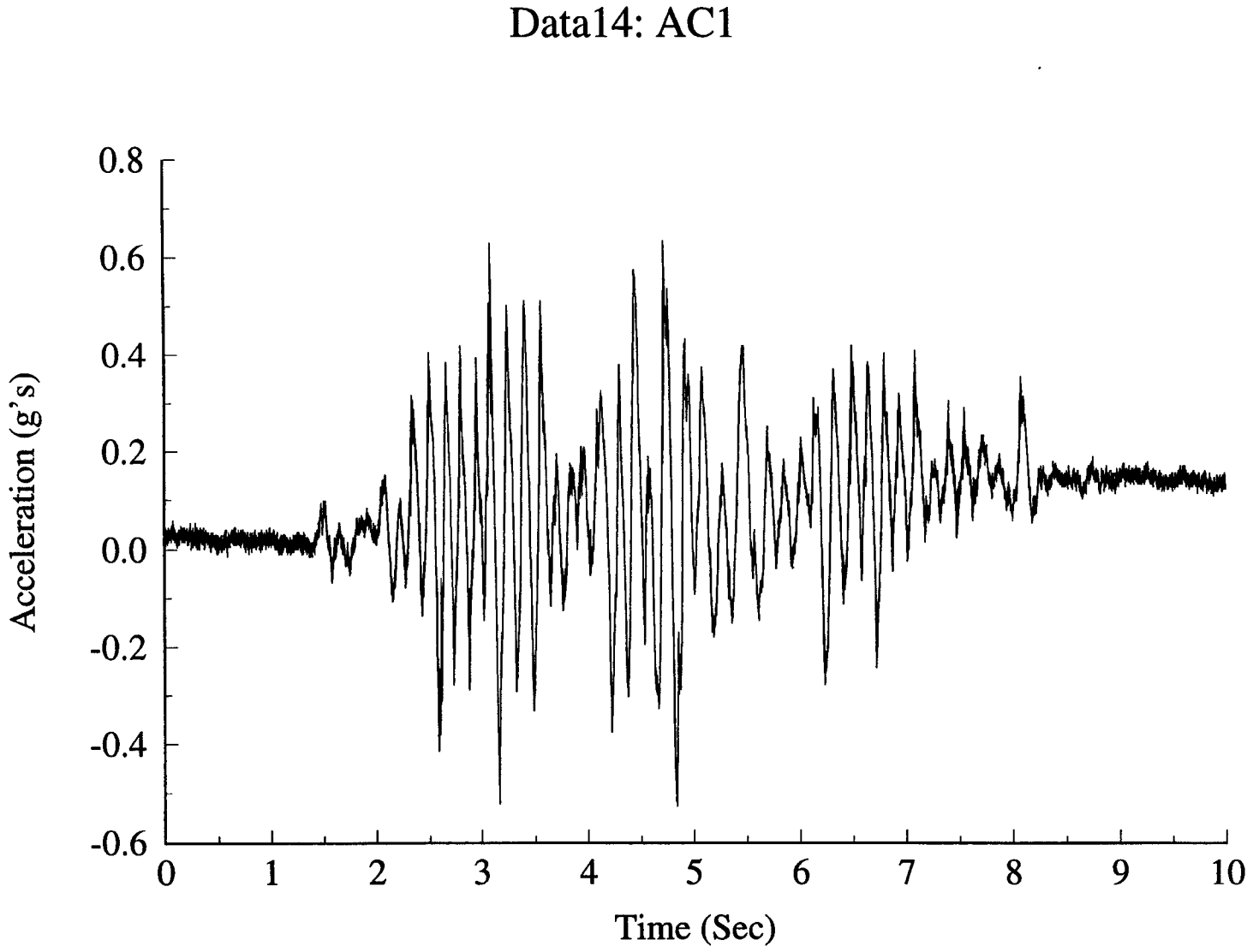

Figure 10-23. Run 5, 7.6 mm peak input: accelerometer AC1

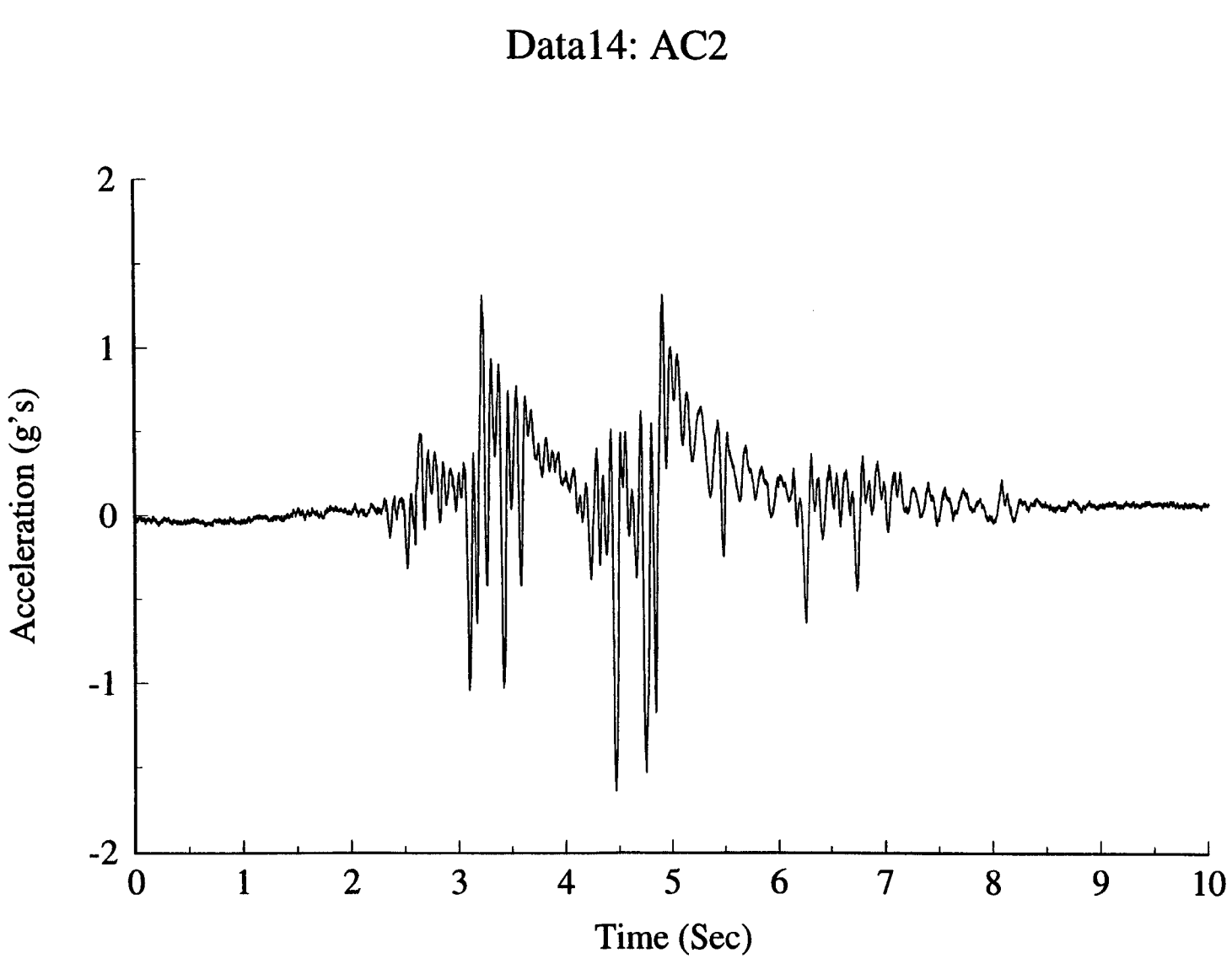

Figure 10-24. Run 5, 7.6 mm peak input: accelerometer AC2

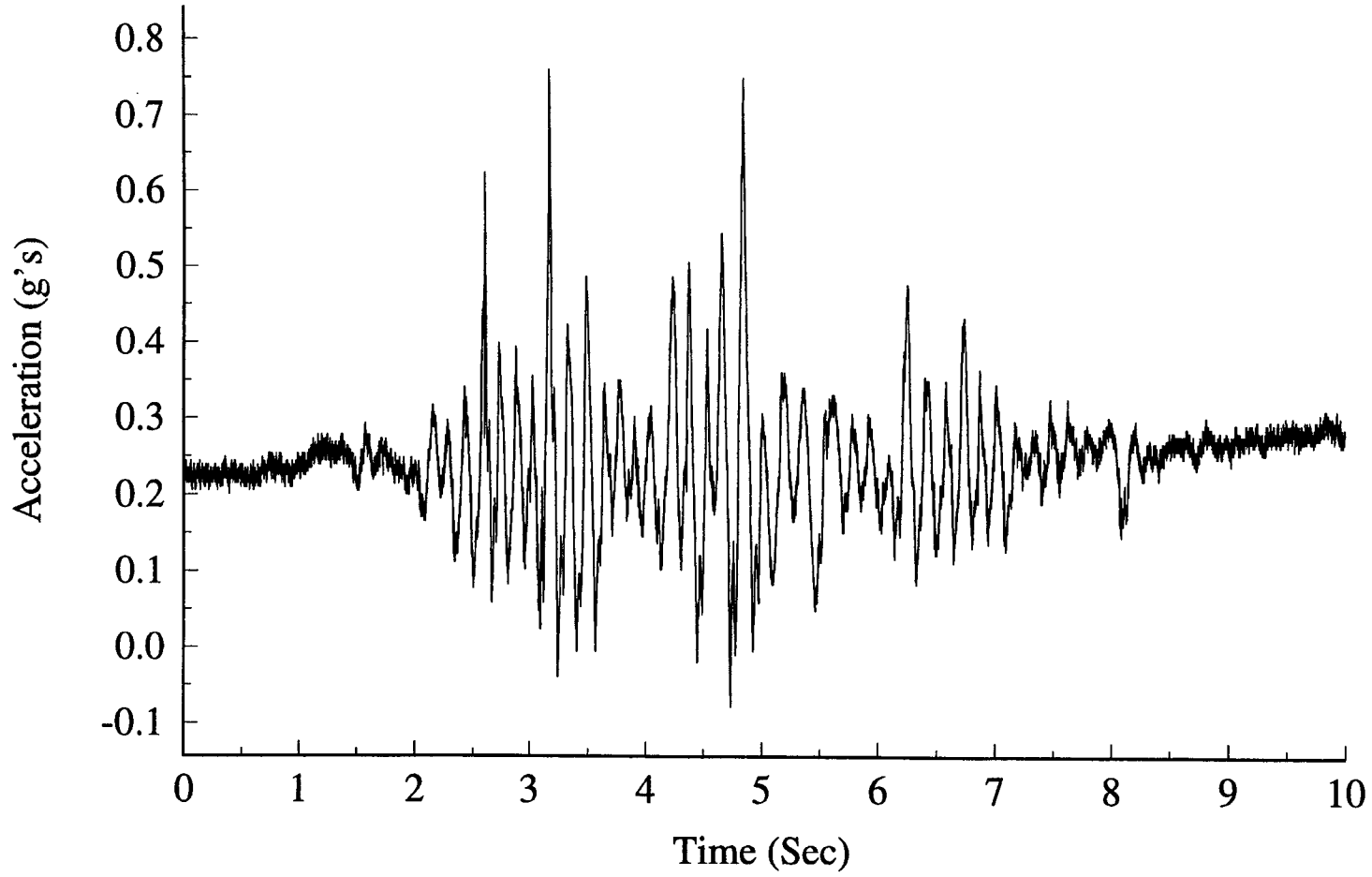

Figure 10-25. Run 5, 7.6 mm peak input: accelerometer AC3

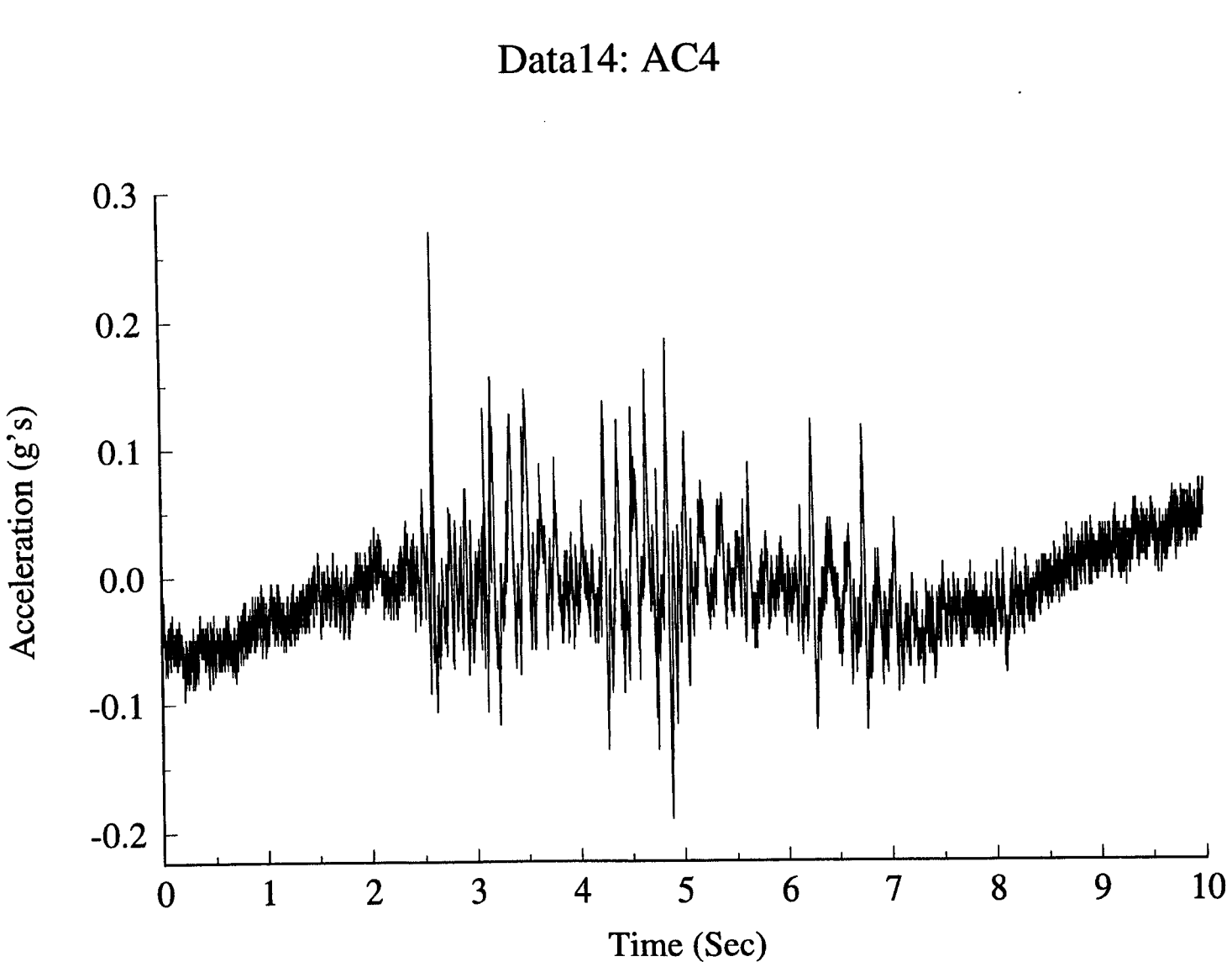

Figure 10-26. Run 5, 7.6 mm peak input: accelerometer AC4

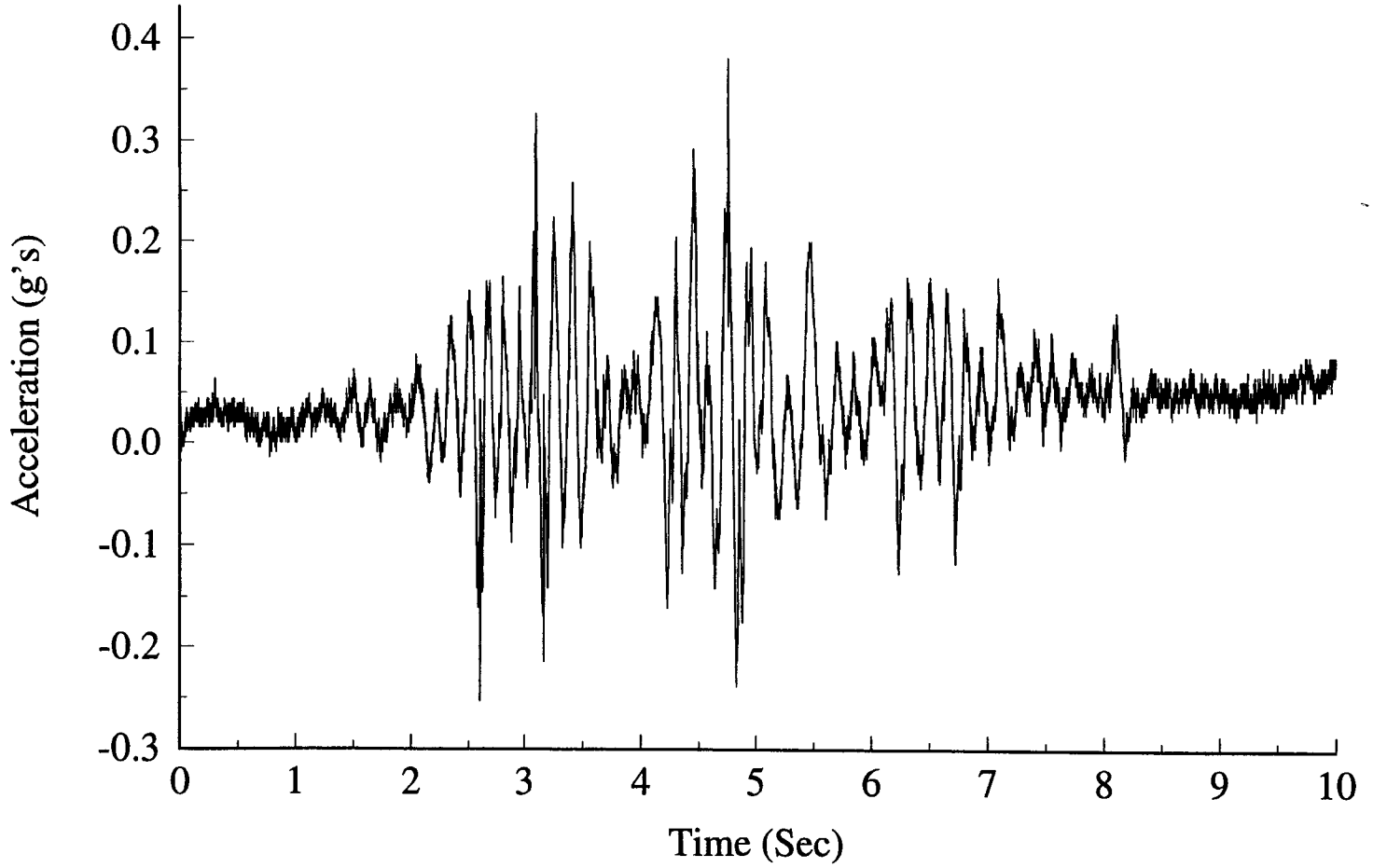

Figure 10-27. Run 5, 7.6 mm peak input: accelerometer AC5

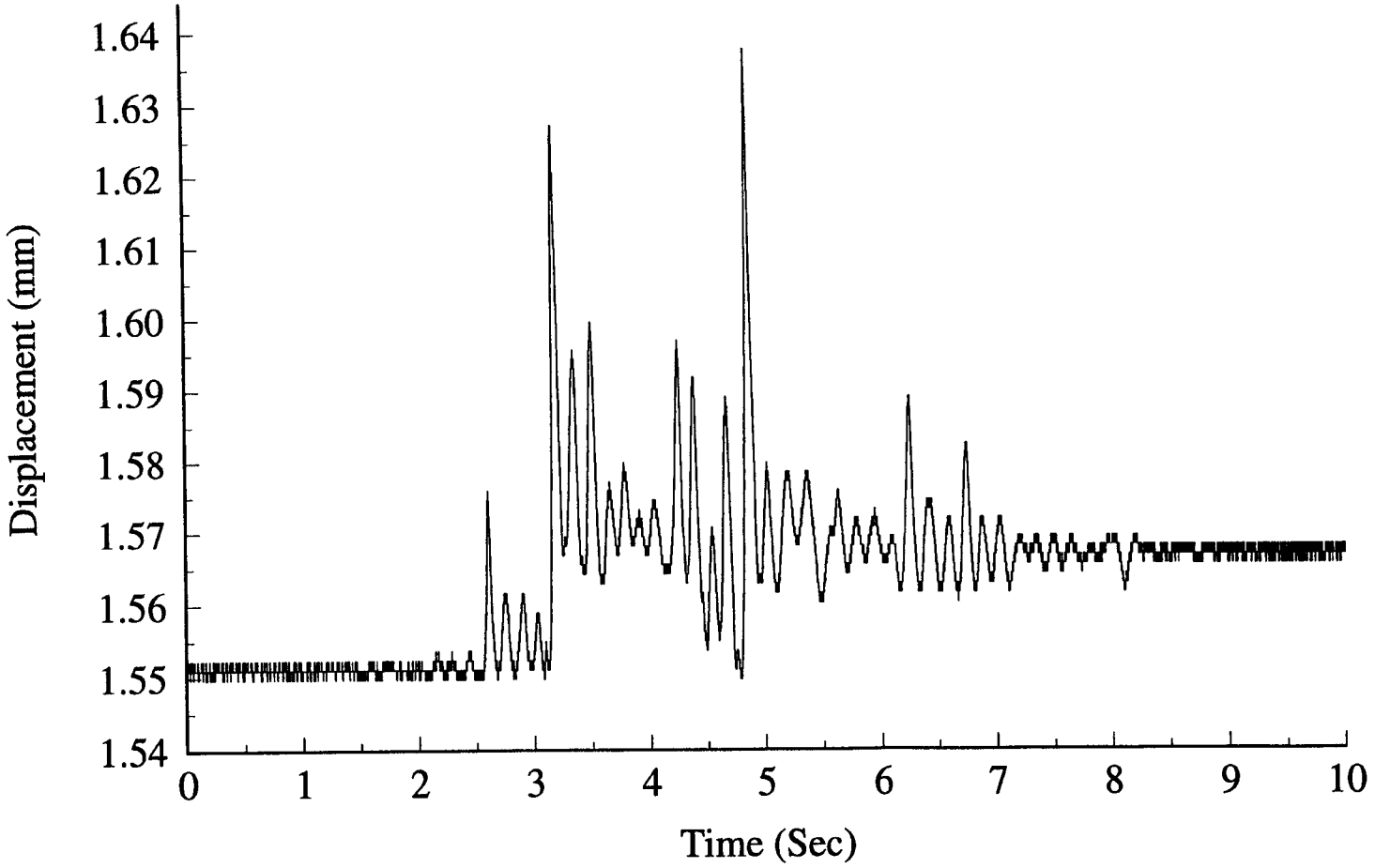

Figure 10-28. Run 5, 7.6 mm peak input: bentley proximeter probe BP1

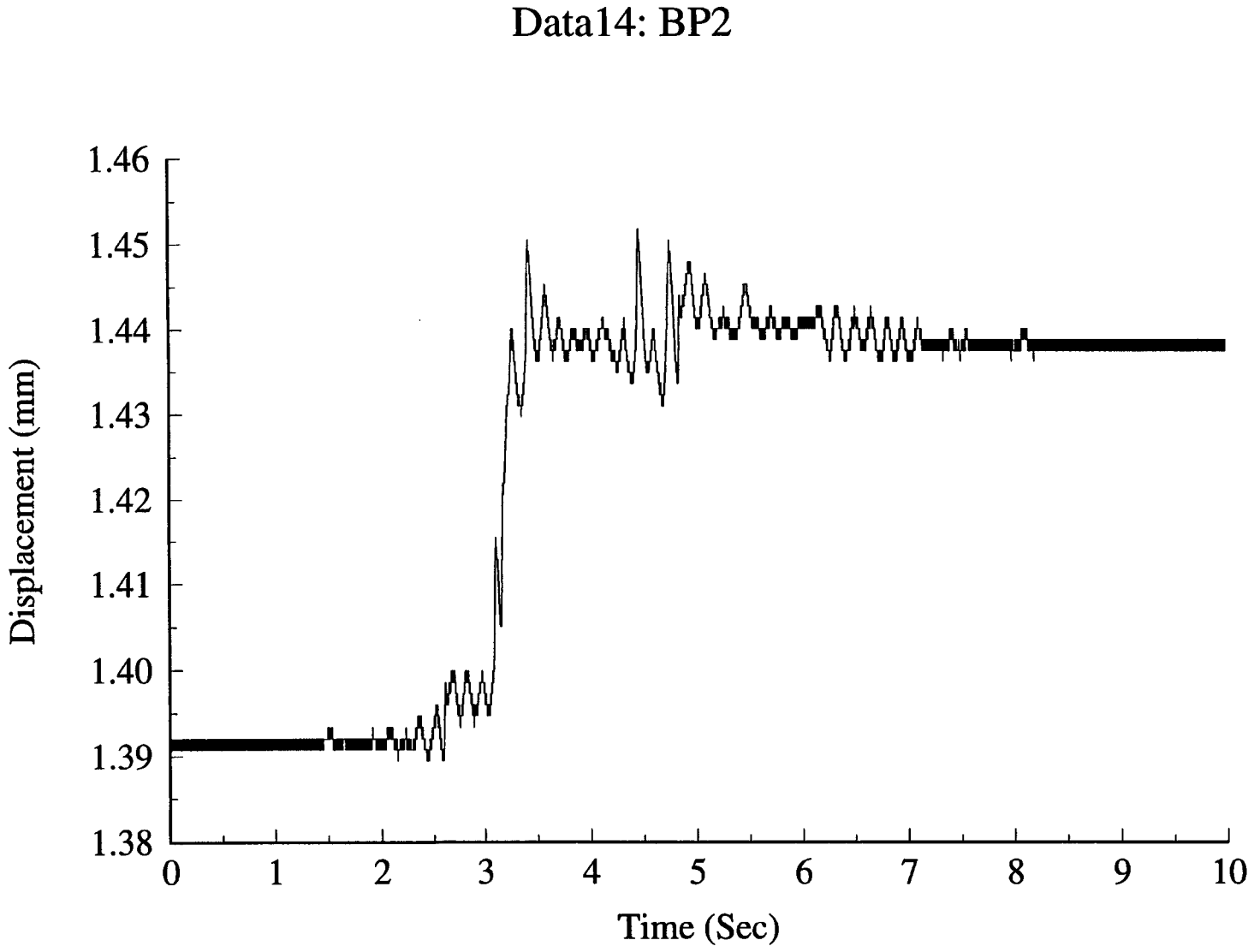

Figure 10-29. Run 5, 7.6 mm peak input: bentley proximeter probe BP2

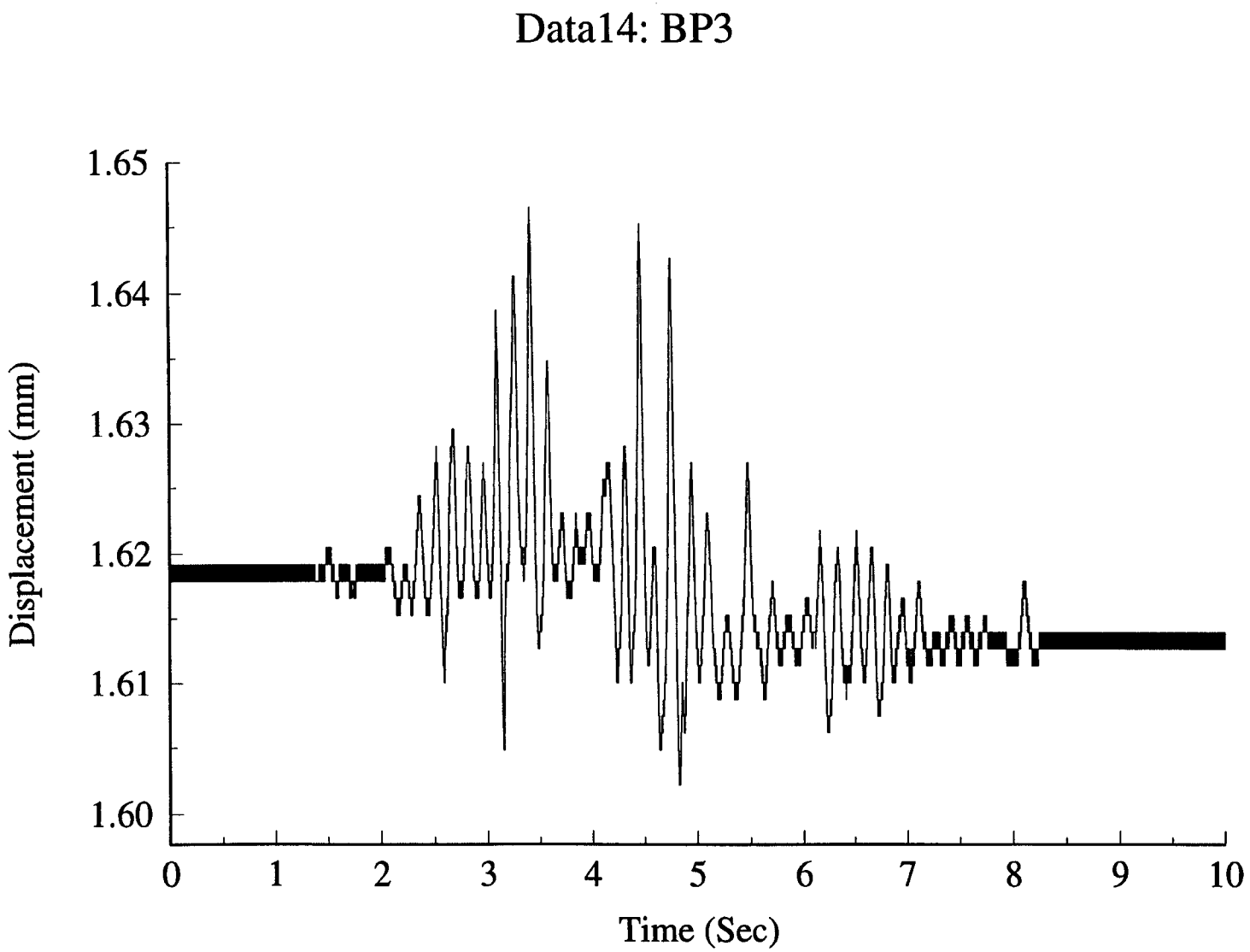

Figure 10-30. Run 5, 7.6 mm peak input: bentley proximeter probe BP3

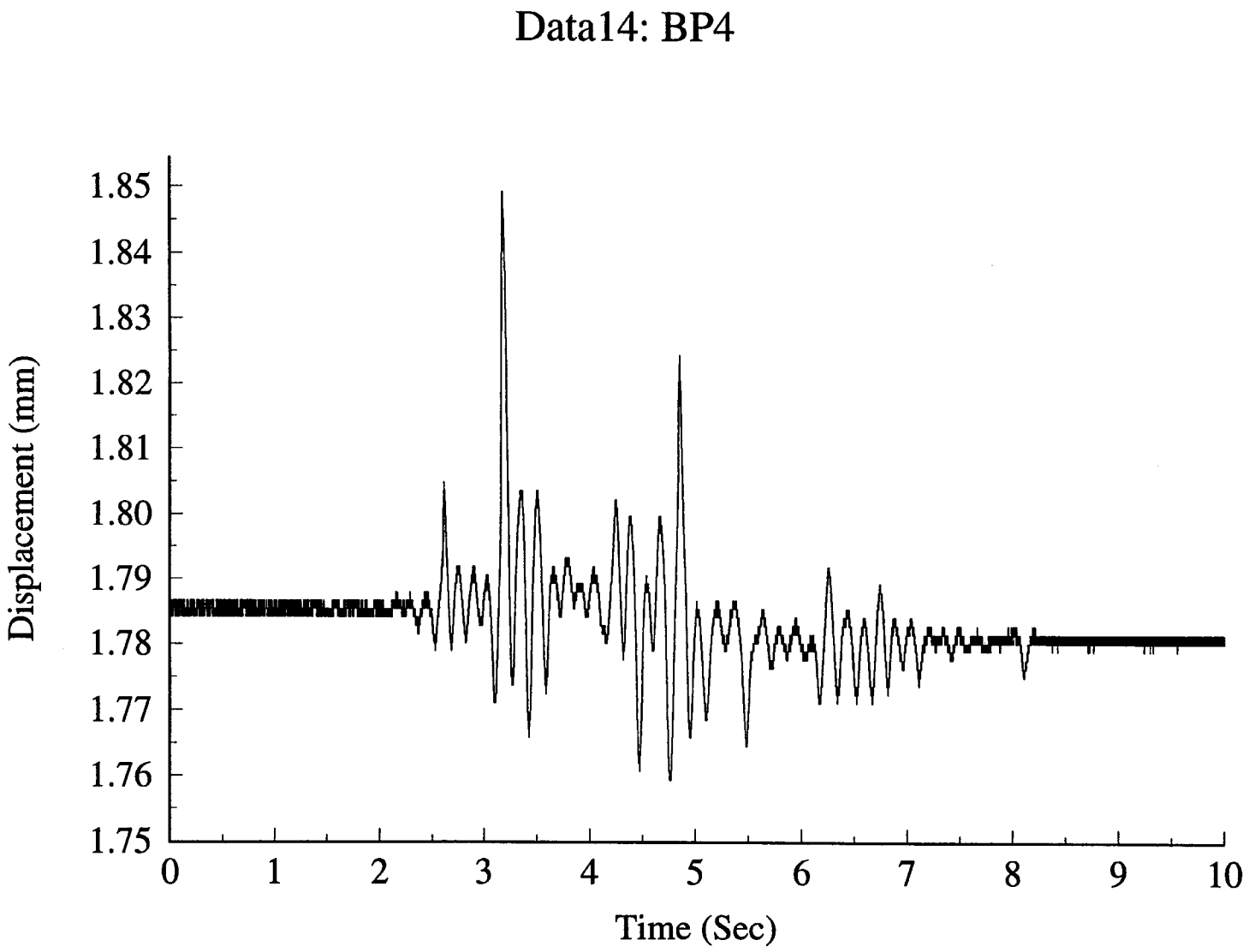

Figure 10-31. Run 5, 7.6 mm peak input: bentley proximeter probe BP4

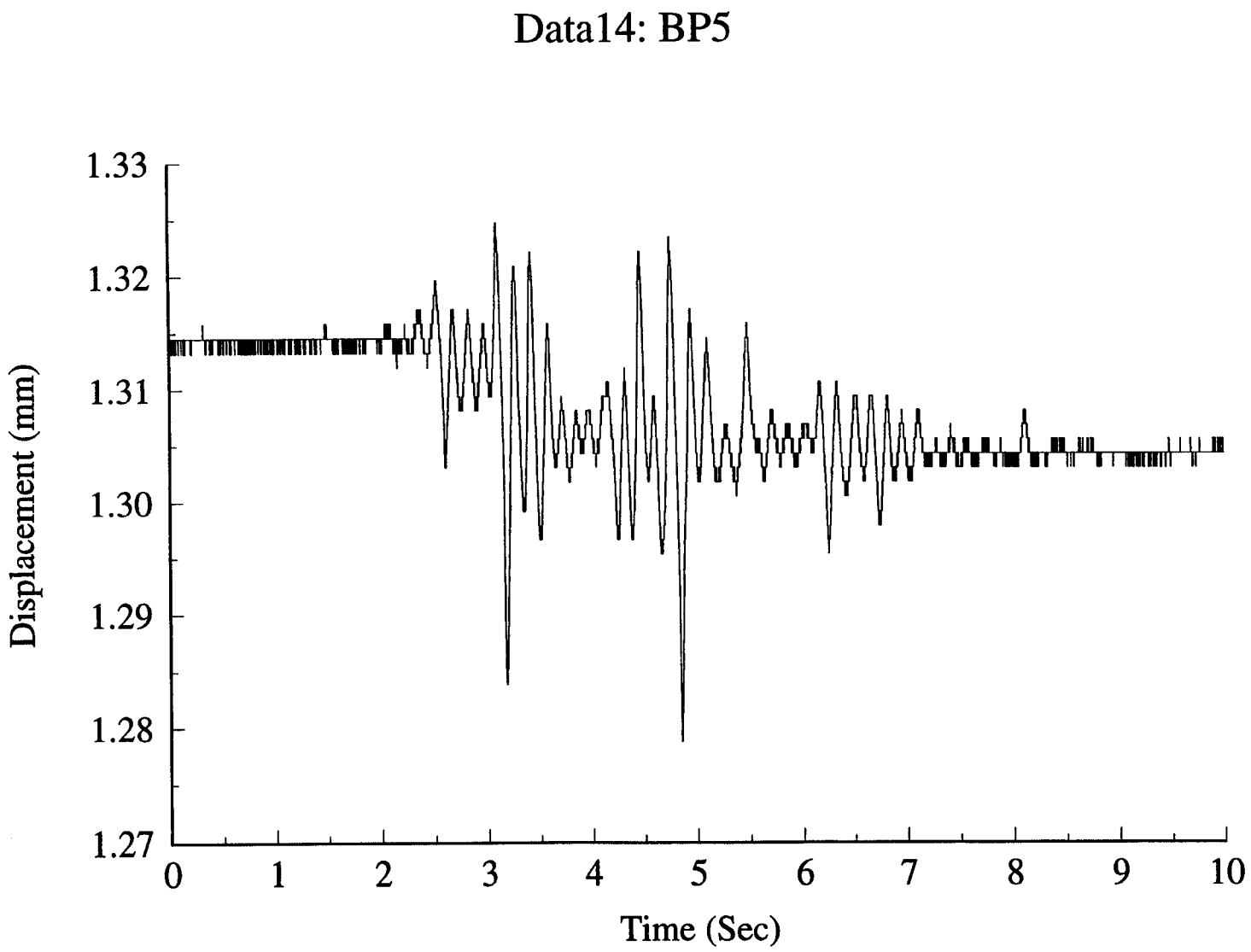

Figure 10-32. Run 5, 7.6 mm peak input: bentley proximeter probe BP5

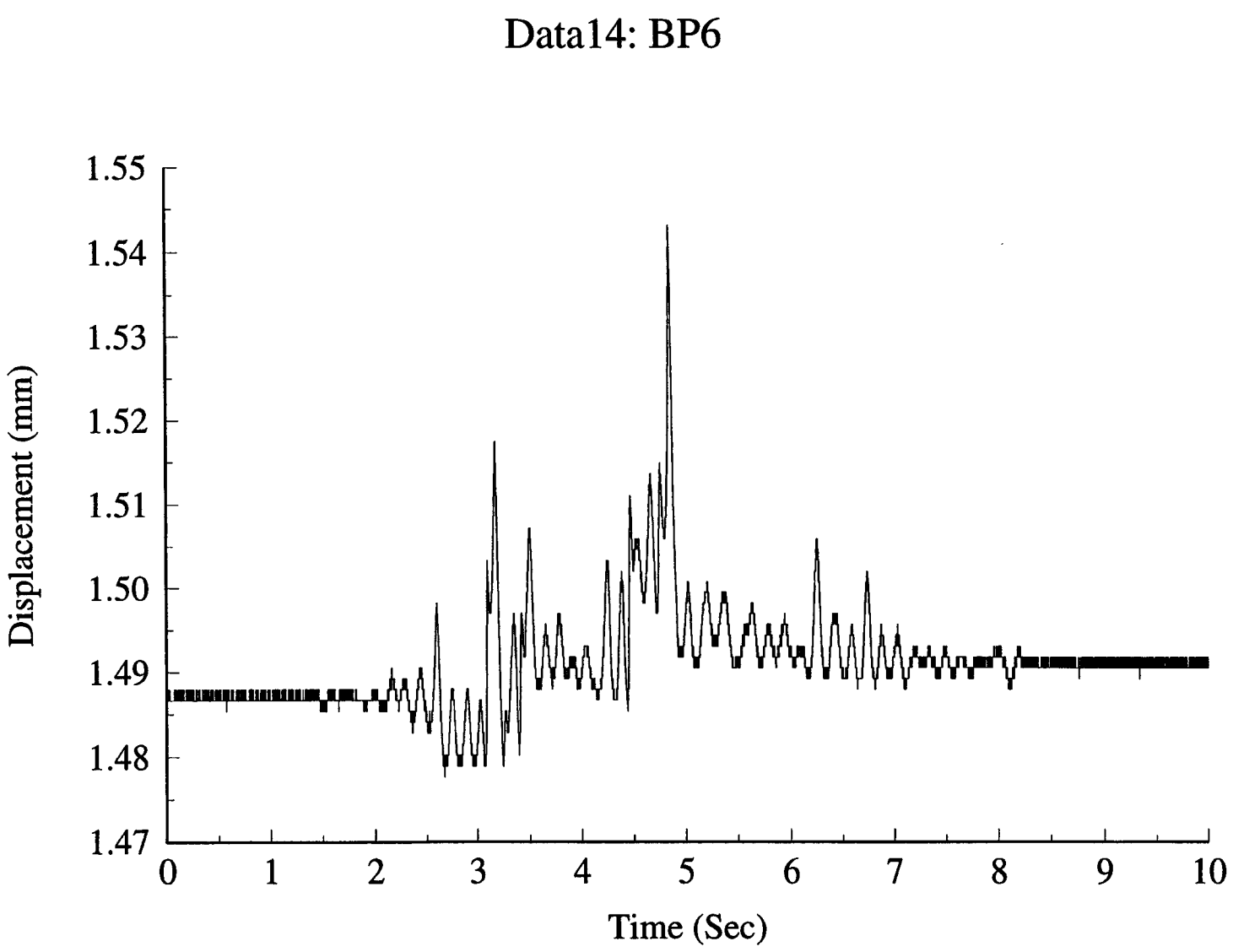

Figure 10-33. Run 5, 7.6 mm peak input: bentley proximeter probe BP6

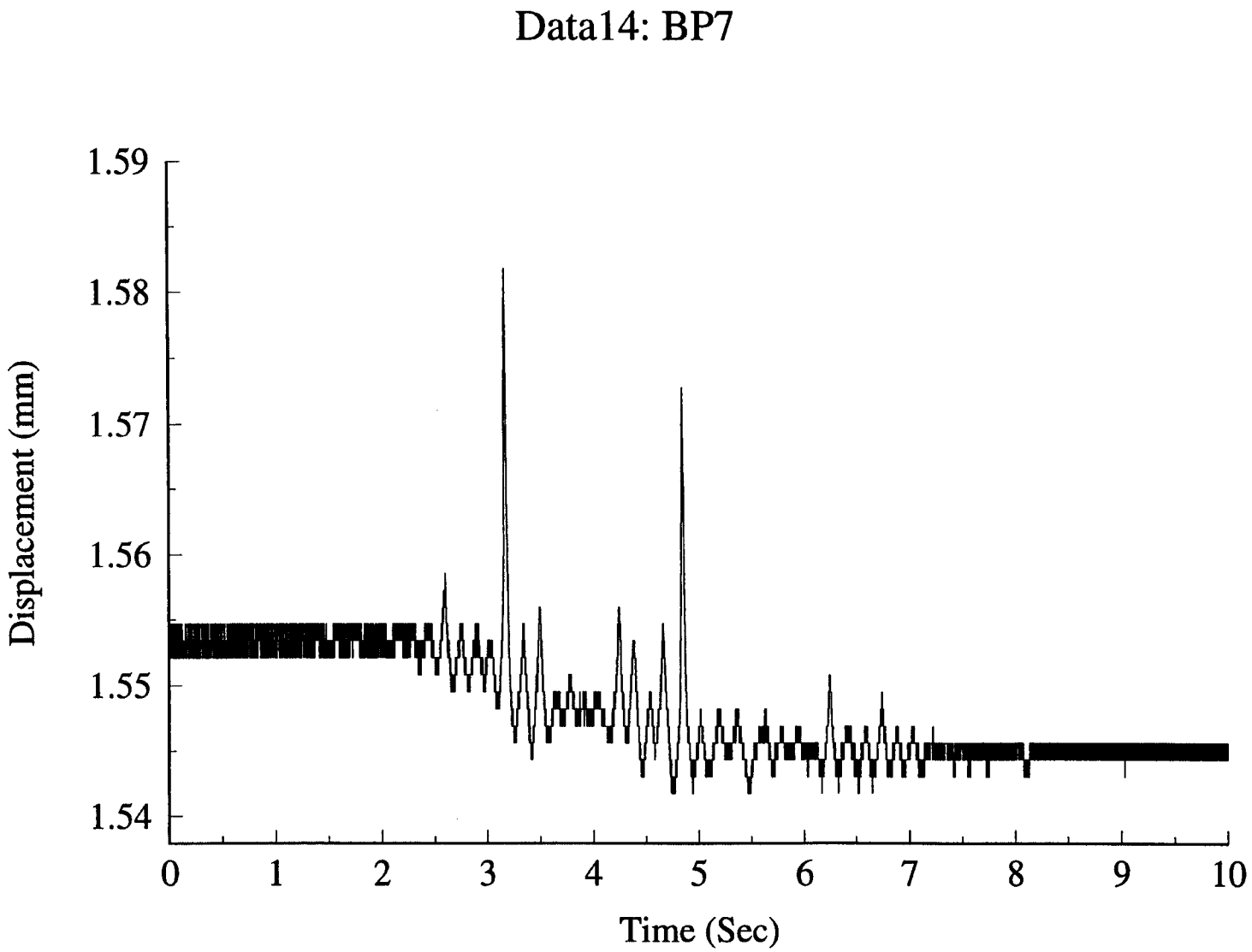

Figure 10-34. Run 5, 7.6 mm peak input: bentley proximeter probe BP7

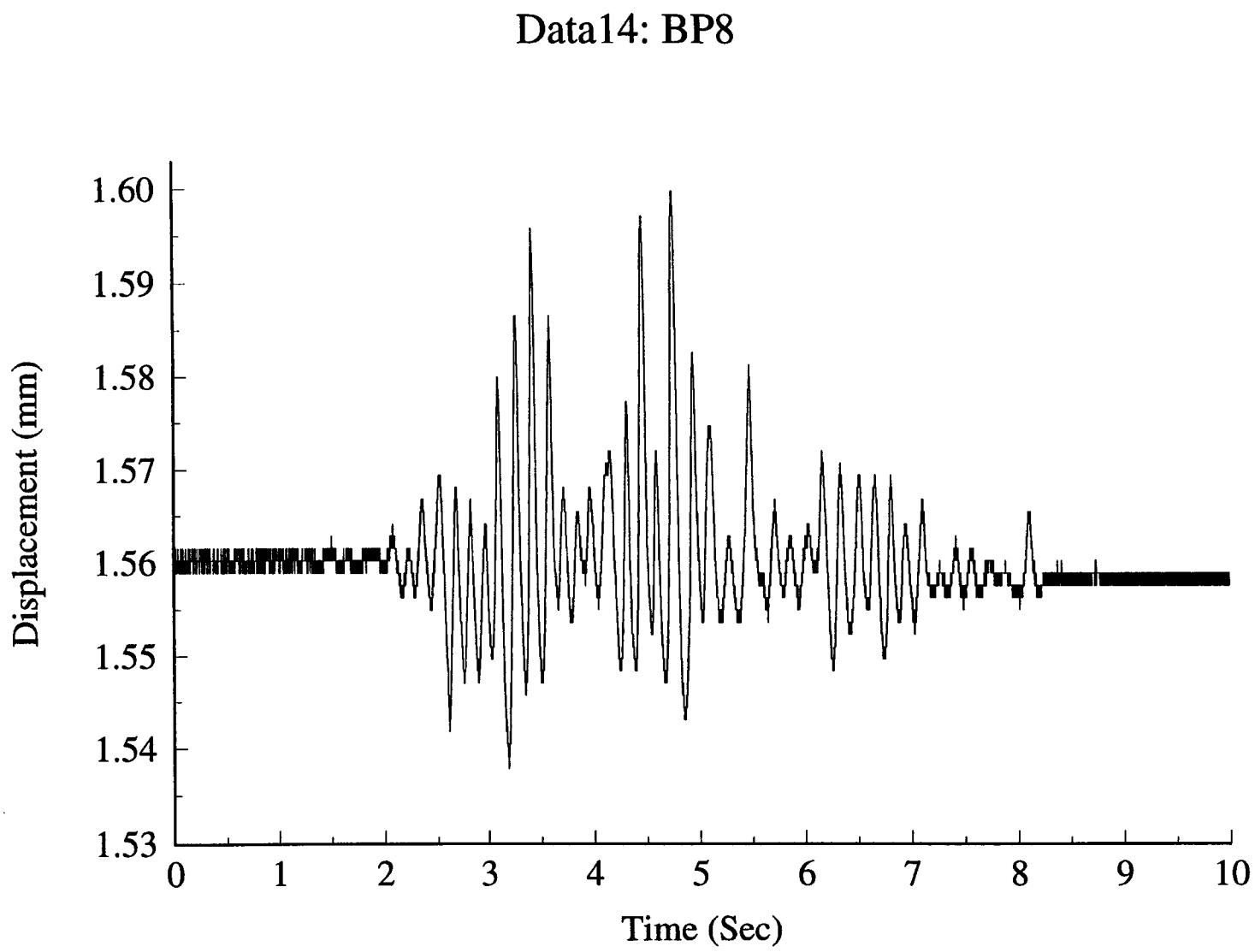

Figure 10-35. Run 5, 7.6 mm peak input: bentley proximeter probe BP8

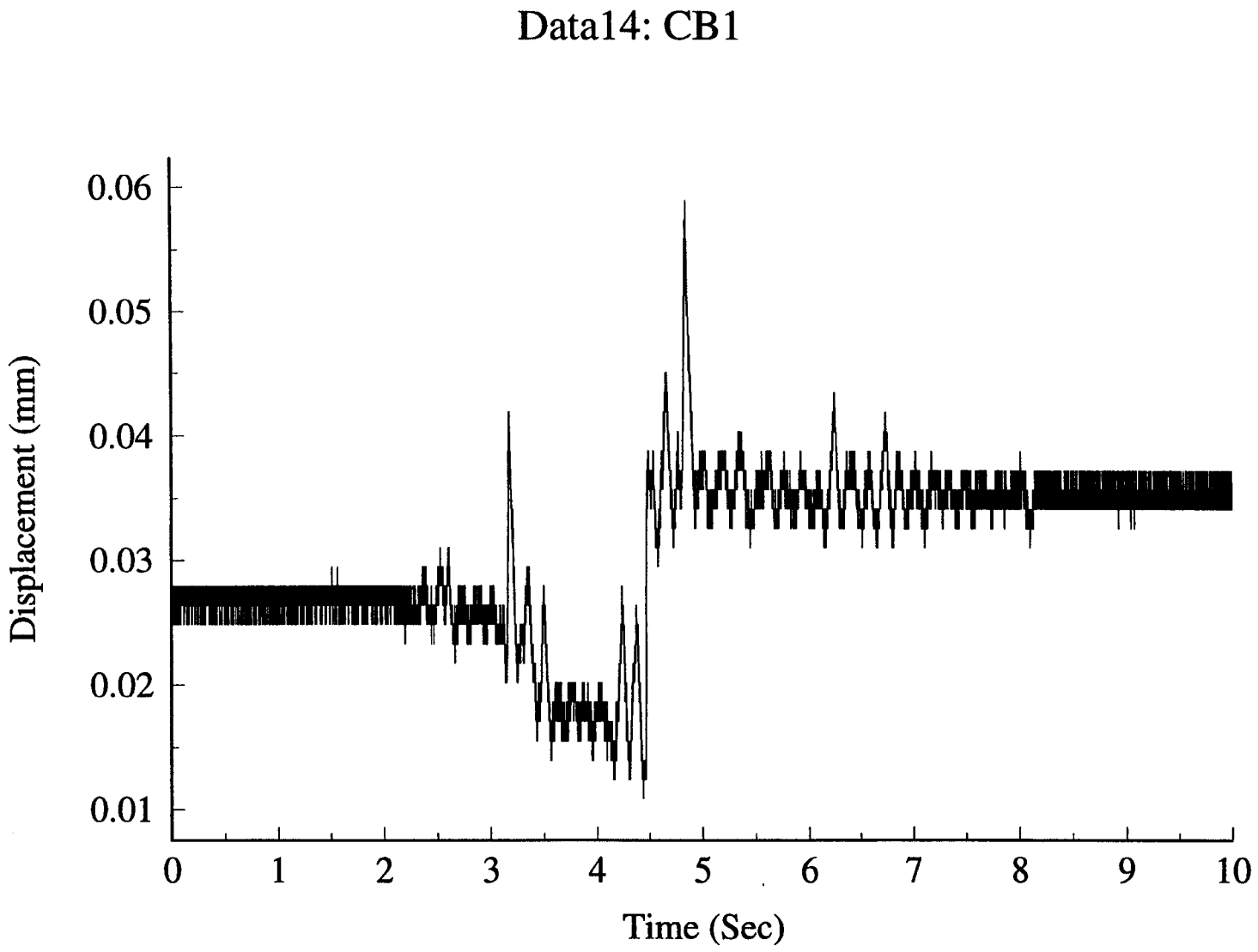

Figure 10-36. Run 5, 7.6 mm peak input: cantilever beam CB1

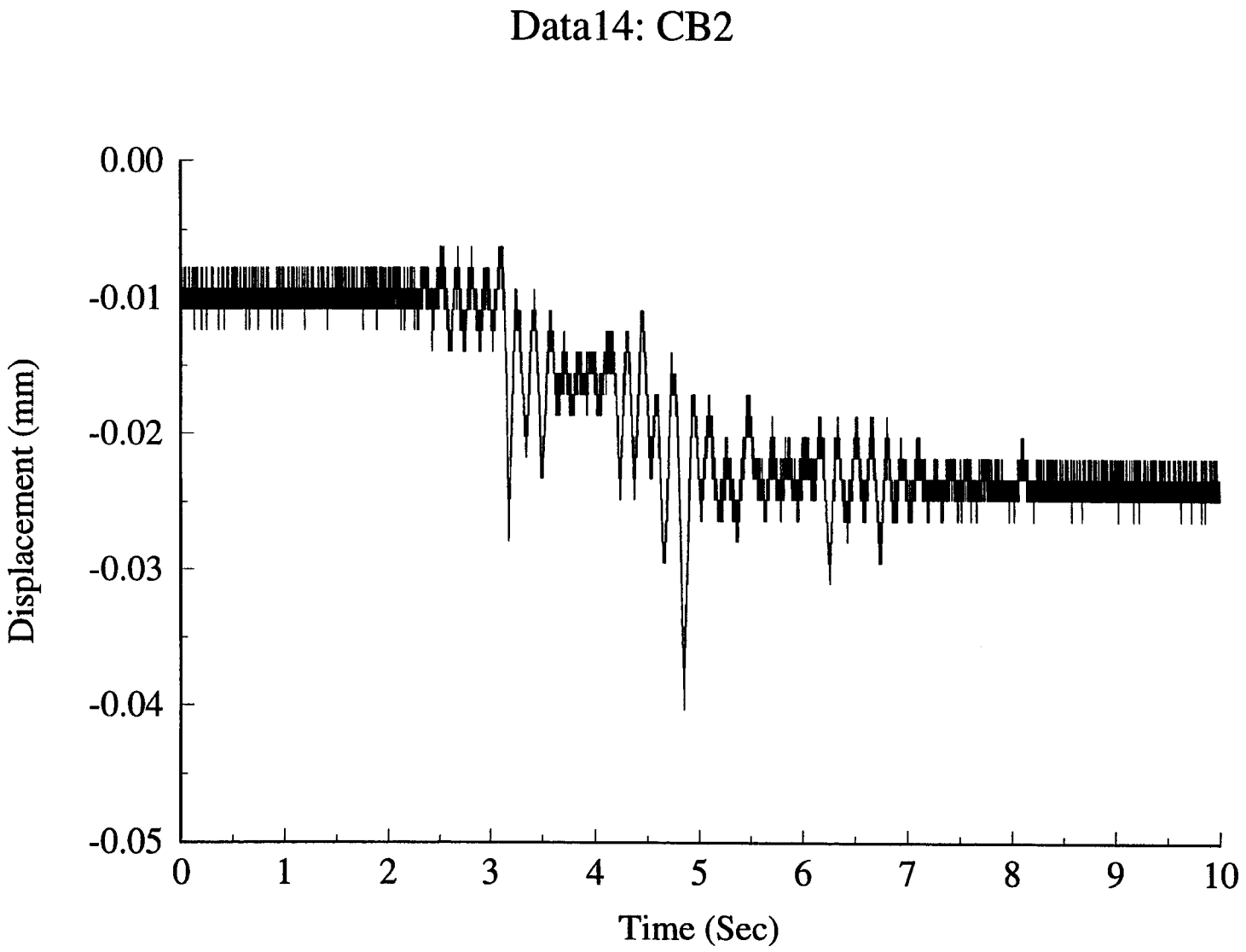

Figure 10-37. Run 5, 7.6 mm peak input: cantilever beam CB2

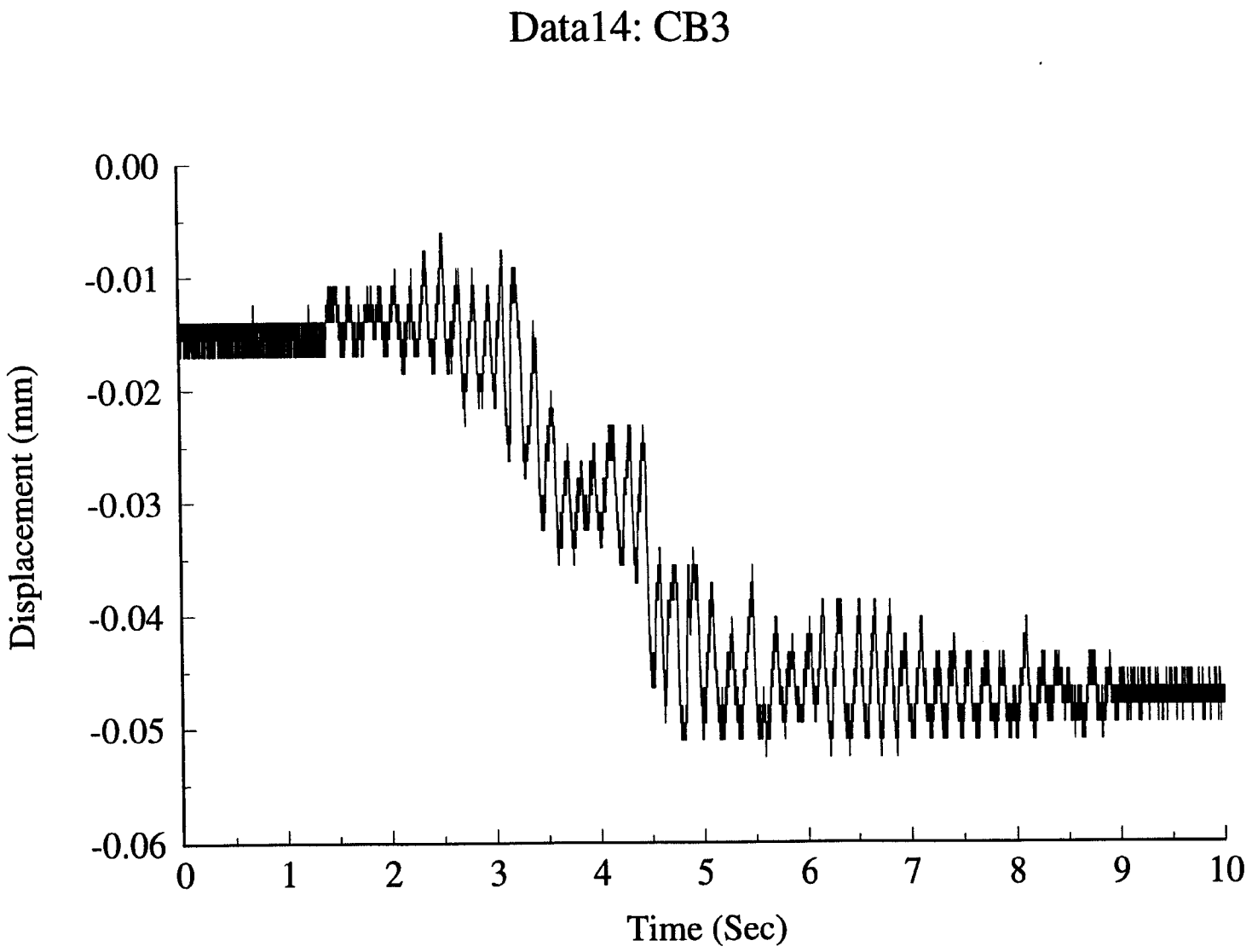

Figure 10-38. Run 5, 7.6 mm peak input: cantilever beam CB3

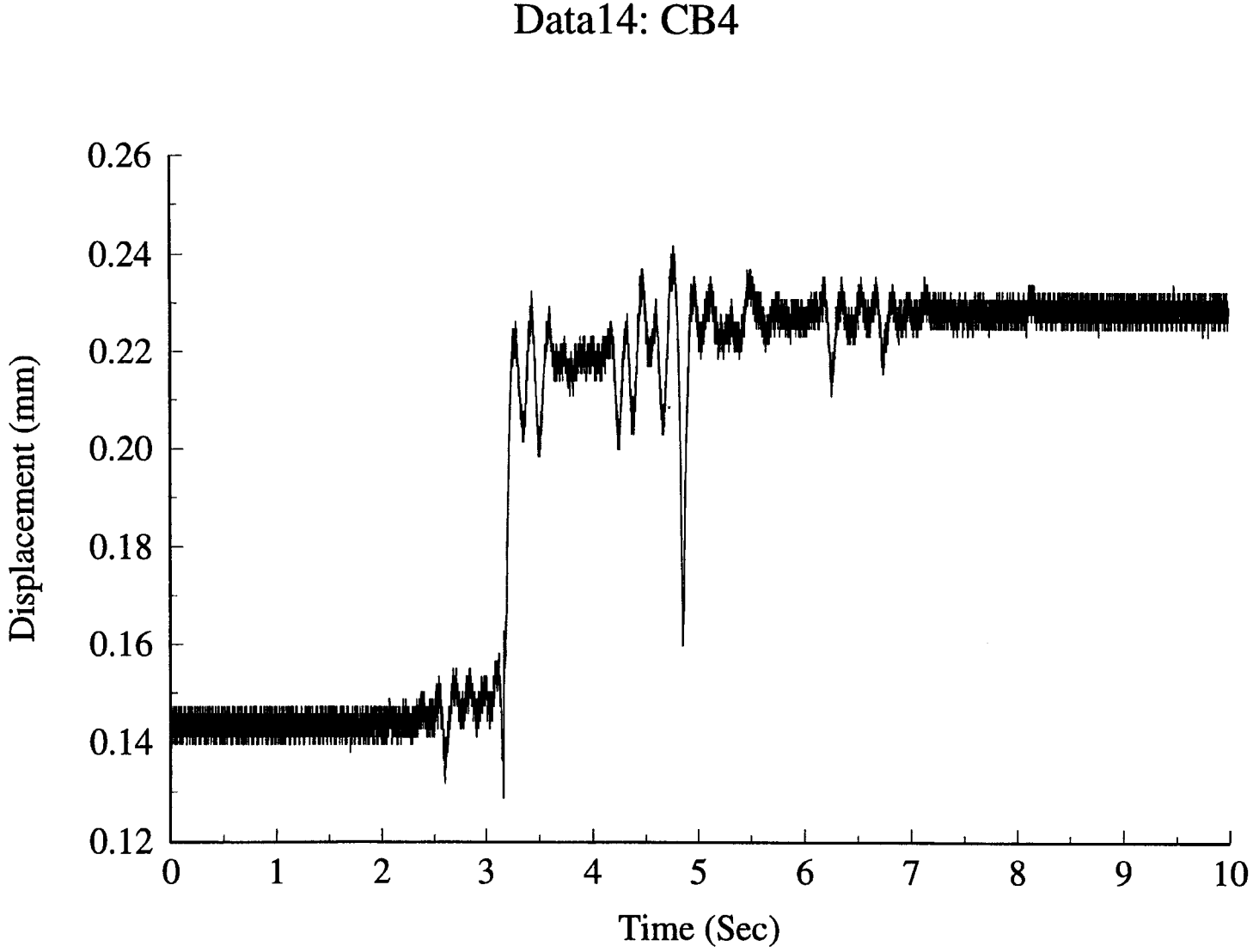

Figure 10-39. Run 5, 7.6 mm peak input: cantilever beam CB4

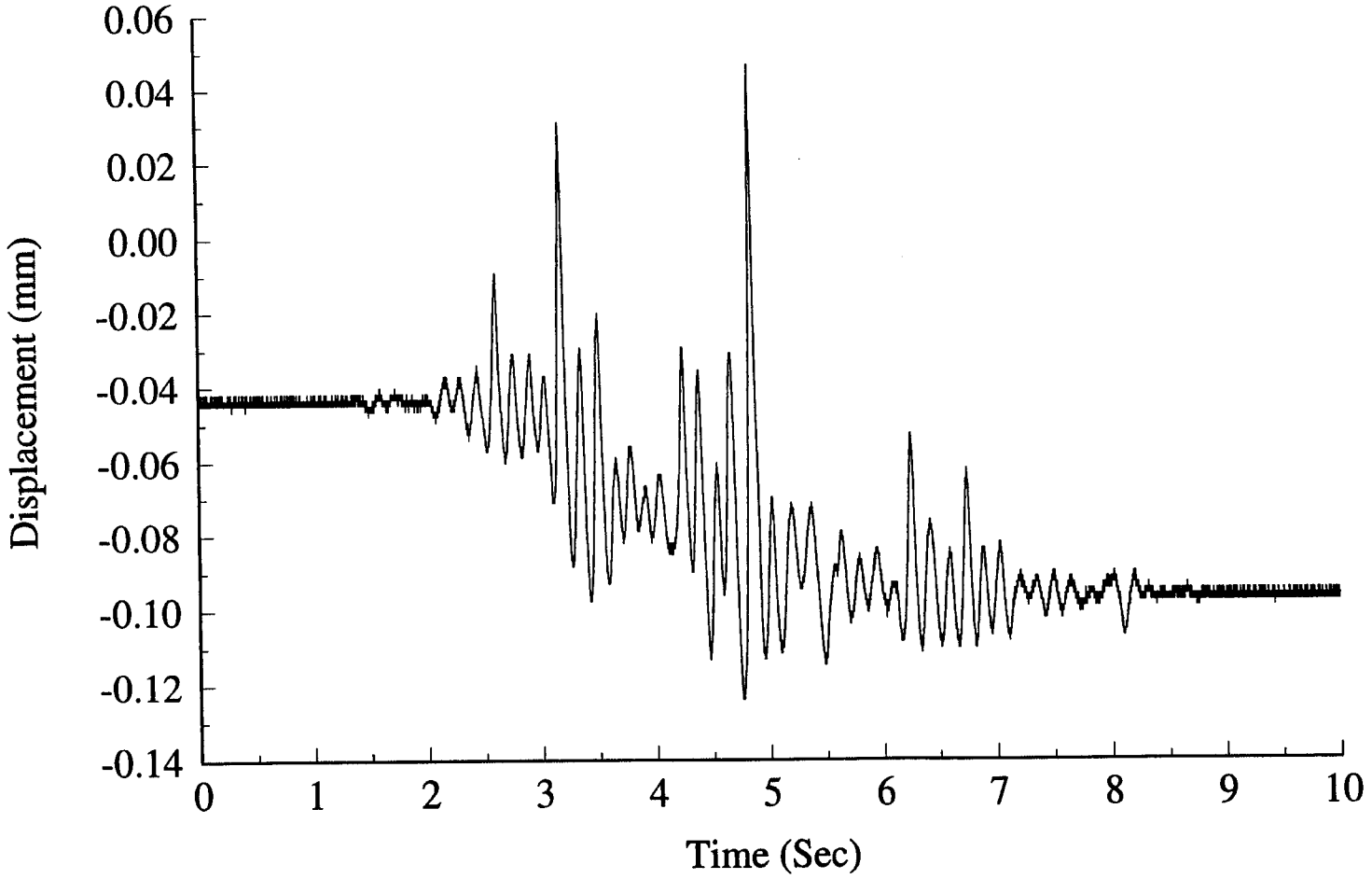

Figure 10-40. Run 5, 7.6 mm peak input: cantilever beam CB5

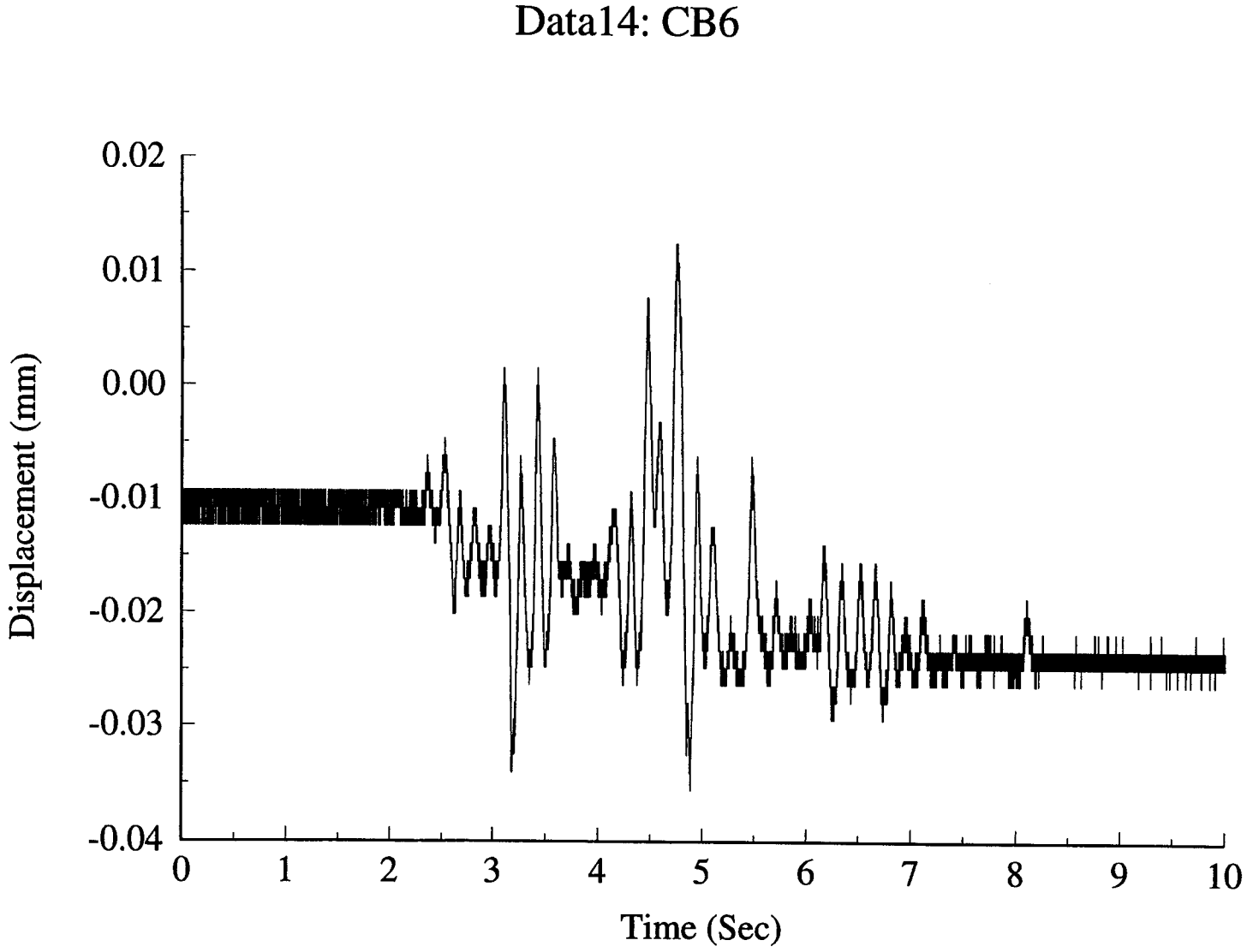

Figure 10-41. Run 5, 7.6 mm peak input: cantilever beam CB6

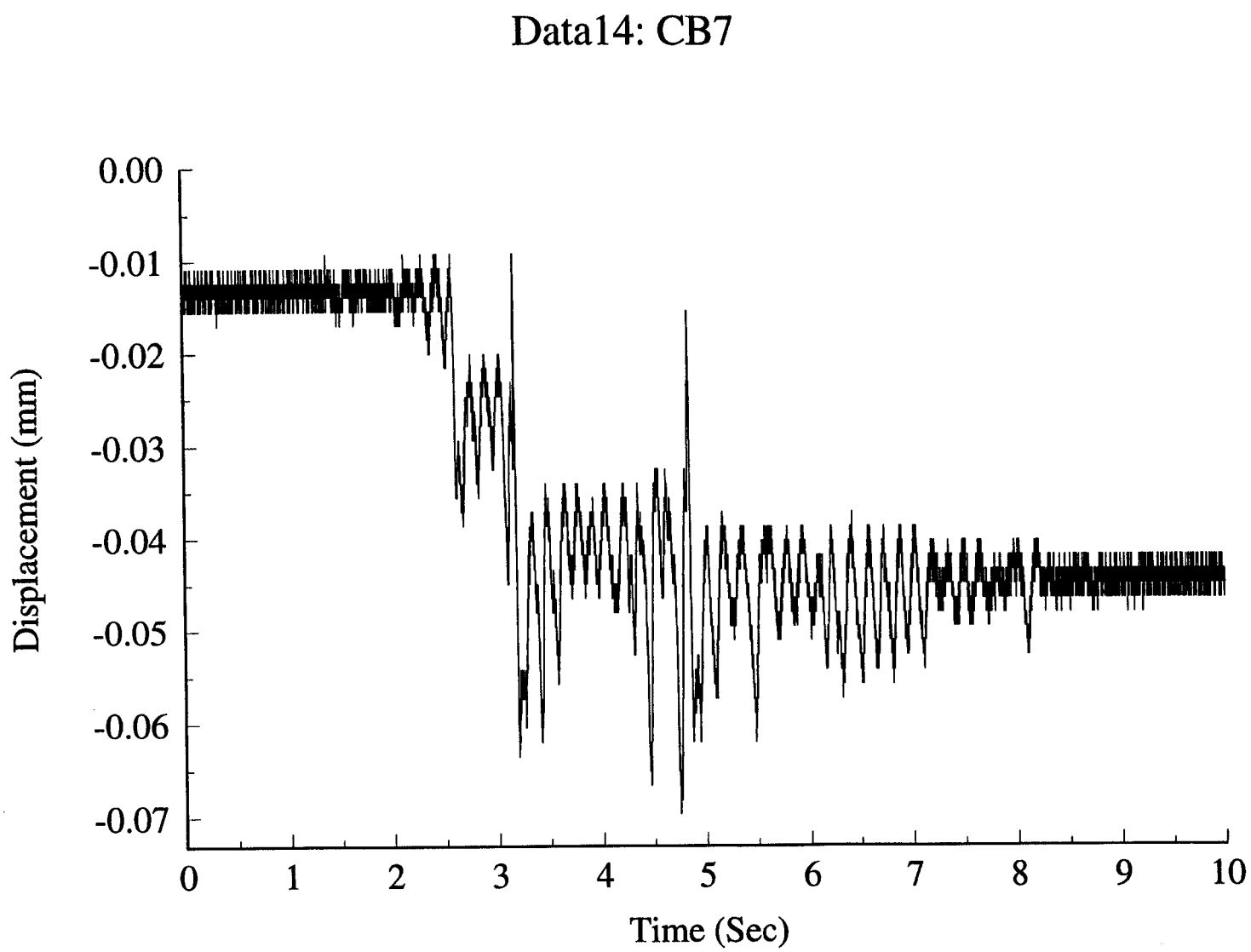

Figure 10-42. Run 5, 7.6 mm peak input: cantilever beam CB7

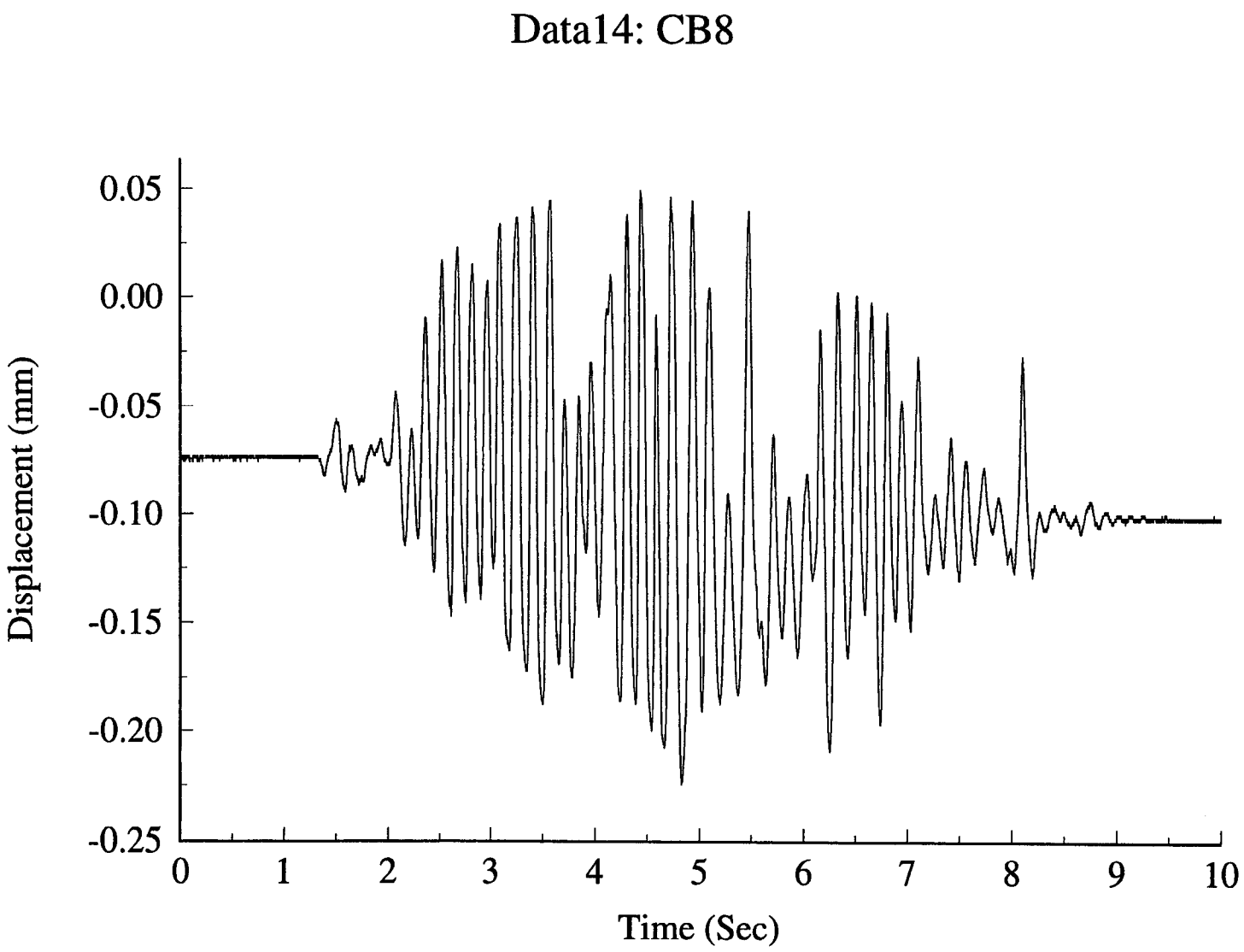

Figure 10-43. Run 5, 7.6 mm peak input: cantilever beam CB8

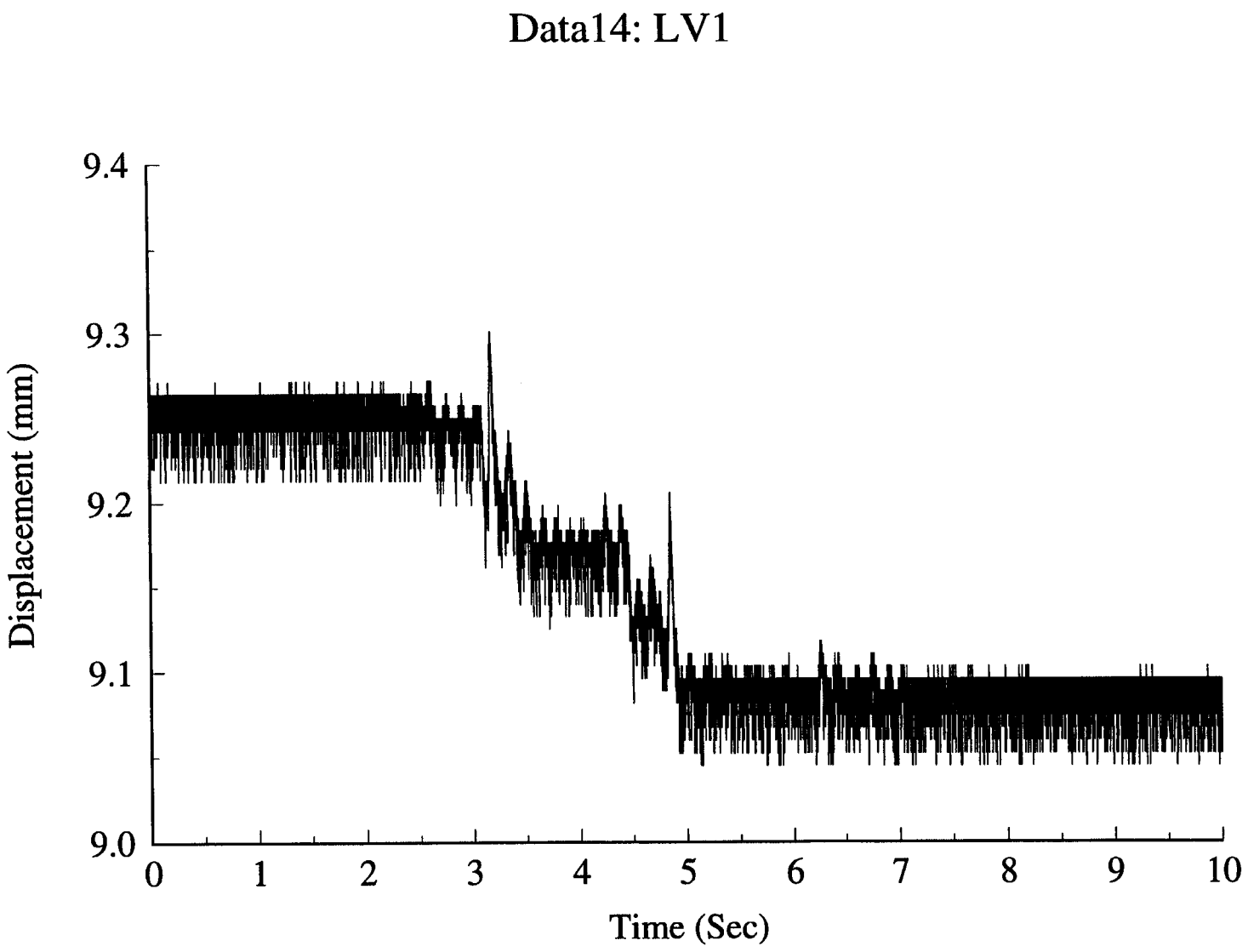

Figure 10-44. Run 5, 7.6 mm peak input: LVDT transducer LV1

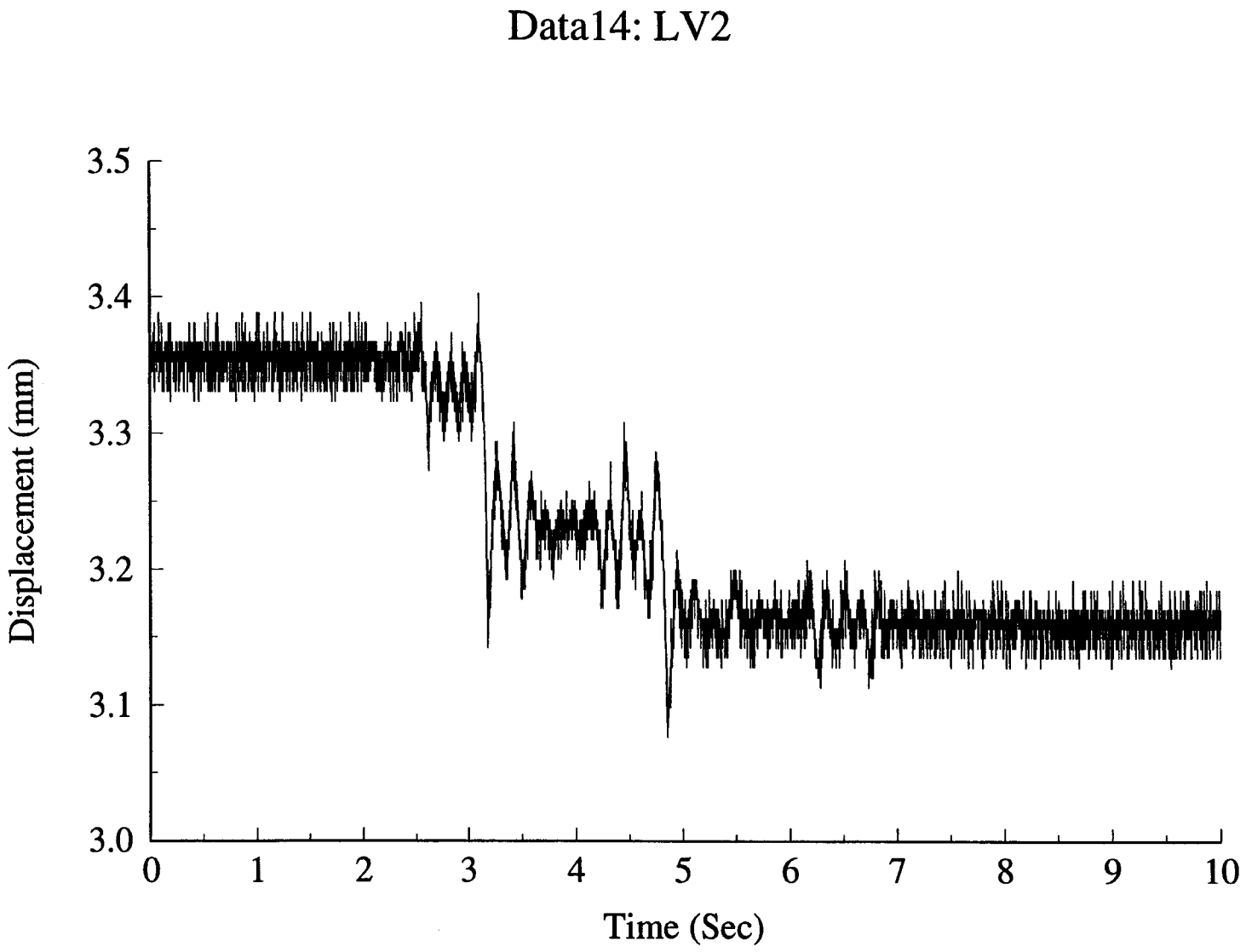

Figure 10-45. Run 5, 7.6 mm peak input: LVDT transducer LV2

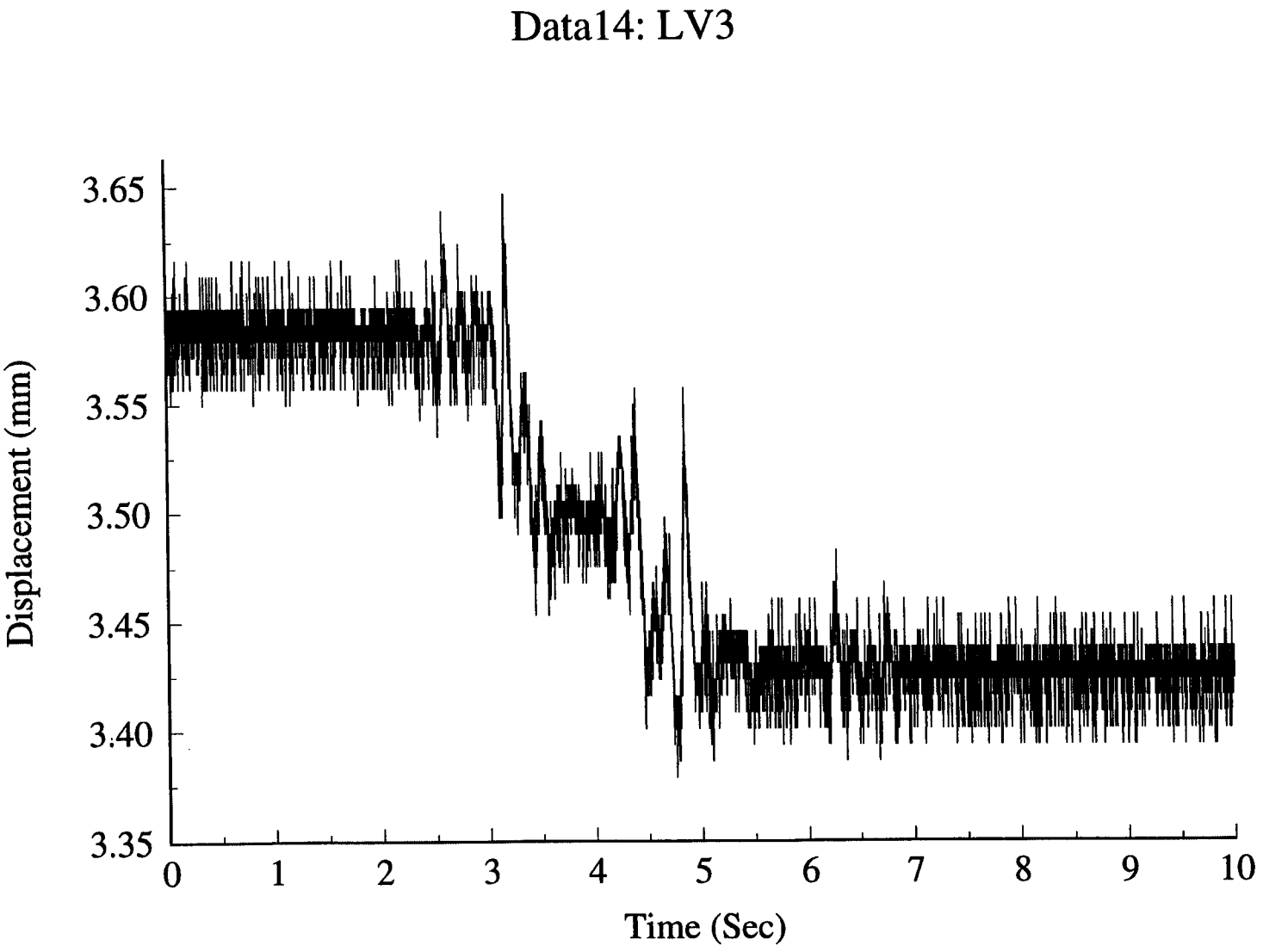

Figure 10-46. Run 5, 7.6 mm peak input: LVDT transducer LV3

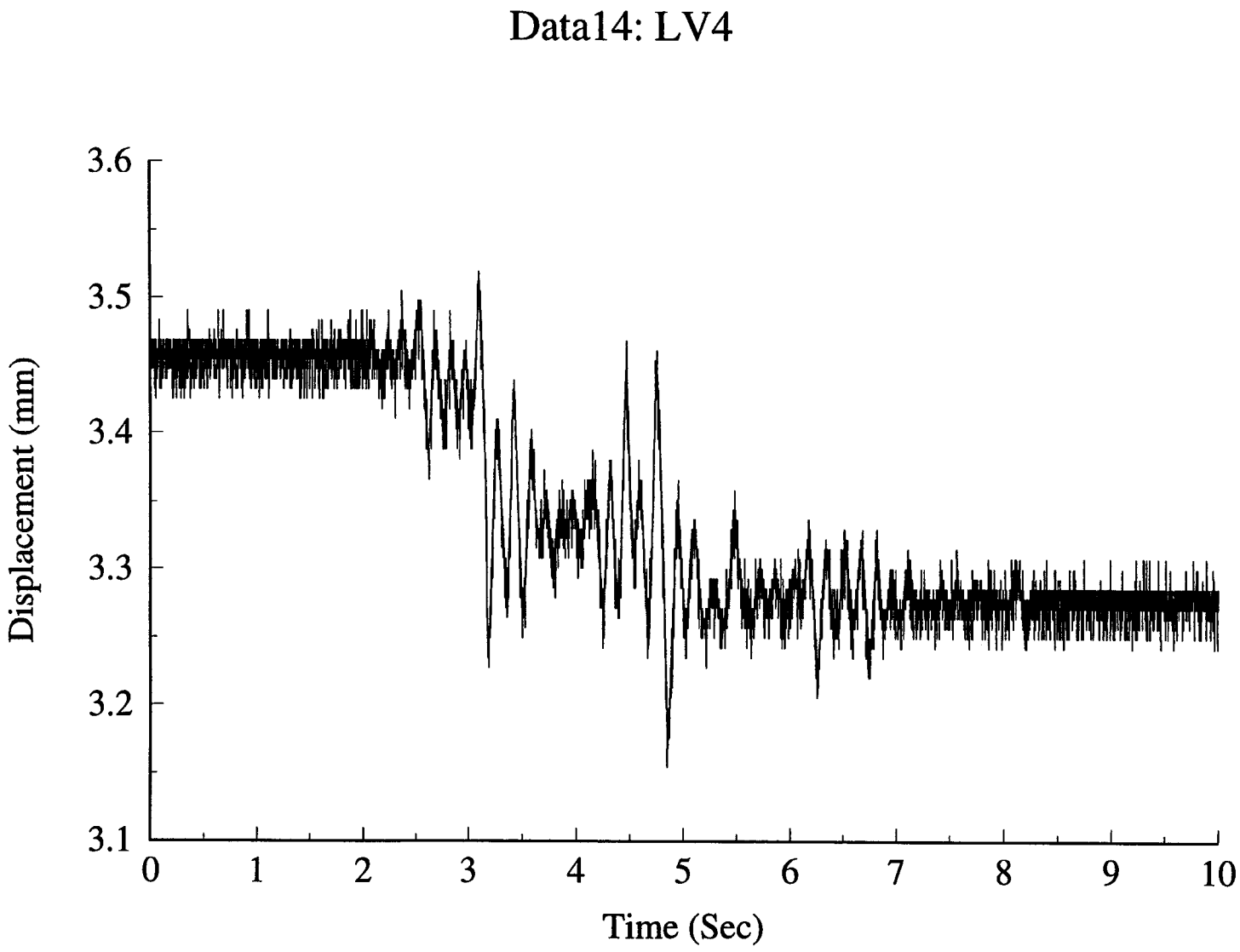

Figure 10-47. Run 5, 7.6 mm peak input: LVDT transducer LV4

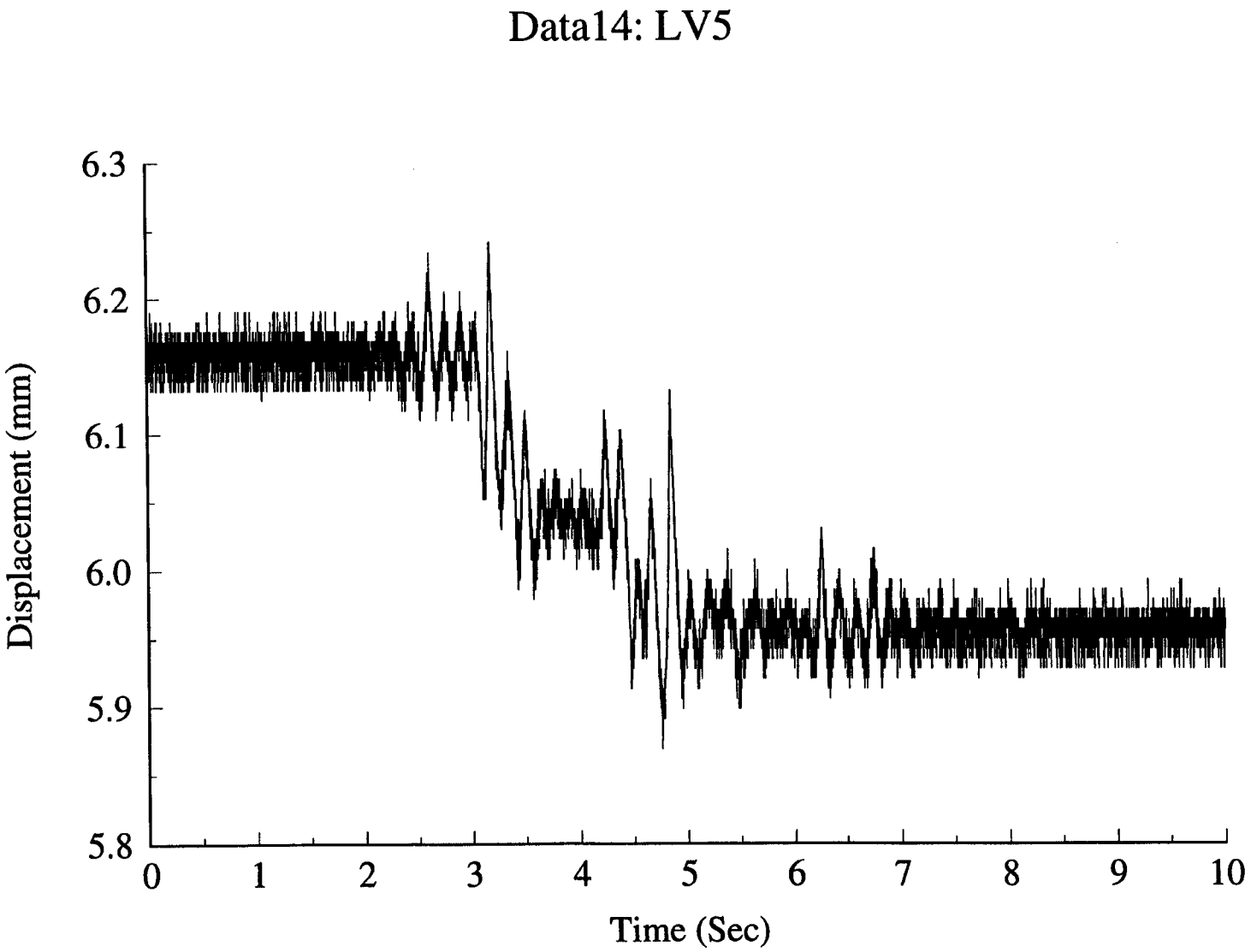

Figure 10-48. Run 5, 7.6 mm peak input: LVDT transducer LV5

11 COMPOSITE MODEL BOUNDARY RESPONSE

The data presented in Section 10 can be used to determine the type of motion the rock mass model underwent as a whole, especially with respect to the boundary conditions built into the system. This section takes advantage of data from the boundary accelerometers (AC6 to AC11, see Figure 5-1) and the tension cable load cells (LC2 to LC6, see Figure 5-1).

For Run 5, as presented in Section 10, the actual seismic table excitation acceleration and displacement data are shown in Figures 10-1 and 10-2. Table accelerations at three seismic amplitudes are shown in Figures 11-1 to 11-3. The table accelerations were very consistent between runs at the same amplitude. However, the character of the accelerations differs somewhat at the different amplitude levels.

As mentioned in Section 10, horizontal and vertical accelerations near the top of the model indicated a resonant frequency response at approximately 7 Hz. This response is present throughout all of the runs and appears to be a fundamental natural mode of the model in which the end plates rock back and forth and the upper plates pitch up and down. Therefore, this motion is apparent in the vertical as well as the horizontal responses.

To determine the difference between the boundary motion and the motion of the rock ingots, two accelerometers (AC13 and AC14) were located on the top corner of the near side of the rock mass in the horizontal direction, starting with Run 13, as shown in Figure 11-4. For Run 13, Figure 11-5 is the acceleration of AC9 located on the rock mass boundary (see Figure 5-1); Figure 11-6 is the acceleration of AC13, which is the accelerometer closest to the vertical edge boundary; Figure 11-7 shows the acceleration of AC14, which is located nine ingots from the edge of the boundary. Note that AC9 and AC13, which are closest to each other, have nearly identical acceleration responses, indicating that the boundary measurements are transmitted directly to the rock mass. As the acceleration is transmitted through the rock mass, the high-frequency, high-amplitude responses are filtered, thus leaving a smaller amplitude, lower frequency response as seen in the AC14 response (Figure 11-7). Thus, any high-frequency amplitude anomalies that occur with the boundary plates are quickly attenuated and will have negligible effect on the ingots near the tunnel. Comparing AC14 with AC1 (Figure 11-8), which is a tunnel wall accelerometer on the near side of the rock mass, shows that the acceleration response on the same side of the rock mass is similar near the tunnel and away from the tunnel in the transverse direction.

The cable tension was monitored using a limited number of load cells as indicated in Figure 5-1. As the rock ingots settled during the seismic events, the cable tensions would change. Typically, the vertical cables would lose tension as the ingots settled down vertically, and the horizontal cables would increase tension as the settling ingots would spread horizontally. Figure 11-9 shows the change in cable tension during each data run. Three of the cables (LC1, LC2, and LC3) are horizontal cables that all had an increase in tension during each run. The other three cables (LC4, LC5, and LC6) are vertical cables which, in general, decreased in tension during each run (except for some small increases in Runs 19 and 20).

Also included in Figure 11-9 are the seismic input amplitudes for each run. In general, the cable tensions change the most during the first run at each amplitude (Runs 1, 5, 9, 13, and 21) except for the last run at the highest seismic amplitude in which no cable tension change occurred. This change in tension would indicate that ingot settling was greatest during the first seismic event at a particular amplitude. Subsequent events at the same level had a decreasing effect. As the ingots settled during the course of the testing, increases in seismic input amplitude had a decreasing effect on the change in cable tension. Even though

the general ingot settling, as measured by the changes in cable tension, was decreasing, it will be shown that the ingot motion around the tunnel increased with seismic amplitude (as would be expected). Thus, the cable tension change had less to do with movement of the ingots in toward the tunnel as it did with the general settling of the ingots in the mass as a whole.

From Figure 11-9, the ingots appear to have a threshold level at which dramatic settling occurs. This threshold is seen in the markedly greater cable tension change noted in Run 5 than in Run 1. After Run 4, the cables were retuned to the original levels as shown in Table 7-1. This cable retuning was performed before each of the Runs 5 through 11 as indicated in Figure 11-9. Following Run 11, the cables were left "as is" for each of the subsequent test runs. The only exception to this procedure was that the vertical cables were tightened to 667 N (150 lb) before Run 17 in order to even the vertical load throughout the rock mass.

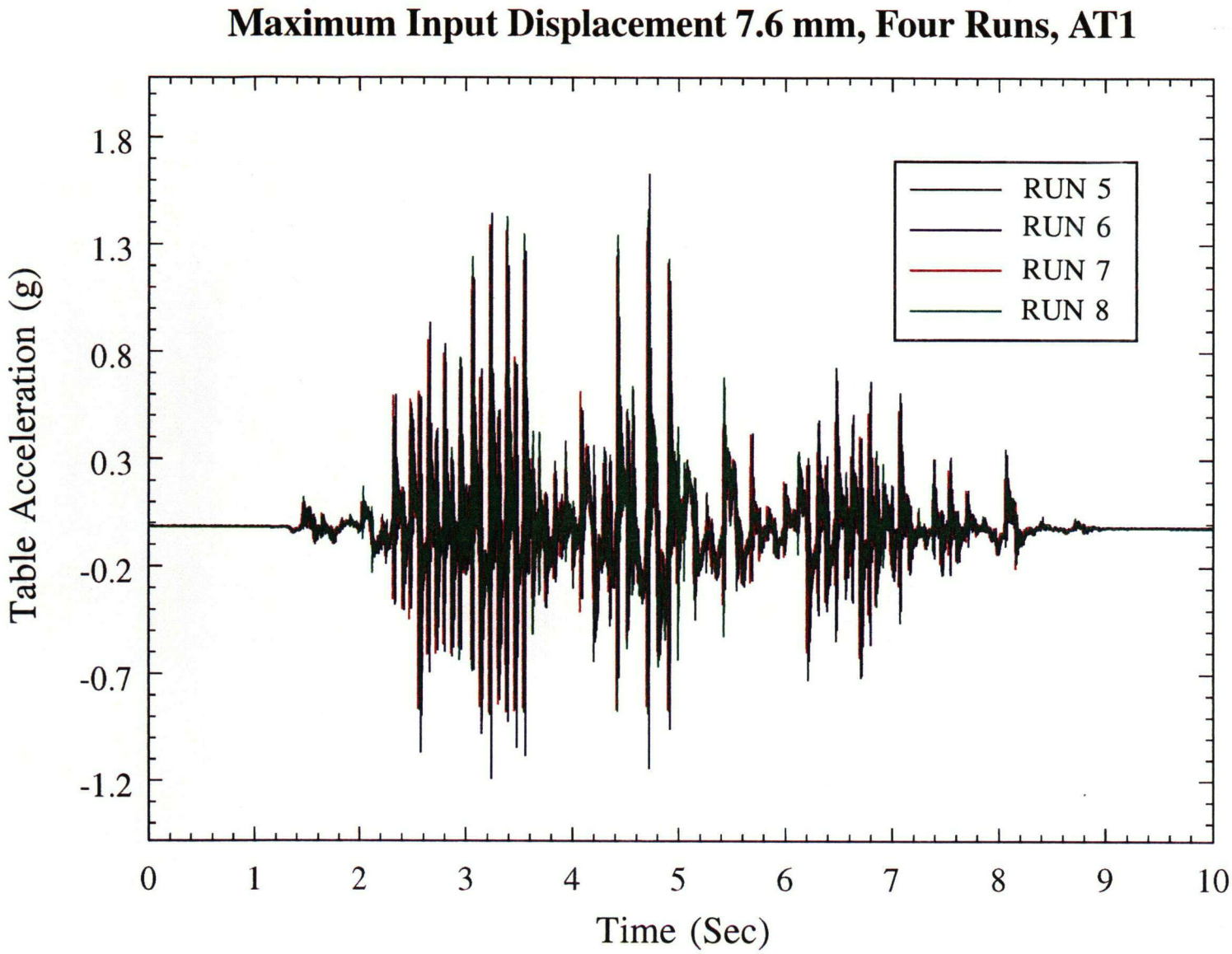

Figure 11-1. Comparison of table accelerations for 7.6 mm peak input runs 5–8

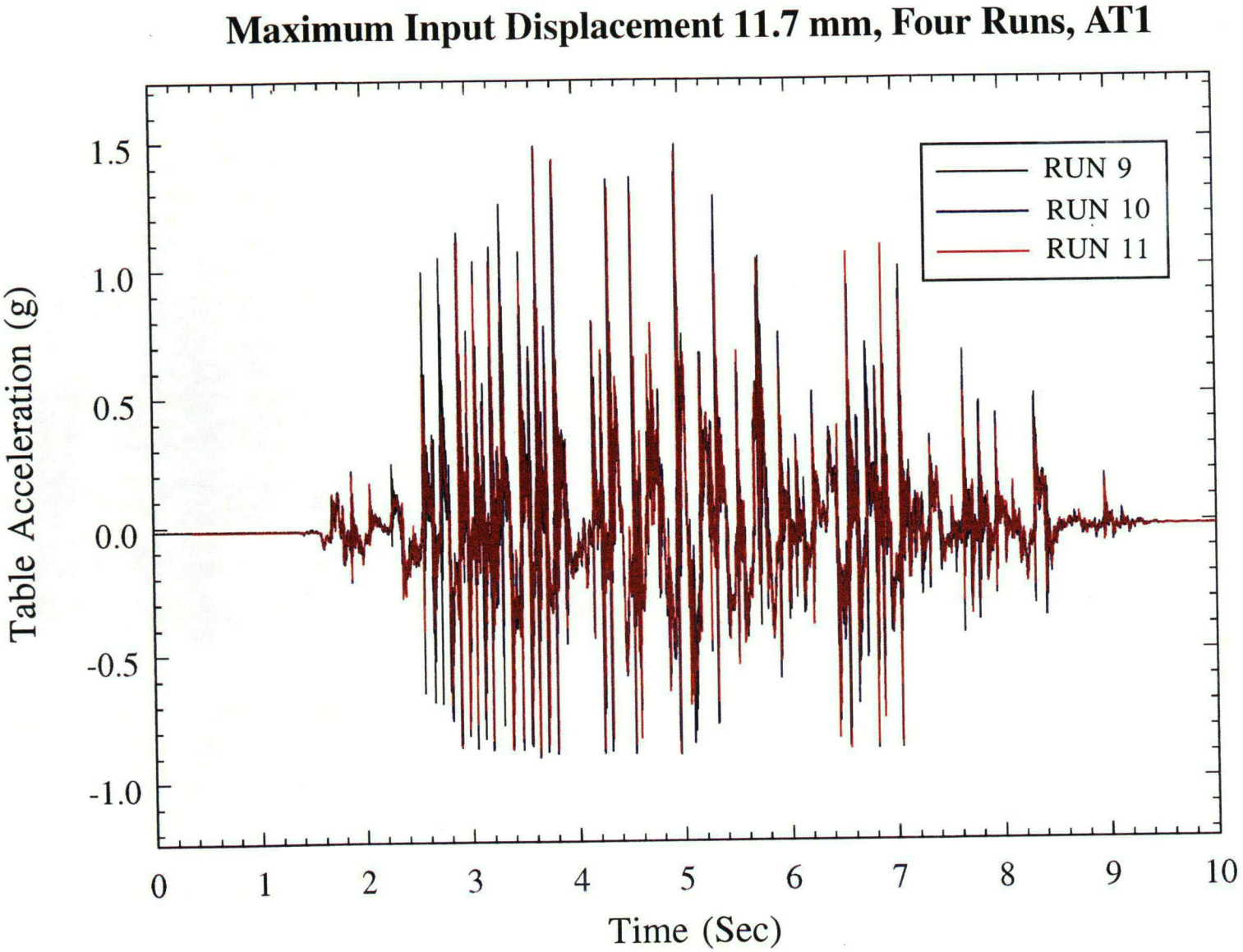

Figure 11-2. Comparison of table accelerations for 11.7 mm peak input runs 9–11

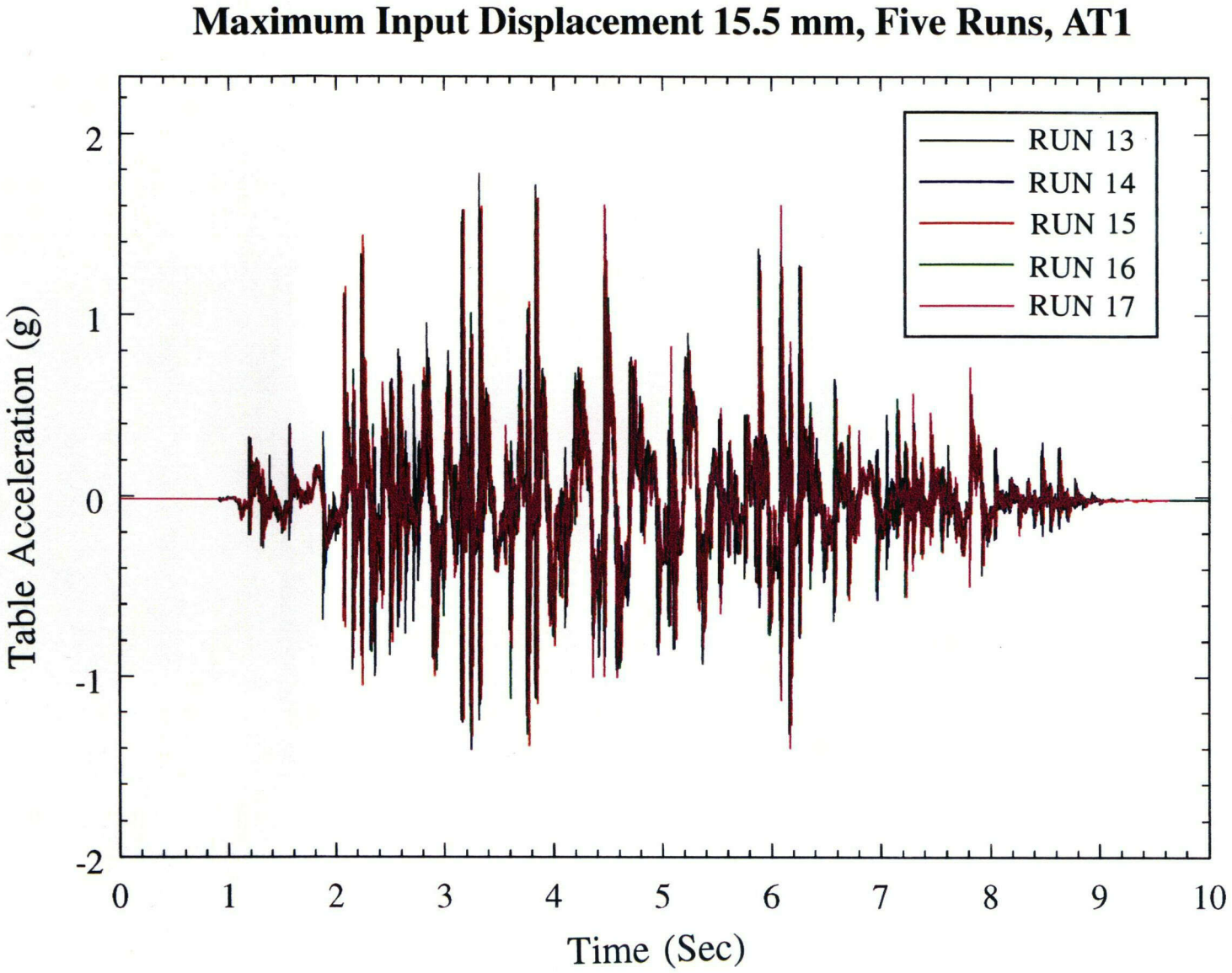

Figure 11-3. Comparison of table accelerations for 15.5 mm peak input runs 13–17

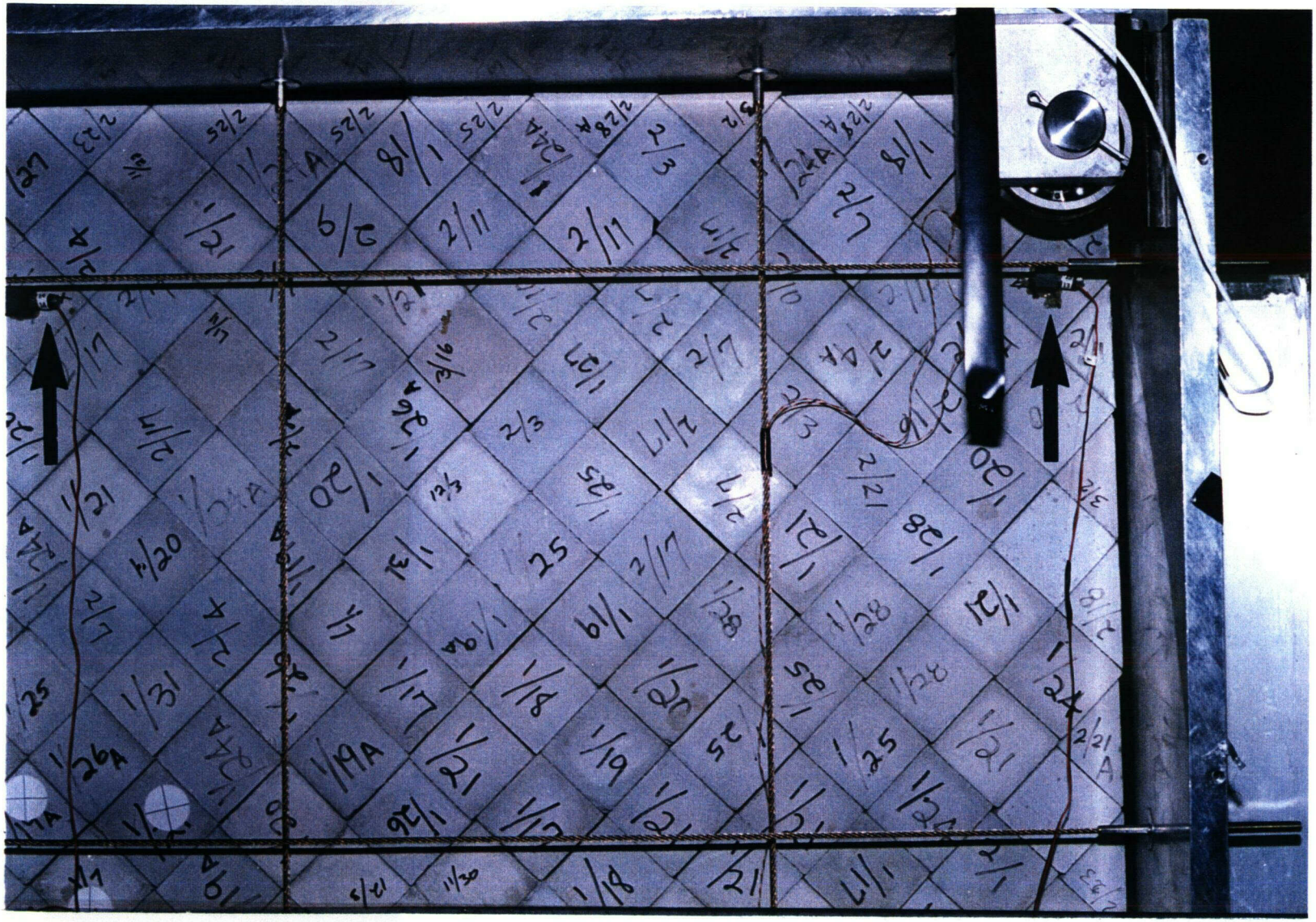

Figure 11-4. Location of ingot accelerometers AC13 and AC14 on near side

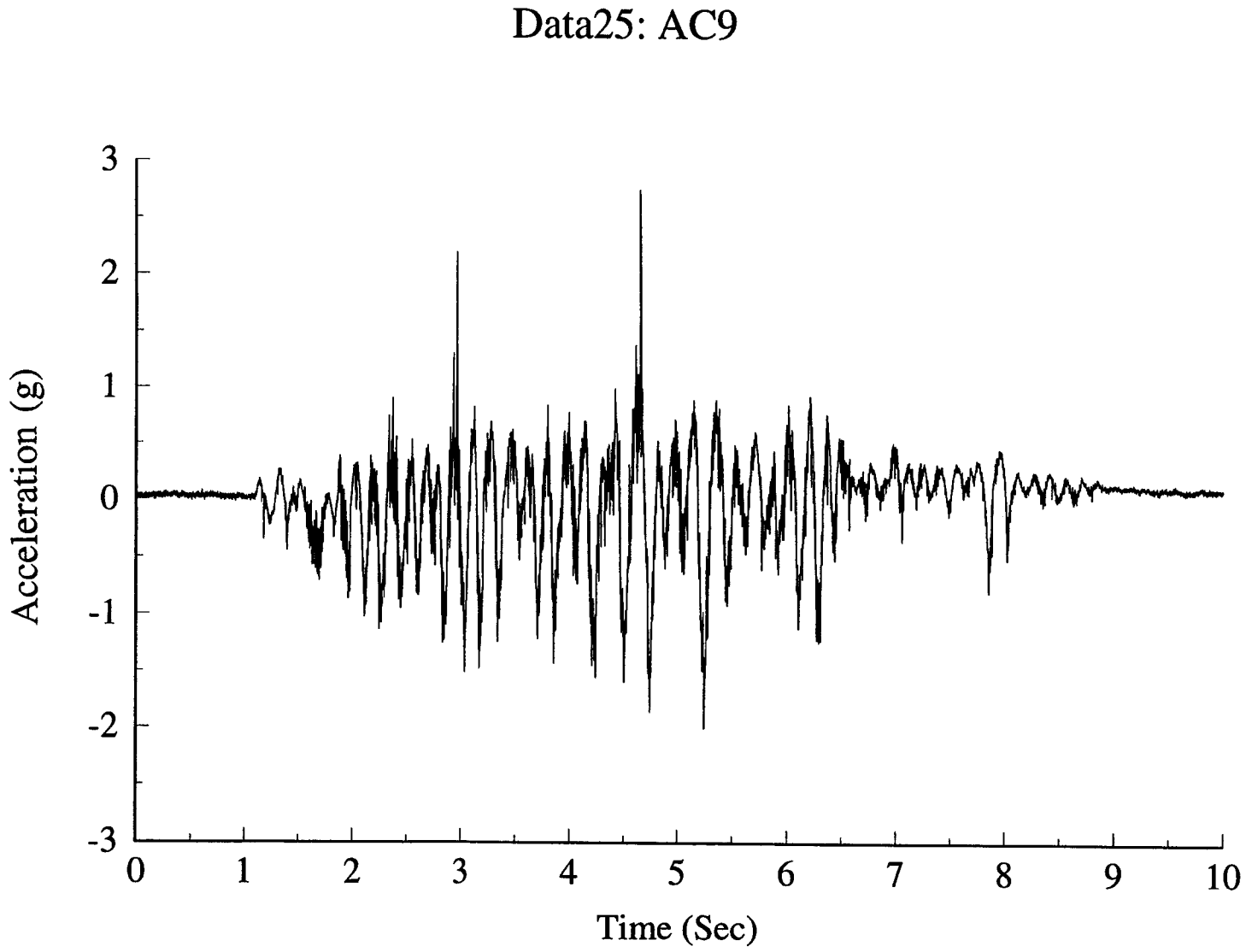

Figure 11-5. Scale model boundary acceleration (AC9) for run 13

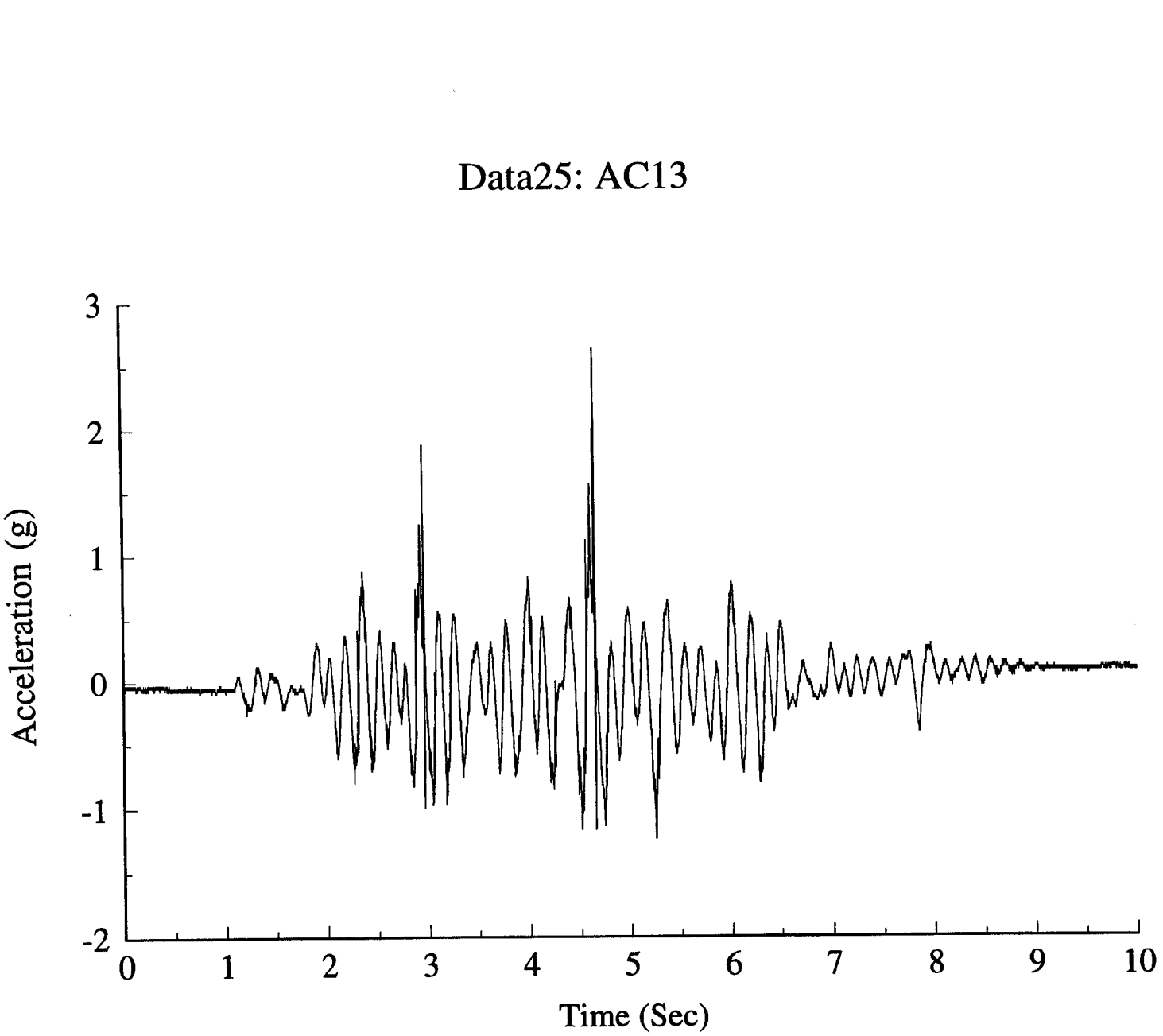

Figure 11-6. Scale model ingot acceleration near boundary (AC13) for run 13

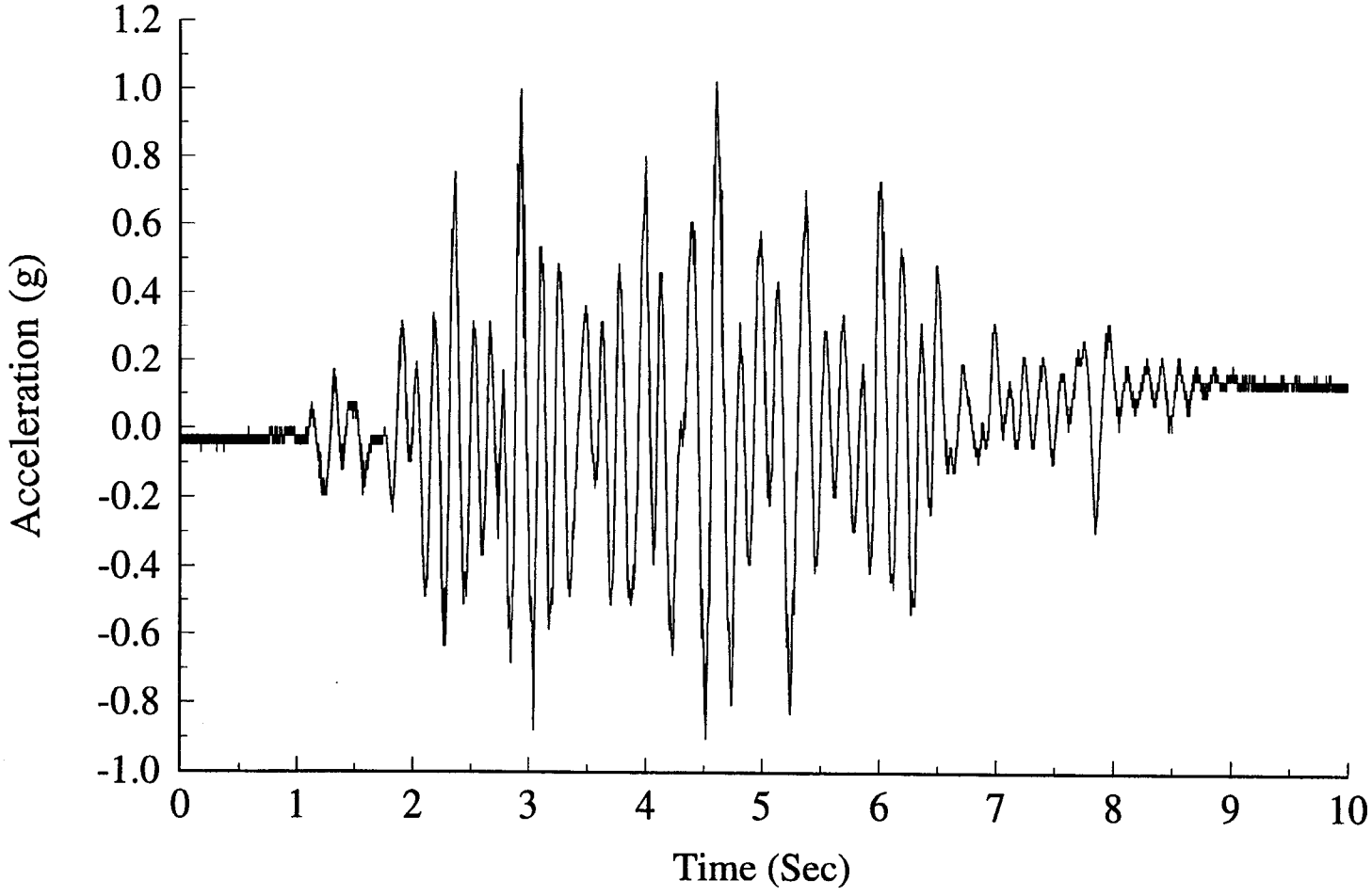

Figure 11-7. Scale model ingot acceleration away from tunnel (AC14) for run 13

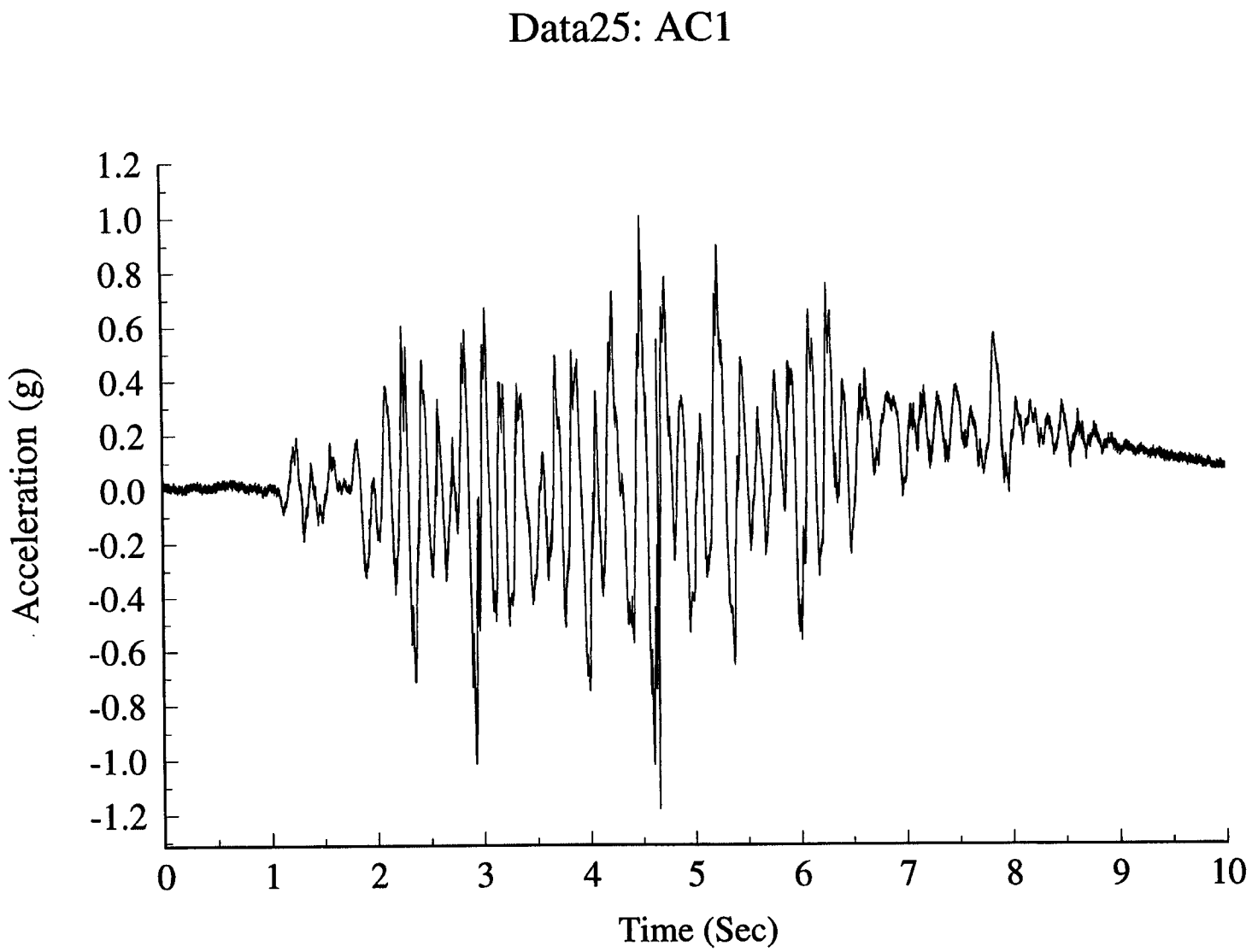

Figure 11-8. Scale model ingot acceleration at tunnel (AC1) for run 13

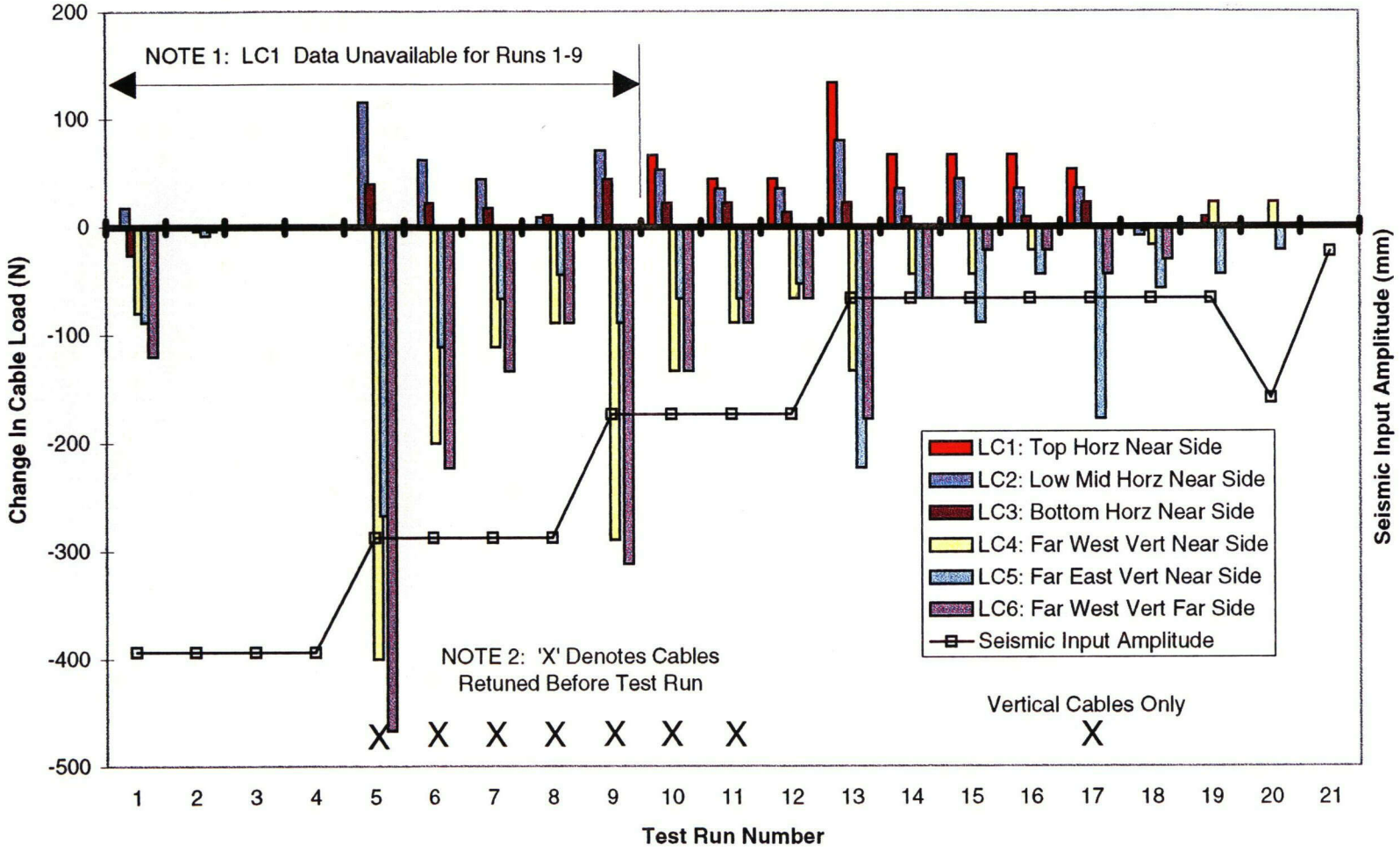

Figure 11-9. Permanent changes in cable tension as a function of seismic event

12 ROCK INGOT DYNAMIC RESPONSE

12.1 DYNAMIC RESPONSE VERSUS PERMANENT DISPLACEMENT

Although the permanent displacement of the rock ingots due to repetitive seismic loads was of primary concern, the dynamic responses of the system to produce these displacements were also of interest. A definition of terms is appropriate. Continuous dynamic response is the oscillating response of each transducer that occurs throughout the seismic event. All the transducers will measure a continuous dynamic response with the possible exception of the strain gages, since the strain amplitudes are extremely small. A permanent displacement is a discontinuous event in which the quasi-static amplitude of the transducer is shifted. This displacement is most apparent when comparing the static levels of the transducers before the start of and after the conclusion of a seismic event. If a permanent displacement has occurred, the before and after static levels will not be equal. A closer look at the transducer data will reveal that such permanent displacements can occur at various discrete instances in the seismic event. The accelerometers, being dynamic response transducers only, will not measure a permanent dislocation.

The data presented in Section 10 clearly indicate that the amplitude of the continuous dynamic response is not necessarily an indicator of the amplitude of the permanent displacement. For instance, proximeter probe BP1 (Figure 10-28) measured dynamic amplitudes of greater than 0.08 mm (0.003 in.), but a permanent displacement of less than 0.02 mm (0.0008 in.). In contrast to BP1 is proximeter probe BP2 (Figure 10-29), which measured continuous dynamic amplitudes of less than 0.03 mm (0.001 in.) but a permanent displacement of approximately 0.05 mm (0.002 in.).

12.2 DYNAMIC CAUSES OF PERMANENT DISPLACEMENT

As mentioned, the permanent displacements occur at various discrete instances in the seismic event. The pattern of these discrete instances provides valuable information as to the cause of the displacements. Figures 12-1 to 12-4 show the cable tension loads, LVDT displacement, cantilever beam displacements, and Bentley Probe displacements for Run 5. The amplitude of these transducers has been scaled to show the similar patterns of response. Even though the dynamic response shows some difference, the transducers in general show permanent displacements occurring at essentially the same point in the seismic event even for transducers monitoring different ingots. Thus the tunnel ingots seem to simultaneously displace at specific instances of the seismic event. These instances are noted by the arrows in Figures 12-1 to 12-4. Simultaneous displacement would be expected since the slipping of one ingot would influence the slipping of surrounding ingots to some degree. To determine the cause of the permanent displacements, the specific instances of displacement noted in Figures 12-1 to 12-4 are also noted on the table displacement and table acceleration responses for Run 5 (Figure 12-5). It is apparent from Figure 12-5 that permanent displacements generally occur at local amplitude extremes of displacement and not at acceleration peaks. However, displacements do not necessarily occur at the overall peak displacements.

Figures 12-6 to 12-10 and 12-11 to 12-15 are similar to Figures 12-1 to 12-5 except for Run 9 and Run 15. The same permanent displacement to table displacement relationship is apparent in these two runs as well. For instance, the permanent displacement that occurs near the 2.9 s point in Figure 12-6 corresponds to a local maximum in Figure 12-10 at the same point in time. A more dramatic example of this phenomenon is shown in the permanent displacement that occurs in Figure 12-13 near the 5 s point which corresponds with a local minimum in table displacement in Figure 12-15. Note that in both of these

examples, the permanent displacement does correspond to the overall peak maximum or minimum of the table displacement, but at a local extreme. Since the permanent displacements occur at either local maximums or local minimums, there appears to be no experimental bias toward one direction of seismic amplitude.

Thus, table displacement provides the key to permanent displacements, which, in turn, can lead to tunnel collapse. Recall that the scaled table displacement compared favorably with the representative unscaled seismic displacement (Figures 8-5 and 8-2). Since the table displacement is the important parameter, the experimental results for the scale model are not inappropriately biased by the differences between the scaled table acceleration (Figure 8-4) and representative unscaled seismic acceleration (Figure 8-1). This lack of bias is advantageous for future experimental work in that table displacement is more easily controlled than table acceleration.

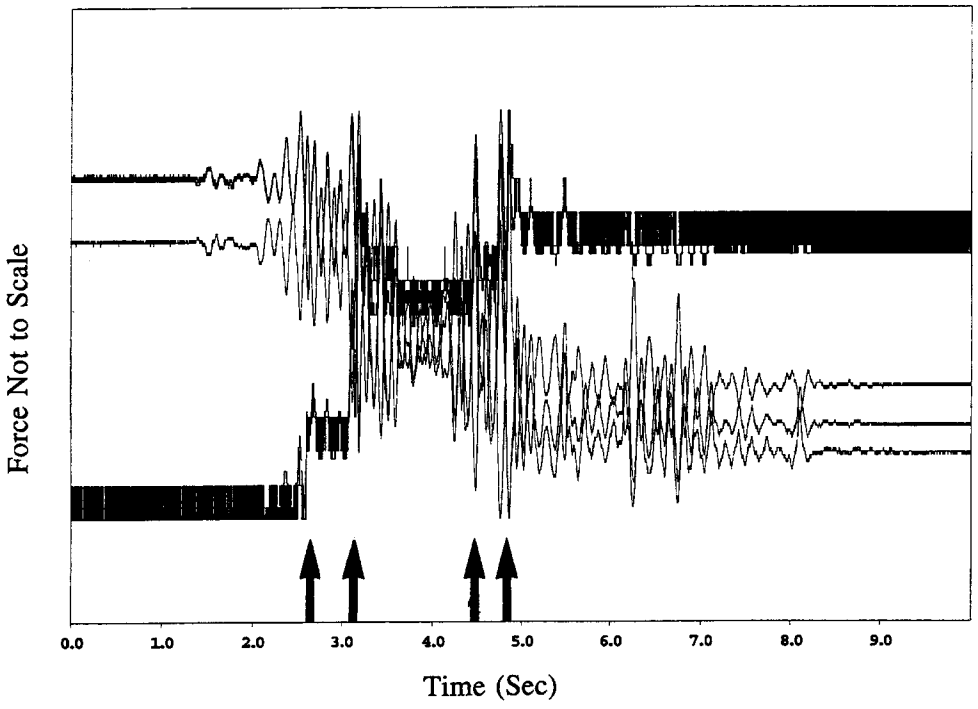

Figure 12-1. Comparison of cable tension loads for run 5, peak input 7.6 mm

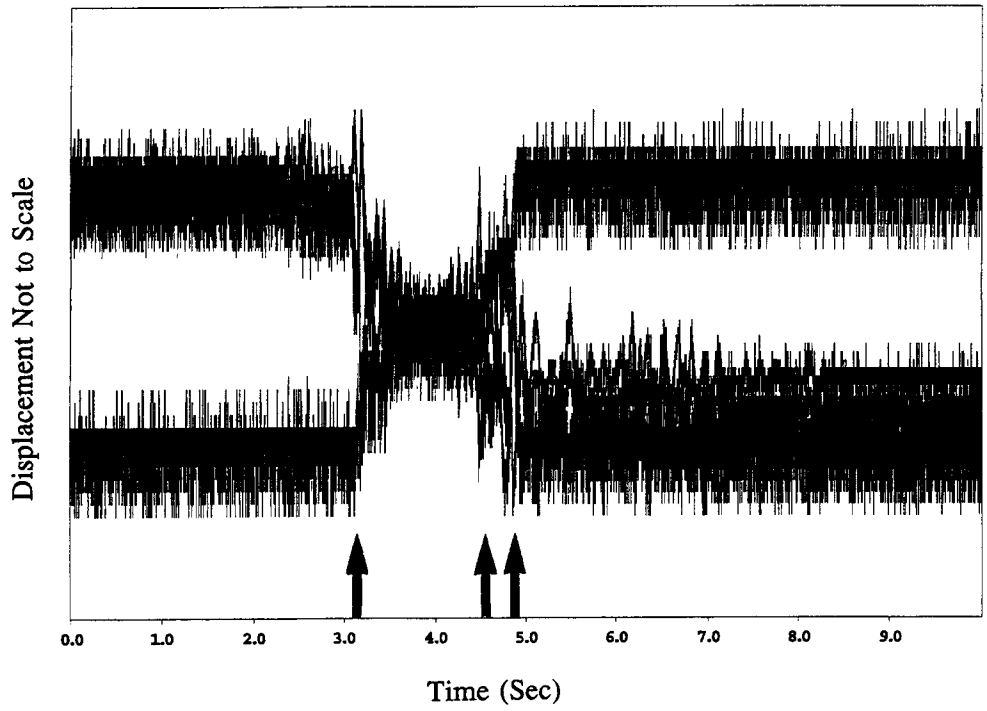

Figure 12-2. Comparison of LVDT displacements for run 5, peak input 7.6 mm

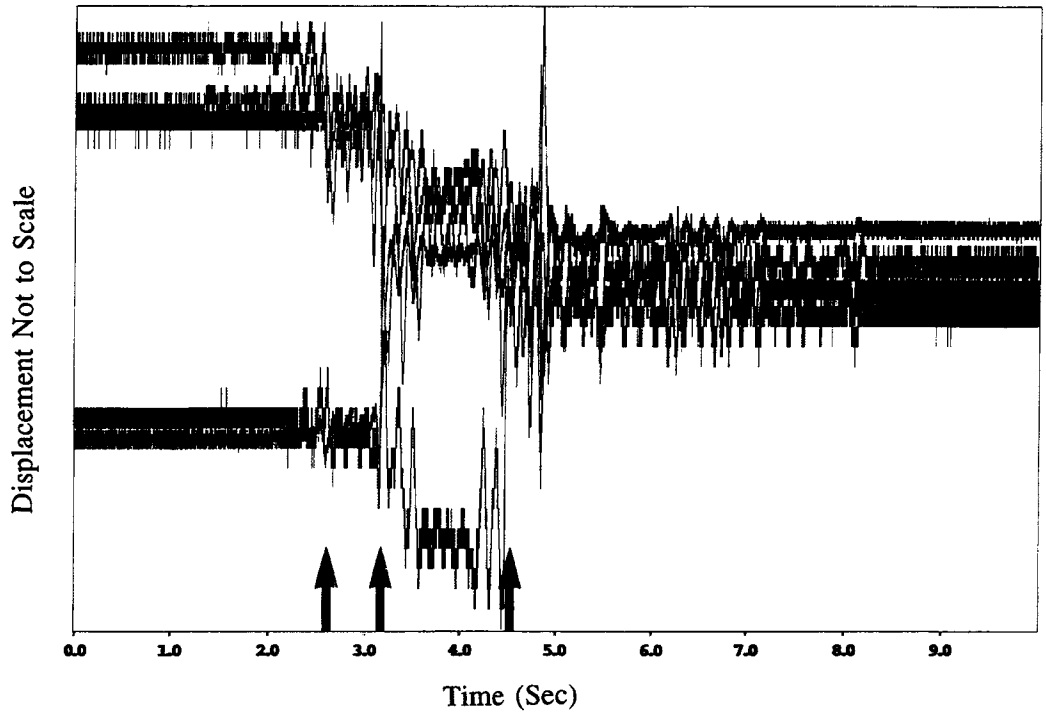

Figure 12-3. Comparison of cantilever beam displacements for run 5, peak input 7.6 mm

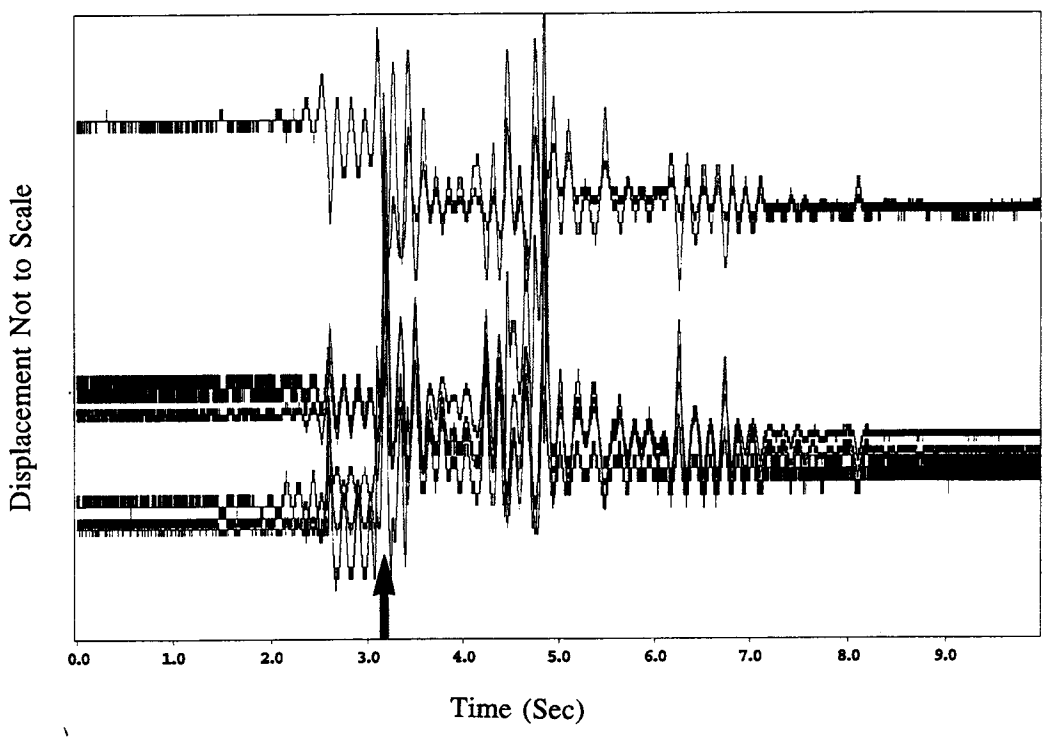

Figure 12-4. Comparison of proximeter displacements for run 5, peak input 7.6 mm

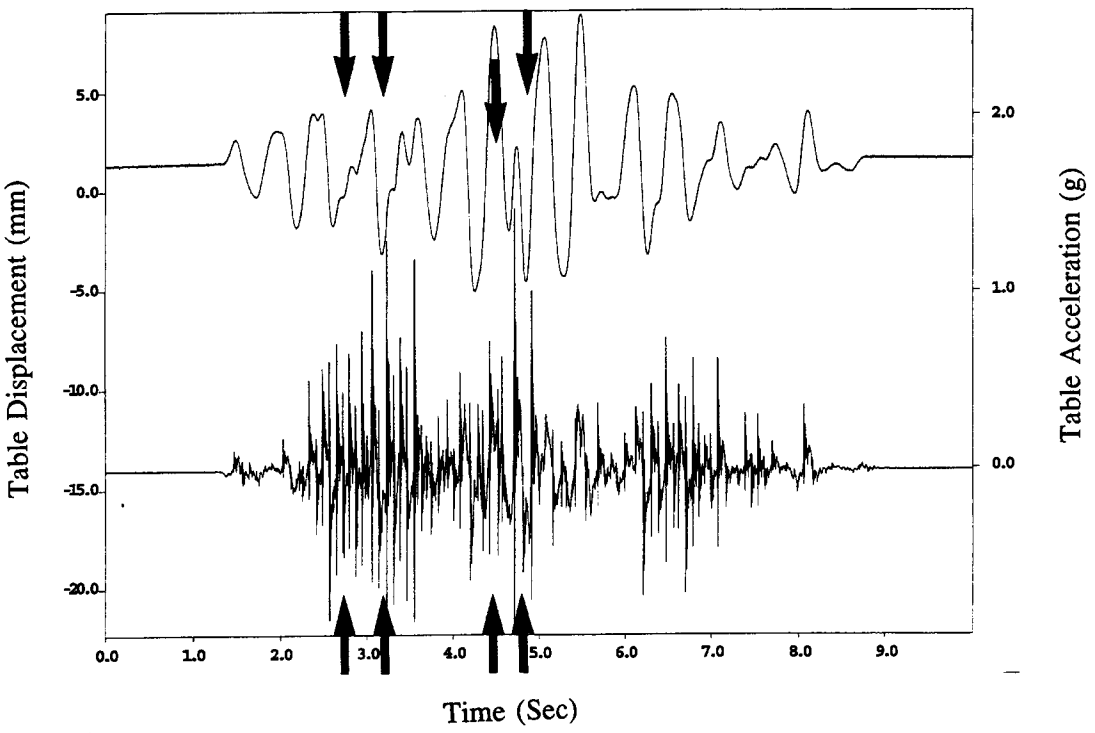

Figure 12-5. Table displacement and table acceleration for run 5, peak input 7.6 mm

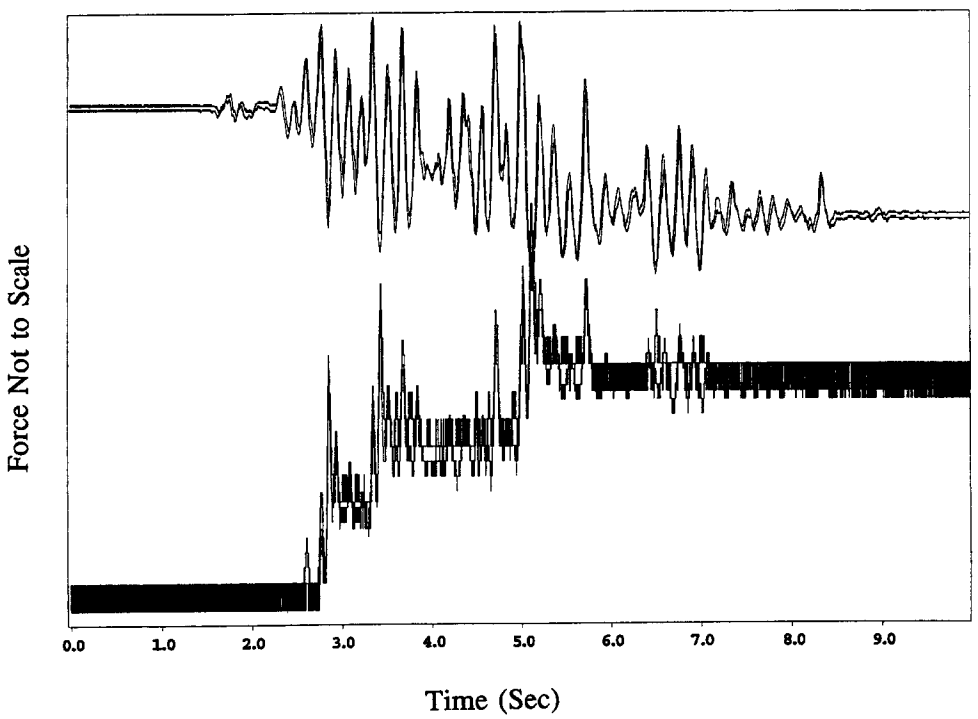

Figure 12-6. Comparison of cable tension loads for run 9, peak input 11.7 mm

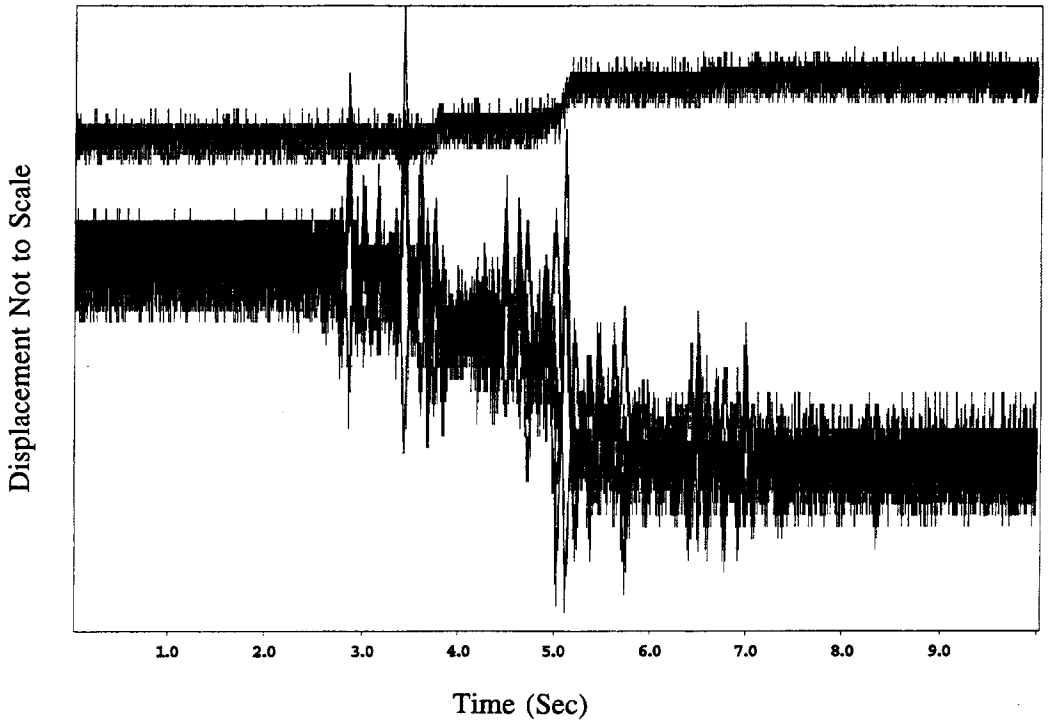

Figure 12-7. Comparison of LVDT displacements for run 9, peak input 11.7 mm

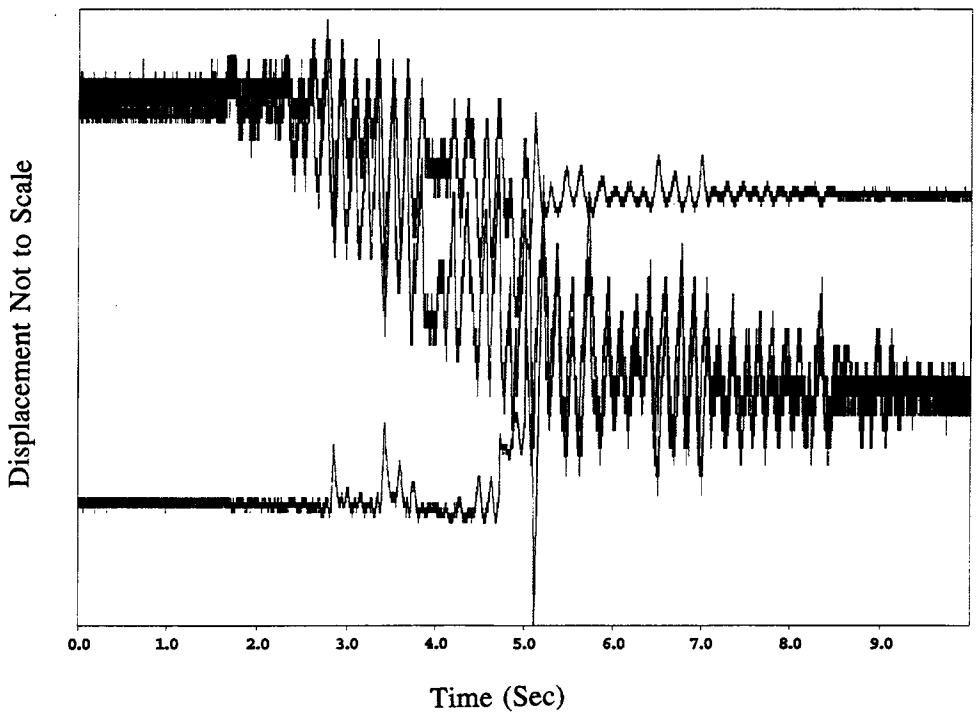

Figure 12-8. Comparison of cantilever beam displacements for run 9, peak input 11.7 mm

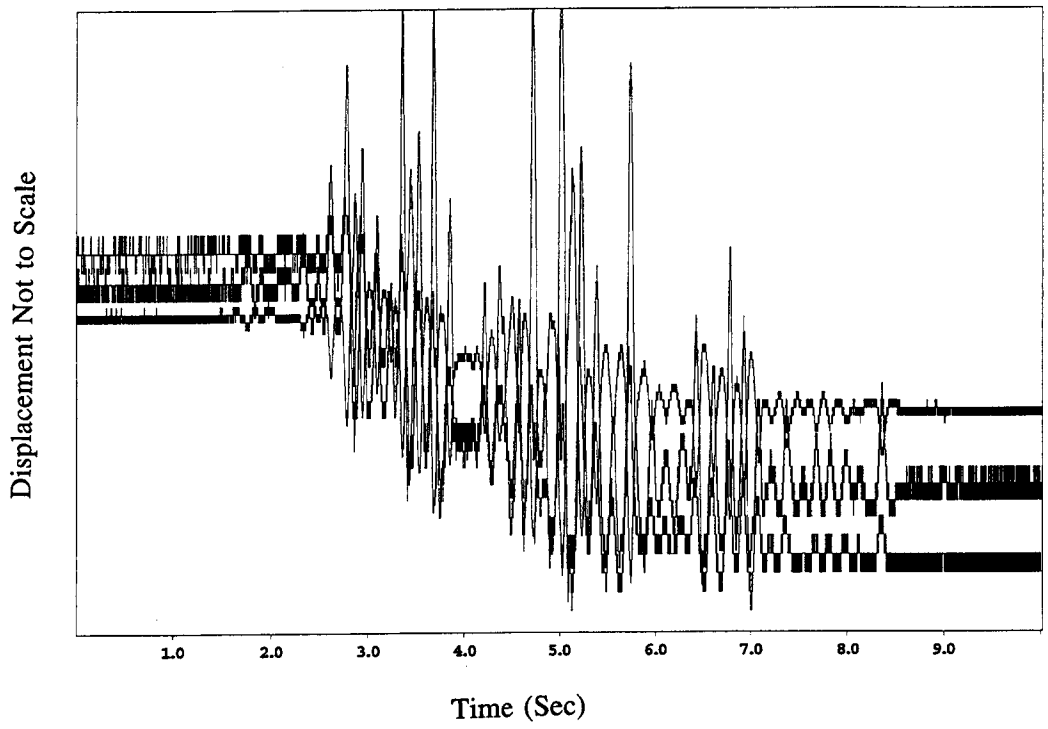

Figure 12-9. Comparison of proximeter displacements for run 9, peak input 11.7 mm

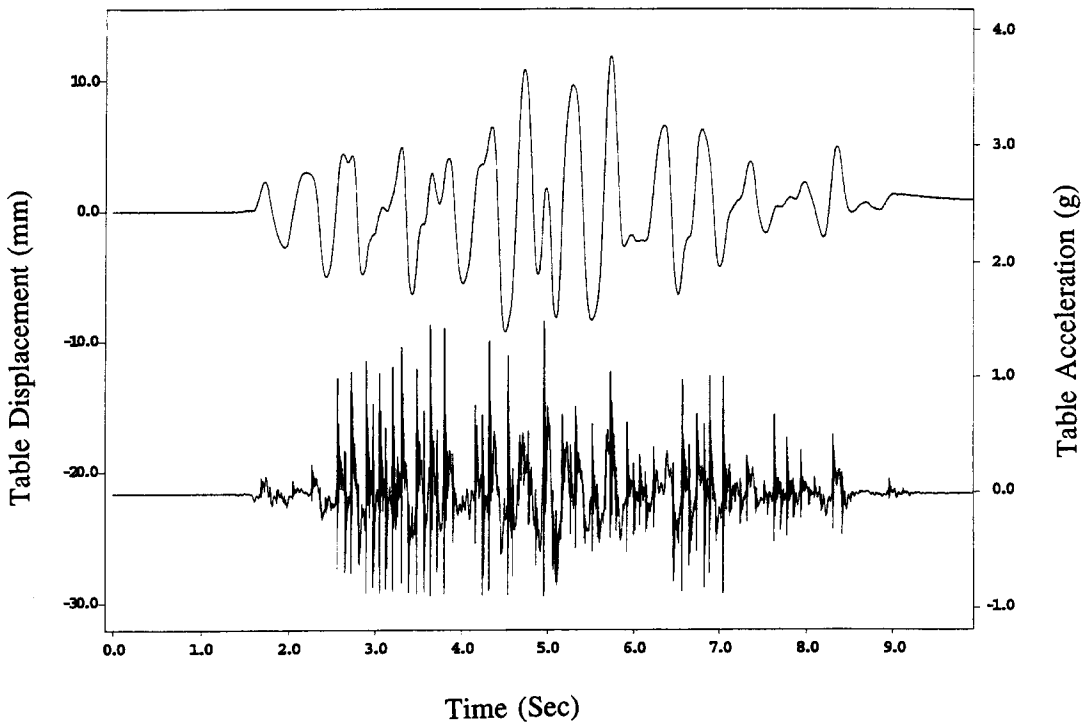

Figure 12-10. Table displacement and table acceleration for run 9, peak input 11.7 mm

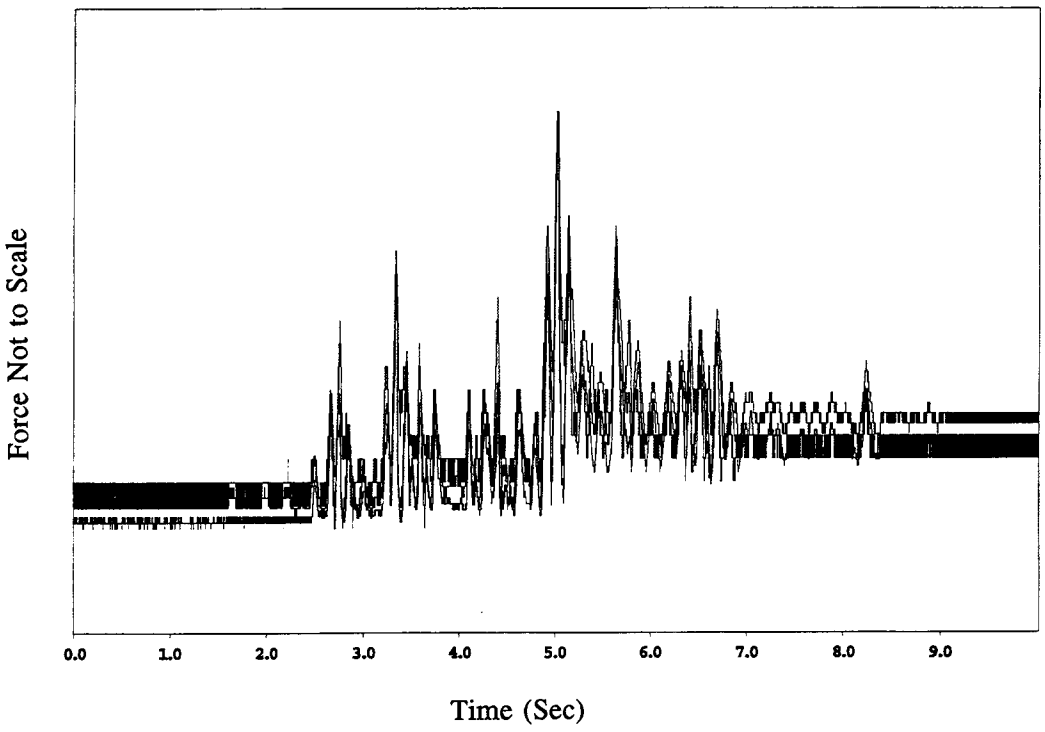

Figure 12-11. Comparison of cable tension loads for run 15, peak input 15.5 mm

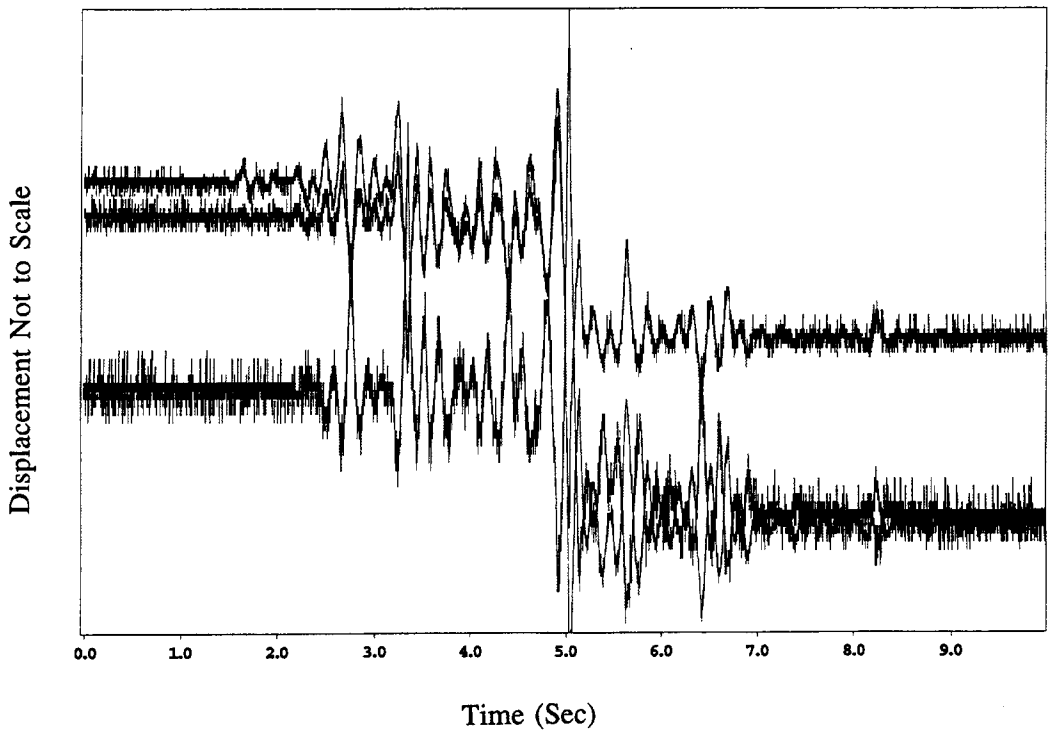

Figure 12-12. Comparison of LVDT displacements for run 15, peak input 15.5 mm

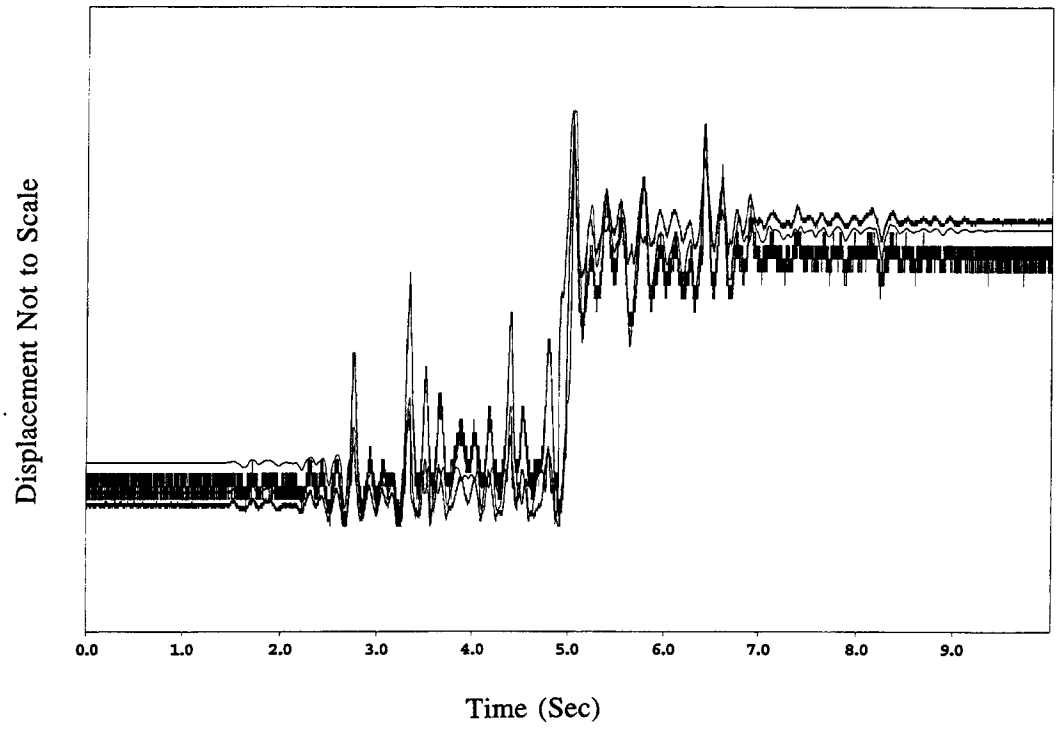

Figure 12-13. Comparison of cantilever beam displacements for run 15, peak input 15.5 mm

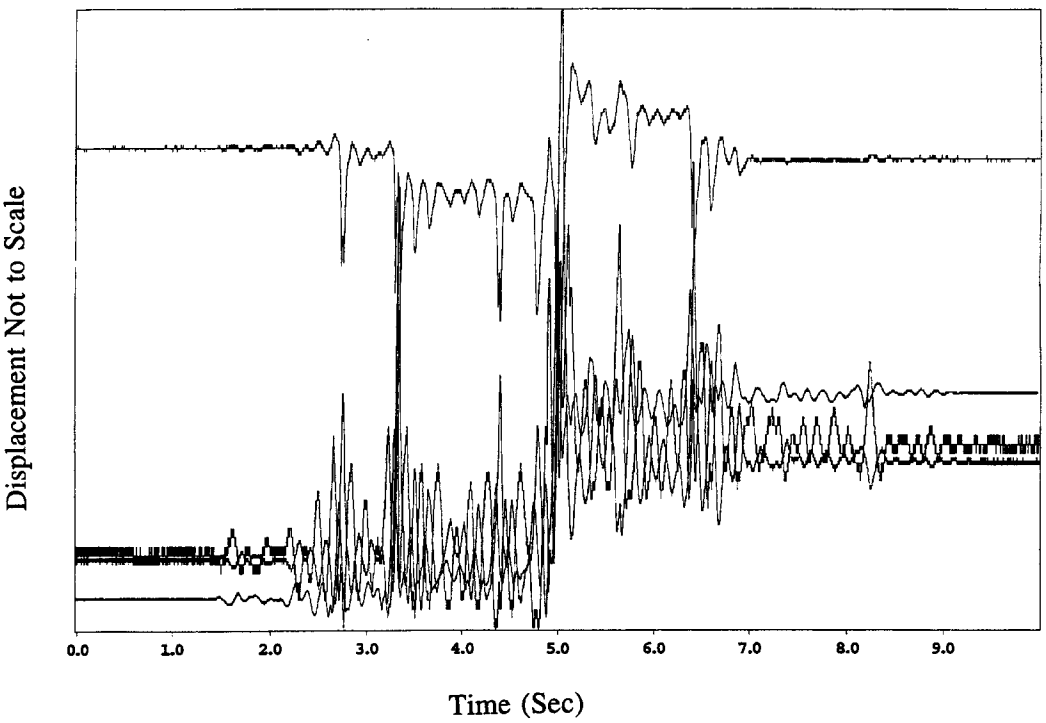

Figure 12-14. Comparison of proximeter displacements for run 15, peak input 15.5 mm

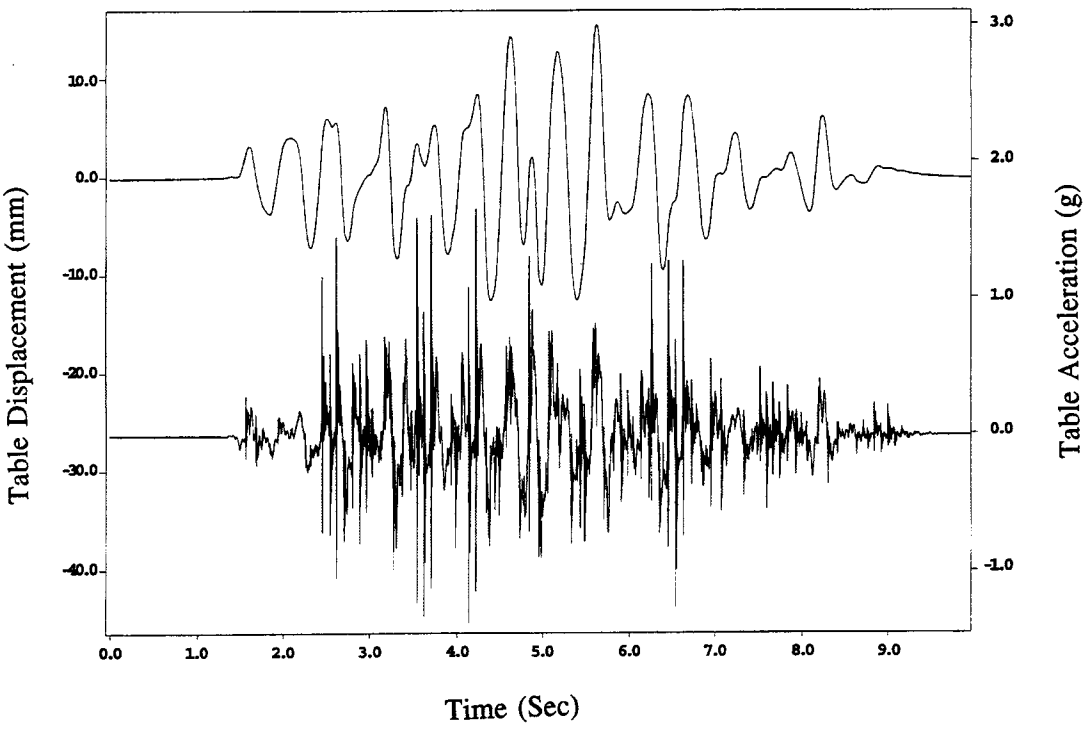

Figure 12-15. Table displacement and table acceleration for run 15, peak input 15.5 mm

13 ROCK INGOT PERMANENT DISPLACEMENT

13.1 ROCK INGOTS AS RIGID BODIES

Figures 10-23 to 10-49, presented previously, show dynamic responses of the various rock ingot motion transducers. Many of these transducers reflect the basic motion of the 7-Hz rocking mode in addition to other dynamic responses. In contrast to the strong dynamic response of the rock ingots as rigid bodies are the strain gage responses at the rock ingot surfaces (Figures 10-14 to 10-22.) These strain responses for Run 5 are typical of strain responses for the other runs, which demonstrate that essentially negligible elastic strain occurs in the cross-section of the ingots. This lack of elastic strain means that the rock ingots shifted overall as cross-sectional rigid bodies, with relative motion and wear deformation occurring only in the near vicinity of the surfaces in contact. However, strain along the length of the ingots probably did occur.

13.2 ROCK INGOT TUNNEL CLOSURE

With the rock ingots treated as rigid bodies, the overall motion of the rock ingots as a function of the seismic tests can be discussed. The general motion of the rock ingots near the tunnel can be described with reference to the video taped results and the still photographs. These pictorial results will present an overview of the results of the scale model test.

Throughout the complete set of runs, a video camera was used to tape the motion of the rock ingots around the tunnel end on the far side (see Figures 5-4 and 5-6). The video camera was useful for viewing relatively large motions of the ingots during each test that otherwise cannot be measured due to the limited measuring range of a particular instrument or due to lack of instrumentation. Table 13-1 lists the gross permanent displacements of the rock ingots as a result of each run. It is estimated that permanent displacements on the order of 0.5 mm or larger were discernible with normal viewing of the video tape. From the table, it is evident that visually, it was difficult to discern any motion until Run 15. In addition, Run 15 is not the first run at the 15.5-mm seismic amplitude, but the third. Thus, at this amplitude, continuous displacement of ingots occurs for seismic events of the same amplitude. Motion of the rock ingots was discernible on only the left side (as being viewed) of the tunnel. As predicted in the preliminary UDEC model (Figure 4-1), tunnel collapse would be most likely on only one side of the tunnel. Unlike the UDEC model, no general trend of aligned 45° rows slipping toward the tunnel in unison was detected.

Still photographs taken on both sides of the tunnel provide additional visual data of the motion of the rock ingots. On the near side of the rock model, very little motion was visually noted. Figures 13-1, 13-2, and 13-3 are photographs of the near side of the rock ingot tunnel (see Figures 5-3 and 5-5) following Runs 4, 15, and 21. No changes are noticed between these photographs. Visually, no discernible changes occurred on the near side of the tunnel throughout the testing even though significant ingot displacement occurred on the far side of the tunnel as the video tape showed. Thus, the rock scale model did not behave globally as a 2-D system throughout the testing as designed.

The far side tunnel ingot permanent displacements are shown in Figures 13-4 to 13-10, which are photographs of the far side of the rock ingot tunnel following Runs 4, 13, 15, 16, 17, 19, and 21, respectively. Here, rock ingot displacement becomes readily apparent during the progression of the runs. Note that the photographs present a visual representation of the general displacements listed in Table 13-1.

Table 13-1. Far side rock ingot motion discernible from video tape

Data Set	Data Run	Peak Excitation	Discernible Motion
DATA 9	RUN 1	3.8 mm (0.15 in.)	None
DATA 10	RUN 2	3.8 mm (0.15 in.)	None
DATA 11	RUN 3	3.8 mm (0.15 in.)	None
DATA 12	RUN 4	3.8 mm (0.15 in.)	None
DATA 14	RUN 5	7.6 mm (0.30 in.)	None
DATA 15	RUN 6	7.6 mm (0.30 in.)	None
DATA 16	RUN 7	7.6 mm (0.30 in.)	None
DATA 17	RUN 8	7.6 mm (0.30 in.)	None
DATA 19	RUN 9	11.7 mm (0.46 in.)	None
DATA 21	RUN 10	11.7 mm (0.46 in.)	None
DATA 22	RUN 11	11.7 mm (0.46 in.)	None
DATA 23	RUN 12	11.7 mm (0.46 in.)	None
DATA 25	RUN 13	15.5 mm (0.61 in.)	None
DATA 27	RUN 14	15.5 mm (0.61 in.)	None
DATA 28	RUN 15	15.5 mm (0.61 in.)	Gap above I, smaller gap above H
DATA 30	RUN 16	15.5 mm (0.61 in.)	Widen Gap Above I
DATA 33	RUN 17	15.5 mm (0.61 in.)	Slight gap widen above I
DATA 34	RUN 18	15.5 mm (0.61 in.)	Slight gap widen above I
DATA 37	RUN 19	15.5 mm (0.61 in.)	Little change
DATA 40	RUN 20	12.2 mm (0.48 in.)	None (with lines added to ingots)
DATA 42	RUN 21	17.3 mm (0.68 in.)	Collapse of I and G, gap widen above H

The first discernible displacement is noted following Run 15 (Figure 13-6). The ingots on the left side moved toward the tunnel. This movement increases slightly following Run 16 (Figure 13-7), following Run 17 (Figure 13-8), and through Run 19 (Figure 13-9), a clear indication of the cumulative nature of rock ingot displacement. Finally, the large-scale collapse of the tunnel is seen following Run 21 (Figure 13-10).

Note that no large-scale motion of ingot rows is seen in these photographs. The motion of the rock ingots may be discernible in the overall view of the rock model at the completion of the seismic tests. Figures 13-11 and 13-12 show the overall rock model on the near side and far side, respectively. For the near side (Figure 13-11), careful observations of the rock ingot 45° lines running left to right show a shifting of three rows of ingots from the upper right of the picture toward the upper right end of the tunnel. Similarly, the far side (Figure 13-12) appears to have a

similar shift of the same rows from the upper left of the picture toward the upper left end of the tunnel (note the symmetrical reversal on opposite sides of the model). Figures 13-13 and 13-14 are close-up photographs of the upper right end of the near side of the model following Runs 4 and 21, respectively. In these close-up views, it appears there was a general shift of the rows in question during Run 4. Only small changes seemed to occur between Run 4 and the conclusion of Run 21. Similar general shifts are also seen in close-up views (Figures 13-15 and 13-16) of the upper left end of the far side of the model following Runs 4 and 21, respectively. Thus, the general shift of these three rows of ingots may have been there from the setup or may have occurred during initial settling caused by the bumps and first three low-amplitude seismic events.

However, to support the possibility of a shift during the seismic tests, it was noted that the two ingots closest to the upper right corner of the near side were loose following Run 9. One reason for these two ingots to be loose is a shift in the rows toward the tunnel. As a conclusion, though, the general shift of the rows as a result of seismic events, as predicted by the UDEC model, was not clearly verified from this rock scale model test. This difference may be attributed to the fact that the ingots in the scale-model are not perfectly aligned, while in the UDEC model a perfect alignment was assumed. As can be observed in Figures 5-3, 5-4, and 7-8, there is a slight interlocking among ingots. This interlocking can change overall rock mass behavior.

In addition to the above visual data, following Run 12, some loose dust was discovered in the tunnel as shown in Figure 13-17. This dust indicates that some ingots were sliding over each other, causing some breakage of roughness asperities from the ingot surfaces. This type of motion, of course, is verified by the oscillating dynamic data discussed in Section 12.1.

Smaller amplitude ingot dislocation near the tunnel as measured by the transducers are discussed in Section 13.4. As seen from the visual data, the majority of the dislocation occurred on the far side of the model, where fewer transducers were located. In addition, the largest tunnel collapse on the far side was attributed to an ingot (ingot I from Figure 5-6) that did not have transducer measurements on the far side.

13.3 TWO- VERSUS THREE-DIMENSIONAL RESPONSE

As noted in the overview of the rock ingot permanent displacement presented in the previous section, the rock model overall behaved more as a 3-D model as the testing progressed toward tunnel collapse. The evidence for the three-dimensionality of the rock scale model is threefold. First, the tunnel collapse occurred on only the far side of the rock model. Second, following Run 15, it was noted that the top plate had tilted 12.7 mm from the near side toward the far side about an axis in line with the direction of the seismic input. Thus, the far side had more vertical settling of the ingots than the near side. Third, following Run 16, a fracture in ingot G (the upper right tunnel rock on the near side and the upper left tunnel rock on the far side) was noted. This fracture occurred near the LV4 transducer attachment on the far side of the model. The tunnel collapse on the far side, the leaning of the top plate toward the far side, and the fracture of the ingot on the far side of a LVDT transducer attachment can all be caused by slight eccentricities in the model. The eccentricities can include curvature in the ingots and nonuniform roughness along the length of the ingots. The resulting responses were thus not exactly 2-D, as was originally planned.

To determine a seismic input level below which the scale-model can be assumed to behave two dimensionally, transducers on opposite sides of the same ingot are compared. Figures 13-18 to 13-33 are divided into two parts, with part "a" showing the transducer on the near side of the scale model and part "b" showing the corresponding transducer on the same ingot on the far side. Four data runs (Runs 10, 14, 19, and 25) are included at increasing seismic amplitudes. For Run 2, the accelerometer data on ingot I on the side wall of the tunnel show some similarities (Figures 13-18a,b) which could indicate some two-dimensionality. The cantilever beams on the same ingot (Figures 13-20a,b) show little response, which maintains the symmetry. However, the accelerometers on Ingot G the upper side of the tunnel (Figures 13-19a,b), though showing similar character, are an order of magnitude different in amplitude. The cantilever beams on Ingot D (Figures 13-19a,b) also show completely different characteristics. Thus even at very low amplitude levels, two-dimensionality may not be present. As the amplitude increases, the disparity between the transducers on opposite sides of the tunnel becomes increasingly large. Compare, for example, Run 5 data shown in Figures 13-22a,b and Figures 13-24a,b which are the same transducers that showed some similarity in Run 2. In particular, the cantilever beams show a rocking of the ingot with a displacement away from the tunnel on the near side and a displacement toward the tunnel on the far side. Throughout these data runs, cantilever beam CB8 contains a strong 7-Hz resonant response. It is unclear if this reading is true data or a signal inaccuracy.

The conclusion concerning the dimensionality of the experimental results is that, at the amplitudes discernible by the transducers and the larger scale motions, the model behaves for the most part as a 3-D structure. The response, however, may be simplified in the cross-axis direction by allowing a simple rotation of the ingots about the center axis of the input motion. This type of response must be included in any numerical modeling.

13.4 PERMANENT DISPLACEMENT AS A FUNCTION OF SEISMIC AMPLITUDE

The permanent displacement movement of the ingots toward the tunnel is, of course, of primary concern in predicting tunnel collapse. Thus, one purpose of this testing program was to determine the effects of seismic input amplitude on rock ingot permanent displacement. The general visual trends of the data presented in Section 13.2 indicate that large permanent displacement occurs when a certain threshold peak input amplitude is exceeded. This input amplitude visually appeared to be between 11.7 and 15.5 mm. In addition, the visually detectable ingot permanent displacement occurred during Run 15, which was not the first run at the 15.5-mm peak amplitude. Thus, cumulative effects must be considered when dealing with tunnel closure.

In this section, the transducer data will be examined to determine whether these evaluations are correct on the smaller scale of dynamic measurements. Note, however, that the ingot with the largest amount of permanent displacement during the experiment did not have transducers located on the far side where the large motion occurred. Figures 13-34 to 13-36 show the displacement amplitudes of the cantilever beams, Bentley probes, and LVDT transducers, respectively. Each of these figures contains a part "a," which shows the data for all the runs and a part "b," which leaves off the last run. The last run had large permanent displacements that shrink the scale of the other seismic runs, hence the two plots. Note that the permanent displacements were determined by subtracting the static displacement amplitude at the start of a seismic run from the static displacement amplitude at the end of the seismic run. In some cases, the entire data set was not available from the seismic run due to computer malfunctions. In these cases, the zero data runs performed before and after these tests were used to reconstruct the total

permanent displacement that occurred during the seismic run. Only the final displacement amplitude is shown in these figures, not the intermediate displacements that occurred during the course of a particular seismic event. In addition to the displacement amplitudes for each run, these figures show the seismic input amplitude for each run.

Figures 13-34b, 13-35b, and 13-36b show the same general trend. For each type of transducer, the first run at each new amplitude produces the largest permanent displacements. Thus, permanent displacements of ingots are measurable in Runs 1, 5, and 9 even though the later runs at the same amplitudes produce negligible permanent displacements. At low seismic amplitudes, very little permanent displacements occur for multiple seismic events of the same magnitude.

As the seismic input amplitude is increased to 15.5-mm for Runs 13 through 19, the trend seen at the lower amplitudes changes. At this 15.5-mm amplitude, incremental permanent displacements are apparent for multiple runs. Visual observations verified this displacement in that the discernible displacement did not occur during Run 13 but Run 15, the third event at the same amplitude. The incremental displacements decrease with each event at this magnitude. Thus, it is conceivable that some limiting level of displacement is possible at this amplitude.

When the seismic event is lowered in amplitude as in Run 20, negligible incremental displacement occurs. This behavior implies that lower level pre- and after-shocks may not cause as much rock motion unless these lesser magnitude shocks occur at levels above a certain seismic amplitude input. This seismic amplitude input may be considered as a threshold. This threshold seems to occur between 12.2- and 15.5-mm peak amplitude for the particular test configuration. Recall that the displacements occur at local table displacement extremes rather than at peak amplitude levels. This phenomenon may be analogous to the relative effects of a sinusoidal input and a random input at the same energy level. The sinusoidal input causes more severe damage even though intermittent peaks for the random input may exceed the peak amplitude of the sinusoidal input. This is an indication that the displacement may be more dependent on the root-mean-square (rms) level of the vibration, rather than the peak amplitude.

In attempting to distinguish global rock motion from local ingot tunnel permanent displacement, the LVDT data from the left and right sides of the tunnel are compared in Figure 13-37. Note that at the lower seismic input amplitudes, until Run 13, the LVDT measurements on each side of the tunnel are essentially identical. Thus the upper arc of the tunnel shifts down slightly as a whole at the lower input amplitudes. After the seismic input threshold is exceeded (which occurs at Run 13 and following), the tunnel begins to experience asymmetric closure. In this case, ingot G moves toward the tunnel at a much higher displacement rate than ingot I on the opposing wall of the tunnel. Similar trends are apparent in the cantilever beam data shown in Figure 13-38, also shown on opposing side of the tunnel wall. Thus, it can be concluded that tunnel closure is relatively symmetric until an input threshold seismic amplitude is exceeded.

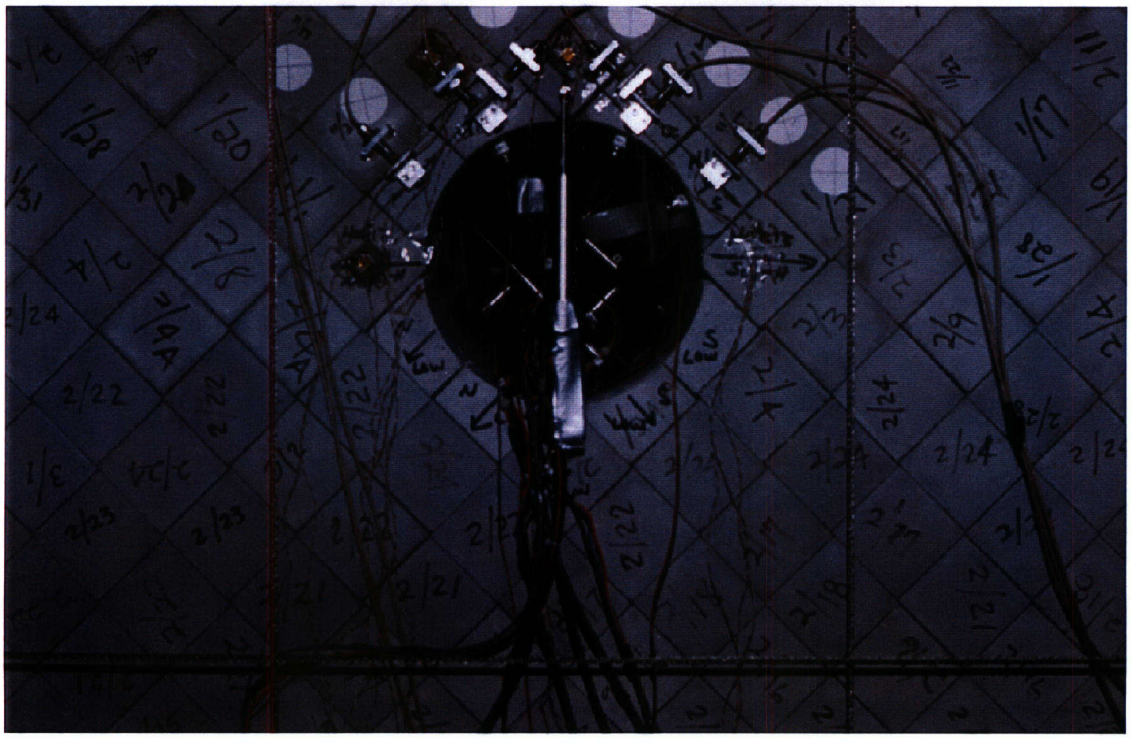

Figure 13-1. Near side tunnel following run 4, peak input 3.8 mm

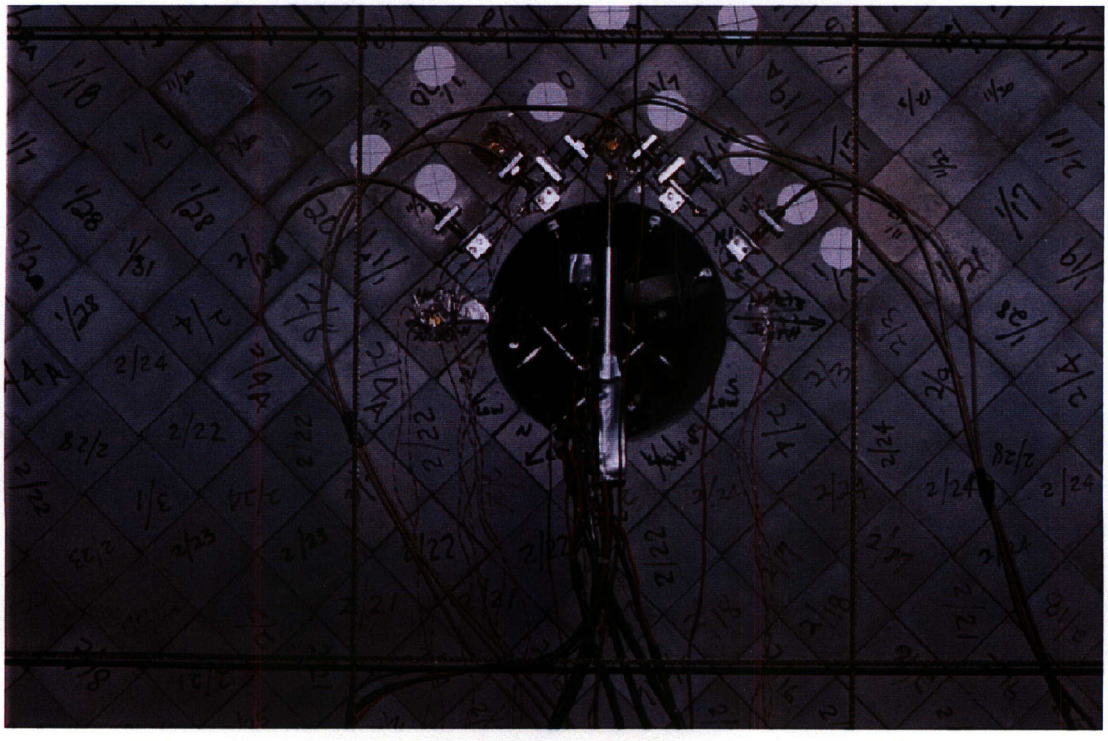

Figure 13-2. Near side tunnel following run 15, peak input 15.5 mm

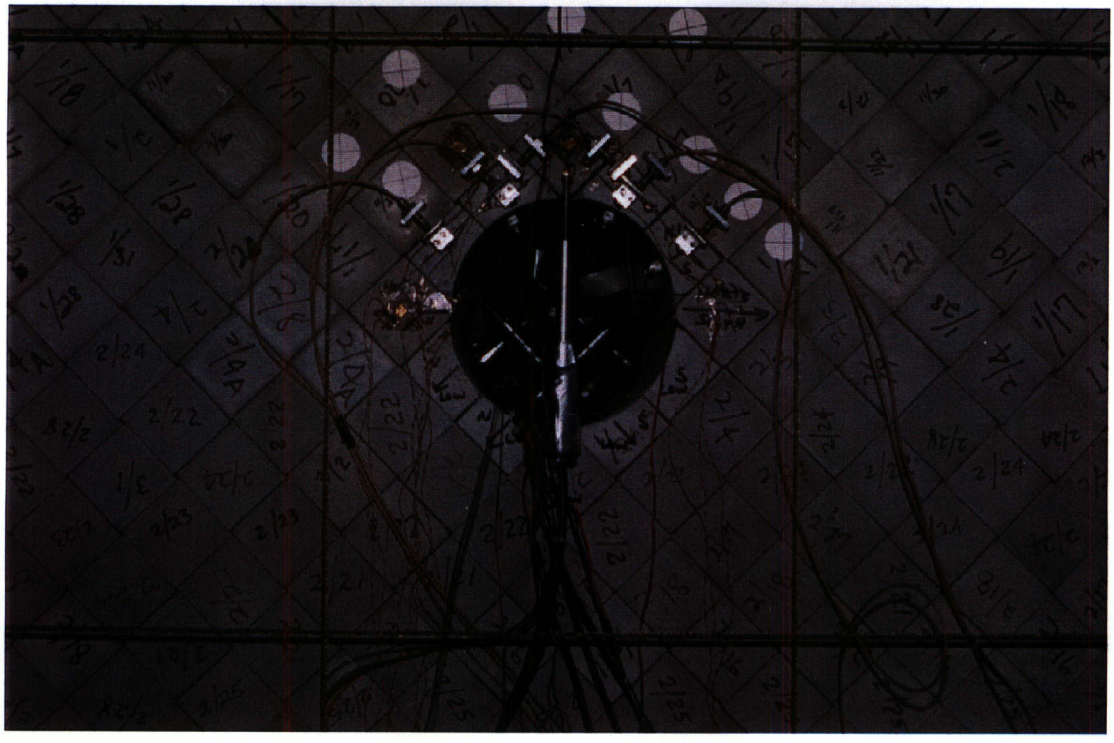

Figure 13-3. Near side tunnel following run 21, peak input 17.0 mm

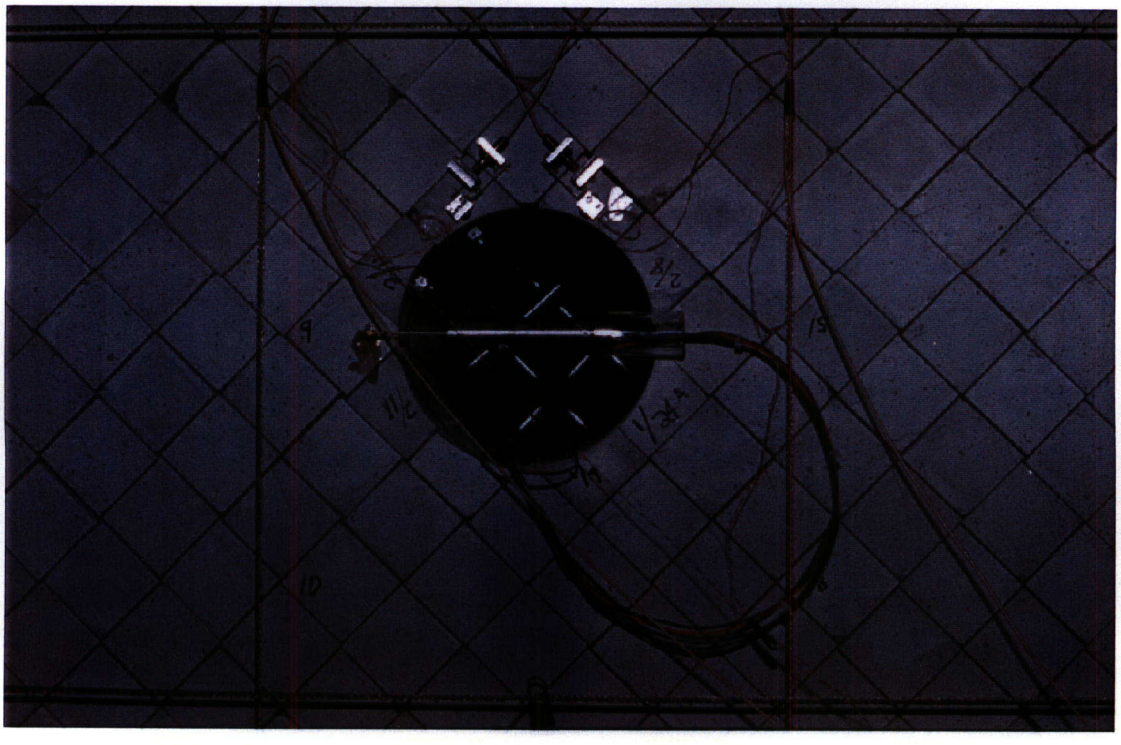

Figure 13-4. Far side tunnel following run 4, peak input 3.8 mm

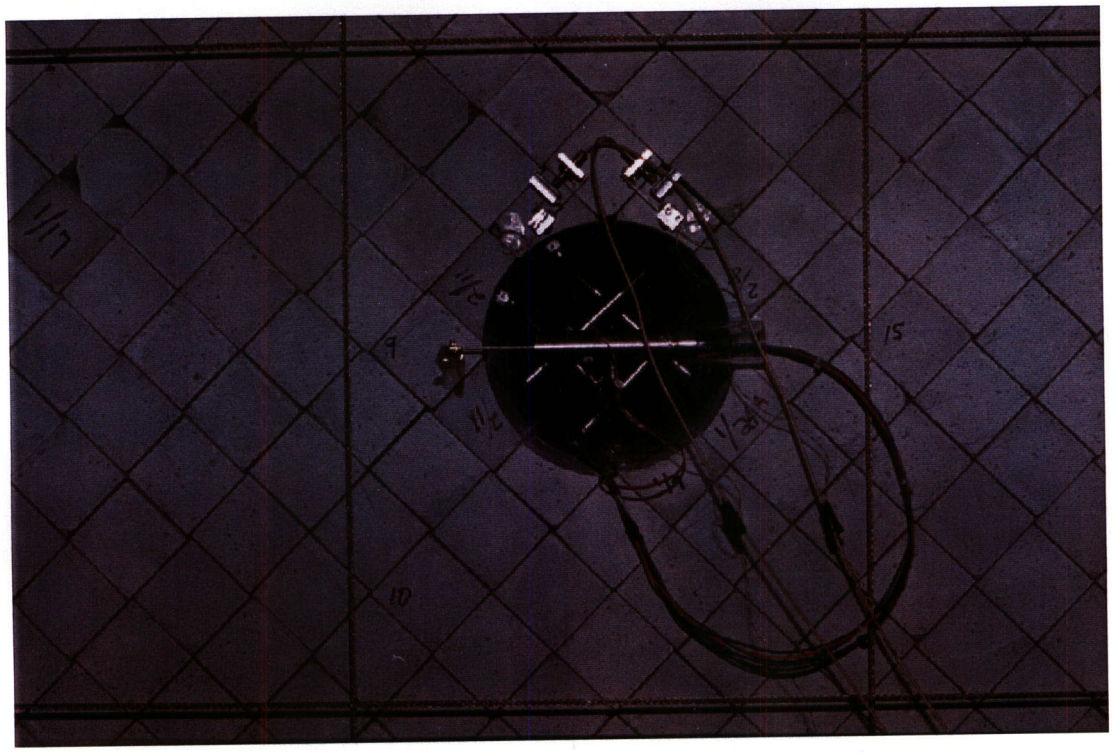

Figure 13-5. Far side tunnel following run 13, peak input 15.5 mm

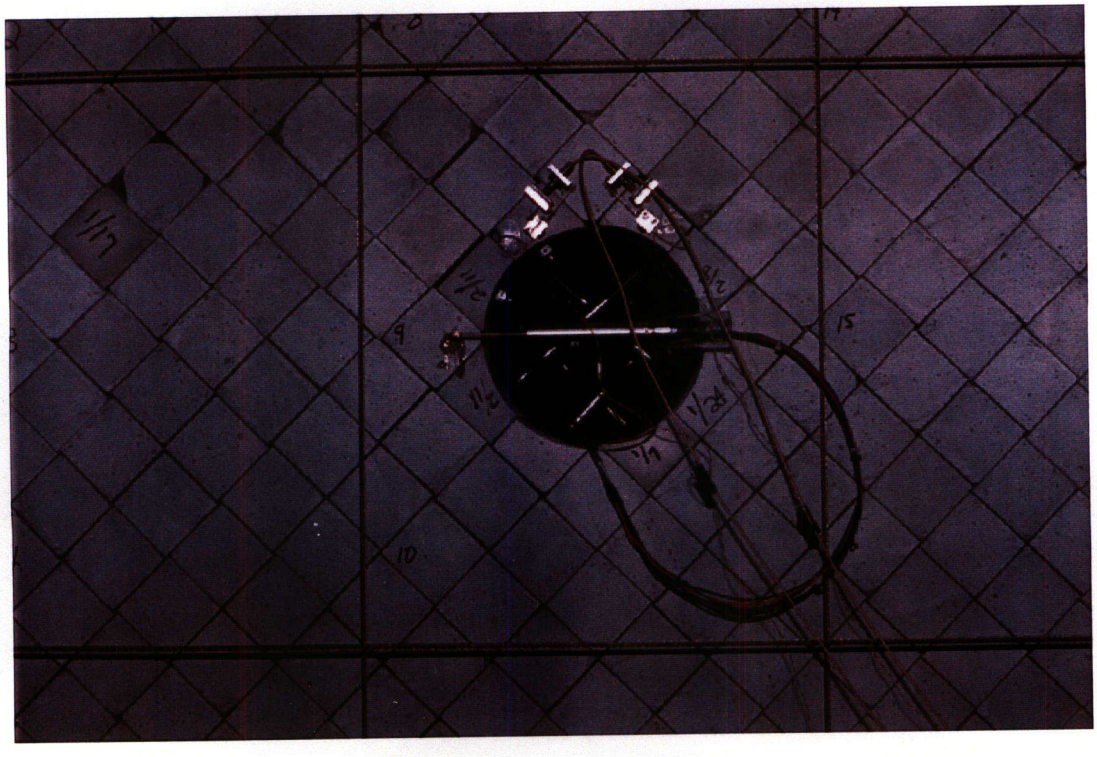

Figure 13-6. Far side tunnel following run 15, peak input 15.5 mm

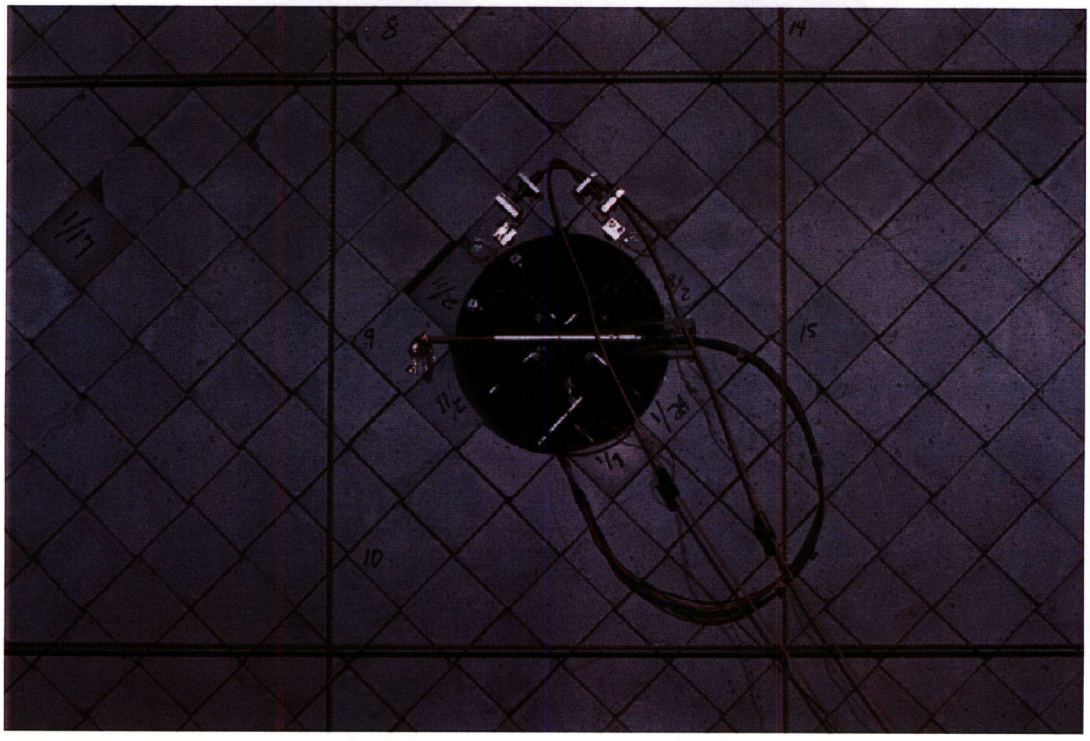

Figure 13-7. Far side tunnel following run 16, peak input 15.5 mm

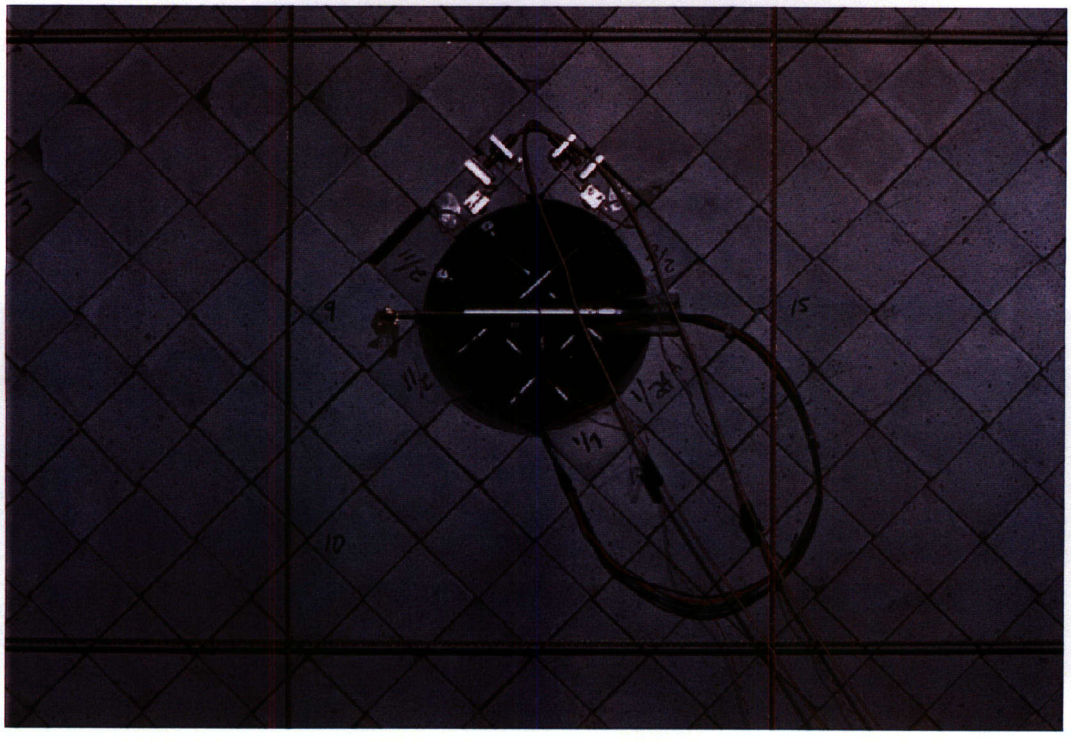

Figure 13-8. Far side tunnel following run 17, peak input 15.5 mm

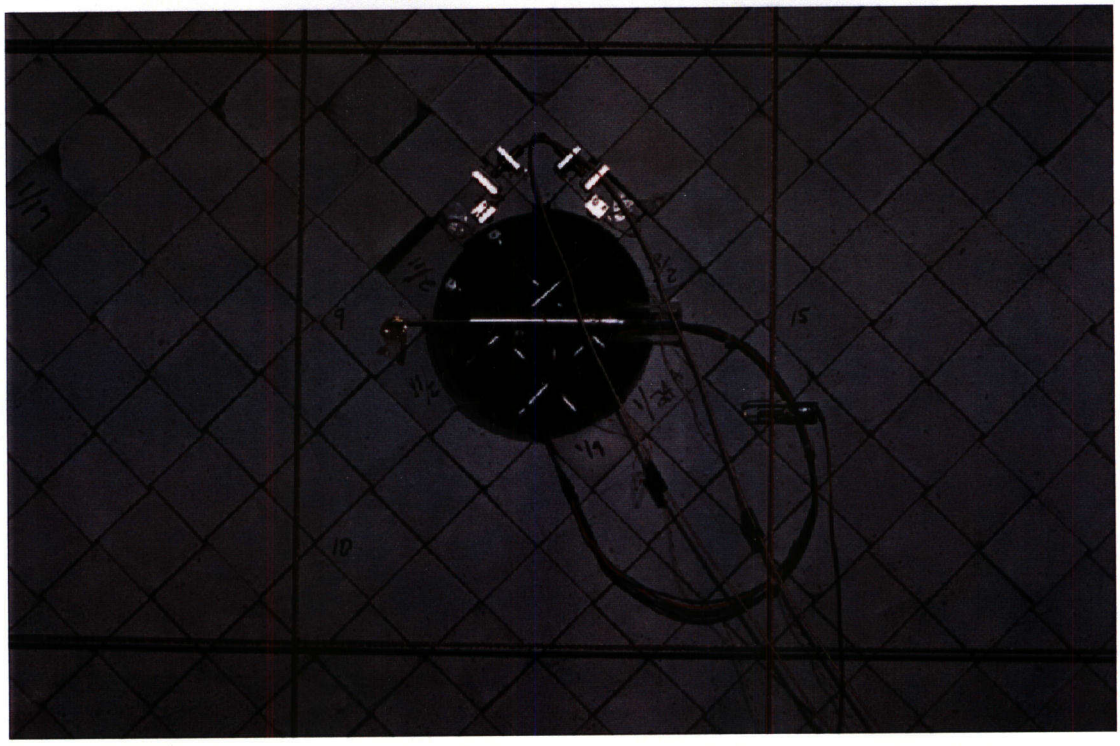

Figure 13-9. Far side tunnel following run 19, peak input 15.5 mm

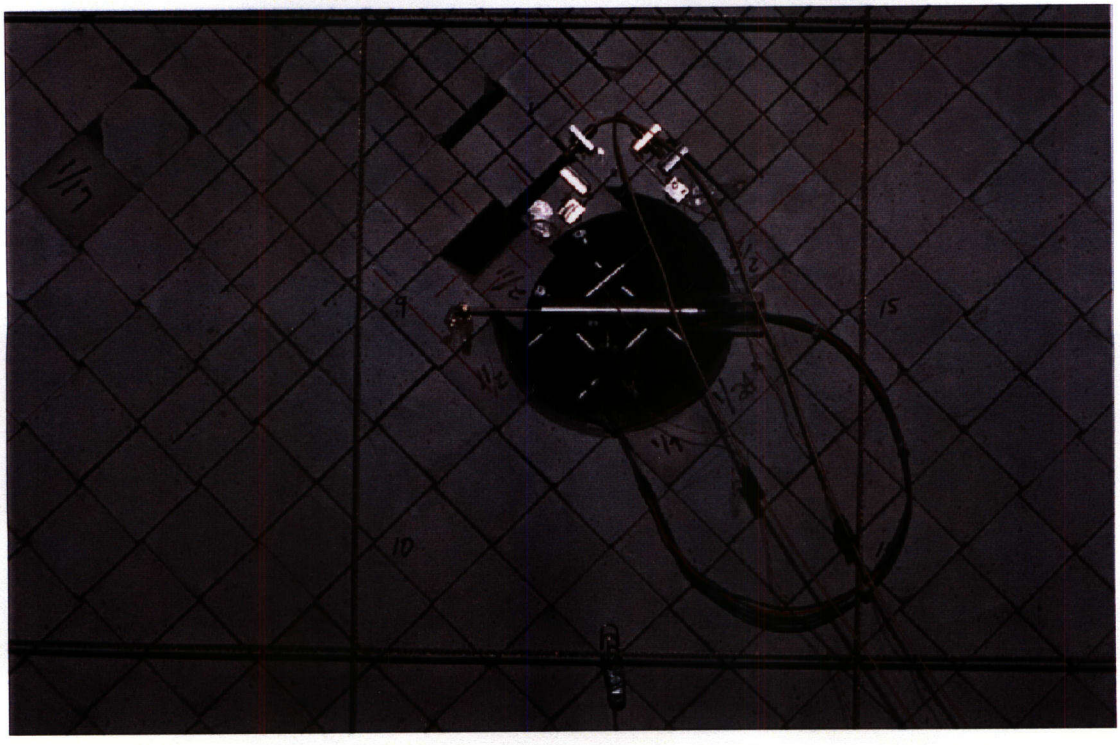

Figure 13-10. Far side tunnel following run 21, peak input 17.0 mm

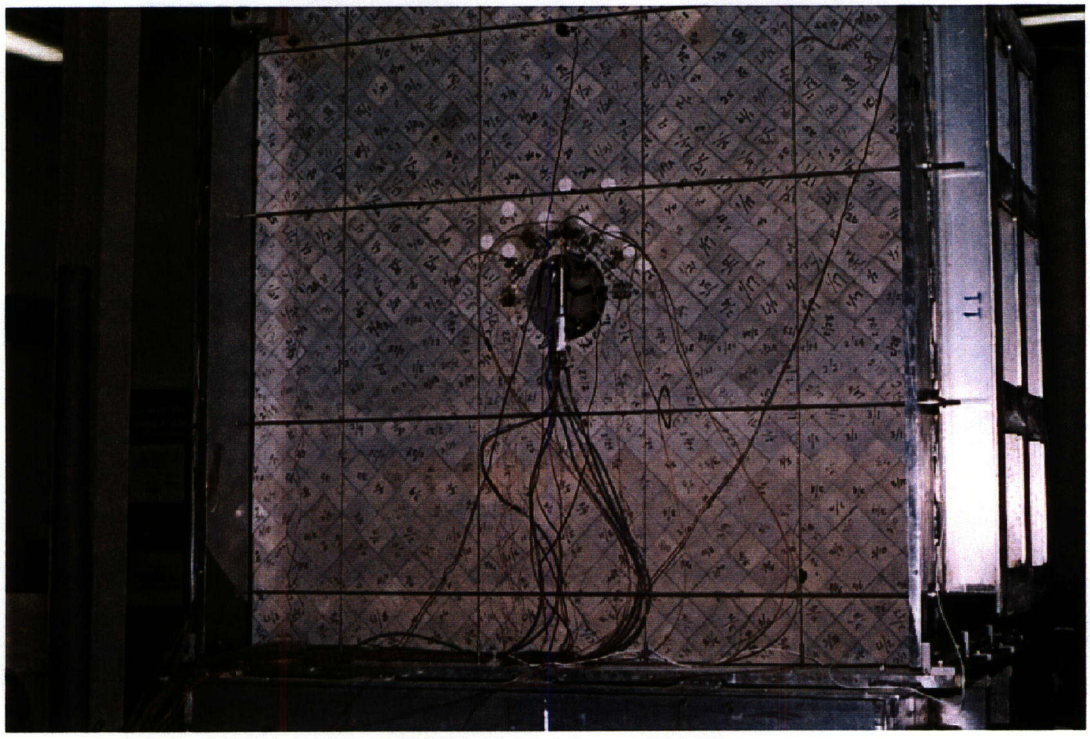

Figure 13-11. Overall scale model at conclusion of testing: near side

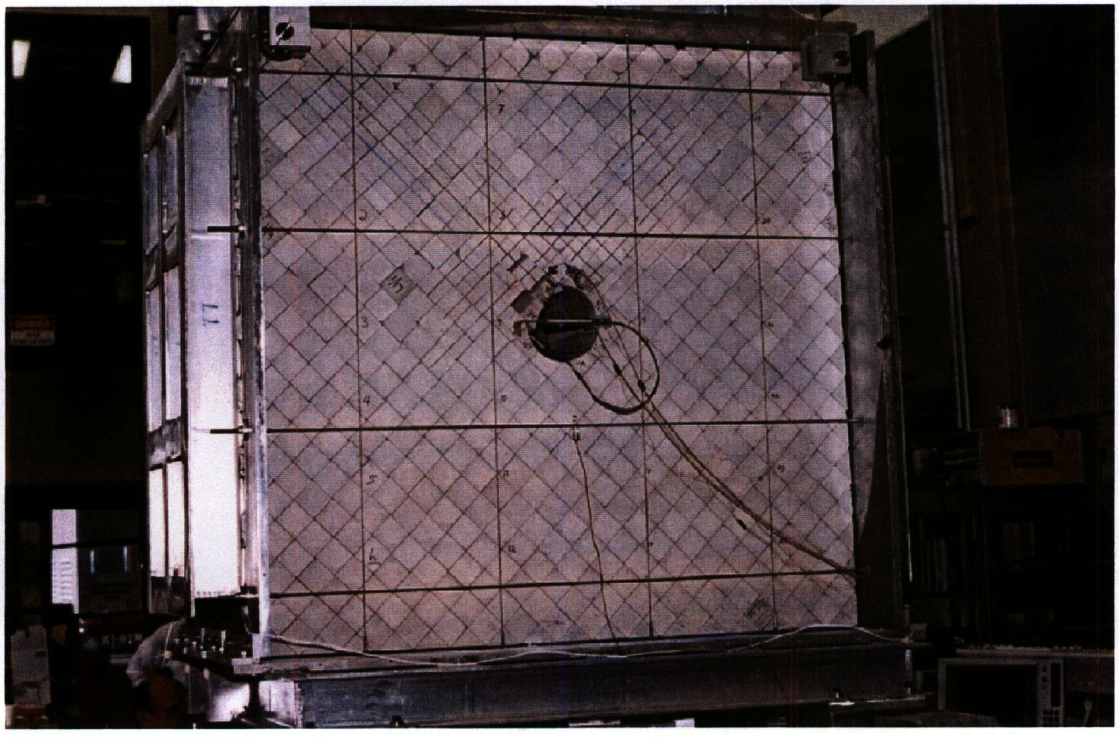

Figure 13-12. Overall scale model at conclusion of testing: far side

Figure 13-13. Upper right side of scale model near side following run 4

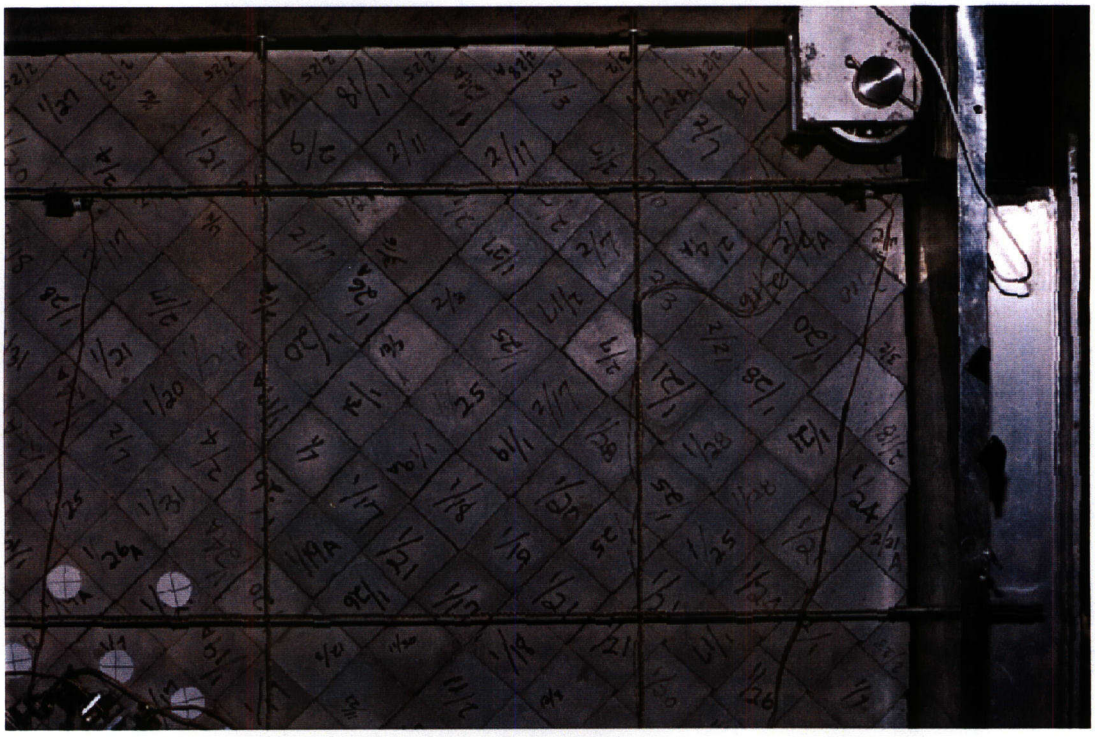

Figure 13-14. Upper right side of scale model near side following run 21

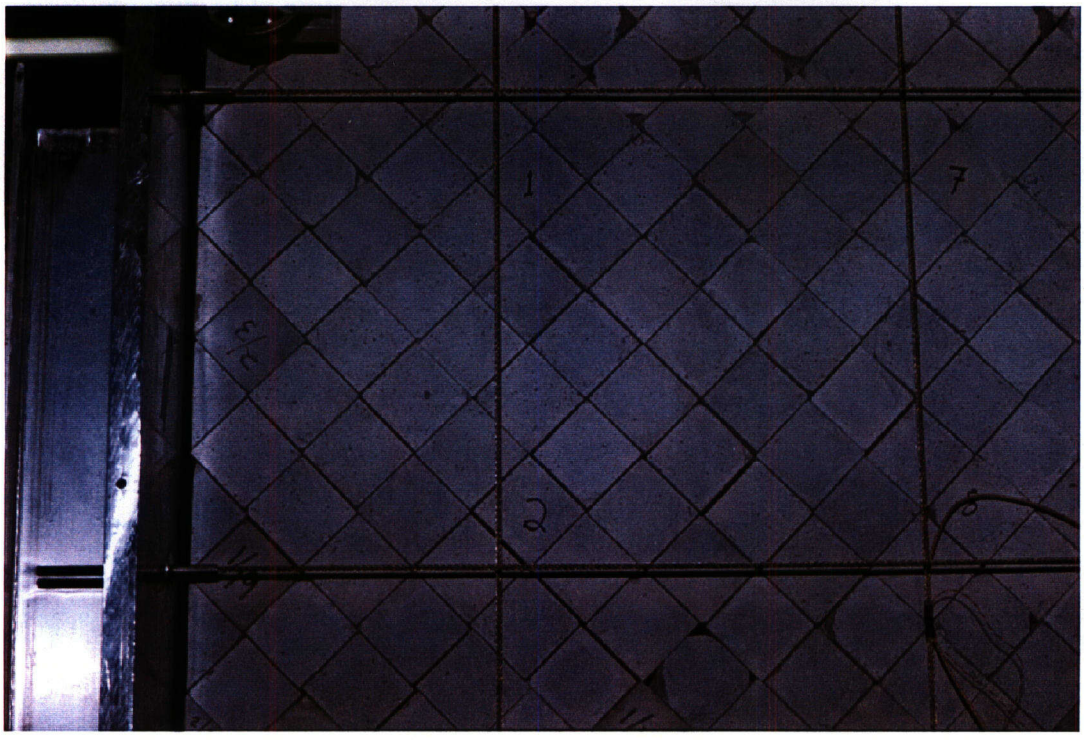

Figure 13-15. Upper right side of scale model far side following run 4

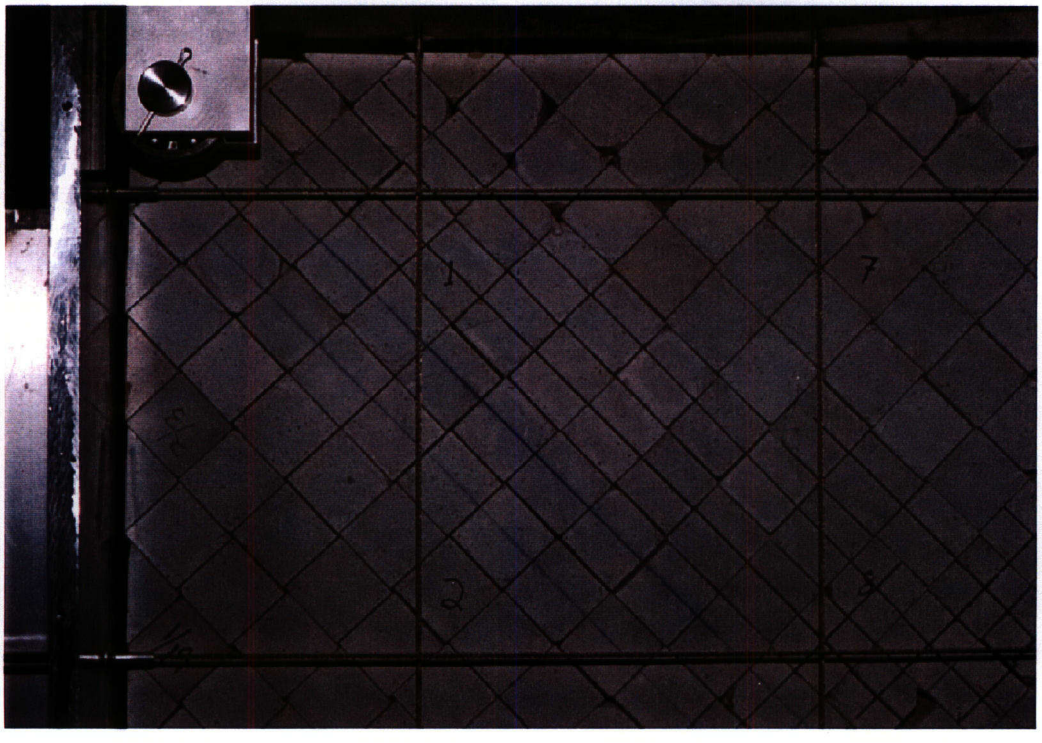

Figure 13-16. Upper right side of scale model far side following run 21

Table 13-17. Loose dust in tunnel following run 12

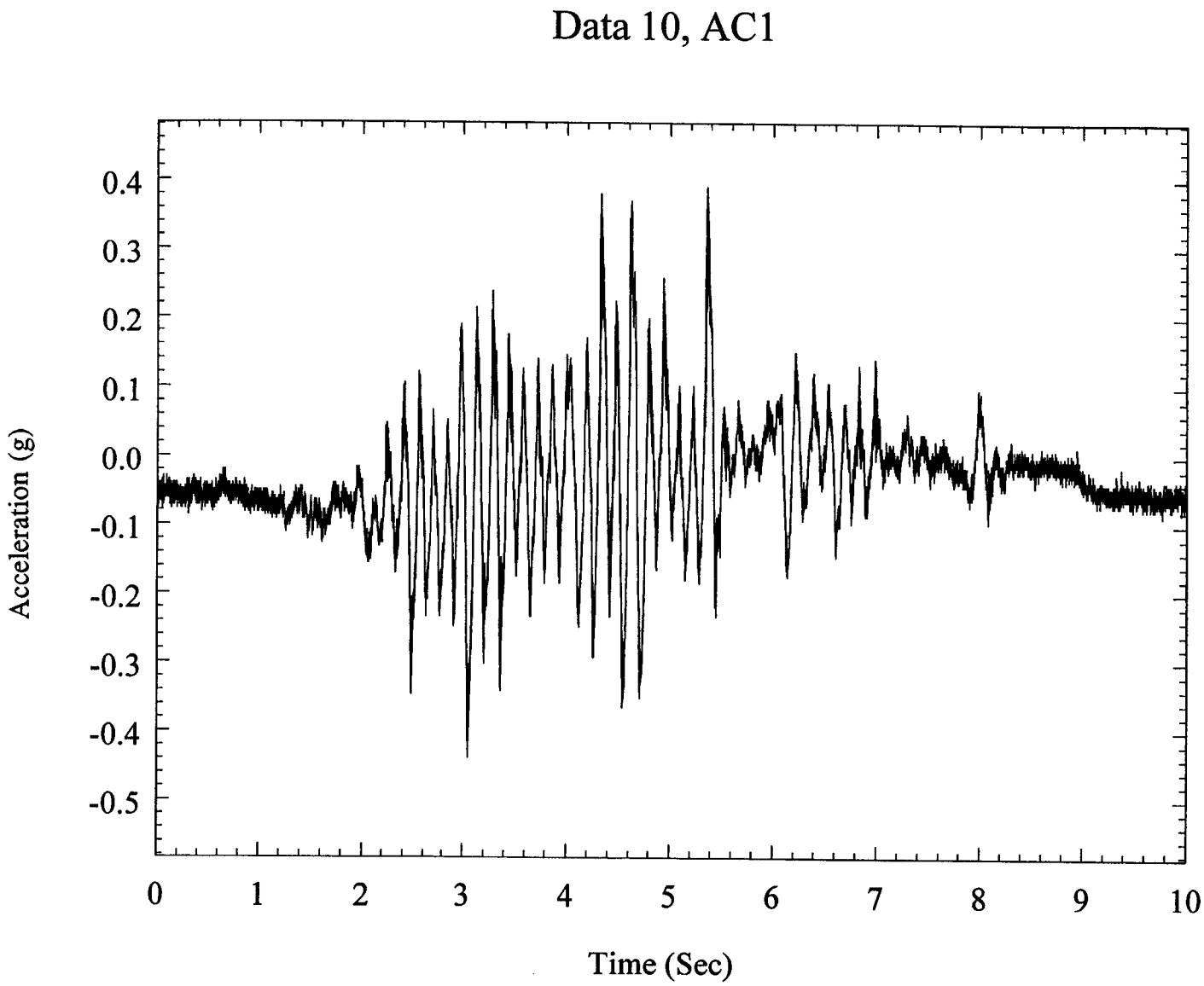

Figure 13-18a. Near side acceleration (AC1) on ingot I (tunnel side wall) for run 2

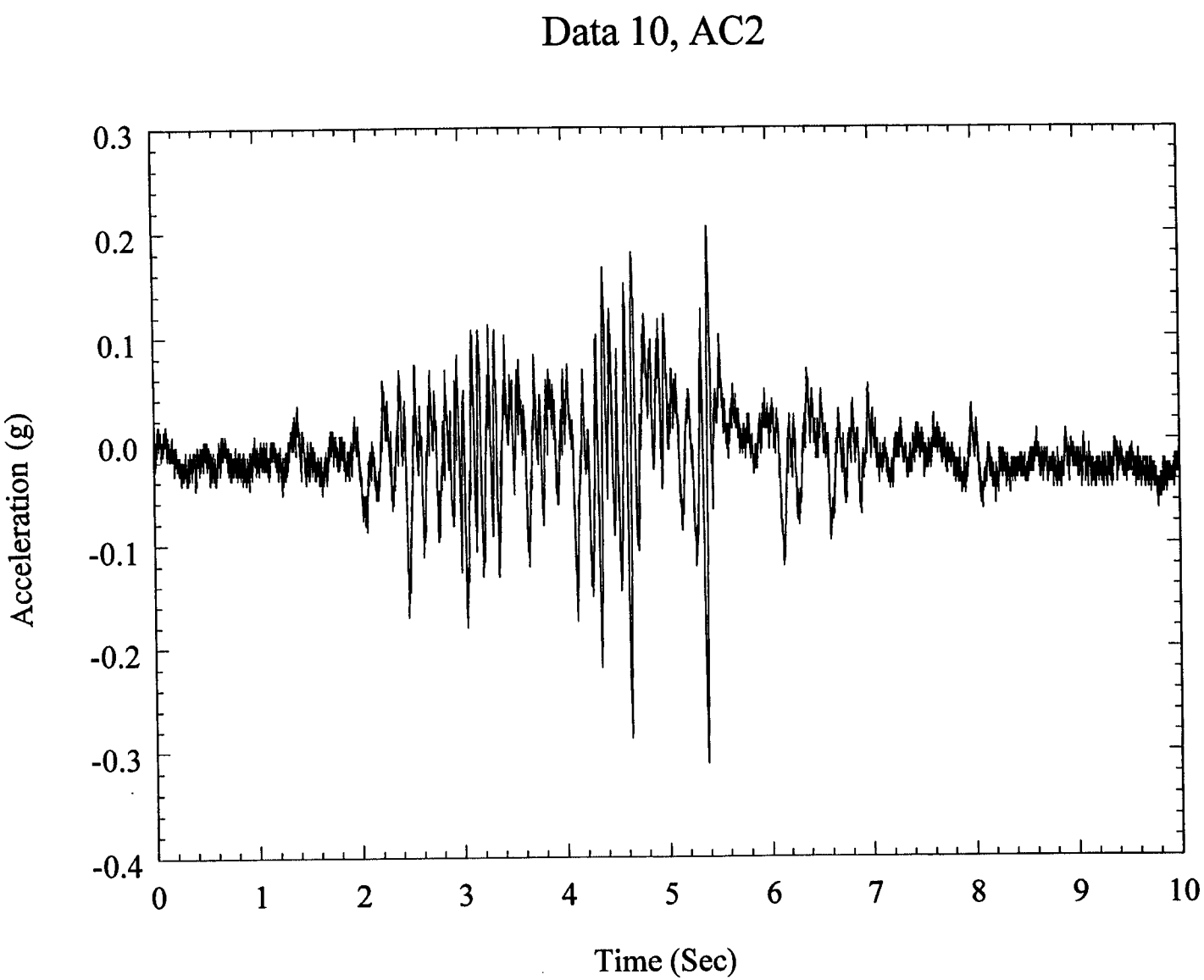

Figure 13-18b. Far side acceleration (AC2) on ingot I (tunnel side wall) for run 2

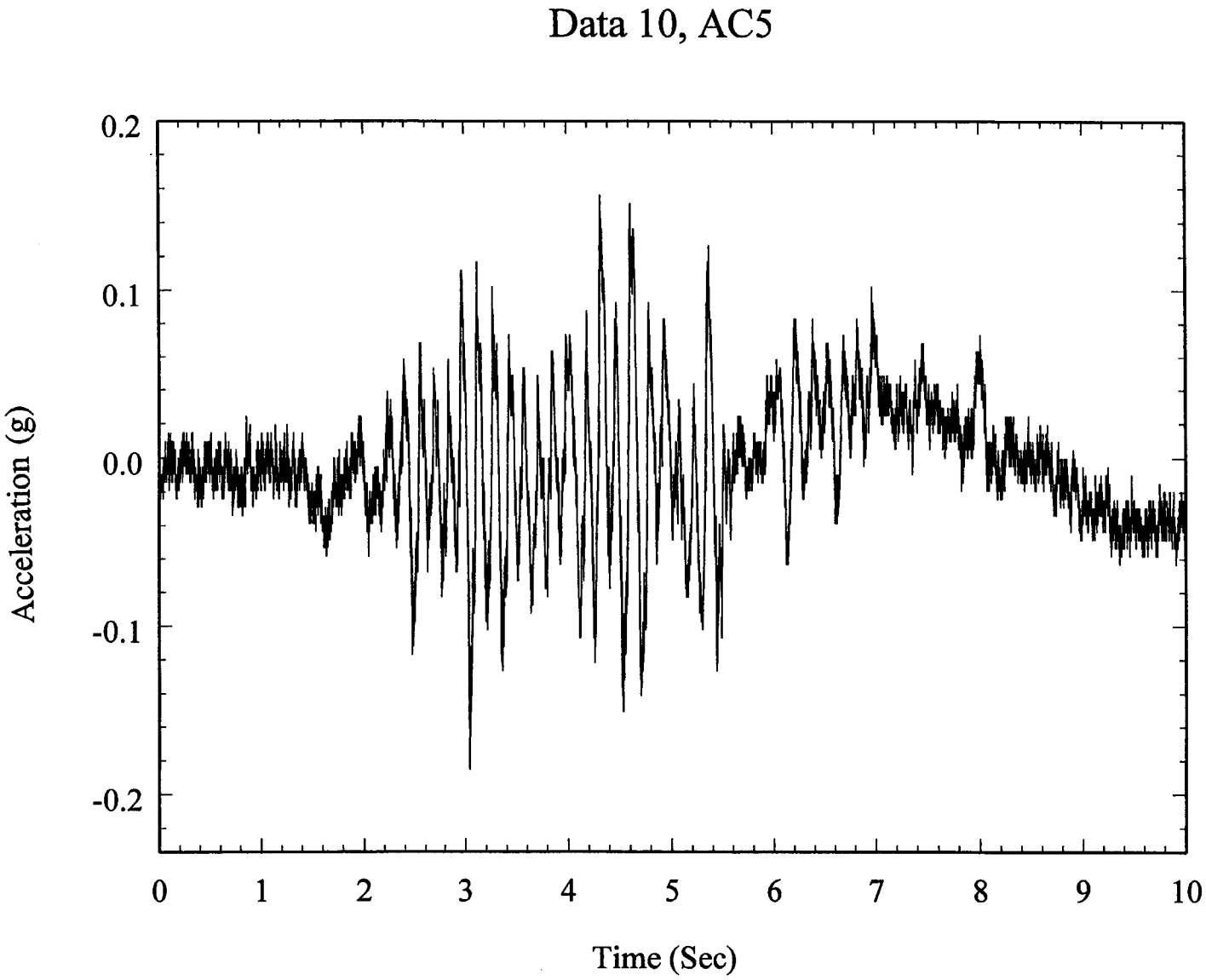

Figure 13-19a. Near side acceleration (AC5) on ingot G (tunnel side wall) for run 2

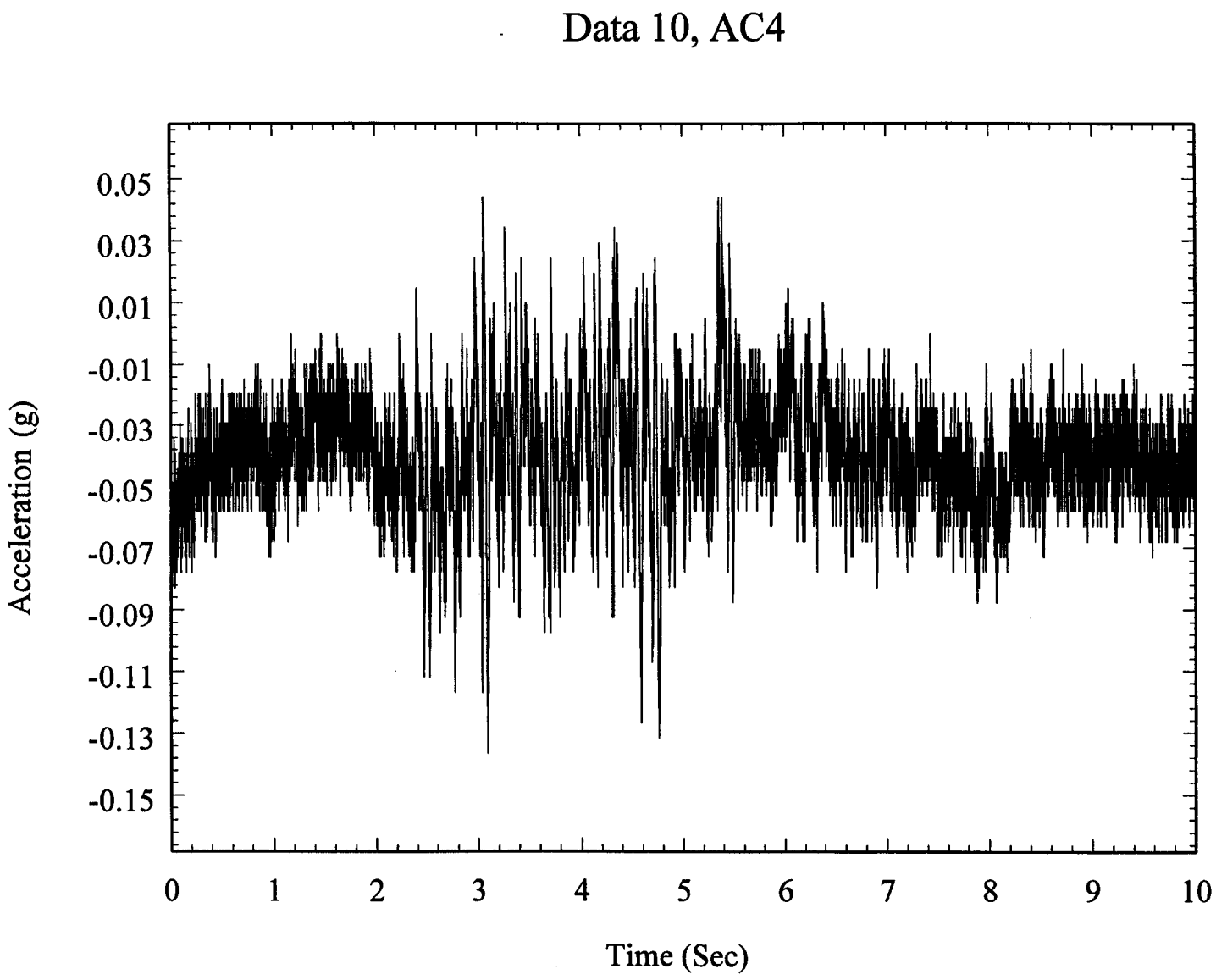

Figure 13-19b. Far side acceleration (AC4) on ingot G (tunnel side wall) for run 2

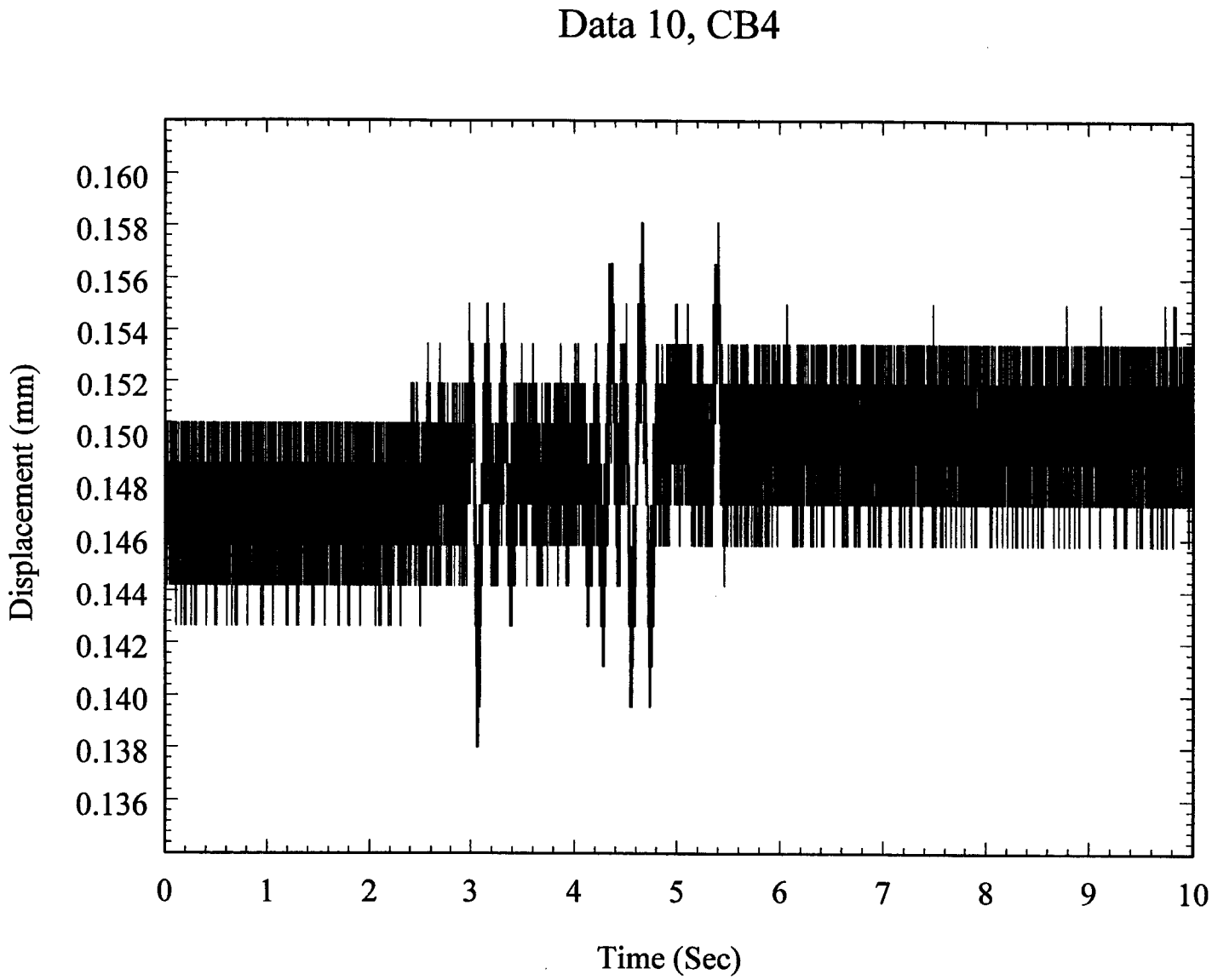

Figure 13-20a. Near side displacement (CB4) of ingot G (tunnel side wall) for run 2

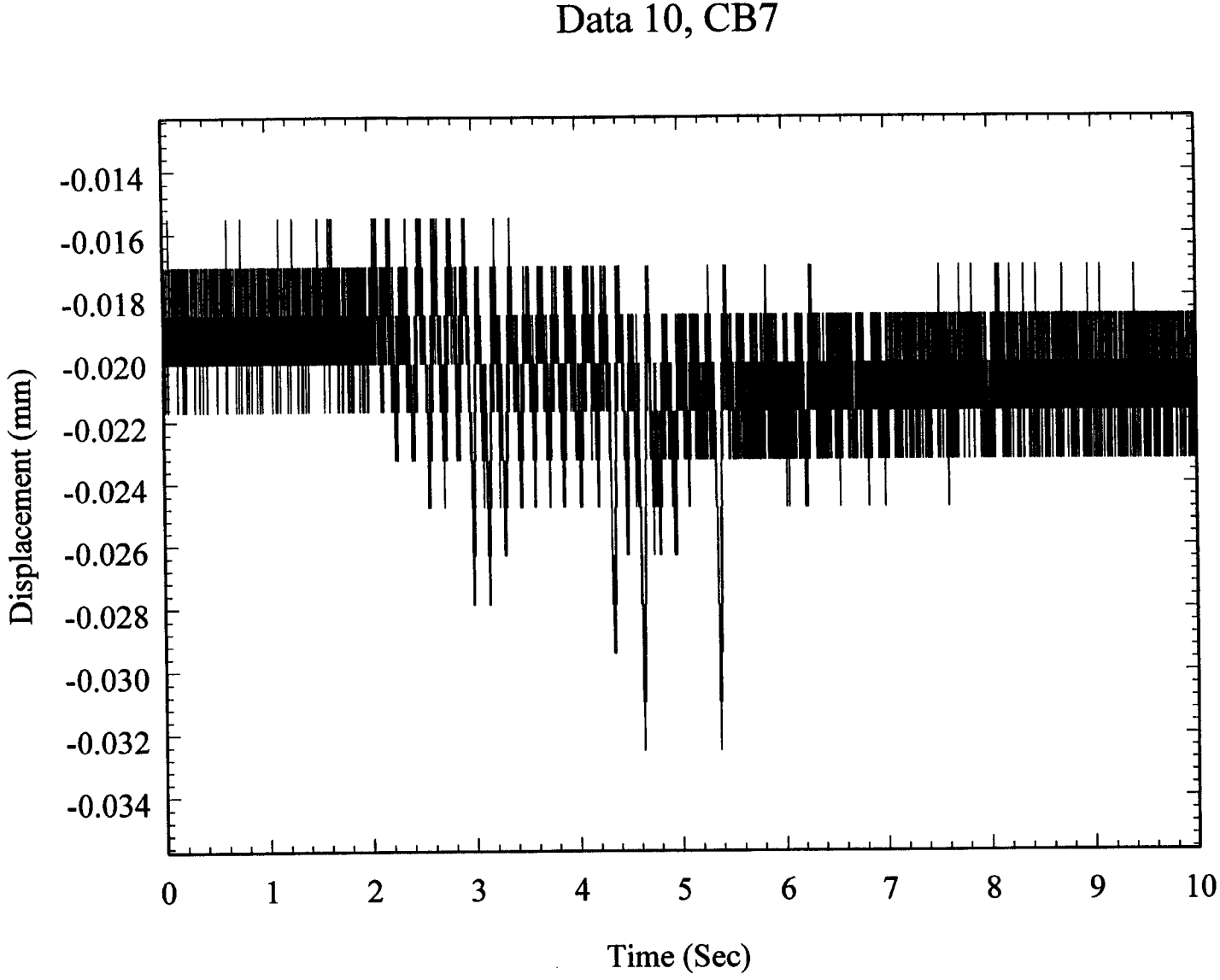

Figure 13-20b. Far side displacement (CB7) of ingot G (tunnel side wall) for run 2

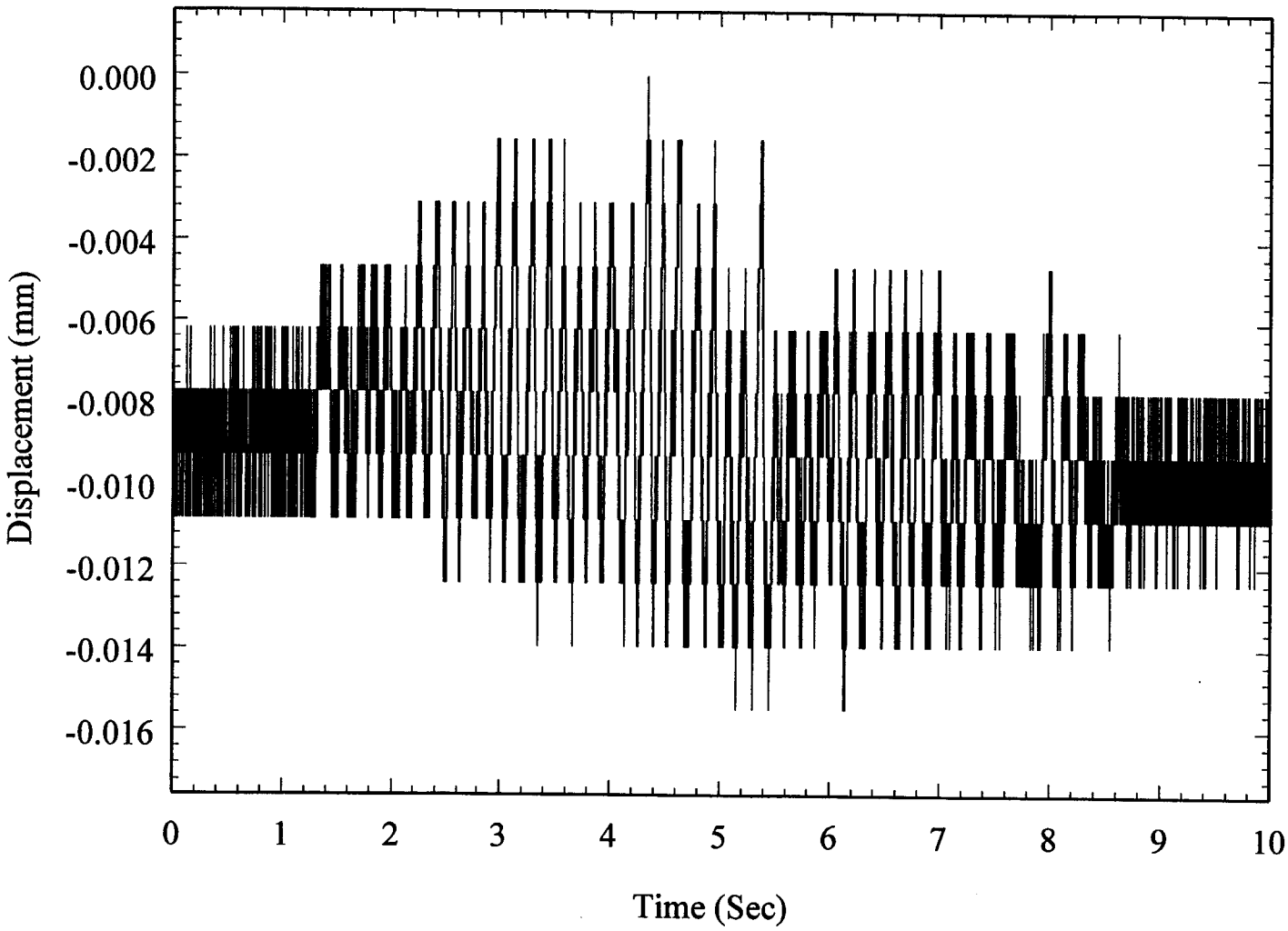

Figure 13-21a. Near side displacement (CB3) of ingot D (tunnel side wall) for run 2

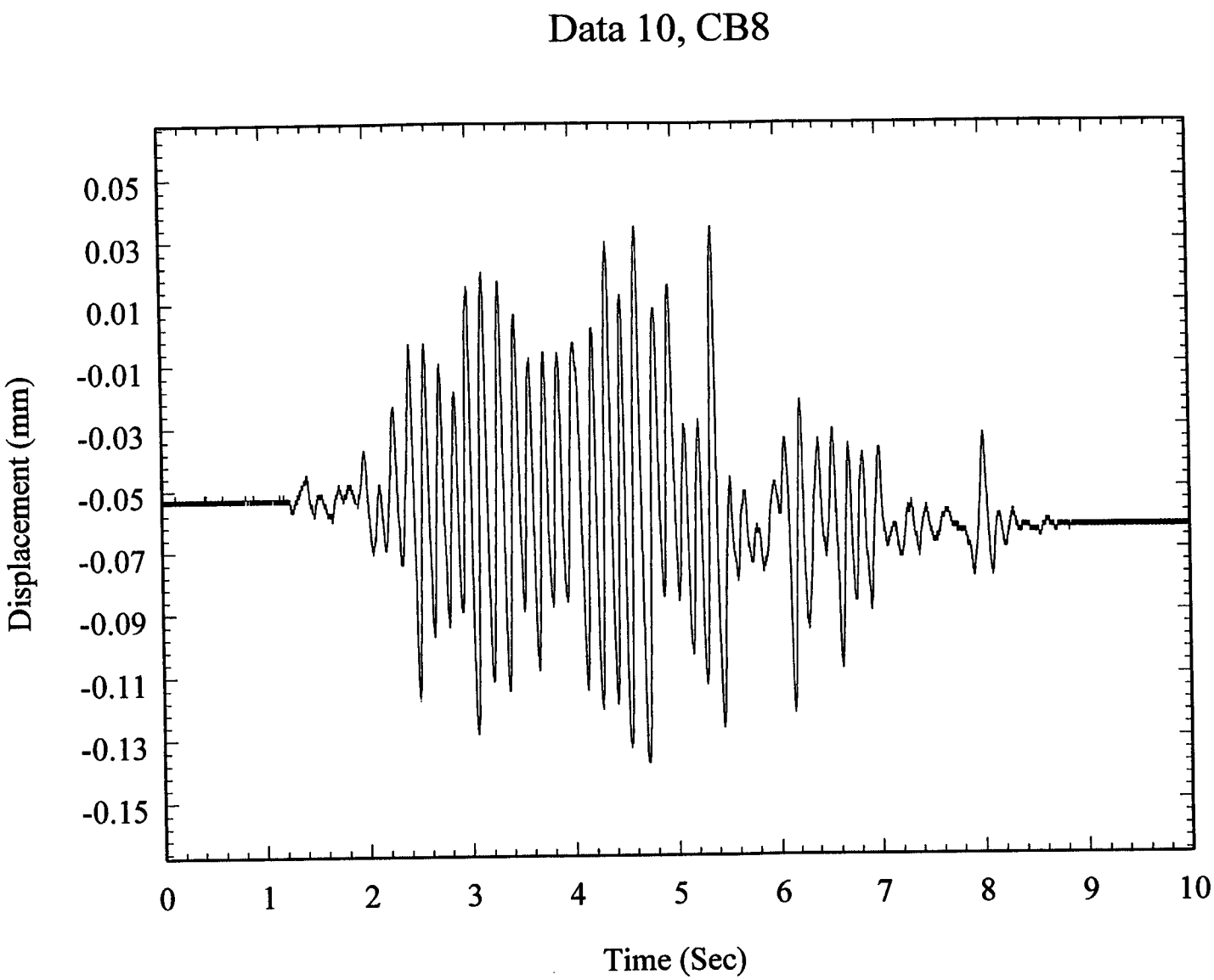

Figure 13-21b. Far side displacement (CB8) of ingot D (tunnel side wall) for run 2

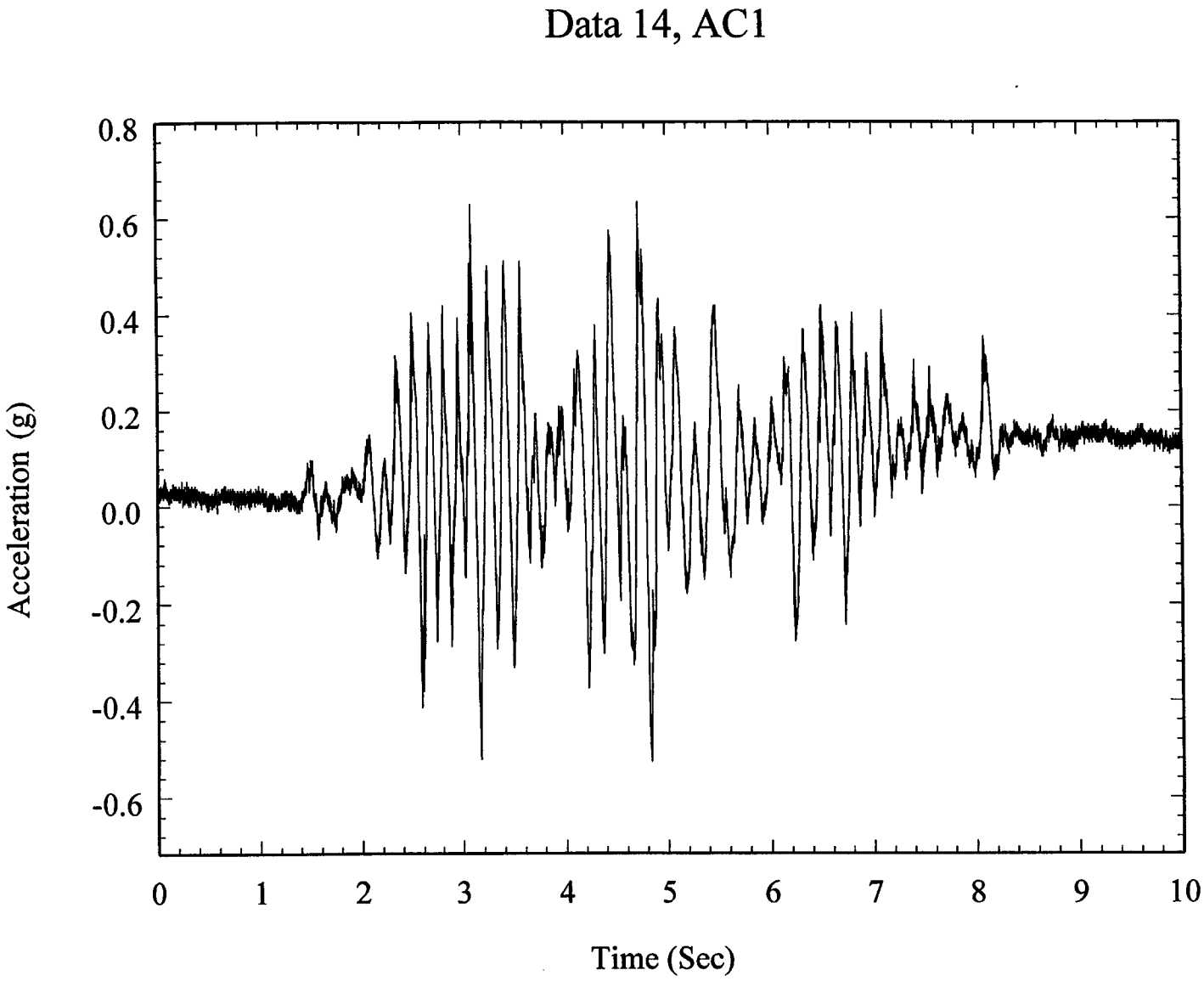

Figure 13-22a. Near side acceleration (AC1) on ingot I (tunnel side wall) for run 5

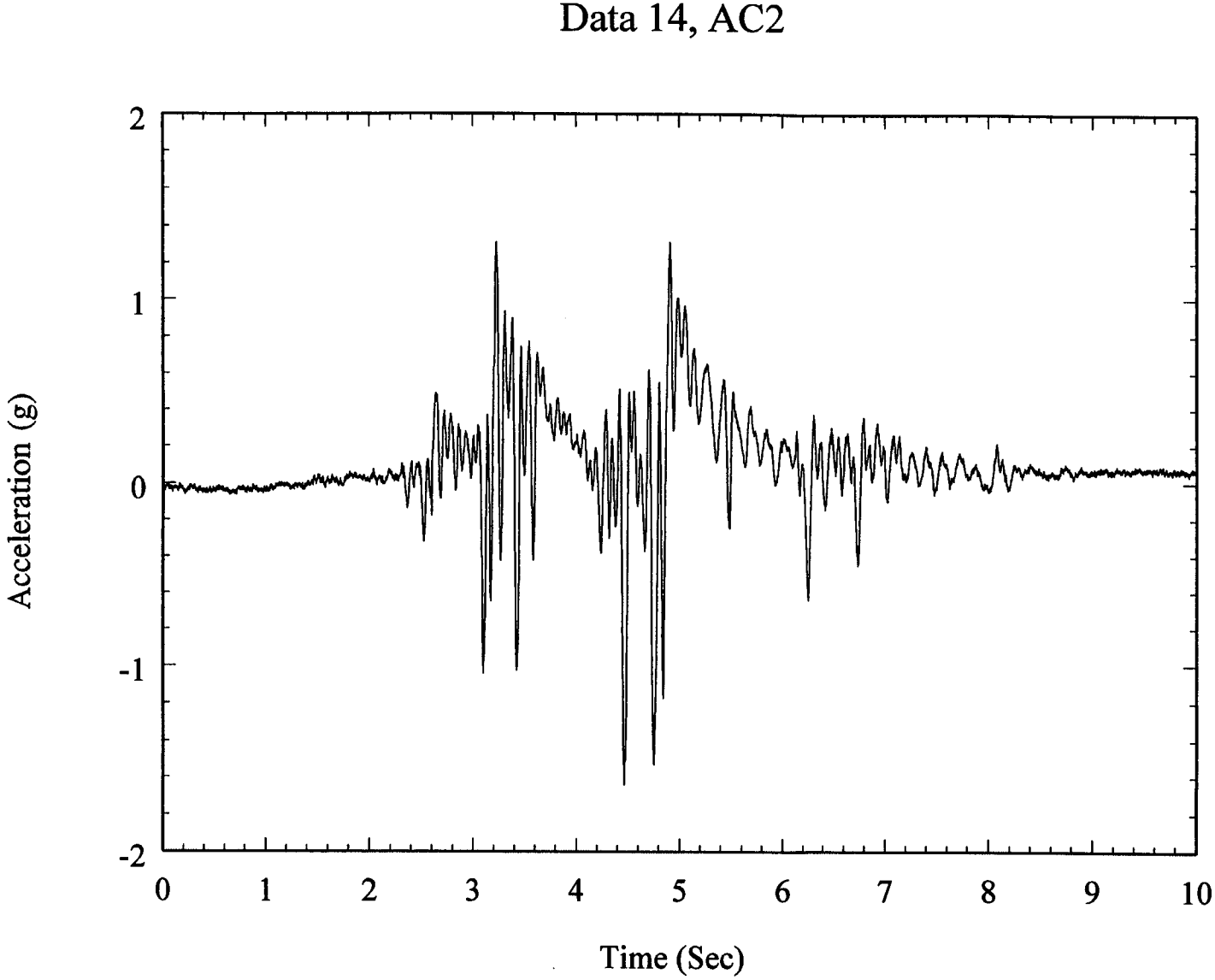

Figure 13-22b. Far side acceleration (AC2) on ingot I (tunnel side wall) for run 5

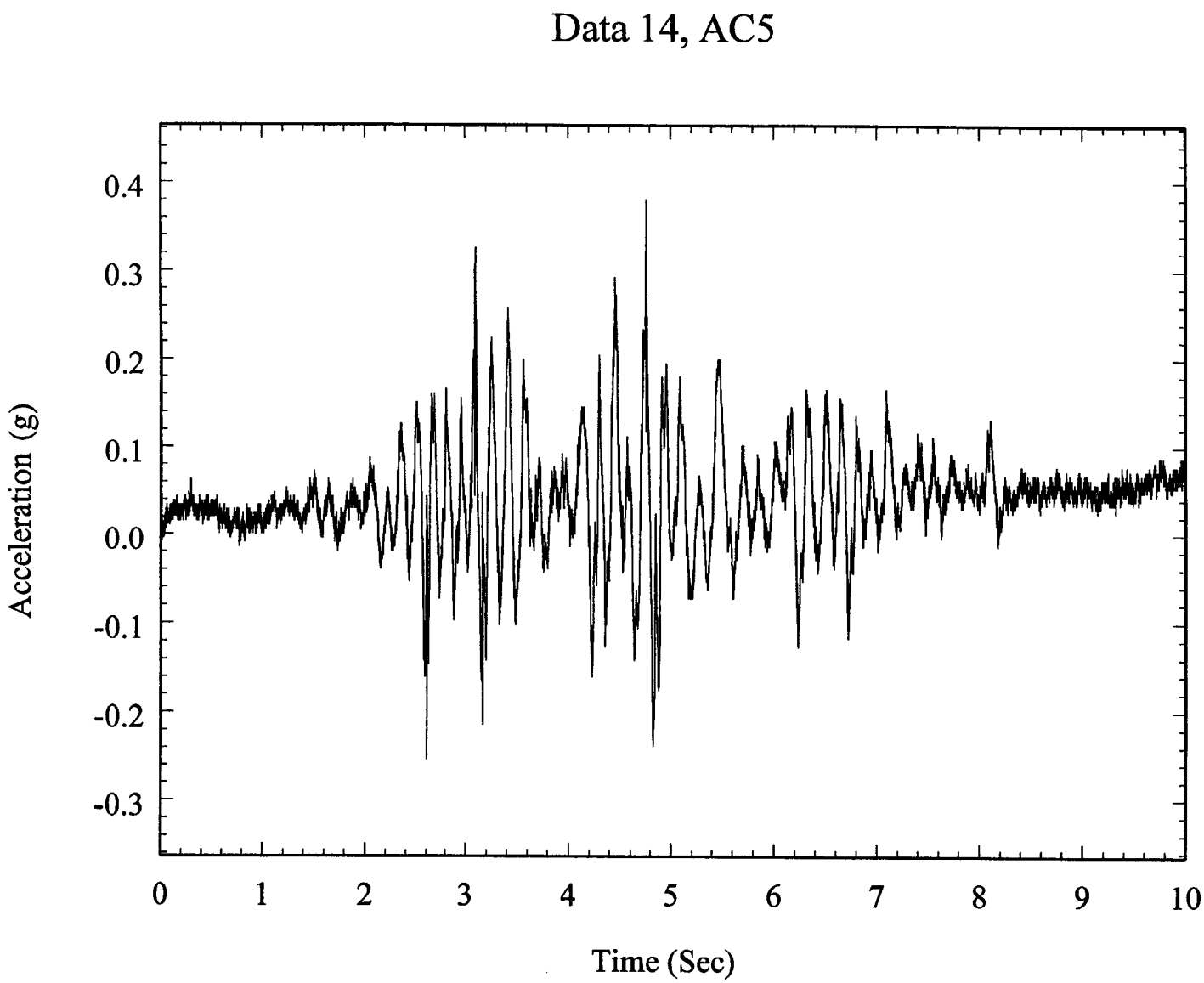

Figure 13-23a. Near side acceleration (AC5) on ingot G (tunnel side wall) for run 5

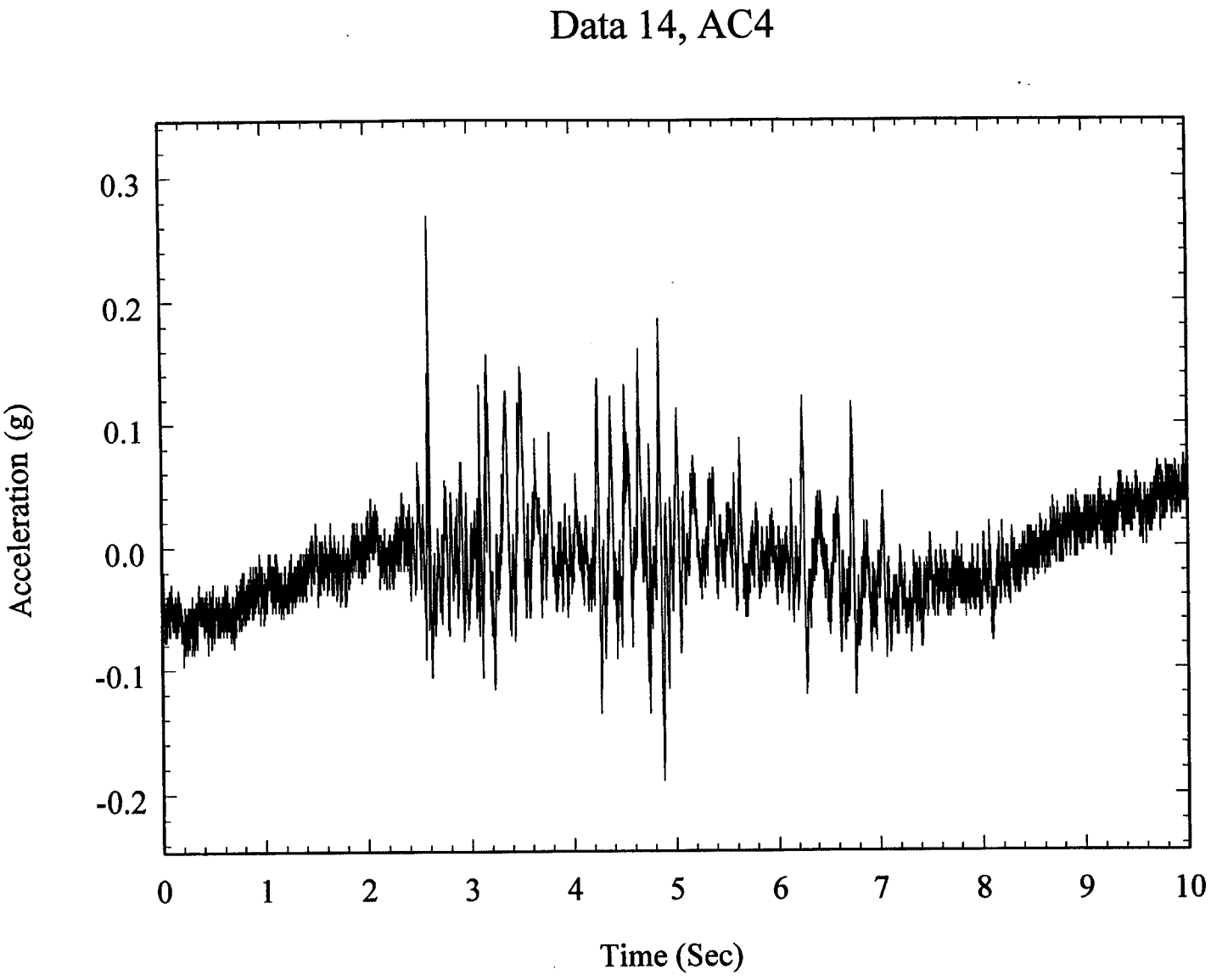

Figure 13-23b. Far side acceleration (AC4) on ingot G (tunnel side wall) for run 5

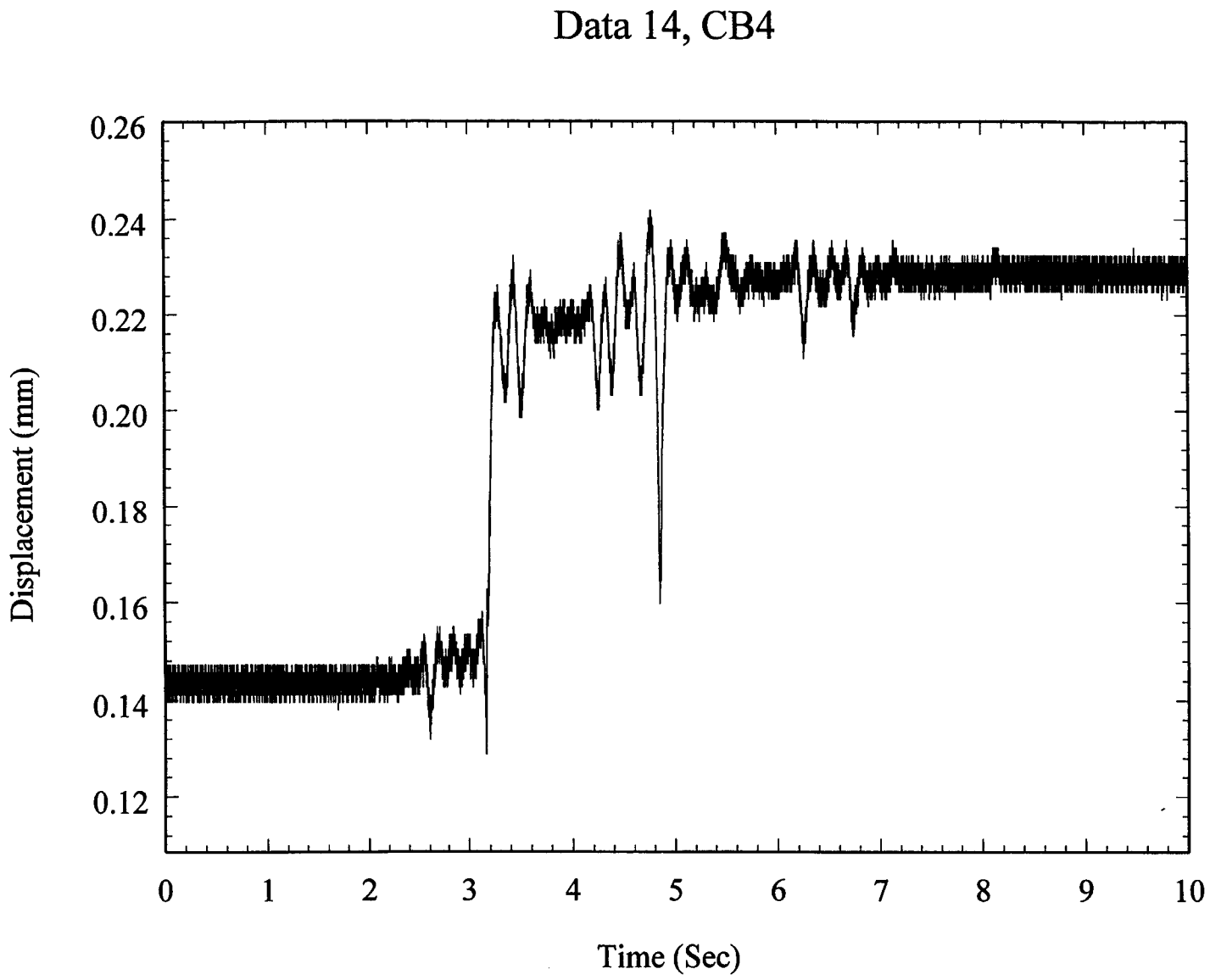

Figure 13-24a. Near side displacement (CB4) of ingot G (tunnel side wall) for run 5

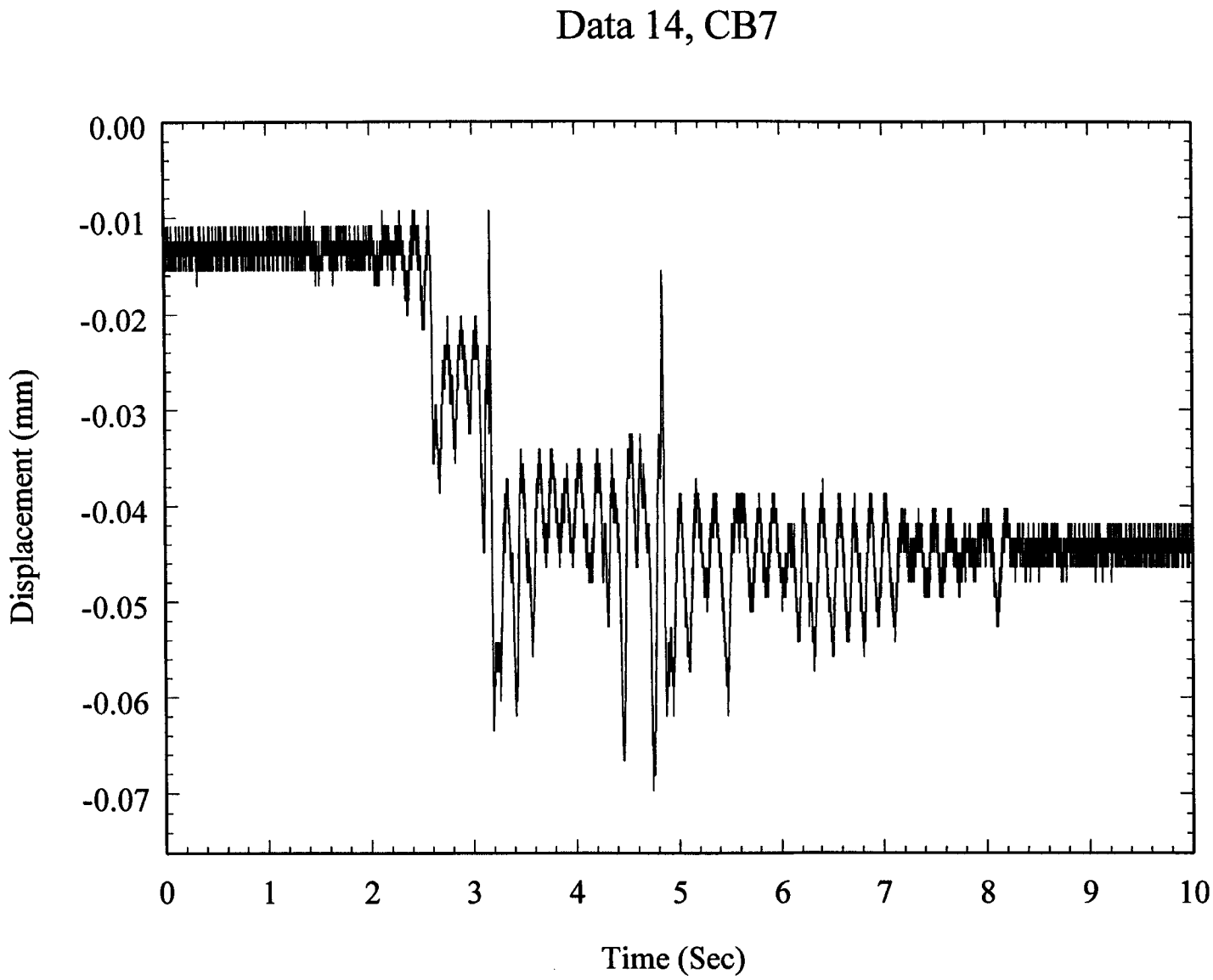

Figure 13-24b. Far side displacement (CB7) of ingot G (tunnel side wall) for run 5

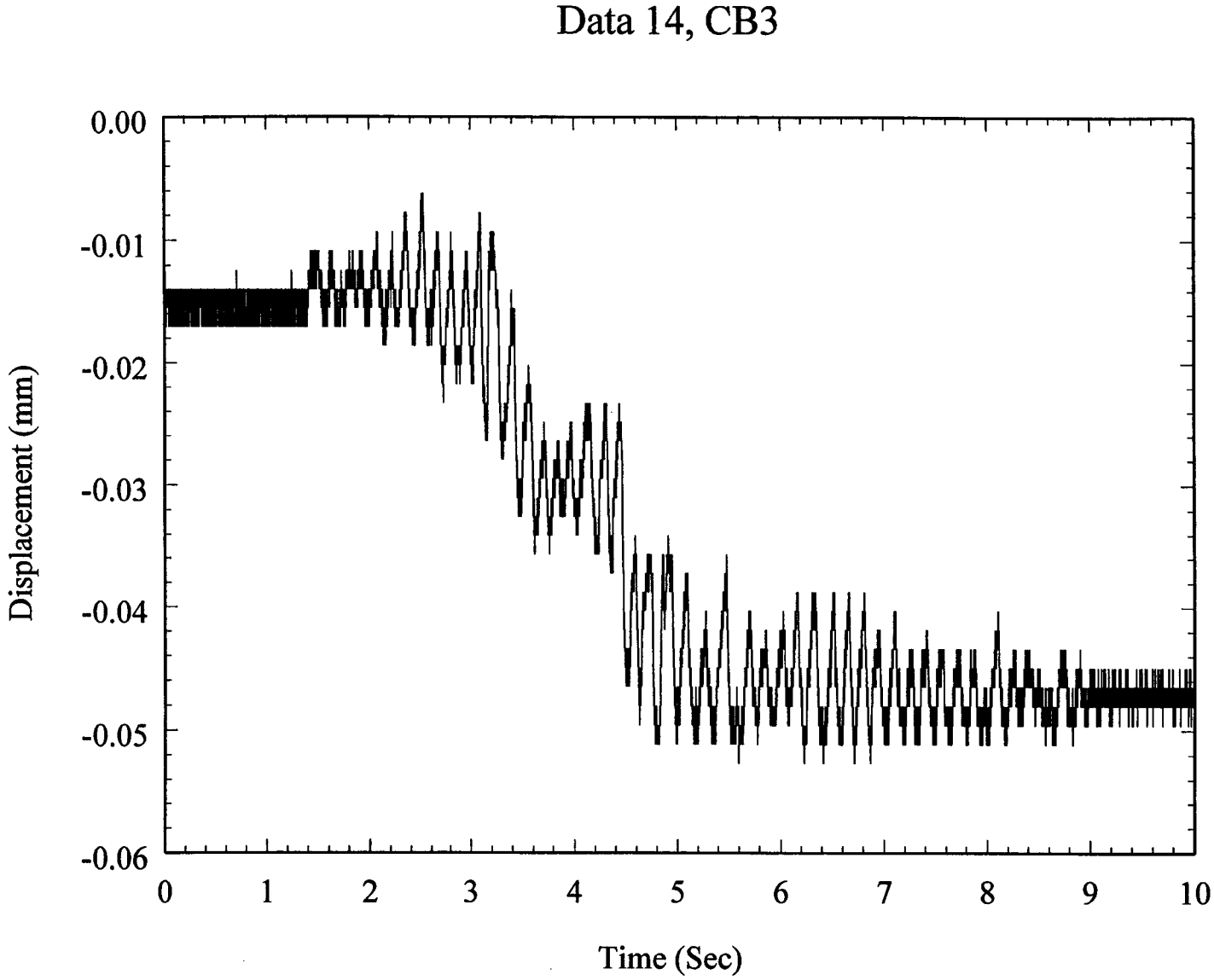

Figure 13-25a. Near side displacement (CB3) of ingot D (tunnel side wall) for run 5

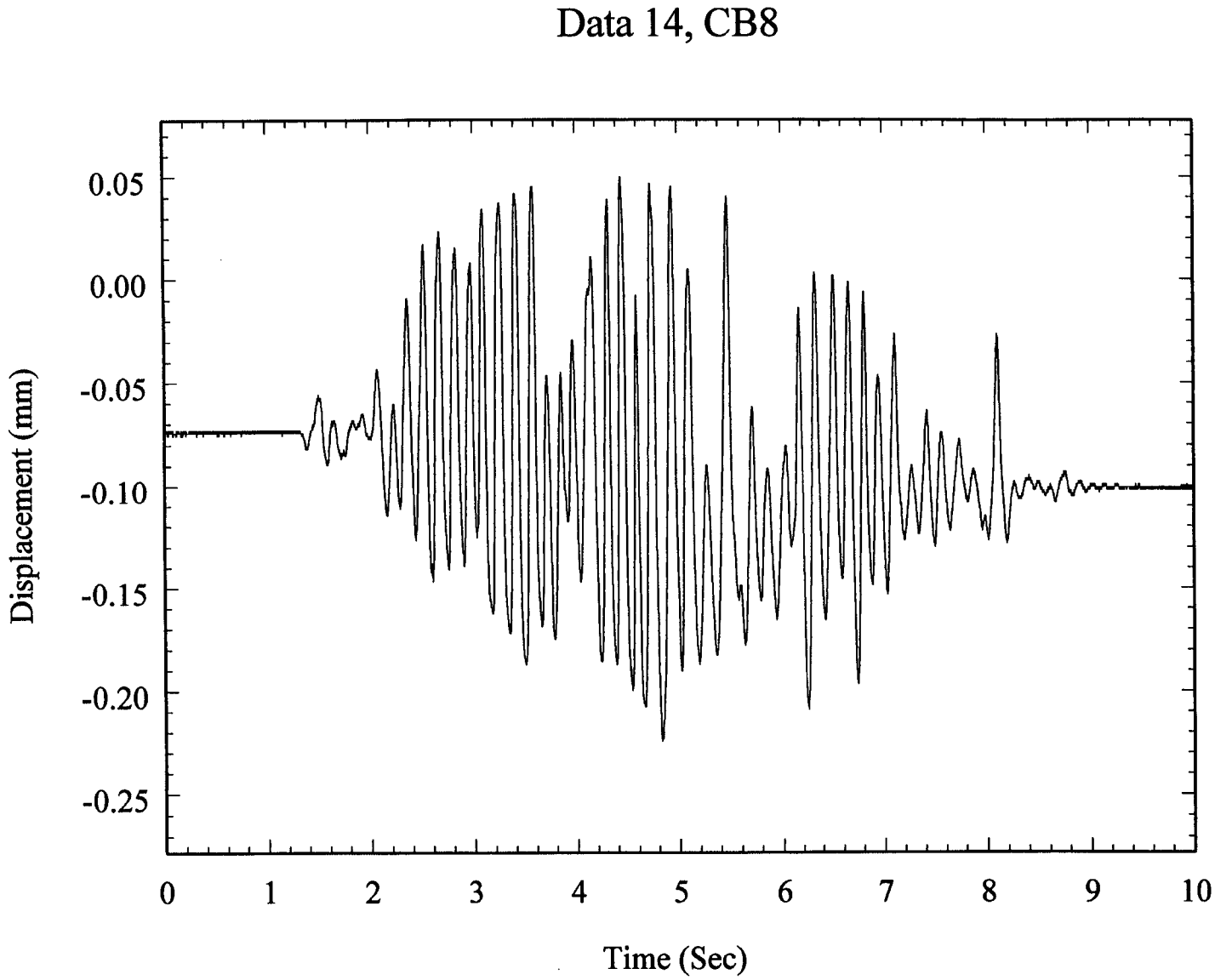

Figure 13-25b. Far side displacement (CB8) of ingot D (tunnel side wall) for run 5

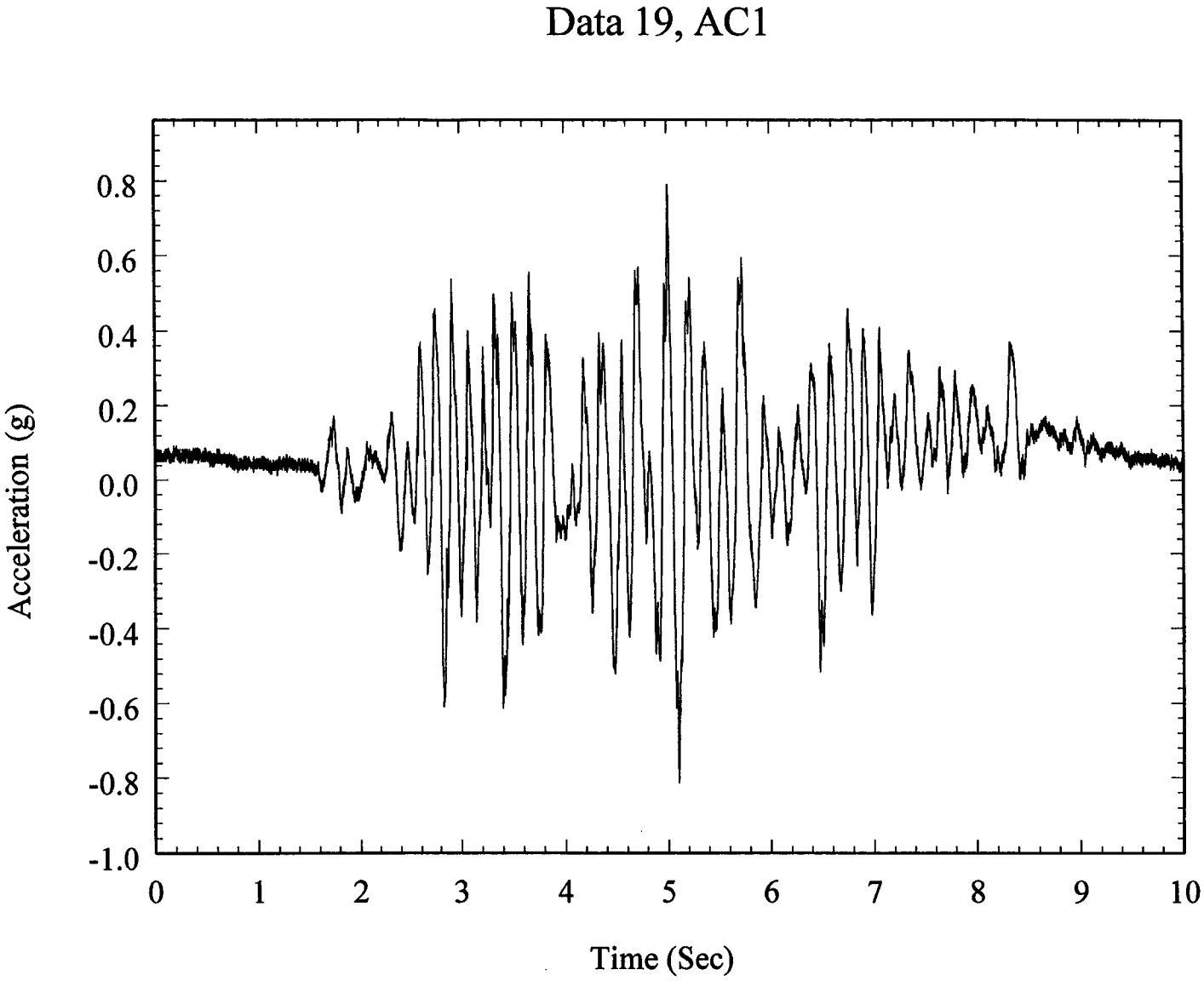

Figure 13-26a. Near side acceleration (AC1) on ingot I (tunnel side wall) for run 9

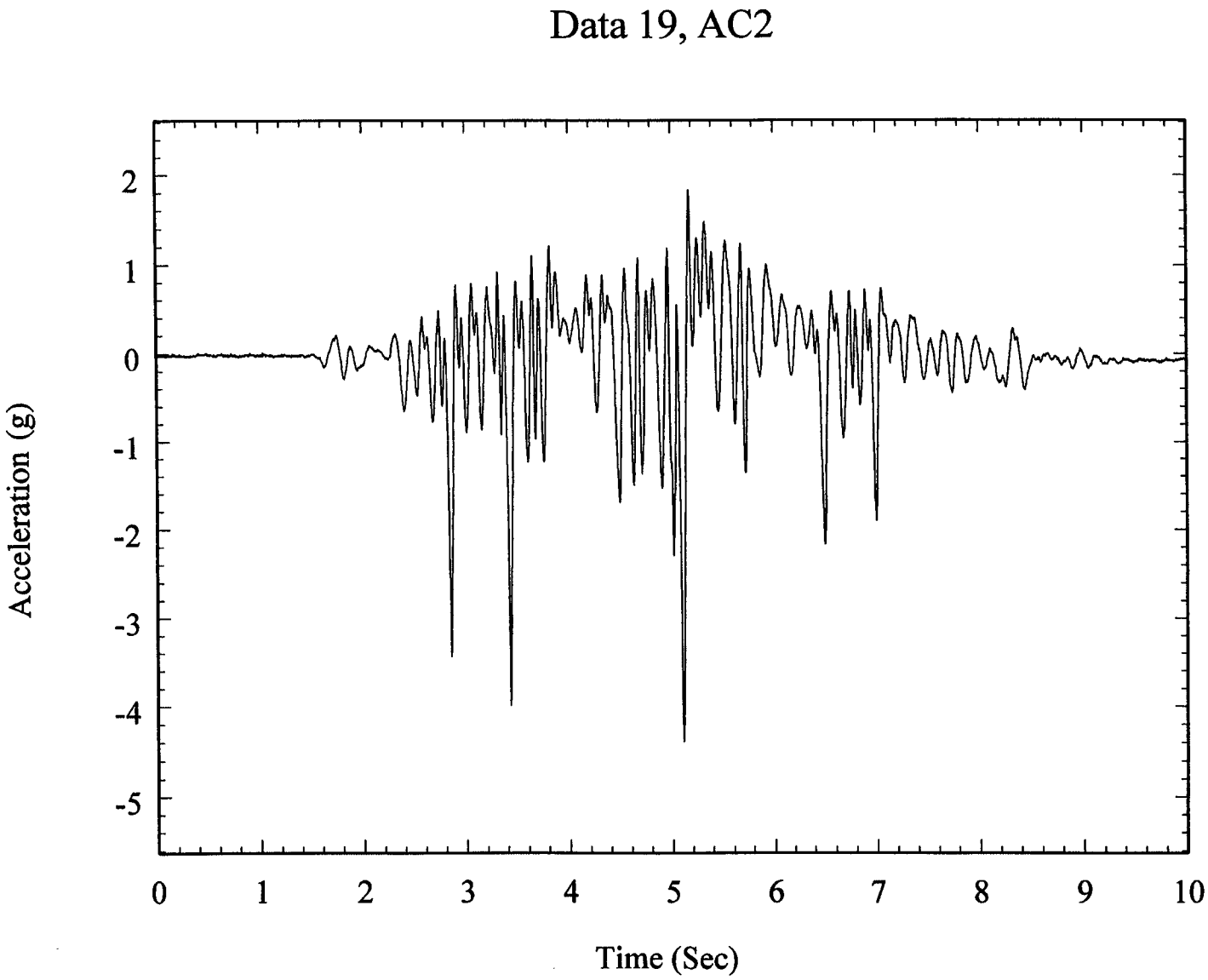

Figure 13-26b. Far side acceleration (AC2) on ingot I (tunnel side wall) for run 9

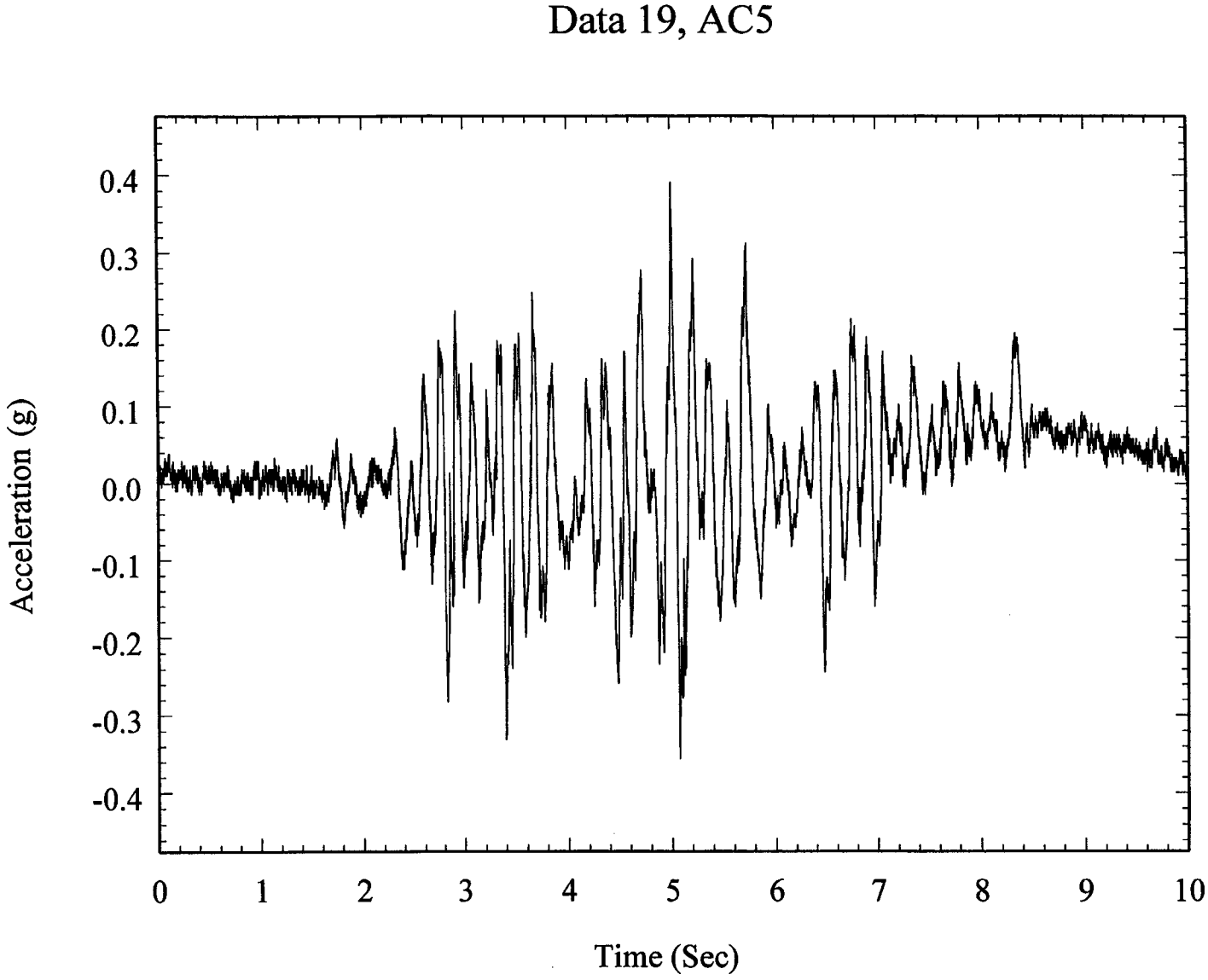

Figure 13-27a. Near side acceleration (AC5) on ingot G (tunnel side wall) for run 9

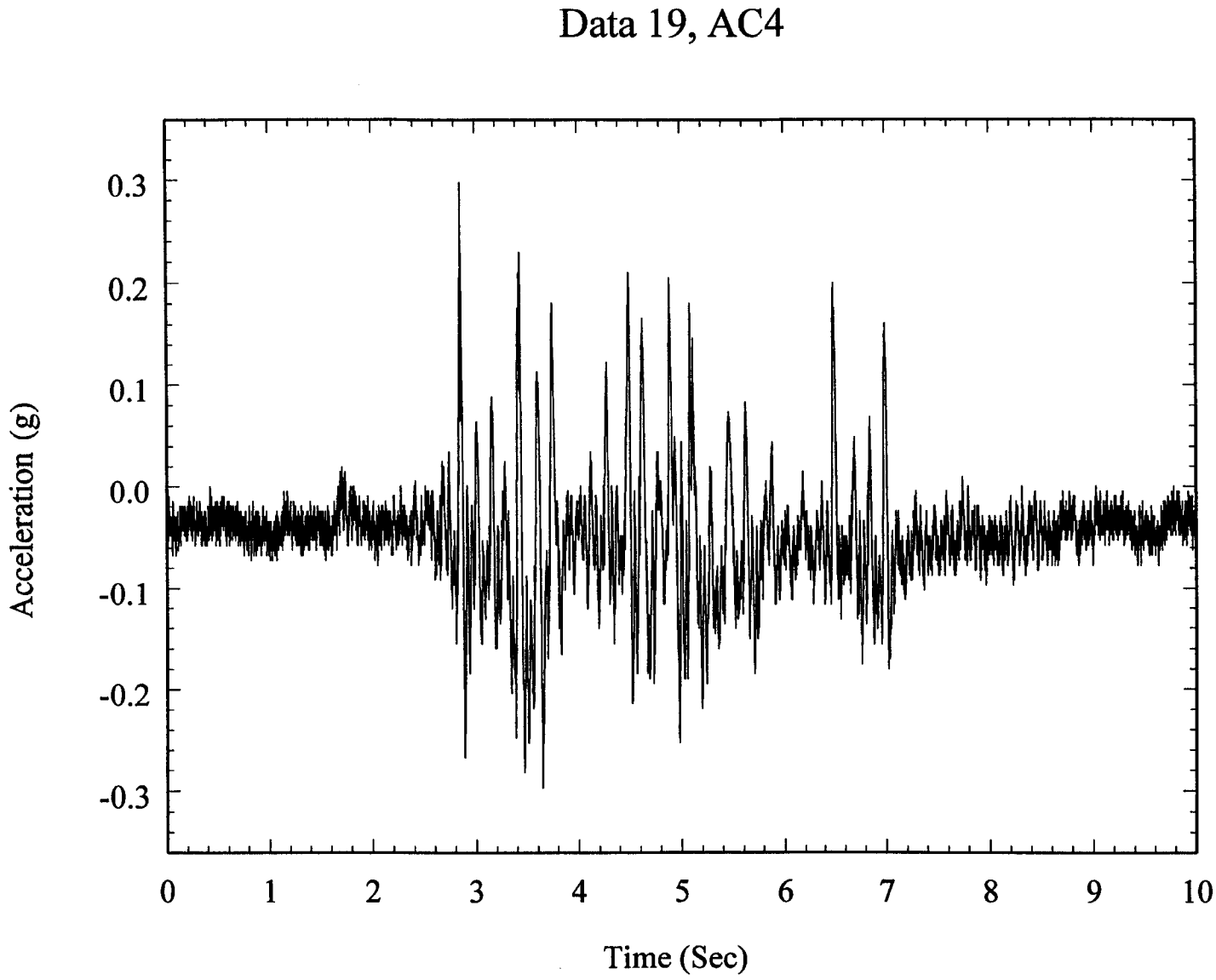

Figure 13-27b. Far side acceleration (AC4) on ingot G (tunnel side wall) for run 9

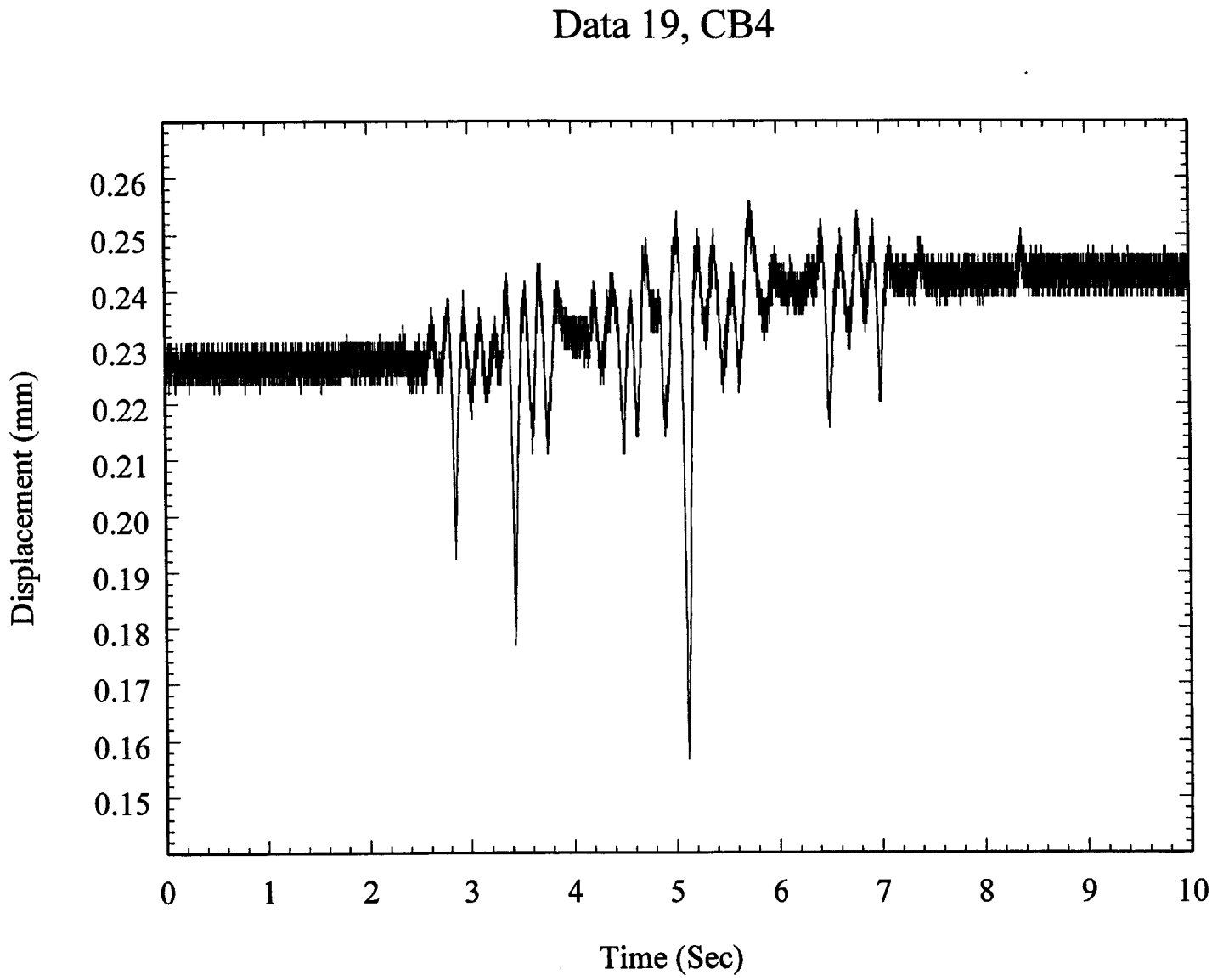

Figure 13-28a. Near side displacement (CB4) of ingot G (tunnel side wall) for run 9

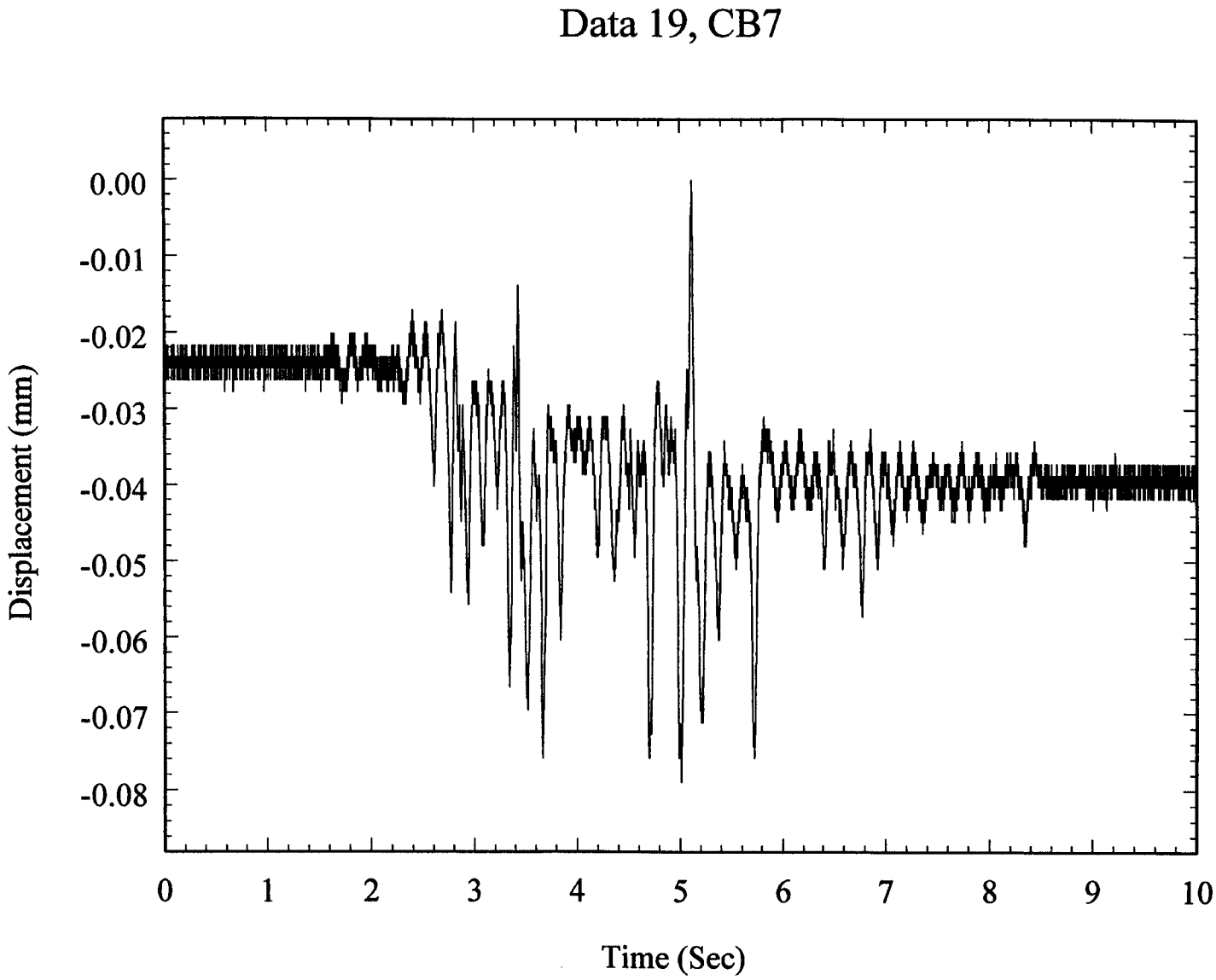

Figure 13-28b. Far side displacement (CB7) of ingot G (tunnel side wall) for run 9

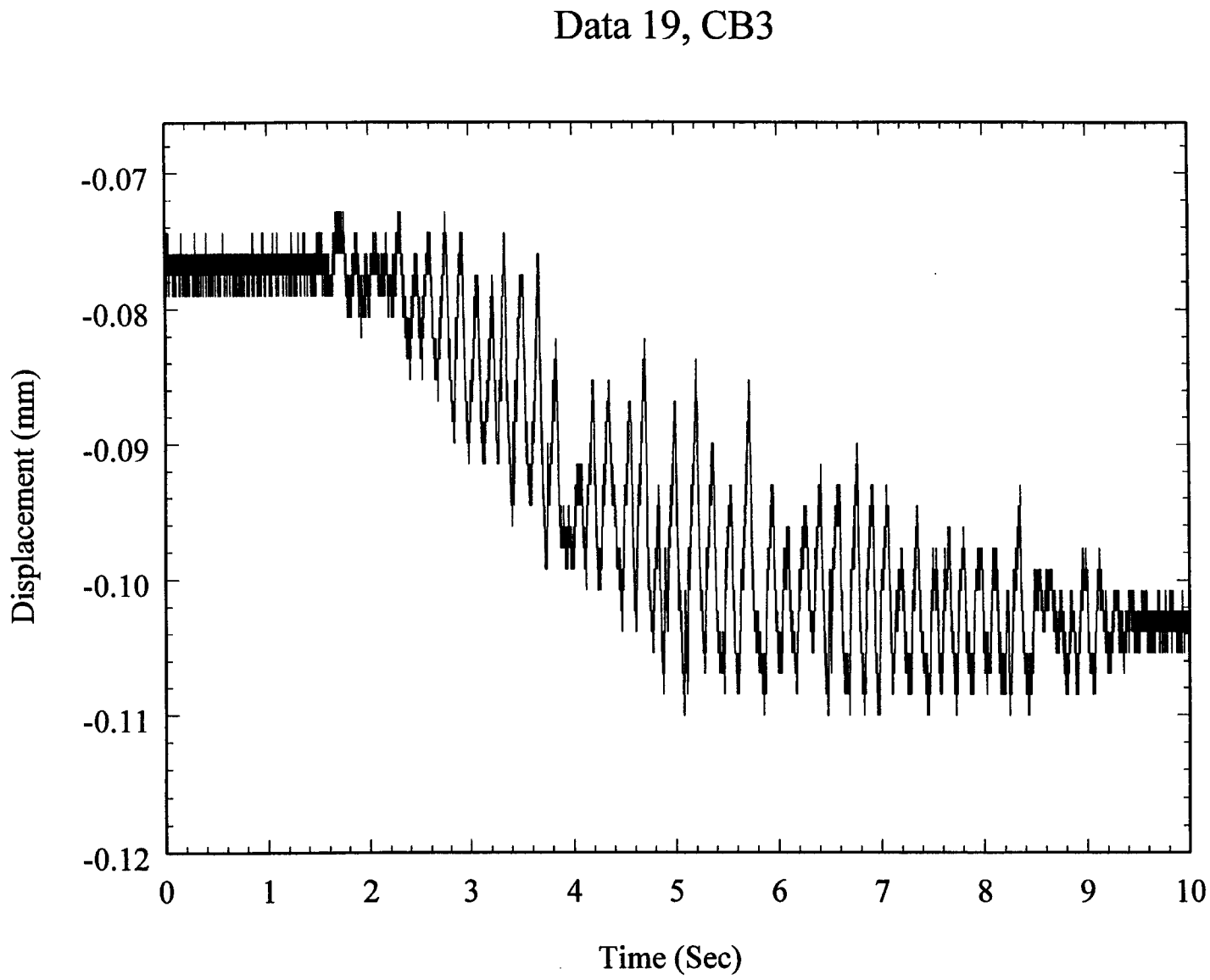

Figure 13-29a. Near side displacement (CB3) of ingot D (tunnel side wall) for run 9

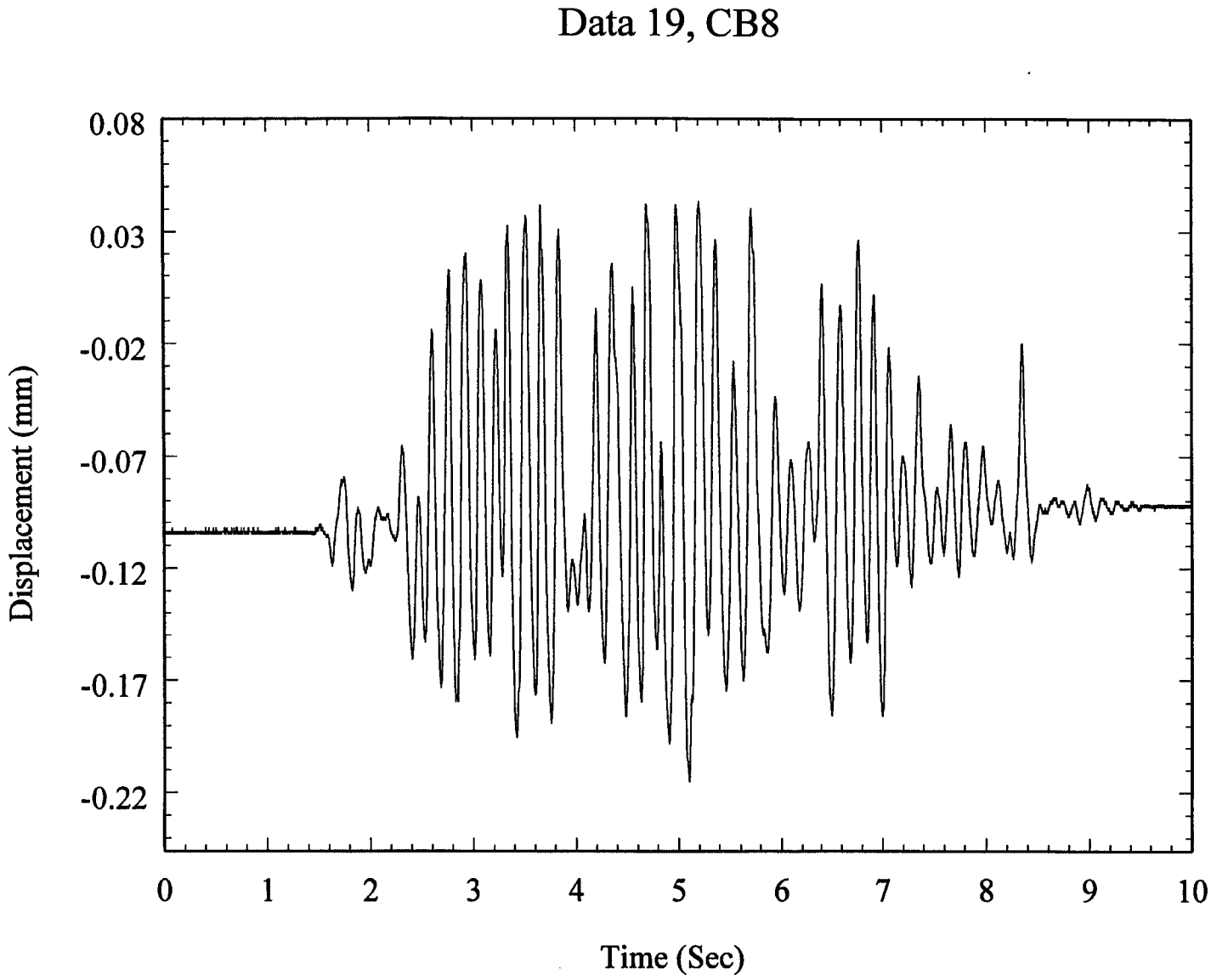

Figure 13-29b. Far side displacement (CB8) of ingot D (tunnel side wall) for run 9

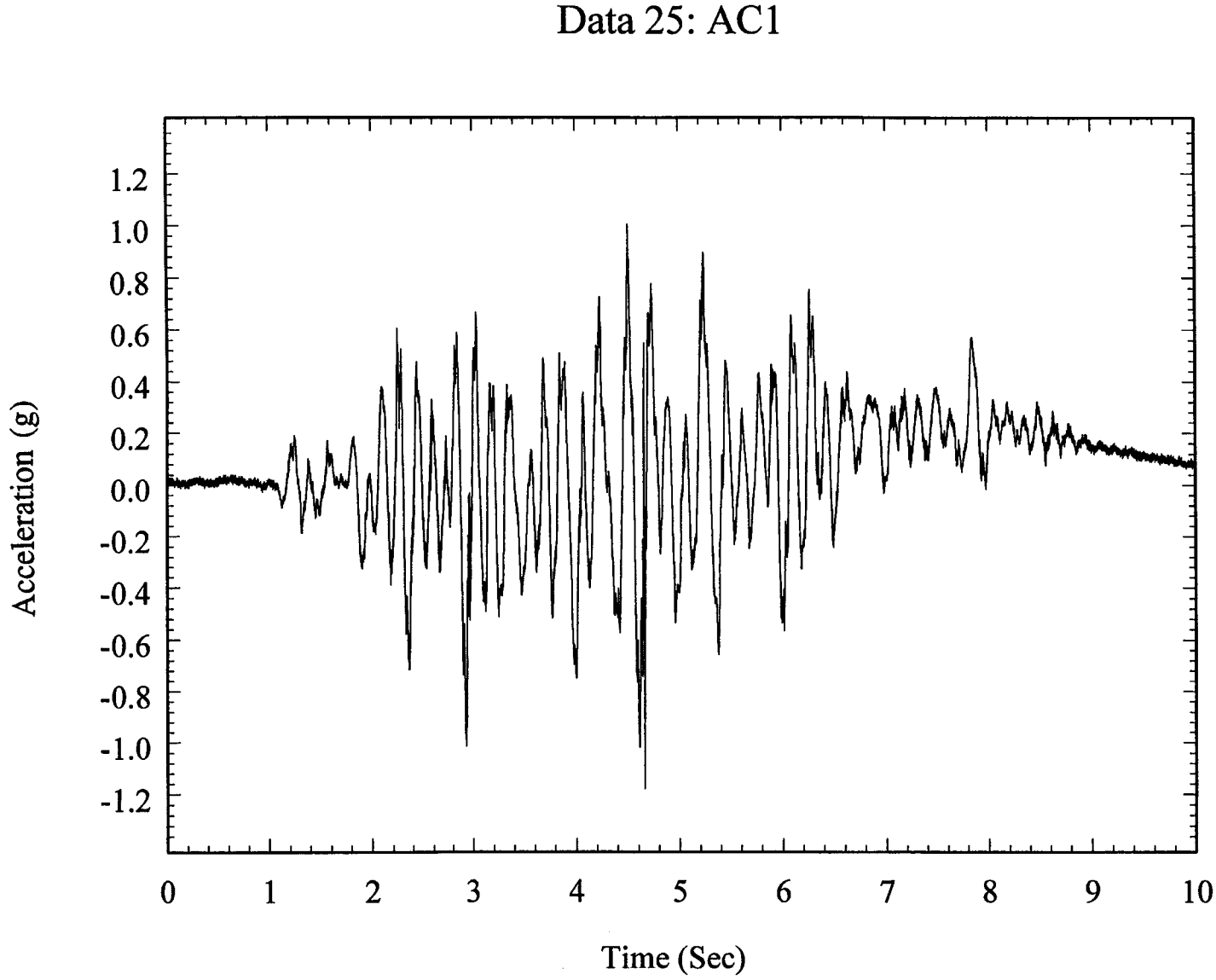

Figure 13-30a. Near side acceleration (AC1) on ingot I (tunnel side wall) for run 13

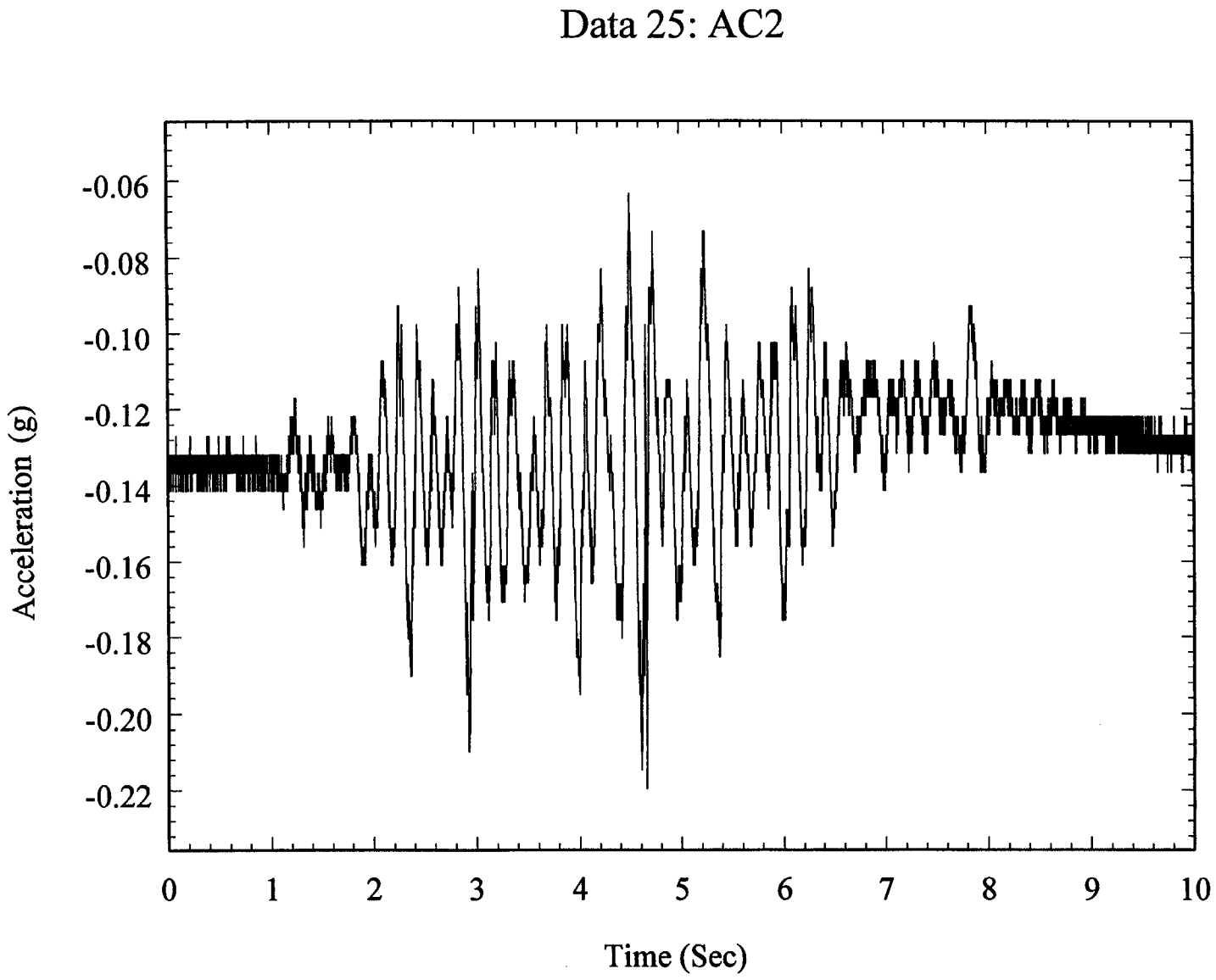

Figure 13-30b. Far side acceleration (AC2) on ingot I (tunnel side wall) for run 13

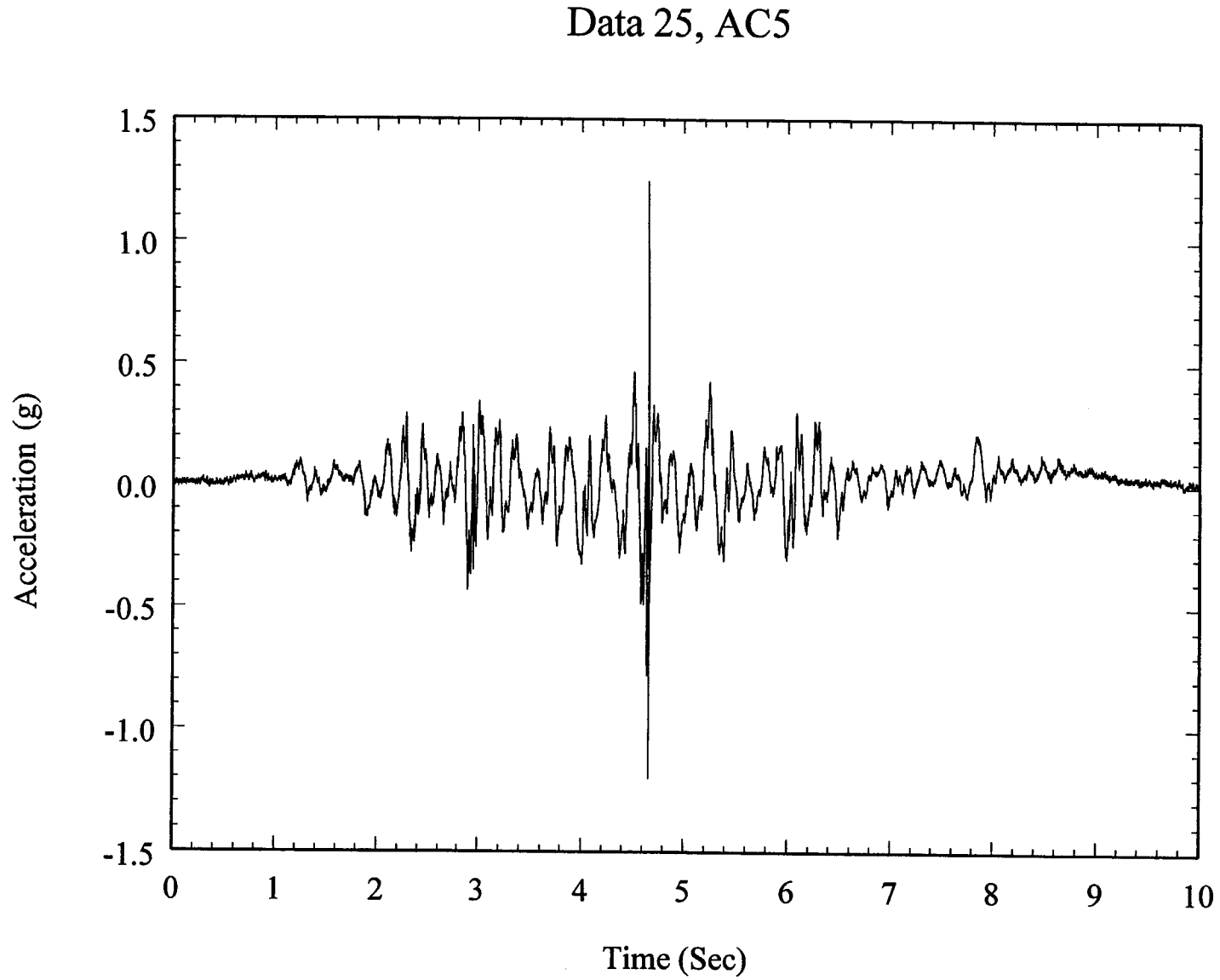

Figure 13-31a. Near side acceleration (AC5) on ingot G (tunnel side wall) for run 13

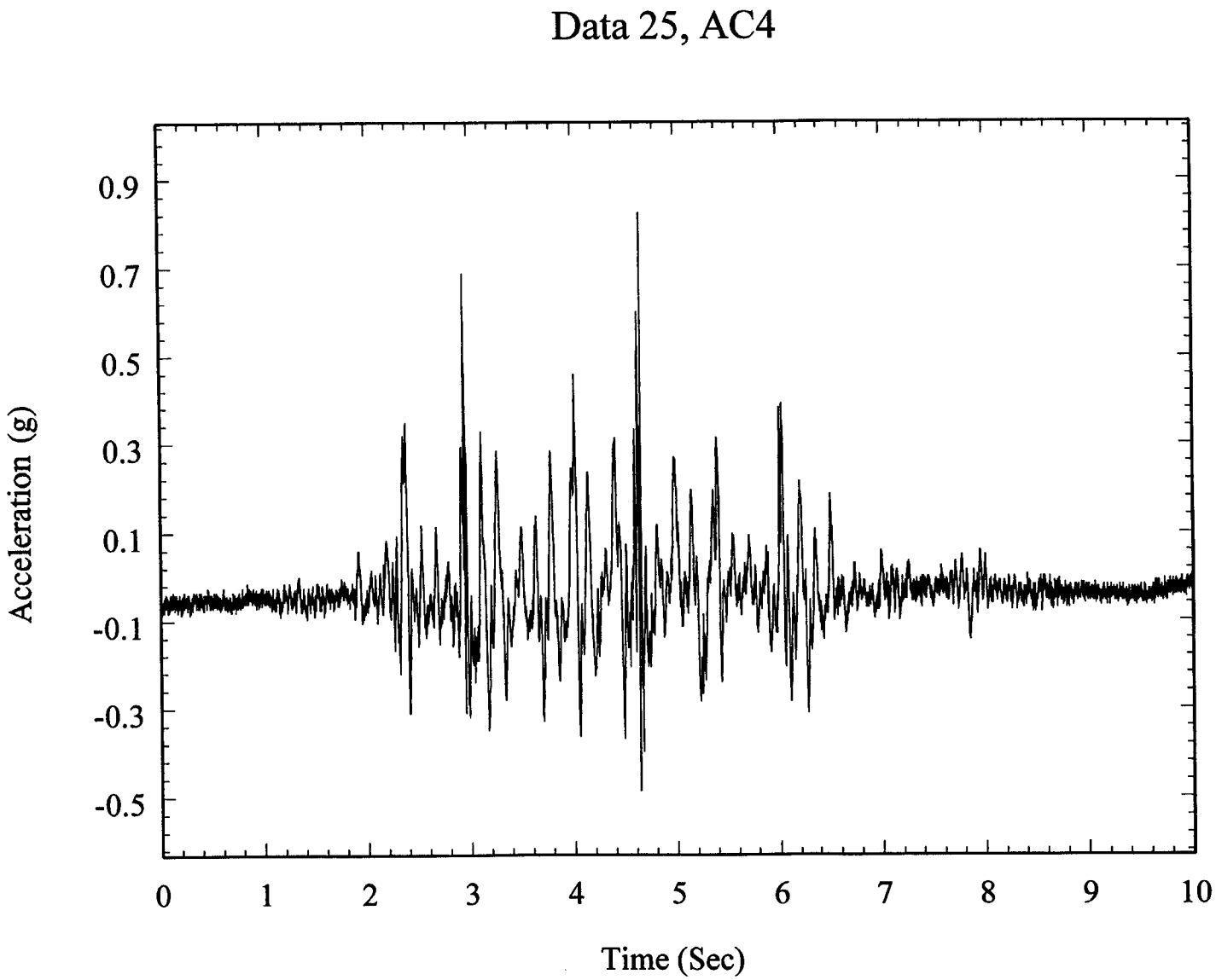

Figure 13-31b. Far side acceleration (AC4) on ingot G (tunnel side wall) for run 13

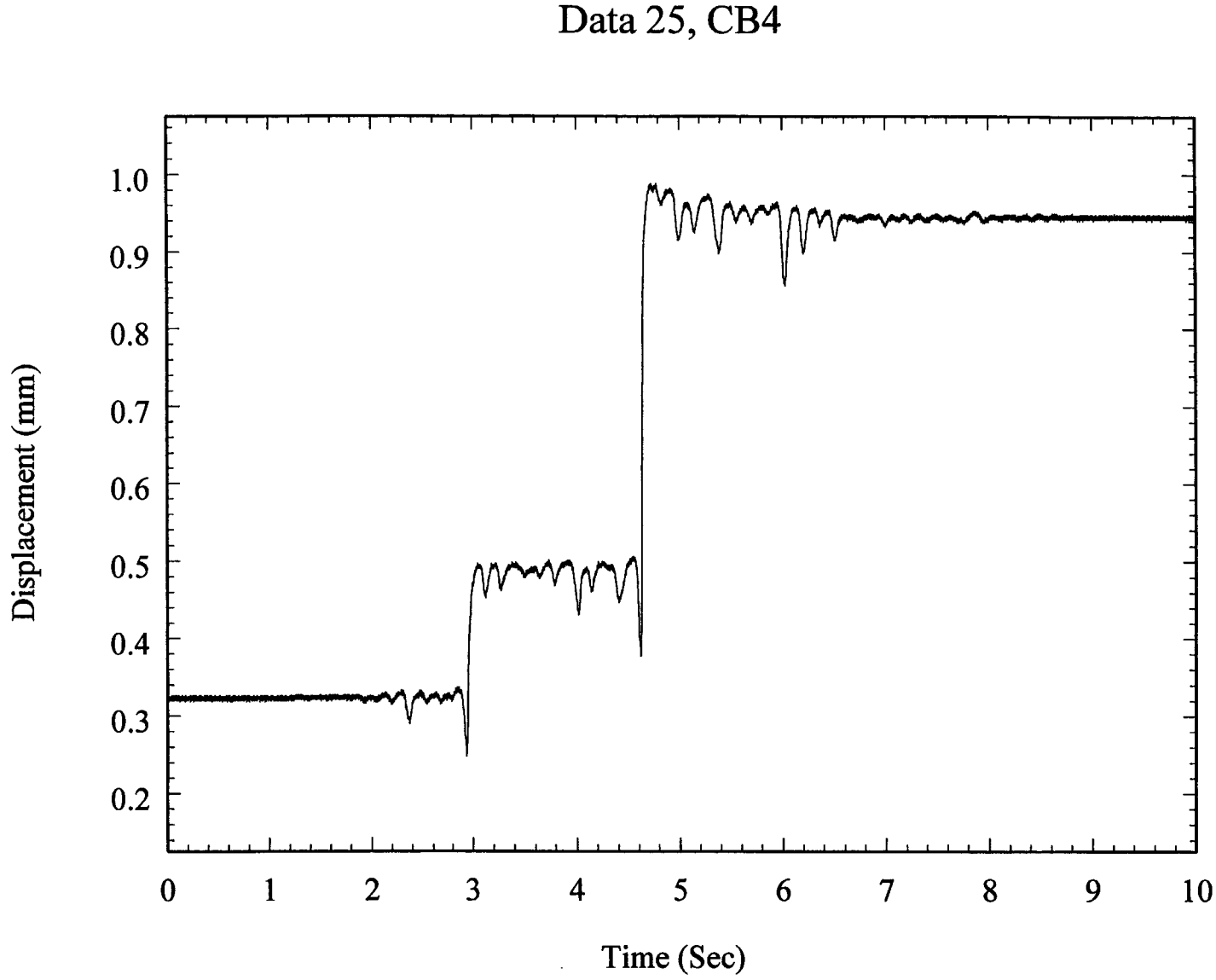

Figure 13-32a. Near side displacement (CB4) of ingot G (tunnel side wall) for run 13

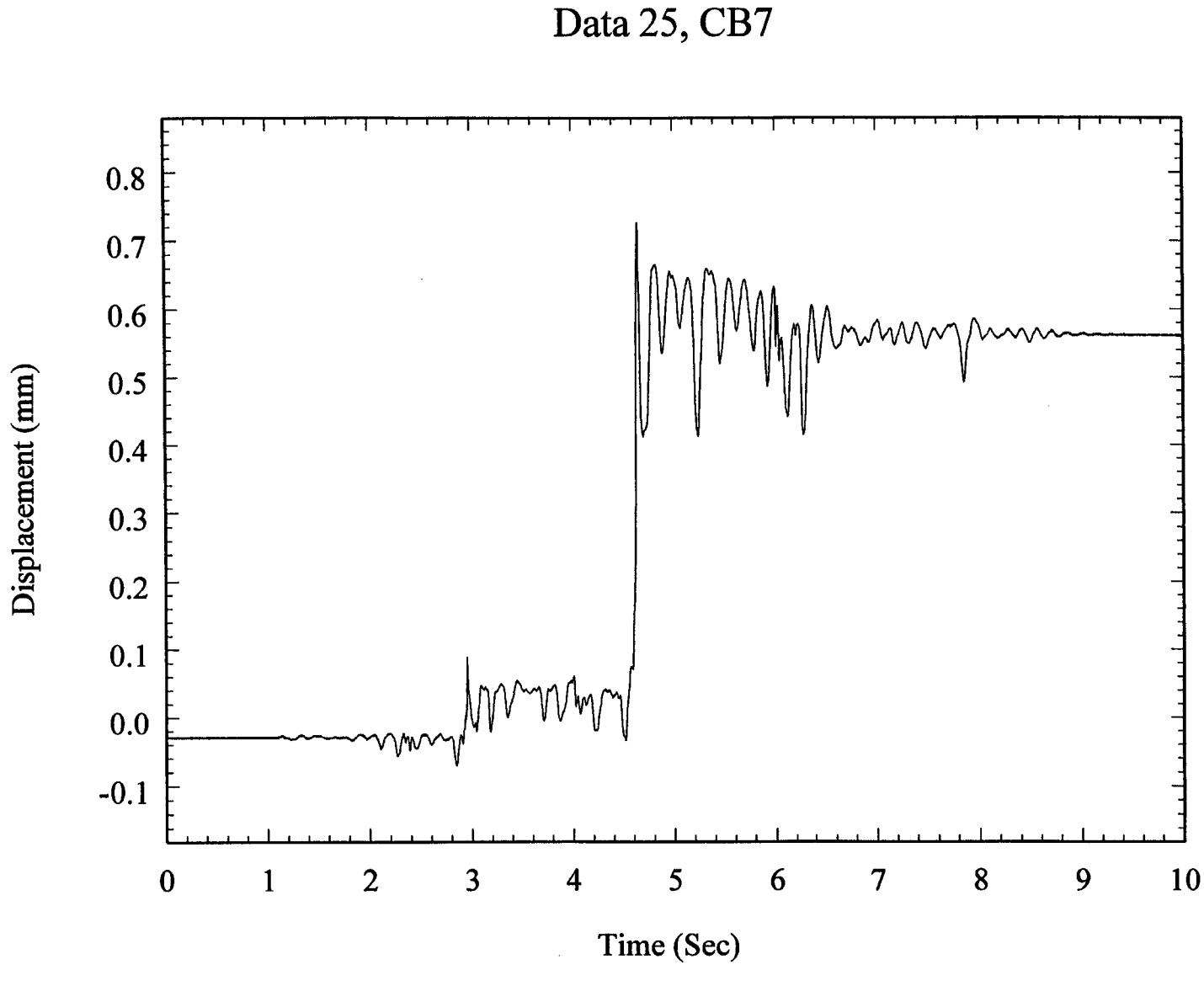

Figure 13-32b. Far side displacement (CB7) of ingot G (tunnel side wall) for run 13

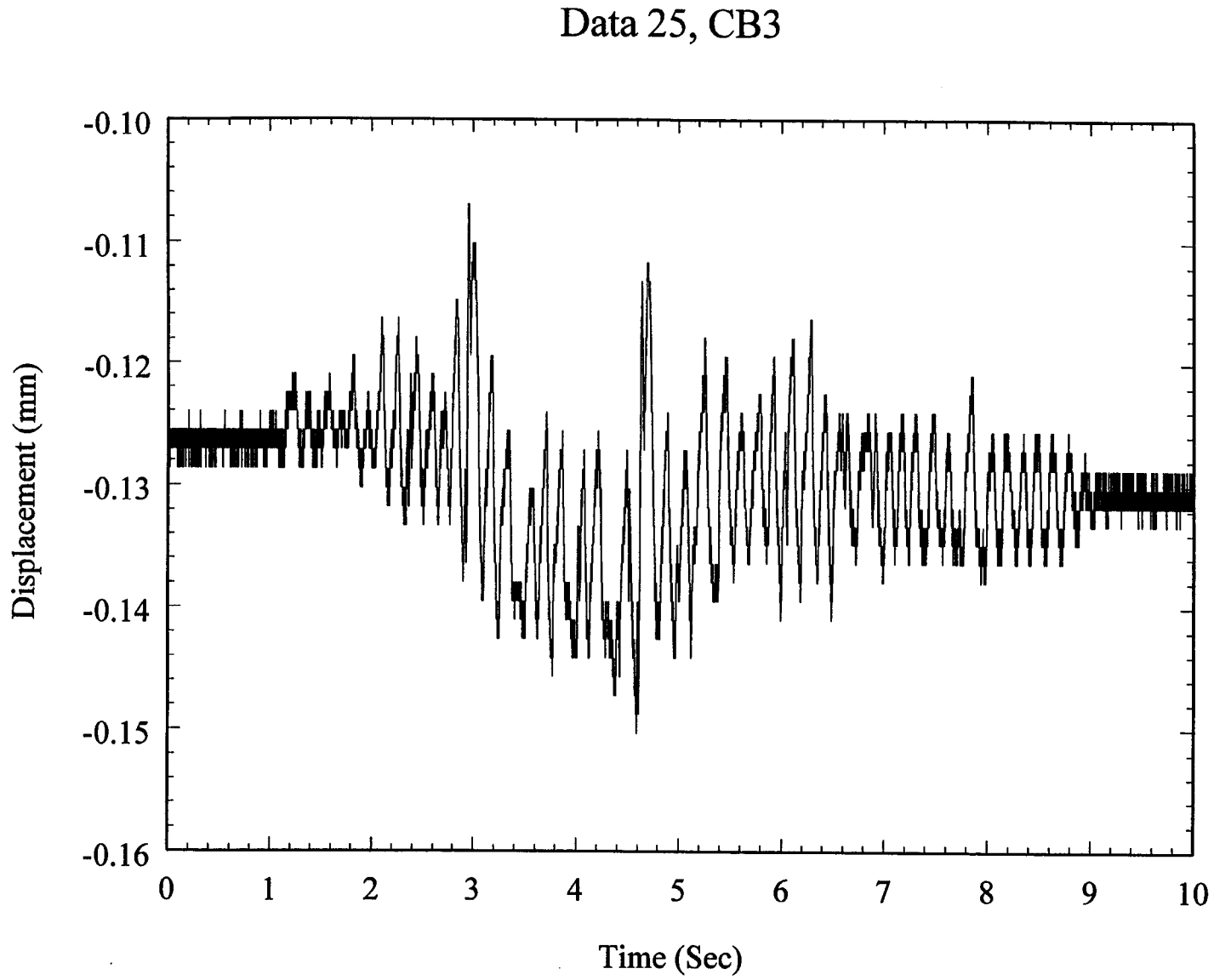

Figure 13-33a. Near side displacement (CB3) of ingot D (tunnel side wall) for run 13

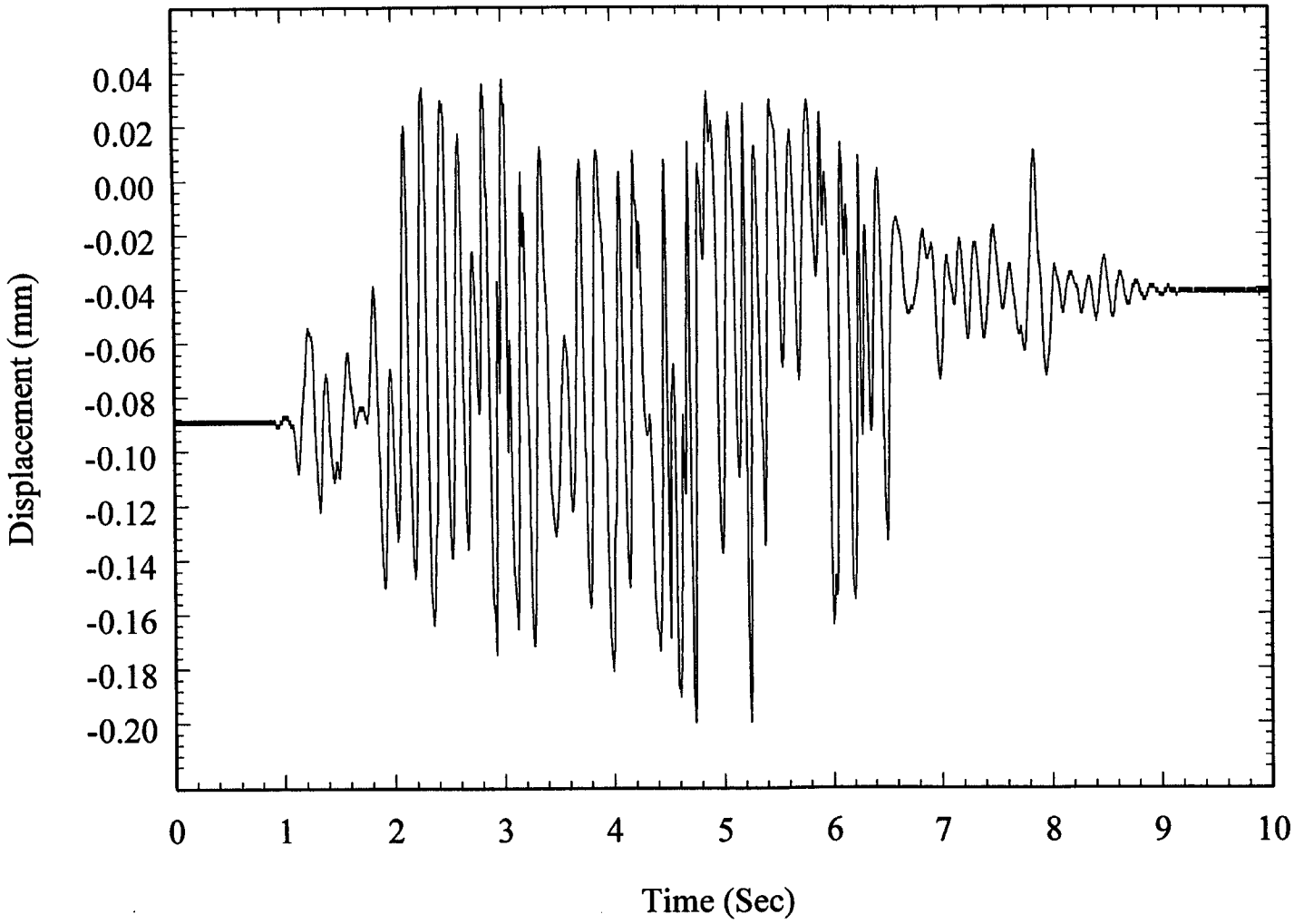

Figure 13-33b. Far side displacement (CB8) of ingot D (tunnel side wall) for run 13

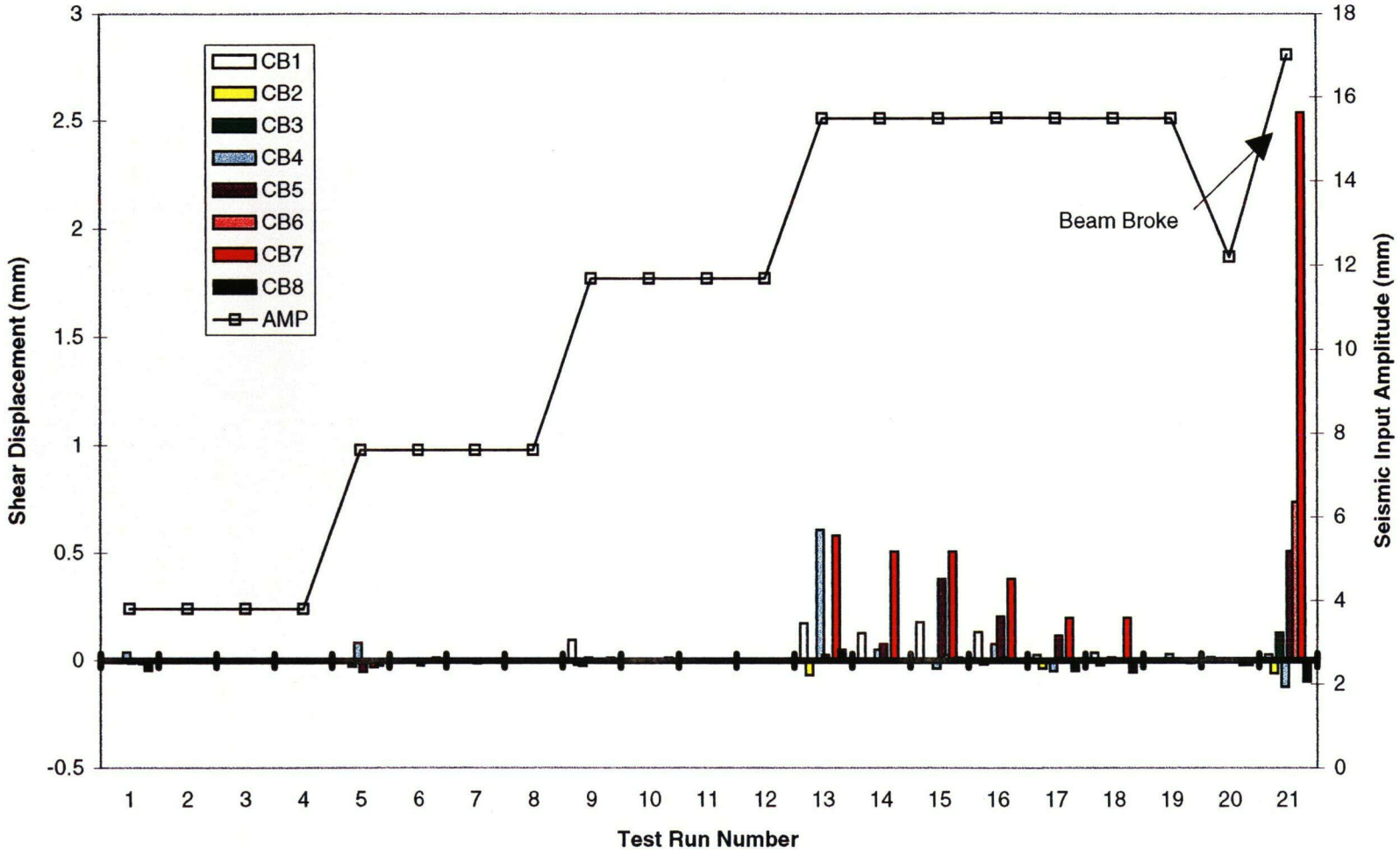

Figure 13-34a. Interface permanent shear displacement resulting from each test run (runs 1 to 21)

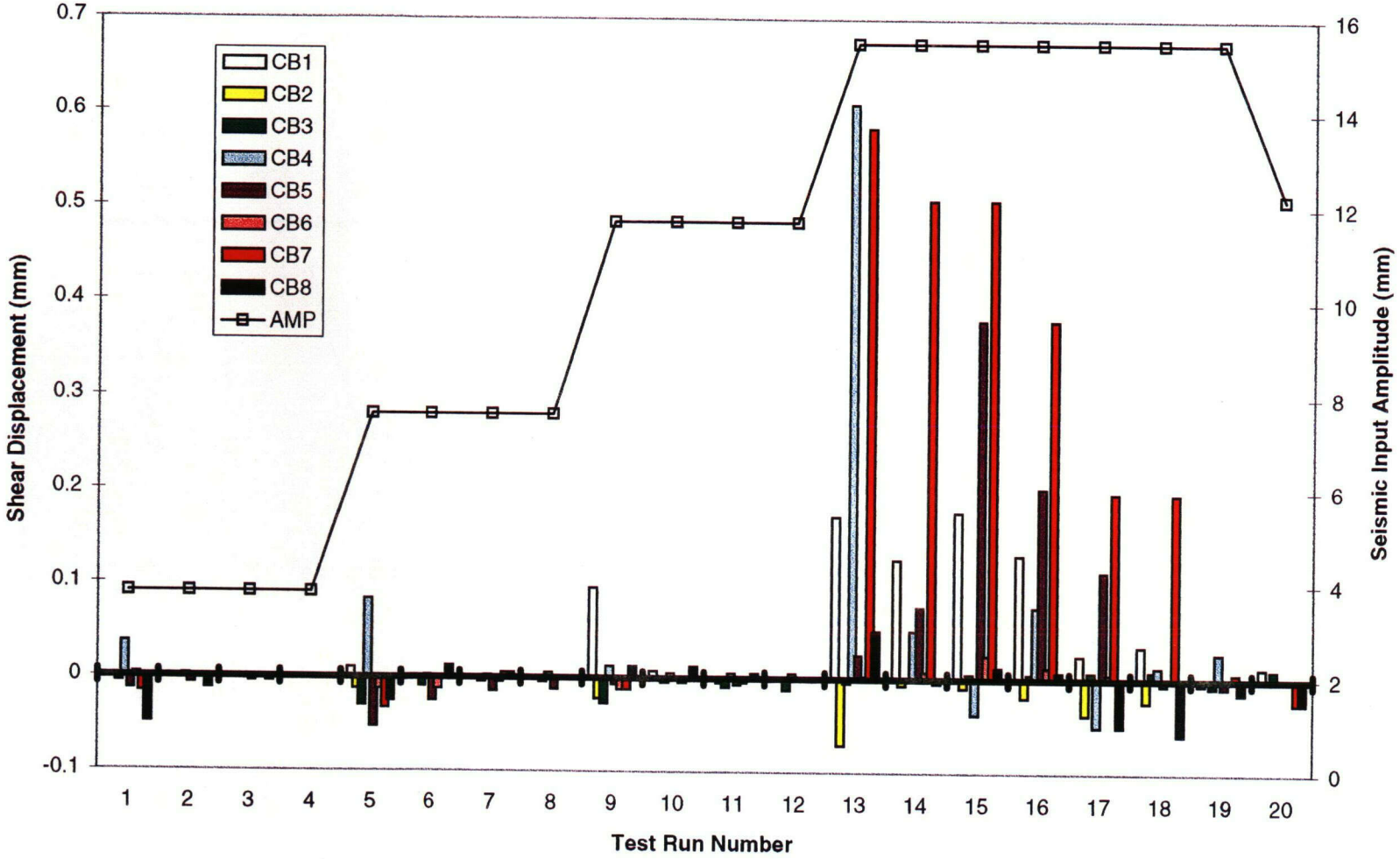

Figure 13-34b. Interface shear displacement resulting from each test run (runs 1 to 20)

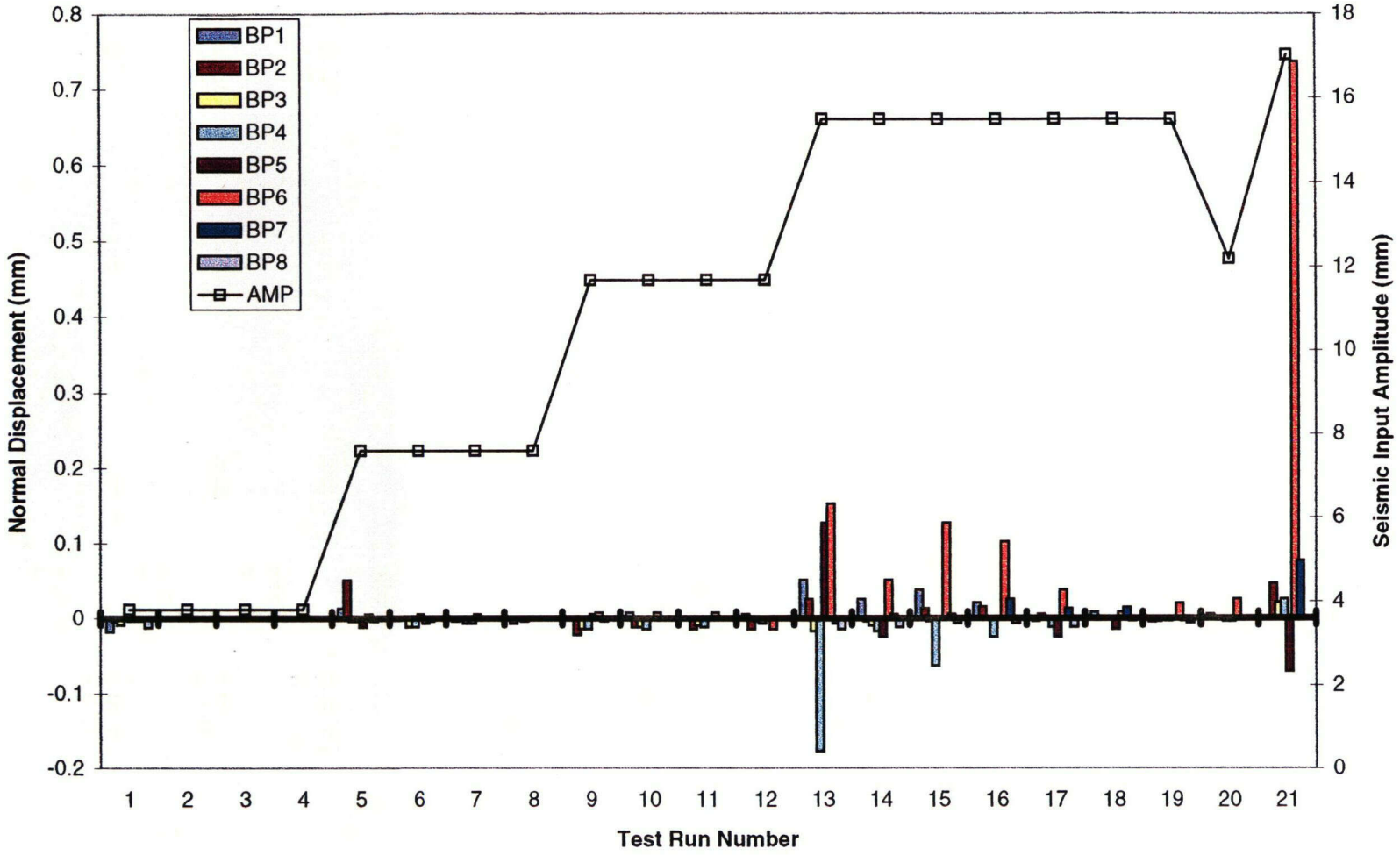

Figure 13-35a. Interface permanent normal displacement resulting from each test run (runs 1 to 21)

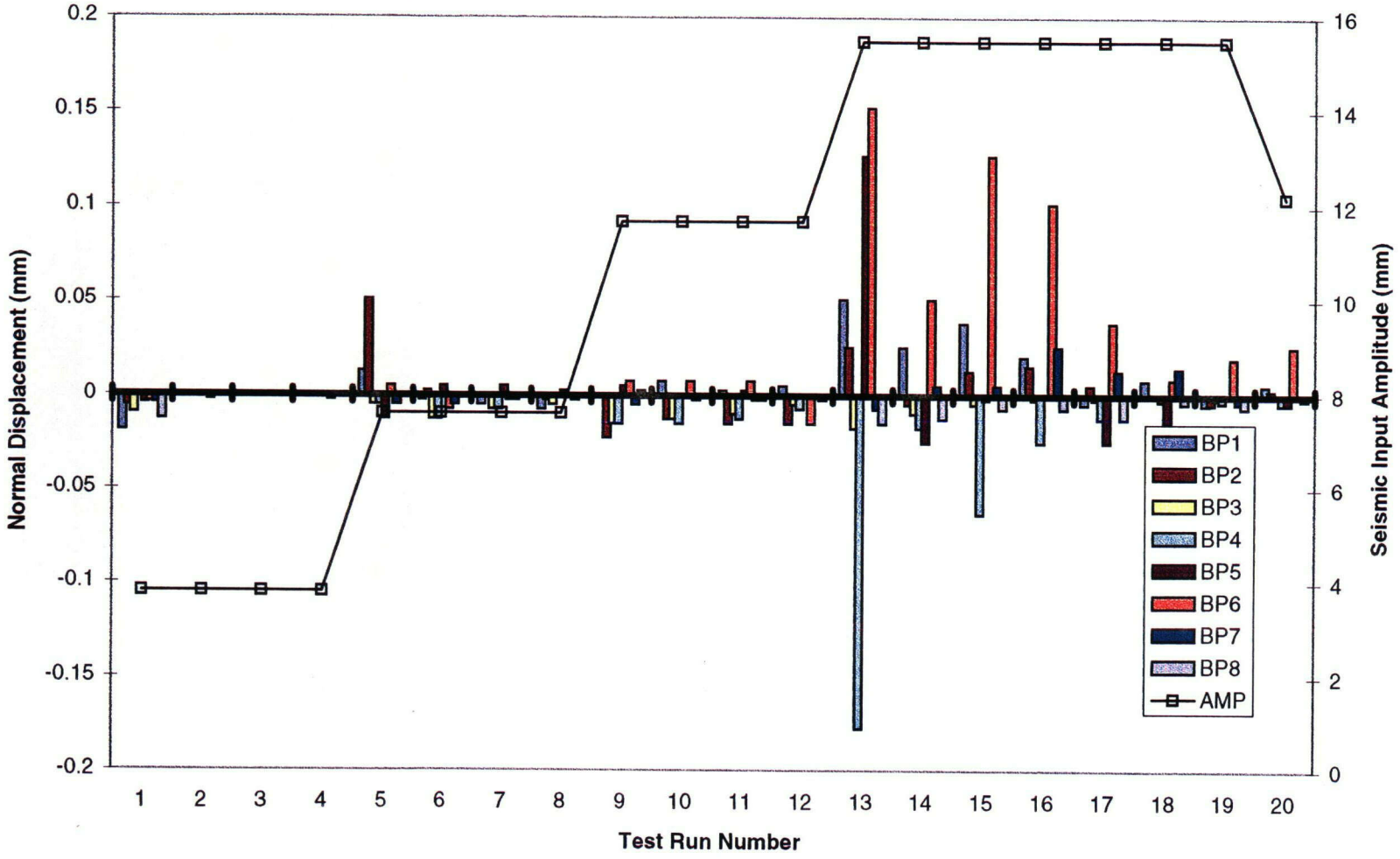

Figure 13-35b. Interface permanent normal displacement resulting from each test run (runs 1 to 20)

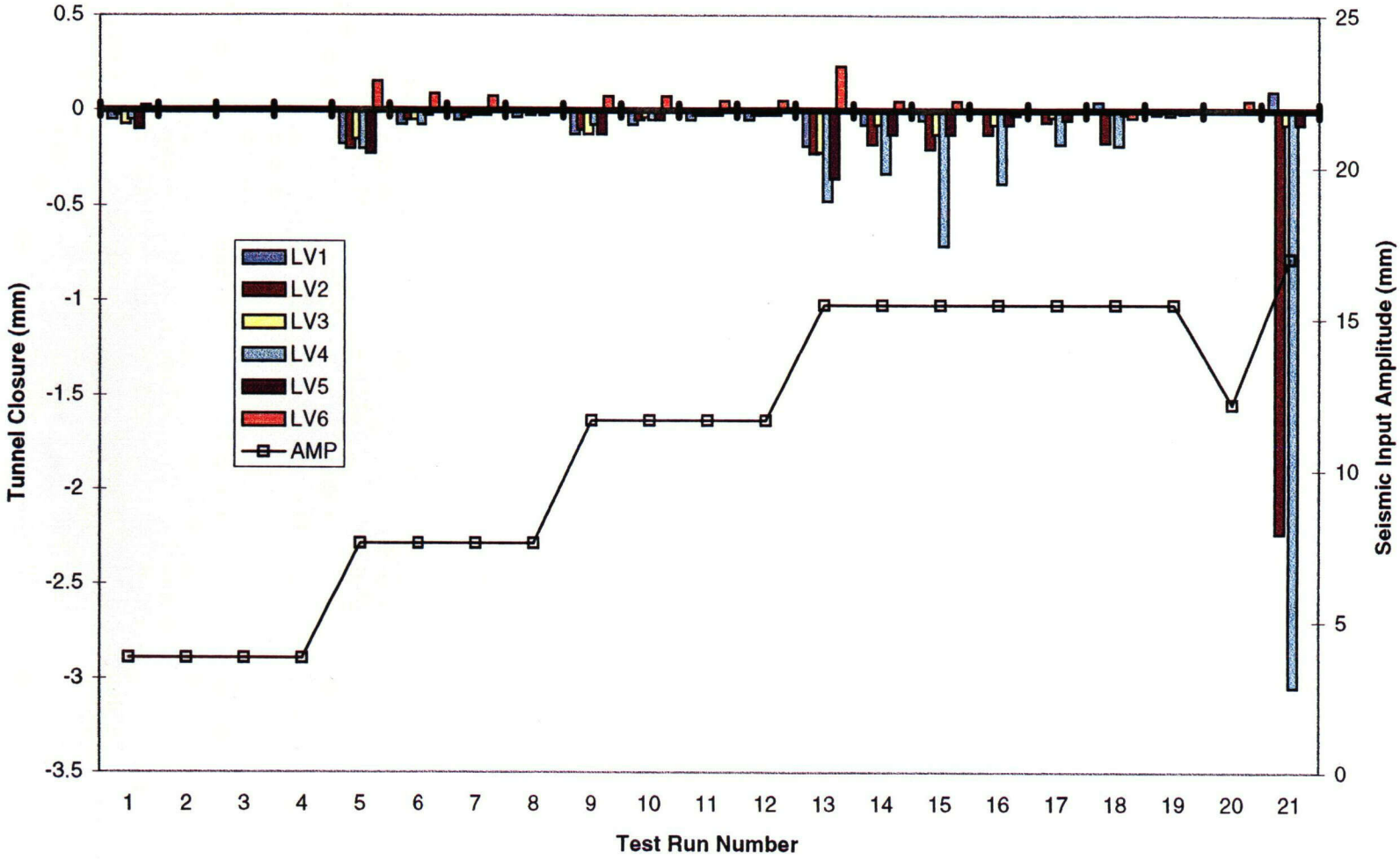

Figure 13-36a. Permanent tunnel closure resulting from each test run (runs 1 to 21)

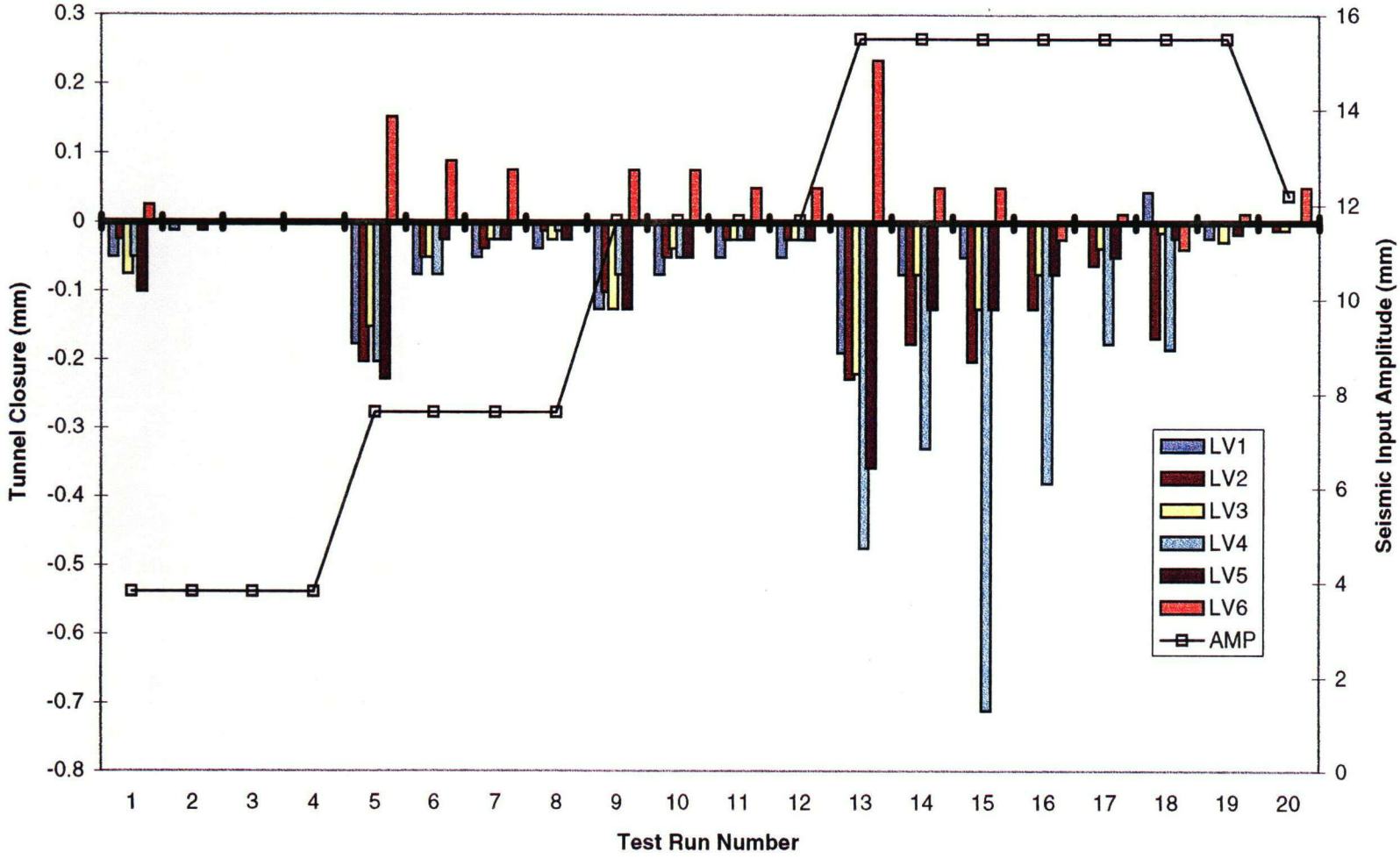

Figure 13-36b. Permanent tunnel closure resulting from each test run (runs 1 to 20)

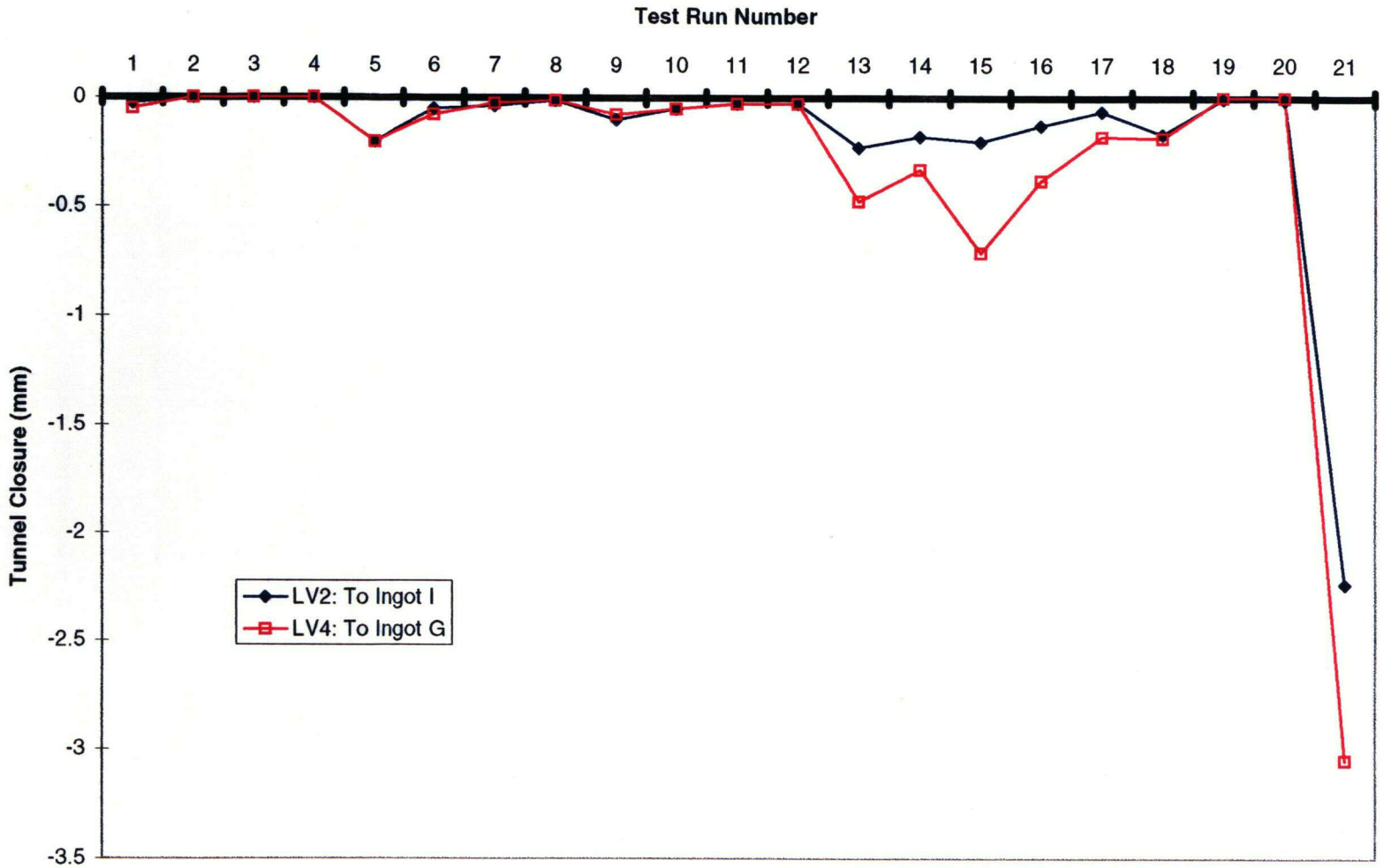

Figure 13-37. Comparison of far side tunnel closure (LV2, LV4)

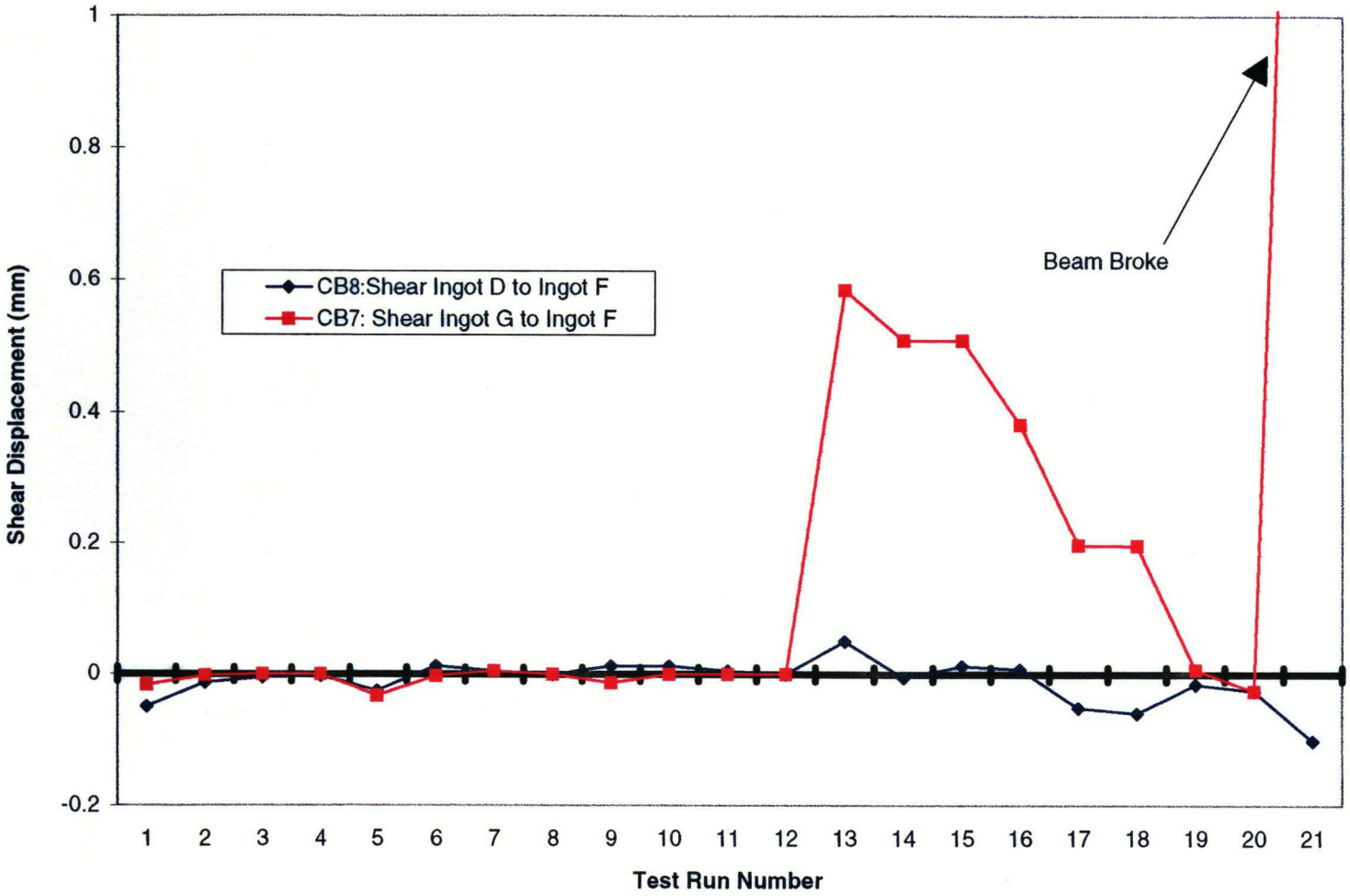

Figure 13-38. Comparison of far side opposing wall ingot shear displacement (CB7, CB8)

14 DISCUSSION AND CONCLUSION

Evidence from this scale-model testing indicates that permanent displacement of an individual ingot will be small unless a threshold seismic input amplitude is exceeded. The scale-model results presented here suggest that the critical seismic amplitude should be expressed in terms of displacement, rather than acceleration. Permanent rock displacements do not appear to be of much significance at lower seismic input amplitudes. Significant permanent deformation only occurs when the threshold seismic input amplitude is exceeded. This permanent deformation was observed to be cumulative, confirming the CNWRA field study result at the Lucky Friday Mine (Hsiung et al., 1992). The field study showed that rock mass deformation around an excavation as a result of repetitive episodes of seismic events is expressed as accumulation of joint shear displacement, which gradually weakens the rock mass.

It should be noted that the threshold seismic amplitude concept discussed here is different from the common concept of damage threshold above which damages to the opening will occur. The former is a threshold above which permanent deformation of rock mass around openings will occur, thus weakening the rock mass surrounding the openings while not yet producing observeable damage. In contrast, the latter is a value above which observed damage to the openings. The concept of a seismic displacement threshold is more conservative and, thus, may be a more pertinent parameter than the damage threshold for design of underground openings in a geologic repository. After the threshold seismic amplitude is determined, this level can be used as a limiting value for tunnel design.

The scale-model testing determined that the response of the model was not 2-D, as was designed. Eccentricities in the model preclude such ideal model behavior. Thus, any attempt to numerically model the laboratory scale-model tests must account for the spanwise in addition to the vertical and lateral dimensions. This dimension may be adequately modeled by allowing the ingots to rigidly rotate about the input axis. The fact that a critical tunnel ingot cracked during the test may also need to be carefully considered in that two ingots may be needed to model the original single ingot. However the analytical model is built, it appears that differences in ingot motion from the near side to the far side of the test array must be accounted for. Some evidence exists that entire rows of ingots shifted toward the tunnel. In addition, only one side of the tunnel showed significant permanent deformation. Another important factor that warrants consideration in the numerical modeling is the effect of the slight interlocking among ingots in the scale-model throughout the structure as can be evidenced in Figures 13-1 to 13-17. This interlocking occurred because the ingots did not perfectly line up during construction. It may be necessary to implement some type of randomized repositioning of the ingots in the analytical model to account for this experimental overlap.

This report describes the design, fabrication, and testing of a relatively complex scale-model for studying the seismic response in the vicinity of an underground opening in a layered rock mass. By all observations during the test sequence, it appears that the instrumentation and associated data acquisition systems performed adequately. The most interesting result is that of the seismic threshold level for permanent rock deformations. As discussed in the second paragraph of this section, this concept may be of considerable value in seismic design of underground facilities and, therefore, warrants further investigation.

15 REFERENCES

Hsiung, S.M., A.H. Chowdhury, W. Blake, M.P. Ahola, and A. Ghosh. 1992. Field Site Investigation: Effect of Mine Seismicity on a Jointed Rock Mass. CNWRA 92-012. San Antonio, TX: Center for Nuclear Waste Regulatory Analyses.

Hsiung, S.M., Kana, D.D., Ahola, M.P., Chowdhury, A.H., and Ghosh, A. 1993. *Laboratory Characterization of Rock Joints.* CNWRA 93-013. San Antonio, TX: Center for Nuclear Waste Regulatory Analyses.

ITASCA Consulting Group, Inc. 1992. *UDEC Universal Distinct Element Code Version 1.8 Volume I: User's Manual.* Minneapolis, MN: ITASCA Consulting Group, Inc.

Kana, D.D., Brady, B.H.G., Vanzant, B.W., and Nair, P.K. 1991. *Critical Assessment of Seismic and Geomechanics Literature Related to a High-Level Nuclear Waste Underground Repository.* NUREG/CR-5440. Washington, DC: Nuclear Regulatory Commission.

Nuclear Waste Technical Review Board. 1992. *Fifth Report to the U.S. Congress and the U.S. Secretary of Energy.* Washington, DC: U.S. Government Printing Office.

Unruh, J.F. 1982. Digital control of a shaker to a specified response spectrum. *The Shock and Vibration Bulletin* 52.

APPENDIX A

Appendix A Instrumentation Identification List

Computer Channel	Transducer Identification	Transducer Mfgr/Model	Amplifier Mfgr./Model	Filter Mfgr./Model
1	AC1	PCB/303A	PCB/483B07	Ithaco/4302
2	AC2	PCB/303A	PCB/483B07	Ithaco/4302
3	AC3	PCB/303A	PCB/483B07	Ithaco/4302
4	AC4	PCB/303A	PCB/483B07	Ithaco/4302
5	AC5	PCB/303A	PCB/483B07	Ithaco/4302
6	AC6	PCB/303A	PCB/483B07	Ithaco/4302
7	AC7	PCB/303A	PCB/483B07	Ithaco/4302
8	AC8	PCB/303A	PCB/483B07	Ithaco/4302
9	AC9	PCB/303A	PCB/483B07	Ithaco/4302
10	AC10	PCB/303A	PCB/483B07	Ithaco/4302
11	AC11	PCB/303A	PCB/483B07	Ithaco/4302
12	SG1*	Measurements Group CEA-1250W	Measurements Group/2120A	None
13	SG2*	Measurements Group CEA-1250W	Measurements Group/2120A	None
14	SG3*	Measurements Group CEA-1250W	Measurements Group/2120A	None
15	SG4*	Measurements Group CEA-1250W	Measurements Group/2120A	None
16	SG5	Measurements Group CEA-1250W	Measurements Group/2120A	Ithaco/4302
17	SG6	Measurements Group CEA-1250W	Measurements Group/2120A	Ithaco/4302
18	SG7	Measurements Group CEA-1250W	Measurements Group/2120A	Ithaco/4302
19	SG8	Measurements Group CEA-1250W	Measurements Group/2120A	Ithaco/4302
20	SG9	Measurements Group CEA-1250W	Measurements Group/2120A	Ithaco/4302
21	CB1	SwRI	Measurements Group/2120A	Ithaco/4302
22	CB2	SwRI	Measurements Group/2120A	Ithaco/4302
23	CB3	SwRI	Measurements Group/2120A	Ithaco/4302
24	CB4	SwRI	Measurements Group/2120A	Ithaco/4302
25	CB5	SwRI	Measurements Group/2120A	Ithaco/4302
26	CB6	SwRI	Measurements Group/2120A	Ithaco/4302
27	CB7	SwRI	Measurements Group/2120A	Ithaco/4302
28	CB8	SwRI	Measurements Group/2120A	Ithaco/4302
29	BP1	Bentley/21500	Bentley/18745	None
30	BP2	Bentley/21500	Bentley/18745	Ithaco/4302
31	BP3	Bentley/21500	Bentley/18745	Ithaco/4302
32	BP4	Bentley/21500	Bentley/18745	Ithaco/4302
33	BP5*	Bentley/21500	Bentley/18745	Ithaco/4302
34	BP6*	Bentley/21500	Bentley/18745	None
35	BP7	Bentley/21500	Bentley/18745	None
36	BP8	Bentley/21500	Bentley/18745	None
37	LV1*	Trans-Tek/0243	Trans-Tek/D15.200	None
38	LV2	Trans-Tek/0243	Trans-Tek/D15.200	None
39	LV3	Trans-Tek/0243	Trans-Tek/D15.200	None
40	LV4	Trans-Tek/0243	Trans-Tek/D15.200	None
41	LV5	Trans-Tek/0243	Trans-Tek/D15.200	None
42	LV6	Trans-Tek/0243	Trans-Tek/D15.200	None
43	LC2	Sensotec/D-622-06	Measurements Group/2120A	Ithaco/4302
44	LC3	Sensotec/D-622-06	Measurements Group/2120A	Ithaco/4302
45	LC4	Sensotec/D-622-06	Measurements Group/2120A	Ithaco/4302
46	LC5	Sensotec/D-622-06	Measurements Group/2120A	Ithaco/4302
47	LC6	Sensotec/D-622-06	Measurements Group/2120A	Ithaco/4302
48	AT1	Bell & Howell 4-202-1	Moog/F123-211	Ithaco/4302
49	DT1	Temposonics 315RBU0100	Included in XDCR	None
50	CD1	Drive Signal	NA	None

* Initial runs only. Some channels changed for later runs.

APPENDIX B

	Run No/Xdcr																				
Chn	1	2	3	4	5	6	7	8	9	10	11	12	13	14	15	16	17	18	19	20	21
1	AC1	AC1	AC1	AC1	AC1	AC1	AC1	AC1	AC1	AC1	AC1	AC1	AC1	AC1	AC1	AC1	AC1	AC1	AC1	AC1	AC1
2	AC2	AC2	AC2	AC2	AC2	AC2	AC2	AC2	AC2	AC2	AC2	AC2	AC2	AC2	AC2	AC2	AC2	AC2	AC2	AC2	AC2
3	AC3	AC3	AC3	AC3	AC3	AC3	AC3	AC3	AC3	AC3	AC3	AC3	AC3	AC3	AC3	AC3	AC3	AC3	AC3	AC3	AC3
4	AC4	AC4	AC4	AC4	AC4	AC4	AC4	AC4	AC4	AC4	AC4	AC4	AC4	AC4	AC4	AC4	AC4	AC4	AC4	AC4	AC4
5	AC5	AC5	AC5	AC5	AC5	AC5	AC5	AC5	AC5	AC5	AC5	AC5	AC5	AC5	AC5	AC5	AC5	AC5	AC5	AC5	AC5
6	AC6	AC6	AC6	AC6	AC6	AC6	AC6	AC6	AC6	AC6	AC6	AC6	AC6	AC6	AC6	AC6	AC6	AC6	AC6	AC6	AC6
7	AC7	AC7	AC7	AC7	AC7	AC7	AC7	AC7	AC7	AC7	AC7	AC7	AC7	AC7	AC7	AC7	AC7	AC7	AC7	AC7	AC7
8	AC8	AC8	AC8	AC8	AC8	AC8	AC8	AC8	AC8	AC8	AC8	AC8	AC8	AC8	AC8	AC8	AC8	AC8	AC8	AC8	AC8
9	AC9	AC9	AC9	AC9	AC9	AC9	AC9	AC9	AC9	AC9	AC9	AC9	AC9	AC9	AC9	AC9	AC9	AC9	AC9	AC9	AC9
10	AC10	AC10	AC10	AC10	AC10	AC10	AC10	AC10	AC10	AC10	AC10	AC10	AC10	AC10	AC10	AC10	AC10	AC10	AC10	AC10	AC10
11	AC11	AC11	AC11	AC12	AC11	AC11	AC11	AC11	AC11	AC11	AC11	AC11	AC11	AC11	AC11	AC11	AC11	AC11	AC11	AC11	AC11
12	SG1	SG1	SG1	SG1	SG1	SG1	SG1	SG1	SG1	BP5	BP5	BP5	SG1	SG1	SG1	SG1	SG1	SG1	SG1	SG1	SG1
13	SG2	SG2	SG2	SG2	SG2	SG2	SG2	SG2	SG2	LC1	LC1	LC1	LC1	LC1	LC1	LC1	LC1	LC1	LC1	LC1	LC1
14	SG3	SG3	SG3	SG3	SG3	SG3	SG3	SG3	SG3	SG3	SG3	SG3	AC13	AC13	AC13	AC13	AC13	AC13	AC13	AC13	AC13
15	SG4	SG4	SG4	SG4	SG4	SG4	SG4	SG4	SG4	SG4	SG4	SG4	AC14	AC14	AC14	AC14	AC14	AC14	AC14	AC14	AC14
16	SG5	SG5	SG5	SG5	SG5	SG5	SG5	SG5	SG5	SG5	SG5	SG5	SG5	SG5	SG5	SG5	SG5	SG5	SG5	SG5	SG5
17	SG6	SG6	SG6	SG6	SG6	SG6	SG6	SG6	SG6	SG6	SG6	SG6	SG6	SG6	SG6	SG6	SG6	SG6	SG6	SG6	SG6
18	SG7	SG7	SG7	SG7	SG7	SG7	SG7	SG7	SG7	SG7	SG7	SG7	SG7	SG7	SG7	SG7	SG7	SG7	SG7	SG7	SG7
19	SG8	SG8	SG8	SG8	SG8	SG8	SG8	SG8	SG8	SG8	SG8	SG8	SG8	SG8	SG8	SG8	SG8	SG8	SG8	SG8	SG8
20	SG9	SG9	SG9	SG9	SG9	SG9	SG9	SG9	SG9	SG9	SG9	SG9	SG9	SG9	SG9	SG9	SG9	SG9	SG9	SG9	SG9
21	CB1	CB1	CB1	CB1	CB1	CB1	CB1	CB1	CB1	CB1	CB1	CB1	CB1	CB1	CB1	CB1	CB1	CB1	CB1	CB1	CB1
22	CB2	CB2	CB2	CB2	CB2	CB2	CB2	CB2	CB2	CB2	CB2	CB2	CB2	CB2	CB2	CB2	CB2	CB2	CB2	CB2	CB2
23	CB3	CB3	CB3	CB3	CB3	CB3	CB3	CB3	CB3	CB3	CB3	CB3	CB3	CB3	CB3	CB3	CB3	CB3	CB3	CB3	CB3
24	CB4	CB4	CB4	CB4	CB4	CB4	CB4	CB4	CB4	CB4	CB4	CB4	CB4	CB4	CB4	CB4	CB4	CB4	CB4	CB4	CB4
25	CB5	CB5	CB5	CB5	CB5	CB5	CB5	CB5	CB5	CB5	CB5	CB5	CB5	CB5	CB5	CB5	CB5	CB5	CB5	CB5	CB5
26	CB6	CB6	CB6	CB6	CB6	CB6	CB6	CB6	CB6	CB6	CB6	CB6	CB6	CB6	CB6	CB6	CB6	CB6	CB6	CB6	CB6
27	CB7	CB7	CB7	CB7	CB7	CB7	CB7	CB7	CB7	CB7	CB7	CB7	CB7	CB7	CB7	CB7	CB7	CB7	CB7	CB7	CB7
28	CB8	CB8	CB8	CB8	CB8	CB8	CB8	CB8	CB8	CB8	CB8	CB8	CB8	CB8	CB8	CB8	CB8	CB8	CB8	CB8	CB8
29	BP1	BP1	BP1	BP1	BP1	BP1	BP1	BP1	BP1	BP1	BP1	BP1	BP1	BP1	BP1	BP1	BP1	BP1	BP1	BP1	BP1
30	BP2	BP2	BP2	BP2	BP2	BP2	BP2	BP2	BP2	BP2	BP2	BP2	BP2	BP2	BP2	BP2	BP2	BP2	BP2	BP2	BP2
31	BP3	BP3	BP3	BP3	BP3	BP3	BP3	BP3	BP3	BP3	BP3	BP3	BP3	BP3	BP3	BP3	BP3	BP3	BP3	BP3	BP3
32	BP4	BP4	BP4	BP4	BP4	BP4	BP4	BP4	BP4	BP4	BP4	BP4	BP4	BP4	BP4	BP4	BP4	BP4	BP4	BP4	BP4
33	BP5	BP5	BP5	BP5	BP5	BP5	BP5	BP5	BP5	GND	AC10	AC10	BP5	BP5	BP5	BP5	BP5	BP5	BP5	BP5	BP5
34	BP6	BP6	BP6	BP6	BP6	BP6	BP6	BP6	BP6	BP6	BP6	BP6	BP6	BP6	BP6	BP6	BP6	BP6	BP6	BP6	BP6
35	BP7	BP7	BP7	BP7	BP7	BP7	BP7	BP7	BP7	BP7	BP7	BP7	BP7	BP7	BP7	BP7	BP7	BP7	BP7	BP7	BP7
36	BP8	BP8	BP8	BP8	BP8	BP8	BP8	BP8	BP8	BP8	BP8	BP8	BP8	BP8	BP8	BP8	BP8	BP8	BP8	BP8	BP8
37	LV1	LV1	LV1	LV1	LV1	LV1	LV1	LV1	LV1	LV1	LV1	LV1	LV1	LV1	LV1	LV1	LV1	LV1	LV1	LV1	LV1
38	LV2	LV2	LV2	LV2	LV2	LV2	LV2	LV2	LV2	LV2	LV2	LV2	LV2	LV2	LV2	LV2	LV2	LV2	LV2	LV2	LV2
39	LV3	LV3	LV3	LV3	LV3	LV3	LV3	LV3	LV3	LV3	LV3	LV3	LV3	LV3	LV3	LV3	LV3	LV3	LV3	LV3	LV3
40	LV4	LV4	LV4	LV4	LV4	LV4	LV4	LV4	LV4	LV4	LV4	LV4	LV4	LV4	LV4	LV4	LV4	LV4	LV4	LV4	LV4
41	LV5	LV5	LV5	LV5	LV5	LV5	LV5	LV5	LV5	LV5	LV5	LV5	LV5	LV5	LV5	LV5	LV5	LV5	LV5	LV5	LV5
42	LV6	LV6	LV6	LV6	LV6	LV6	LV6	LV6	LV6	LV6	LV6	LV6	LV6	LV6	LV6	LV6	LV6	LV6	LV6	LV6	LV6
43	LC2	LC2	LC2	LC2	LC2	LC2	LC2	LC2	LC2	LC2	LC2	LC2	LC2	LC2	LC2	LC2	LC2	LC2	LC2	LC2	LC2
44	LC3	LC3	LC3	LC3	LC3	LC3	LC3	LC3	LC3	LC3	LC3	LC3	LC3	LC3	LC3	LC3	LC3	LC3	LC3	LC3	LC3
45	LC4	LC4	LC4	LC4	LC4	LC4	LC4	LC4	LC4	LC4	LC4	LC4	LC4	LC4	LC4	LC4	LC4	LC4	LC4	LC4	LC4
46	LC5	LC5	LC5	LC5	LC5	LC5	LC5	LC5	LC5	LC5	LC5	LC5	LC5	LC5	LC5	LC5	LC5	LC5	LC5	LC5	LC5
47	LC6	LC6	LC6	LC6	LC6	LC6	LC6	LC6	LC6	LC6	LC6	LC6	LC6	LC6	LC6	LC6	LC6	LC6	LC6	LC6	LC6
48	AT1	AT1	AT1	AT1	AT1	AT1	AT1	AT1	AT1	AT1	AT1	AT1	AT1	AT1	AT1	AT1	AT1	AT1	AT1	AT1	AT1
49	DT1	DT1	DT1	DT1	DT1	DT1	DT1	DT1	DT1	DT1	DT1	DT1	DT1	DT1	DT1	DT1	DT1	DT1	DT1	DT1	DT1
50	CD1	CD1	CD1	CD1	CD1	CD1	CD1	CD1	CD1	CD1	CD1	CD1	CD1	CD1	CD1	CD1	CD1	CD1	CD1	CD1	CD1

APPENDIX C

ROCK MASS MODEL ASSEMBLY PROCEDURE

ROCK MASS MODEL ASSEMBLY PROCEDURE

1. Attach end structures to base structure with slotted hinges. Square up assembly with 48.5 in. (1.23 m) spacing between vertical end plates, and install two horizontal bars on each side to hold assembly rigid. Install one horizontal bar in top holes and one in bottom holes.

2. Begin laying half-ingots onto base plate and against end plates. Half-ingots have bonded 0.25 in. (6.35 mm) rubber which is coated with silicone grease on metal contact surface.

3. After laying about three or four ingot rows, readjust vertical endplate spacing by loosening hinge slot bolts and horizontal bar nuts. Spacing adjusted for best fit of ingot rows to minimize ingot overlap due to ingot dimensional variations. [48.75 in. (1.24 m) spacing found to work best]. Assembly then retightened.

4. Lay ingots to just above center tunnel for best fit around tunnel. Use four split rings to support top of tunnel.

5. Mark ingots above tunnel to identify position and remove them and four split rings to allow access to inner surface of tunnel ingots. Drill ingots for four LVDT positions, and install LVDT's with bases in lower positions. Use pliable cement for LVDT fixation on both base and core-rod ends.

6. Reinstall four split rings and marked ingots above tunnel and lay rest of ingots into the assembly. Top layer of half-ingots are coated with silicone grease on metal contact surface.

7. Install both side shear plates with tightened bolts and remove four side bars.

8. Install four horizontal cables on each side. Include load cells at right top and midlow positions when facing the near side, and at left bottom position when facing the far side. Tighten cables to following tensions: top-41 lb, midhigh-91 lb, midlow-133 lb, bottom-165 lb.

9. Loosen hinge bolts on one end structure and vertical end/side plate bolts on both sides of same end structure. Remove center tunnel rings. Readjust horizontal cable tensions to above values.

10. Install top structure with corner rollers included and loose adjustment in slots. Readjust horizontal cable tensions to: top-43 lb, midhigh-92 lb, midlow-133 lb, bottom-165 lb.

11. Install two top weights onto top structure with holes aligned only. Readjust horizontal cable tensions to: top-53 lb, midhigh-101 lb, midlow-143 lb, bottom-173 lb.

12. Install remaining two top weights and temporarily clamp all four top weights into place with bolt holes open. Readjust horizontal cable tensions to: top-82 lb, midhigh-153 lb, midlow-188 lb, bottom-205 lb.

13. Install four vertical cables on each side. Include load cell at right position when facing the near side, and at right position when facing the far side.

14. Adjust vertical and horizontal cable tensions in the following two steps: (1) Vertical: all-118 lb; Horizontal: top-131 lb, midhigh-194 lb, midlow-232 lb, bottom-249 lb and (2) Vertical: all-236

lb; Horizontal: top-180 lb, midhigh-234 lb, midlow-275 lb, bottom-293 lb.

15. Tighten hinge bolts on one end structure and end/side bolts on both sides of same end structure. Adjust and tighten roller mounts at four upper corners.

16. Install one critical cantilever beam and several rock surface strain gages and associated readout equipment. Install lift apparatus and perform lift and movement test while monitoring these readouts along with those of the five load cells.

17. Decide whether all remaining instrumentation can be installed before mounting specimen onto seismic table. Remove lifting apparatus and install remaining instrumentation if affirmative. Side shear plates can be removed for this, but must be reinstalled before further lifting of specimen.

18. Install lifting apparatus and move model to seismic table. Remove side shear plates and bolt four top plates to top structure.

19. Perform instrumentation hookup and checkout procedure.

20. Fasten model to seismic table.

APPENDIX D

SPECIFICATIONS FOR SwRI SEISMIC TEST FACILITY

System Description

The seismic test facility at Southwest Research Institute (SwRI) can simulate earthquake motions as well as many other low frequency dynamic environments. It is a true biaxial vibration table capable of delivering simultaneous independent excitation along both horizontal and vertical axes. Drive mechanisms are servo-controlled, with independent control for each axis. Our facility can produce all current types of nuclear plant seismic qualification tests prescribed under USNRC Reg. Guide 1.100 and IEEE 344, Network Equipment Qualification tests, and many other types of tests as well. Detailed capabilities include:

- Maximum payload weight: 6,000 lb
- Payload mounting area: 6 ft × 6 ft
- Payload maximum envelope: 10 ft wide × 10 ft deep × 14 ft high
- Maximum payload CG: Height: 2 ft for 5,000 lb; Above Table Top: 4 ft for 3,000 lb; 6 ft for 1,000 lb

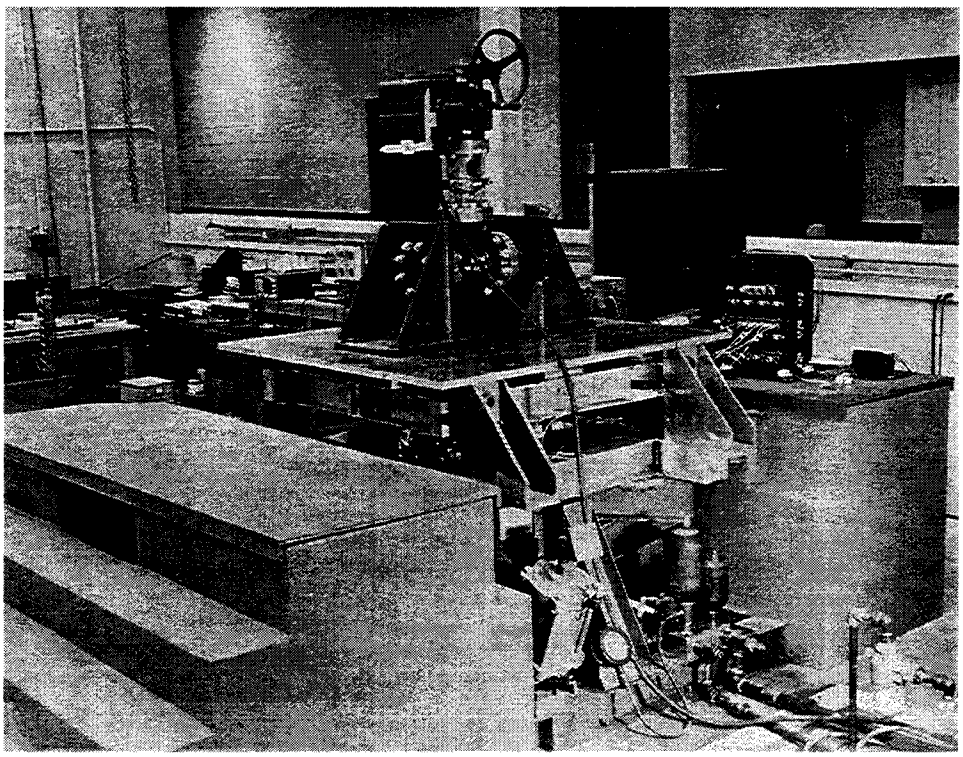

Overview of SwRI biaxial seismic test facility with gate valve mounted test item.

Table Limits	Horizontal	Vertical
Frequency Range*1	0 - 50 Hz	0 - 50 Hz
Force Capacity	10,000 lb	20,000 lb
Max. Stroke	10 in.	8 in.
Max. Velocity	45 in./sec.	22 in./sec.
Max. Acceleration*2	10 g	10 g

*1 Full output, Reduced output to 200 Hz

*2 At zero payload

Associated Instrumentation

Excitation signals are provided typically by digital random or deterministic function generators. Table displacement is accurately controlled at low-to-medium frequencies by automatic feedback. Table motions are monitored by accelerometers whose outputs can be analyzed according to several standard parameters. Acceleration response spectrum can be computed and plotted within seconds. Power spectral density, probability density, and other associated statistical parameters can be computed with digital Real Time Analyzers. All time histories can be digitized and plotted.

For additional information, please contact:

R. L. Bessey, Manager
(210) 522-2345
or
T. A. Fey, Group Leader
(210) 522-3253
Structural Dynamics and Environmental Testing
Division of Mechanical and Fluids Engineering
Southwest Research Institute
6220 Culebra Road • P.O. Drawer 28510
San Antonio, Texas 78228-0510
Fax (210) 522-5122 • Telex 244846